IMPERIAL COLLEGE LONDON

Ultrasonic methods for assessing fatigue degradation in metals

by

Georgios Sarris

A thesis submitted to Imperial College London for the degree of
Doctor of Philosophy

Department of Mechanical Engineering
Imperial College London
London SW7 2BX

September 2022

Declaration of originality

The content of this thesis is my own research work, which was completed with the supervision of Professor Mike Lowe, Dr Peter Huthwaite and Dr Stewart Haslinger. Wherever other work was used I clearly acknowledged, and provided references.

Georgios Sarris

30/09/2022

Copyright

In memory of my grandfather
Στη μνήμη του παππού μου

Abstract

Steel components in nuclear power generation plants suffer from fatigue, due to the cyclic loading to which they are subjected. It is also often the case that the amplitude and frequency of this loading changes in an irregular pattern, as it is directly related to the required power output at any given time. Detecting such damage is made more challenging since the damaged site is often on inaccessible internal surfaces of vessels or pipes. This poses the need to develop a method able to assess the level of such fatigue damage in these components to ensure that they are operating safely.

In this thesis, ultrasound was used as a potential solution to this issue. Previous work with through-thickness longitudinal wave measurements has shown that ultrasound is indeed sensitive to the presence of fatigue, as it will travel more slowly compared with propagating through a non-fatigued volume of a material. However, as fatigue is usually a near surface phenomenon, the bulk longitudinal wave spends limited time inside the fatigue zone, and hence any observed changes are small and difficult to correlate to a specific fatigue state with confidence. Therefore, apart from deriving a fatigue assessment technique, it was also desirable to amplify those changes to minimise the effects of any uncertainties.

The work presented in this thesis begins by verifying the sensitivity of longitudinal waves to the presence of fatigue. The verification was achieved by

constructing longitudinal wave speed C-scans for five flat plates containing fatigue damage, each at a different fatigue level, which verified both that the fatigue spot is visible in those maps, and that also, when changes in speed were considered, the speed reduced monotonically as fatigue progressed.

A natural solution to the issue of amplifying the reduction in a wave's propagation speed due to the presence of a fatigue zone is the use of Rayleigh (surface) waves, as they are restricted to propagate in the surface of a material, where fatigue is usually concentrated. Indeed, when Rayleigh wave B-scans were completed for each of the five plates, it was found that the percentage reduction in speed was amplified by a factor of approximately ten. Additionally, using a stiffness reduction approach, a method able to accurately encapsulate the effects which fatigue has on the time-of-flight of longitudinal and Rayleigh waves in a finite element model was also developed. The results from the finite element models were found to agree well with the experimental measurements.

In an attempt to extend the surface waves method to pipes, an extensive numerical study on the feasibility of using creeping waves for fatigue state characterisation was completed, as those are waves which can be excited on the inner surface of a pipe, without having access to it. It was found that for the geometries which are of interest to the nuclear power generation industry, the use of such an approach did not yield satisfactory results, due to multiple unwanted reflections and secondary modes interfering with the monitoring of the creeping wave. Therefore, for pipe geometries, a through-thickness approach was considered, this time using shear waves, deployed and analysed by raster scanning from the outer surface. The challenge of obtaining shear wave C-scans was overcome with the use of EMATs and a stepper motor frame. The resulting C-scans showed an increase in the sensitivity to fatigue of more than double compared with longitudinal waves. Also, the speed-reduction behaviour was explained and verified by measuring the dislocation density of samples corresponding to different fatigue states and comparing the results to existing theoretical models.

Finally, the use of surface waves in the work completed in this thesis motivated a secondary study on the attenuation of Rayleigh waves when propagating over a rough surface. The well-established scattering theory in two-dimensional (2D) analysis was verified using finite element modelling in all three scattering regimes: Rayleigh, stochastic and geometric, and was also extended to roughness parameters outside the region of validity of the theory. The verification also provides useful insight in terms of verifying the three-dimensional (3D) theory as well.

Acknowledgements

Even though the spine of this thesis suggests that I am the sole author of this work, it is undeniable that its completion would not have been possible without the contribution of many. There are no words that would not fall short of expressing the magnitude of my gratitude to them; however, I will try my utmost best.

First and foremost I would like to thank my supervisors, Mike Lowe, Peter Huthwaite and Stewart Haslinger for their continuous support and encouragement during the past four years, both of which often extended beyond academic matters. Working with you has been a true privilege and I am forever indebted to you for the knowledge which I have inherited. You have set the standard for a good mentor very high; thank you for making the past four years a true journey through science.

I would also like to thank my industrial supervisors, John Taggart from Jacobs and Misty Haith, Tim Skinner and Alex Tam from Rolls-Royce for their valuable input and support throughout this project. For the completion of the experimental work in this thesis, I am grateful to Antonio de Sanctis - without his creativity, many of the results presented here would have been unobtainable.

Completing my PhD in the NDE group has been a great pleasure and I am

very grateful for all the help from my colleagues. I have reserved a special thanks for my dear friend and office-mate Evripides, for his support, immense patience, and the multiple academic and non-academic conversations during the past few years.

Finally, I would like to thank my parents, Christos and Georgia, and my brother, Orestis for their unconditional love, encouragement and ever-lasting support through the entirety of my studies.

Ευχαριστώ!

Contents

List of Figures

List of Tables

List of Publications

1. G. Sarris, S. G. Haslinger, P. Huthwaite, P. B. Nagy and M. J. S. Lowe, "Attenuation of Rayleigh waves due to surface roughness," *Journal of the Acoustical Society of America*, vol. 149, pp. 4298–4308, 2021.
2. G. Sarris , S. G. Haslinger, P. Huthwaite, and M. J. S. Lowe, "Ultrasonic methods for the detection of near surface fatigue damage," *NDT & E International*, vol. 135, pp. 102790, 2023 .
3. G. Sarris, S. G. Haslinger, P. Huthwaite, and M. J. S. Lowe, "Fatigue state characterisation of steel pipes using ultrasonic shear waves," *IEEE Transactions on Ultrasonics, Ferroelectrics, and Frequency Control*, vol. 70, no. 1, 2023.
4. G. Sarris, S. G. Haslinger, P. Huthwaite, P. B. Nagy and M. J. S. Lowe, "Attenuation of Rayleigh waves due to 3D surface roughness," *Journal of the Acoustical Society of America*, (Submitted).

Chapter 1

Introduction

1.1 Motivation

Fatigue is a phenomenon in which a component fails during cyclic loading, at stress levels below those for which it was designed to withstand under regular operation. This failure does not occur due to the inability of the component to support each individual stress cycle, but rather due to the slowly accumulating, infinitesimal damage that each cycle introduces to the component, which progressively leads to the creation of cracks, and eventually, failure.

Due to the cumulative nature of the degradation caused by fatigue, it is important to be able to characterise the fatigue state of components which are prone to it, to ensure that they are inspected and replaced in a timely manner. This becomes increasingly important for safety-critical components - an example of such components, which also motivated this study, are pipes operating within nuclear steam raising plants, which suffer from fatigue due to the cyclic pressure and temperature of the water and steam travelling through them.

There currently exist multiple theoretical models for predicting remaining fatigue life, however, their use is potentially infeasible in industrial applications. This is because they require a priori knowledge of material parameters and loading information, which is either difficult or impractical to accurately determine for a real component, especially when the component is loaded with various amplitudes and at different frequencies for each amplitude. As a result, industry currently uses some very conservative estimates for fatigue state estimation, which results to a high inspection and maintenance costs. This poses the need for the development of a method able to characterise the fatigue state of engineering components in a practical and more precise way to what is currently available.

The work presented in this thesis proposes the use of ultrasound as an alternative practical method for fatigue state assessment. The theory [1–5], predicts that the presence of a fatigue zone in the propagation path of an ultrasonic wave will alter its propagation speed and attenuation coefficient. However, as fatigue is usually a near-surface phenomenon, the use of through-thickness longitudinal wave measurements would cause the waves to spend very little time inside the fatigue zone, rendering any potential changes small and difficult to correlate to a specific fatigue state.

To mitigate this issue, and also accommodate for both flat and cylindrical geometries, the work in this thesis focuses on two fatigue state assessment methods. For flat components, the use of Rayleigh waves is proposed as they travel on the surface of a material and hence would be maximally affected by the presence of a fatigue zone. For cylindrical components, a novel shear wave C-scanning technique is proposed, which utilises the inherently larger sensitivity of shear waves [5] to the presence of a fatigue zone.

Additionally, the use of Rayleigh waves in this thesis also motivated a further area of study - as Rayleigh waves will inherently be affected by the presence of physical obstacles in their propagation path, it is undoubtedly useful to investigate their interaction with a rough surface. This is because any realistic surface possesses a certain degree of roughness and therefore, knowledge of how Rayleigh waves interact with it can provide useful information for either the nature of the roughness itself, or, under the scope of a Rayleigh wave measurement, how the behaviour of the wave will diverge from the expected due to the presence of the roughness.

1.2 Thesis outline

Following the brief introduction to the work presented in this thesis, Chapter 2 explains how the Finite Element (FE) software Pogo [6] and the theory presented in the same chapter were used to derive a method able to excite a clean Rayleigh wave in an FE domain, as well as an extension to this method which enables the correct modelling of the attenuation of these waves. Such a method was of utmost importance to the work presented in this thesis, as a large proportion of the fatigue related simulation, as well as all the rough surface simulations, required the use of Rayleigh waves.

Chapter 3 presents the theory, experimental methods and results relating to the use of Rayleigh waves for fatigue state assessment, achieved via correlating the change in Rayleigh wave propagation speed to the fatigue state of five purposely fatigued plates, each at a different fatigue level. The results are compared against analogous measurements using longitudinal bulk waves, and are also used to derive a model to represent the effects of fatigue damage in the time-of-flight of longitudinal and Rayleigh waves, in an FE domain.

Building on the ideas presented in Chapter 3, Chapter 4 presents a potential method to extend the fatigue state assessment methods for plates into pipes, with the aid of creeping waves. A thorough investigation of selecting the optimal parameters for creeping wave excitation is presented, as well as some preliminary results for idealised conditions. However, this chapter also discusses the issues which arise with this method when more realistic FE conditions were used, which resulted in the exploration of alternative methods, utilising either different types of waves/wave behaviour or more involved FE excitation and processing techniques.

As the results presented in Chapter 4 were deemed unsatisfactory for the purposes of this study, Chapter 5 reverts to the idea of using through-thickness waves for fatigue state assessment, this time with shear waves generated from EMATs. Using the inherent property of EMATs not requiring mechanical coupling to excite ultrasonic waves, a method to obtain results analogous to those in Chapter 3 is presented. However, the use of shear waves, as supported by the theory, also proved to be advantageous in amplifying the changes in speed observed due to the presence of fatigue. Additionally, a method to easily extend this technique to pipe geometries is presented, as well as a preliminary technique to further optimise this method to pipes with smaller diameters.

Finally, Chapter 6 presents a thorough FE study of the attenuation behaviour of Rayleigh waves propagating on a rough surface. In this chapter, the theory and modelling techniques used to complete this study in an efficient, realistic and mathematically meaningful way are discussed, and both quantitative and asymptotic results are presented and compared to the relevant theory.

Chapter 2

Numerical modelling of Rayleigh waves

2.1 Introduction

A significant part of the results presented in this thesis comes from numerical simulations involving Rayleigh waves. Therefore, it was necessary to develop the required methods for generating a clean Rayleigh wave, with minimal noise and with minimal excitation of other modes before proceeding to develop either the fatigue or rough surfaces models. Additionally, the ability to simulate the attenuation of Rayleigh waves correctly was also investigated, since such a capability could prove useful in future work.

The successful generation of clean Rayleigh waves requires thorough understanding of the theory behind them. Therefore, prior to presenting the FE methods, this chapter discusses briefly the theory related to the excitation of Rayleigh waves, with a focus on the particle displacement in such waves. Following this derivation, this chapter presents the method developed to excite

Rayleigh waves of good quality in an FE domain and presents examples of the Rayleigh wave signals obtained by implementing this method. Additionally, as an extension to the aforementioned method, a derivation of a supplementary method able to model the attenuation of Rayleigh waves is presented, accompanied by four attenuation examples of increasing complexity, which verify the capabilities of the method.

2.2 Rayleigh wave theory

The derivations presented here follow the work in [7] and [8]. Let us consider a semi-infinite, homogeneous, isotropic material occupying an infinite half space extending in the positive z direction, as shown in Figure 2.1. Let us also assume that vacuum occupies the space for $z < 0$. If the displacement field of the Rayleigh wave is denoted by $\mathbf{u}$, with x and z components u_x and u_z respectively, and a smooth wave field is assumed, $\mathbf{u}$ can be written as

$$\mathbf{u} = (u_x, u_z) = \nabla\phi + \nabla \times \boldsymbol{\psi}, \tag{2.1}$$

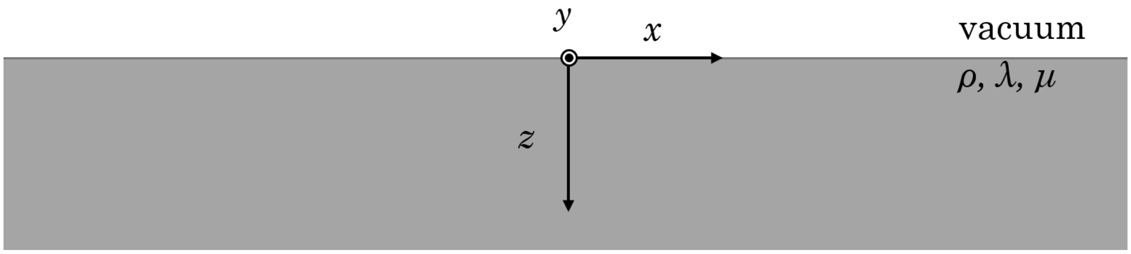

Figure 2.1: Schematic the setup and coordinate axis used for the derivation of the displacements of a Rayleigh wave.

Additionally, the equation of motion in such a medium with no body force is [7]:

$$\mu\nabla^2\mathbf{u} + (\lambda+\mu)\nabla\nabla\cdot\mathbf{u} = \rho\left(\frac{\partial^2\mathbf{u}}{\partial t^2}\right), \tag{2.2}$$

where λ and μ are the first and second Lamè constants respectively, ρ is the density and t denotes time.

Substituting (2.1) into (2.2) yields

$$\mu\nabla^2[\nabla\phi + \nabla\times\boldsymbol{\psi}] + (\lambda+\mu)\nabla\nabla\cdot[\nabla\phi + \nabla\times\boldsymbol{\psi}] = \rho\left(\frac{\partial^2}{\partial t^2}[\nabla\phi + \nabla\times\boldsymbol{\psi}]\right)$$

which when rearranged yields:

$$\nabla\times\left[\mu\nabla^2\boldsymbol{\psi} - \rho\frac{\partial^2\boldsymbol{\psi}}{\partial t^2}\right] + \nabla\left[(2\mu+\lambda)\nabla^2\phi - \rho\frac{\partial^2\phi}{\partial t^2}\right] = 0.$$

Therefore, for Equation (2.2) to hold true, ϕ and $\boldsymbol{\psi}$ must satisfy

$$\begin{aligned}\nabla^2\phi &= \frac{1}{C_L^2}\frac{\partial^2\phi}{\partial t^2},\\ \nabla^2\boldsymbol{\psi} &= \frac{1}{C_T^2}\frac{\partial^2\boldsymbol{\psi}}{\partial t^2}.\end{aligned} \tag{2.3}$$

In Equation (2.3), the longitudinal and transverse wave speeds, (C_L and C_T respectively) are defined as:

$$C_L = \sqrt{\frac{\lambda+2\mu}{\rho}}, \tag{2.4}$$

and

$$C_T = \sqrt{\frac{\mu}{\rho}}. \tag{2.5}$$

Equations (2.3) further simplify to

$$\begin{aligned} \nabla^2 \phi &= -k_L^2 \phi, \\ \nabla^2 \boldsymbol{\psi} &= -k_T^2 \boldsymbol{\psi}, \end{aligned} \tag{2.6}$$

under the assumption of a time harmonic solution, where the longitudinal (k_L) and shear (k_T) wavenumbers are defined as

$$k_L = \frac{\omega}{C_L}, \tag{2.7}$$

$$k_T = \frac{\omega}{C_T}, \tag{2.8}$$

and ω is the angular frequency of the waves.

For the particular case of Rayleigh waves, which are waves occurring in solids at sound-soft boundaries, particle motion is restricted within the $x - z$ plane, and therefore, $\boldsymbol{\psi} = (0, \psi, 0)$.

Now, in the right-hand side of Equation (2.1),

$$\nabla \phi = \left(\frac{\partial \phi}{\partial x}, \frac{\partial \phi}{\partial y}, \frac{\partial \phi}{\partial z} \right), \tag{2.9}$$

and

$$\nabla \times \boldsymbol{\psi} = \left(-\frac{\partial \psi}{\partial z}, 0, \frac{\partial \psi}{\partial x} \right). \tag{2.10}$$

By substituting Equations (2.9) and (2.10) in (2.1), the x and z components of the displacement can be expressed in terms of the scalar and vector potentials as follows:

$$\begin{aligned} u_x &= \frac{\partial \phi}{\partial x} - \frac{\partial \psi}{\partial z}, \\ u_z &= \frac{\partial \phi}{\partial z} + \frac{\partial \psi}{\partial x}. \end{aligned} \tag{2.11}$$

Since solutions representing plane, time harmonic waves are required, ϕ and ψ can be written as:

$$\begin{aligned} \phi &= \Phi(z)\mathrm{e}^{j(kx-\omega t)}, \\ \psi &= \Psi(z)\mathrm{e}^{j(kx-\omega t)}, \end{aligned} \tag{2.12}$$

where j is the imaginary unit and k is the wavenumber. As these equations are indeed time harmonic, they can be substituted in (2.6), and the resulting ϕ and ψ values will still satisfy Equation (2.2). Equation (2.6) is satisfied when $\Phi(z)$ and $\Psi(z)$ are such that:

$$\begin{aligned} &\frac{d^2}{dz^2}\Phi(z) - (k^2 - k_L^2)\Phi(z) = 0, \\ &\frac{d^2}{dz^2}\Psi(z) - (k^2 - k_T^2)\Psi(z) = 0. \end{aligned} \tag{2.13}$$

The solution to the above differential equations, along with the stress-free boundary conditions [8] yields

$$\begin{aligned} \phi &= -A\mathrm{e}^{j(kx-\omega t)-\zeta z}, \\ \psi &= jA\frac{2k\zeta}{k^2+\xi^2}\mathrm{e}^{j(kx-\omega t)-\xi z}, \end{aligned} \tag{2.14}$$

where $\zeta^2 = k^2 - k_L^2$, $\xi^2 = k^2 - k_T^2$ and A is a constant. Finally, the expressions for ϕ can ψ can be substituted in Equation (2.11), to obtain the displacements for a Rayleigh wave by using the real part of the result:

$$\begin{aligned} u_x &= A k_R \left(\mathrm{e}^{-\zeta_R z} - \frac{2\zeta_R \xi_R}{k_R^2 + \xi_R^2} \mathrm{e}^{-\xi_R z} \right) \sin(k_R x - \omega t), \\ u_z &= A \zeta_R \left(\mathrm{e}^{-\zeta_R z} - \frac{2 k_R^2}{k_R^2 + \xi_R^2} \mathrm{e}^{-\xi_R z} \right) \cos(k_R x - \omega t), \end{aligned} \tag{2.15}$$

with $k_R = \omega / C_R$ being the Rayleigh wavenumber, $\zeta_R^2 = k_R^2 - k_L^2$, $\xi_R^2 = k_R^2 - k_T^2$, and C_R being the Rayleigh wave speed. The first interesting feature of Equation (2.15) is that it reveals the well-known elliptic trajectory which particles in a material follow when a Rayleigh wave propagates, as (u_x, u_z) has the form of the standard parametrisation of an ellipse, for a given frequency and material. Additionally, the non-dispersive nature of the Rayleigh wave is also evident, as the result does not require a dependence of k_R or C_R on the frequency. This reinforces the motivation of using the speed of a Rayleigh wave as a method to characterise the fatigue state of steel components, because non-dispersive waves allow for more accurate speed measurements, since the peaks in the time-trace of such signals do not exhibit dispersion-related shifts which potentially lead to inaccuracies in speed measurements.

Furthermore, C_R can be approximated by [7, 8]

$$C_R = \frac{0.87 + 1.12\nu}{1 + \nu} C_T, \tag{2.16}$$

where ν is the Poisson's ratio. This implies that for real materials ($0 < \nu < 0.5$), $C_R \in [0.87 C_T, 0.96 C_T]$. Finally, it is worth noting that subsequent studies have shown that the ratio between u_x and u_z depends solely on ν and is therefore constant for a given material [9]. This result became relevant in this study when attempting to excite clean Rayleigh waves in a Finite-Element (FE) simulation.

2.3 Finite element modelling theory

All of the numerical simulations in this thesis were completed using the high-fidelity GPU-based FE software Pogo [6]. Pogo uses the standard discretisation method used in most FE packages, which involves discretising the domain into regions of finite size, connected by nodes [10]. Pogo then calculates the displacement at each node by implementing the finite-difference method in the time domain, and utilising the boundary conditions (i.e. the values of the displacement at pre-determined nodes). For a general model with damping terms, the equation of elasticity is

$$\mathbf{M}\ddot{\mathbf{U}} + \mathbf{C}\dot{\mathbf{U}} + \mathbf{K}\mathbf{U} = \mathbf{F}. \tag{2.17}$$

In Equation (2.17) **M**, **C**, **K** and **F** are the mass, damping, stiffness and the applied force matrices, and $\mathbf{U}$, $\dot{\mathbf{U}}$ and $\ddot{\mathbf{U}}$ denote the nodal displacement, speed and acceleration matrices respectively. Each of the entries in the aforementioned matrices corresponds to a degree of freedom for a particular node. By implementing the finite difference method, Equation (2.17) becomes:

$$\mathbf{M}\frac{\mathbf{U}^{s+1} - 2\mathbf{U}^{s} + \mathbf{U}^{s-1}}{\Delta t^2} + \mathbf{C}\frac{\mathbf{U}^{s+1} - \mathbf{U}^{s-1}}{2\Delta t} + \mathbf{K}\mathbf{U}^{s} = \mathbf{F}, \tag{2.18}$$

where the superscript s denotes the s^{th} time step, and Δt is the duration of that time step. Knowledge of the displacement at the previous two time steps allows Equation (2.18) to be solved for finding the displacement at the $(s+1)^{\text{th}}$ step. This approach for FE-studies of elastic wave propagation, implemented in Pogo has also been used in many other studies [11–13].

2.4 Obtaining a clean Rayleigh wave signal

An FE model comprised of a rectangular FE domain, a single source and single monitor node (both on the lower boundary of the FE domain), as shown in Figure 2.2, was initially created to assess the quality of Rayleigh waves excited simply by displacing the source node in either the horizontal or vertical direction, and to determine potential issues that arise with the excitation of Rayleigh waves in 2D plate-like domains. Monitor nodes are points in the domain whose displacement is recorded and stored during the solution of the model, and can therefore be used in the post-processing of the results.

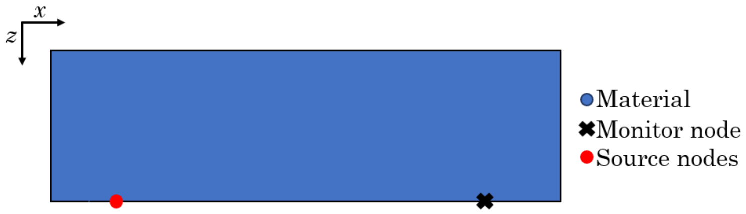

Figure 2.2: Schematic of the initial model used to derive the method for creating a good quality Rayleigh wave. This model contains a single source node and a single monitor node.

In this model, the length of the domain was set to 30 mm, and the thickness was set to 5 mm. The source and monitor nodes were placed 20 mm apart. The domain was meshed using 2D square elements, and the mesh size was set to be approximately equal to $\lambda_R/30$, where λ_R is the Rayleigh wavelength, calculated at the centre frequency. This level of discretisation is necessary to minimise numerical dispersion to a suitable level and hence to avoid numerical dispersion of the solutions [14]. Almost all FE-related work in this thesis was done using 4-node rectangular, linear elements and, in some cases, using 3-node, triangular, linear elements. In the simulations for this section, the material properties for the simulation were set to E = 200 GPa, ν = 0.25

and $\rho = 7800$ kg/m^3, where E is the Young's Modulus.

A very simplistic method to excite a Rayleigh wave in such a domain is to displace the source node, which is located on the surface of the domain, in either the horizontal or vertical direction. To investigate the quality of Rayleigh waves excited with this simple method, a 5-cycle, Hann-windowed toneburst, with a centre frequency of 10 MHz was applied to the source node. Two models were created, one where this signal was applied to the node in the horizontal direction, and one where it was applied in the vertical direction. After solving the models, the resulting wave fields were visualised using Paraview 5.6.0 (New Mexico, USA). Paraview is a software allowing the user to input eXtensible Data Model and Format (XDMF) files, which can be generated by PogoPro, and visualise the wave field in the model at predetermined time instances. The results are shown in Figure 2.3.

As shown in Figure 2.3, both methods have successfully excited Rayleigh waves, travelling on the bottom boundary of the domain, however, two issues can be seen in both subfigures. Firstly, two Rayleigh waves of approximately equal magnitude were excited instead of one, travelling in opposite directions. Additionally, in both subfigures, this method has excited large longitudinal and shear waves, which both occupy almost the entire thickness of the FE domain, potentially leading to unwanted reflections, and interference/noise in measurements.

From the above-mentioned observations it was evident that it was necessary to develop a method able to minimise the excitation of other modes, without compromising the quality of the Rayleigh waves. Using the pair of equations in (2.15), and exploiting the fact that particles follow an elliptical trajectory in a Rayleigh wave [15], it was expected that if one were able to implement elliptical excitation to the source, then a pure Rayleigh wave mode would be excited.

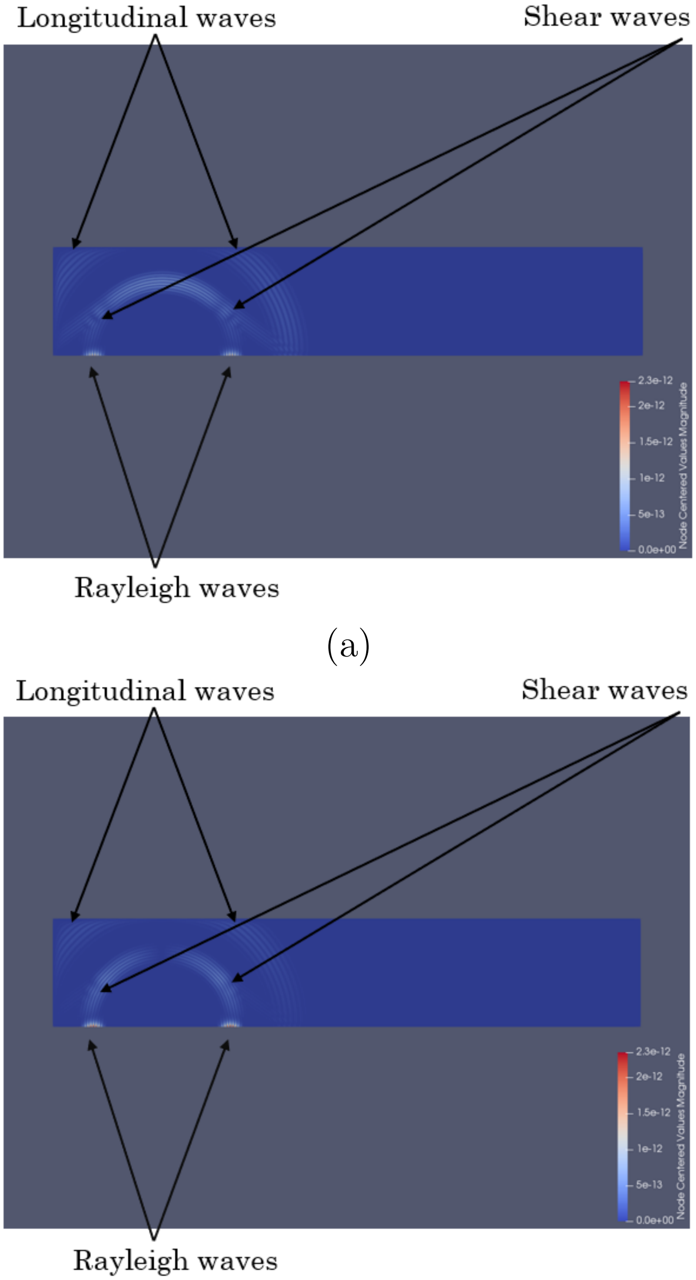

(a)

(b)

Figure 2.3: Example of the wave fields created by exciting a source node in either the horizontal (a) or vertical (b) direction. The colour scale in the figure represents the absolute magnitude of the displacement at each node. The QR code directs to an animation of this process.

To achieve this, the single source node was replaced by a source line, as shown in Figure 2.4, comprised of multiple source nodes. The length of the source line was chosen to be $3\lambda_R$, calculated at the centre frequency of the simulation. The monitor node remained 20 mm away from the centre of the source line.

Figure 2.4: Schematic of the model used to improve the quality of Rayleigh waves in an FE model. This model contains a source line and a single monitor node.

Each of the source nodes in the source line was assigned two time harmonic excitation signals with a $\pi/2$ phase difference between them - the presence of a sine and a cosine signal allows for the implementation of the elliptical mode shape excitation to the source nodes, when one is applied orthogonally to the other. This is because the standard parametrisation of an ellipse, in Cartesian coordinates, is of the form $(\mathrm{a}\cos(\iota), \mathrm{b}\sin(\iota))$, where a and b are arbitrary constants whose ratio determines the eccentricity of the ellipse and ι is the positive, counter-clockwise angle measured from the x axis. Additionally, phase delays were implemented to each source node, such that constructive interference occurred in the desired direction. This method is described in detail below:

- Two sinusoidal, Hann-windowed time-domain tonebursts were created, with a 90° phase shift between them. This amplitude was selected arbitrarily, as the absolute magnitude of the signal is not important for speed or attenuation measurements.

- Pogo provides the ability to assign each source node a unique amplitude, which scales the time domain signal assigned to that node accordingly. Therefore, the amplitude at each node was selected in a way such that a clean Rayleigh wave, with the correct amplitude and phase was created by the interference of the signal from all the nodes.

- Namely, the complex amplitude assigned the i^{th} source node, a_i, located at the x_i position in the model is given by:

$$a_i = \frac{1}{2}\left[1 - \cos\left(2\pi\frac{x_i - x_{\min}}{x_{\max} - x_{\min}}\right)\right] \mathrm{e}^{jk_R x_i}, \tag{2.19}$$

  where, $x_{\min}$ is the position of the leftmost source node and $x_{\max}$ is the position of the rightmost source node. The collective use of a unique amplitude at each node, according to Equation (2.19), results in the constructive interference of the signals from all source nodes, in the correct direction, which generates a clean Rayleigh wave.

- The first signal was applied to the i^{th} node with a weighting of [$\Im(a_i)$, -$\Re(a_i)$] and the second signal with a weighting of [-$\Re(a_i)$, -$\Im(a_i)$], where the two entries in the previous vectors denote the x and z direction respectively, and the notations. $\Re()$ and $\Im()$ denote the real and imaginary part of their argument respectively. This method of assigning the x and z amplitudes has the effect of imitating the elliptical mode shape of a Rayleigh wave. Again, the amplitudes of the x and z components of the Rayleigh wave were arbitrarily selected since those do not affect speed or attenuation measurements.

An example of a Rayleigh wave field generated by implementing this method is shown in Figure 2.5. As shown in Figure 2.5, a clean Rayleigh wave field has been generated. The minimal head waves which lie above the Rayleigh wave have a very small amplitude, and also lie away from the measuring locations,

Figure 2.5: Rayleigh wave field, travelling in the positive x-direction created using the method described in this section. The colour scale in the figure represents the absolute magnitude of the displacement at each node. The Rayleigh wave's centre frequency is 10 MHz.

therefore they will not interfere with the attenuation measurements. It is worth noting that the method discussed here is also applicable to all source lengths, as long as the length is larger than one Rayleigh wavelength.

Additionally, the x and z displacements of the wave field shown in Figure 2.5, are shown in subfigures 2.6a and 2.6b respectively. As shown in Figure 2.6, both signals are clean, have distinguishable peaks and minimal noise. One more interesting observation in Figure 2.6 is that the ratio of the z to the x displacement is approximately 1.54 - this reflects well the physics of a Rayleigh wave. As explained by Hassan & Nagy [9], the allowable range for the z over x amplitude of a Rayleigh wave for a real material is 1.3-1.8; the ratio obtained here is well within this range.

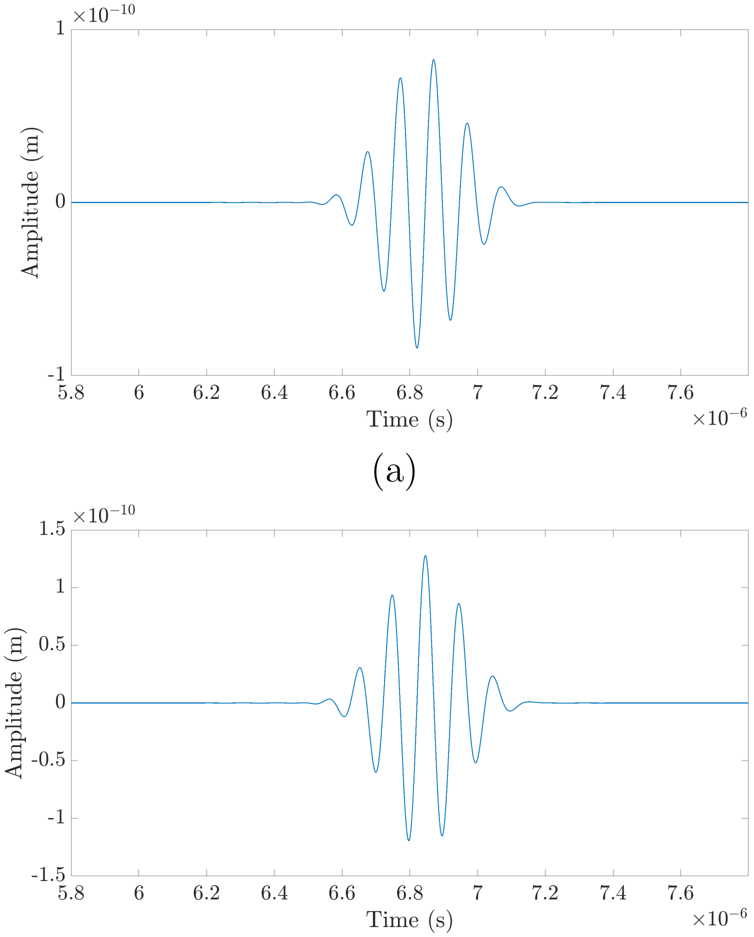

(a)

(b)

Figure 2.6: Example of the Rayleigh wave displacements in the (a) x and (b) z directions, obtained by the use of the method described in this chapter.

2.5 Attenuation of Rayleigh waves

As demonstrated in the previous subsection, the particle displacements in a Rayleigh wave follow elliptical trajectories, whose eccentricity is a function of the material's Poisson ratio. This elliptical motion makes correctly modelling the attenuation of Rayleigh waves not as straightforward in an FE domain compared with waves where the particle motion lies in a straight line.

However, due to superposition, elliptical displacements can always be separated into horizontal (x) and vertical (z) components, and hence, a Rayleigh wave can be treated as the exact sum of its longitudinal and shear components. Therefore, if it is possible to derive FE simulation parameters such that those longitudinal and shear components attenuate by the correct amount independently, those parameters are expected to correctly attenuate the Rayleigh wave to which these longitudinal and shear waves correspond.

Since such a technique involves attenuating of two independent components to begin with, it is required to use two methods of energy loss in FE. In Pogo, this can be achieved through the use of the Pogo attenuation coefficient α_{Pogo}, and the kinematic viscosity, η. Let us assume two points, x_1 and x_2 separated by a distance d in an FE domain. Let us also denote the amplitude of the wave at those points by A_{x_1} and A_{x_2} respectively, and the speed of that wave by C. Then, α_{Pogo} is defined as:

$$\alpha_{\mathrm{Pogo}} = -\frac{2C}{\mathrm{d}} \ln\left(\frac{A_{x_2}}{A_{x_1}}\right) = -\frac{2C}{\mathrm{d}} \ln\left(p\right), \tag{2.20}$$

where p is the ratio of the amplitude of the wave at location x_2 to x_1. Therefore, a value of α_{Pogo} in a Pogo FE model will cause the wave amplitude to drop to p of its initial amplitude after having travelled distance d.

When a value of α_{Pogo} is introduced in Pogo, the density parameter in the model becomes complex:

$$\rho \rightarrow \rho + j\frac{\alpha_{\text{Pogo}}}{\omega}, \tag{2.21}$$

and therefore, the wavenumber, which is a function of the speed, and hence, the density, also becomes complex. As a result, when this complex wavenumber is substituted in time harmonic solutions representing waves, which are of the form $u = e^{j(kx-\omega t)}$, where u is any component of the displacement, the exponent becomes complex and hence, the real part represents a loss of energy as the wave propagates.

Now, if η is introduced in a model, a separate loss of energy will occur. In Pogo, the presence of η populates the $\mathbf{C}$ matrix with the appropriate entries, such that, during the solution of Equation (2.18), a loss of amplitude occurs. Let the subscripts L and T denote quantities related to longitudinal and shear waves respectively, and $p_{\alpha_{\text{Pogo}}}$ and p_{η} denote the amplitude drop between a given distance due to the presence of α_{Pogo} or η in an FE model respectively. Assuming a model with both α_{Pogo} and η, due to superposition, the effect of each loss mechanism can be treated separately, and therefore, the total drop in amplitude of longitudinal (p_L) or shear (p_T) wave can be written as:

$$p_L = p_{L_{\alpha_{\text{Pogo}}}} \times p_{L_{\eta}}, \tag{2.22}$$

$$p_T = p_{T_{\alpha_{\text{Pogo}}}} \times p_{T_{\eta}}. \tag{2.23}$$

For a given material, the amount by which a Rayleigh wave must attenuate (i.e. the values of p_L and p_T) is known. Now, let us assume that a value of η is selected, which over a distance d generated an amplitude drop of $p_{L_{\eta}}$ and $p_{T_{\eta}}$ to a longitudinal and shear wave respectively. From Equations (2.22) and

(2.23), a value for α_{Pogo} has to be found then, such that

$$p_{L_{\alpha_{\mathrm{Pogo}}}} = \frac{p_L}{p_{L_\eta}}, \tag{2.24}$$

$$p_{T_{\alpha_{\mathrm{Pogo}}}} = \frac{p_T}{p_{T_\eta}}. \tag{2.25}$$

To achieve this, the value of α_{Pogo} that must be defined in the model should be either equal to

$$\alpha_{\mathrm{Pogo}} = -\frac{2C_L}{\mathrm{d}} \ln\left(\frac{p_L}{p_{L_\eta}}\right), \tag{2.26}$$

or

$$\alpha_{\mathrm{Pogo}} = -\frac{2C_T}{\mathrm{d}} \ln\left(\frac{p_T}{p_{T_\eta}}\right), \tag{2.27}$$

depending on whether the calculation is completed based on the properties of the longitudinal or the shear wave. There can only exist one value of α_{Pogo} in a model, and hence, the right-hand sides of Equations (2.26) and (2.27) must be equal:

$$\begin{aligned} C_L \ln\left(\frac{p_L}{p_{L_\eta}}\right) &= C_T \ln\left(\frac{p_T}{p_{S_\eta}}\right) \\ \implies \left(\frac{p_L}{p_{L_\eta}}\right)^{C_L} &= \left(\frac{p_T}{p_{T_\eta}}\right)^{C_T} \\ \implies \frac{p_L^\gamma}{p_T} &= \frac{p_{L_\eta}^\gamma}{p_{T_\eta}}, \end{aligned} \tag{2.28}$$

where the ratio of wave speeds, γ is defined as

$$\gamma = \frac{C_L}{C_T}. \tag{2.29}$$

Equation (2.28) has very useful implications. The arithmetic value of the left-hand side can be calculated for a Rayleigh wave on a given material, as γ, p_L and p_T are all known. Therefore, if η is selected such that the resulting p_{L_η} and p_{T_η} satisfy Equation (2.28), then α_{Pogo} can be found using either Equation (2.26) or (2.27) as both will yield the same result. That particular combination of η and α_{Pogo} will attenuate the Rayleigh wave correctly.

The efficacy of this method is illustrated below, by using two hypothetical examples, with arbitrary p values, and two examples involving material properties of steel. The validation is also done at different distance and frequency (f) values, to demonstrate that there is no loss in generality under this method.

For calculating the p_{L_η} and p_{T_η} values, a simple rectangular FE domain was created in Pogo as shown in Figure 2.7. The source line was defined to have a length of 40 mm in the z direction, and the source nodes were excited in either the z or x directions, for the excitation of longitudinal or shear waves respectively. Two monitor nodes were defined on the $z = 0$ line, to record the amplitude of the signal at their locations. Both the spacing of the monitor nodes, and the absolute size of the model were chosen based on the needs of each particular example which was studied.

For each of the examples, after finding the η value satisfying Equation (2.28) using the above mentioned mode, and thus calculating the α_{Pogo} value, the η and α_{Pogo} values were used simultaneously in a Rayleigh wave model to investigate whether the said combination indeed attenuated the Rayleigh wave correctly. To verify this, a similar Rayleigh wave FE model to the one depicted in Figure 2.4 was used, with the sole difference that two monitor nodes were defined on the surface instead of one, to measure the drop in the Rayleigh wave amplitude, p_R, over a given distance.

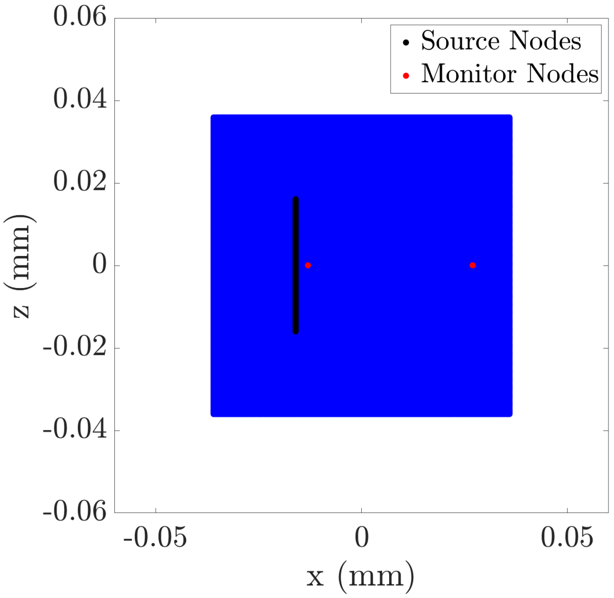

Figure 2.7: Schematic of the FE domain used to obtain the p_{L_η} and p_{S_η} values, for different values of η (cross-sectional view). The spacing of the monitor nodes and the dimensions of the model were altered depending on the particular needs of each example which was studied.

2.5.1 Hypothetical example A

Let us assume a hypothetical material, with $E = 210$ GPa, $\rho = 8000$ kg/m^3, $\nu = 0.33$ ($C_L = 6055.3$ m/s and $C_T = 3162.3$ m/s). Let us also assume that if a longitudinal wave, with a frequency of 1 MHz travels through 10 mm of such a material , its amplitude drops to 0.5 from its initial value, and if a shear wave with the same frequency travels over the same distance, its amplitude drops to 0.25 from its initial value, i.e. $p_L = 0.5$ and $p_T = 0.25$. Since this was a study on a hypothetical material, it was necessary to use DISPERSE [16, 17] to predict the attenuation of a Rayleigh wave travelling on such a material. DISPERSE is a commercially available software, able to calculate dispersion curves and hence provides us with the required attenuation values. DISPERSE measures the loss of energy in the form of the attenuation coefficient, α, where α is defined as

$$\alpha = -\frac{1}{\mathrm{d}} \ln\left(\frac{A_{x_2}}{A_{x_1}}\right). \tag{2.30}$$

Disperse predicts that for a Rayleigh wave propagating on this material, at 1 MHz, $\alpha = 149.0\ \mathrm{m}^{-1}$.

Also, for this material,

$$\gamma = \frac{6055.3}{3162.3} = 1.915. \tag{2.31}$$

Hence, the required value of η, from Equation (2.28) should be such that the resulting p_{L_η} and p_{T_η} satisfy:

$$\frac{p_{L_\eta}^{\gamma}}{p_{T_\eta}} = \frac{0.5^{1.915}}{0.25} = 1.061.$$

It was found that $\eta = 130\ \mathrm{m}^2\mathrm{s}^{-1}$ gives $p_{L_\eta} = 0.988$ and $p_{T_\eta} = 0.920$, and therefore $\left(\frac{p_{L_\eta}^{\gamma}}{p_{T_\eta}}\right)$=1.062, which is very close to the desired value.

Therefore, the required α_{Pogo} value, from either of Equations (2.26) or (2.27) is:

$$\begin{aligned}\alpha_{\mathrm{Pogo}} =& \frac{2 \times 6055.3}{0.01} \ln(0.5/0.988) = \frac{2 \times 3162.3}{0.01} \ln(0.25/0.920) \\ &\approx 8.24 \times 10^5\ \mathrm{s}^{-1}.\end{aligned}$$

When those values of η and α_{Pogo} were used simultaneously in the Pogo model shown in Figure 2.7, the measured values of p_L and p_T were 0.51 and 0.26 respectively, showing that this combination of viscosity and attenuation gave the correct drop in amplitude for each component separately.

Subsequently, those η and α_{Pogo} were used in a Rayleigh wave model. The signal recorded by the monitor nodes in the Rayleigh wave model is shown

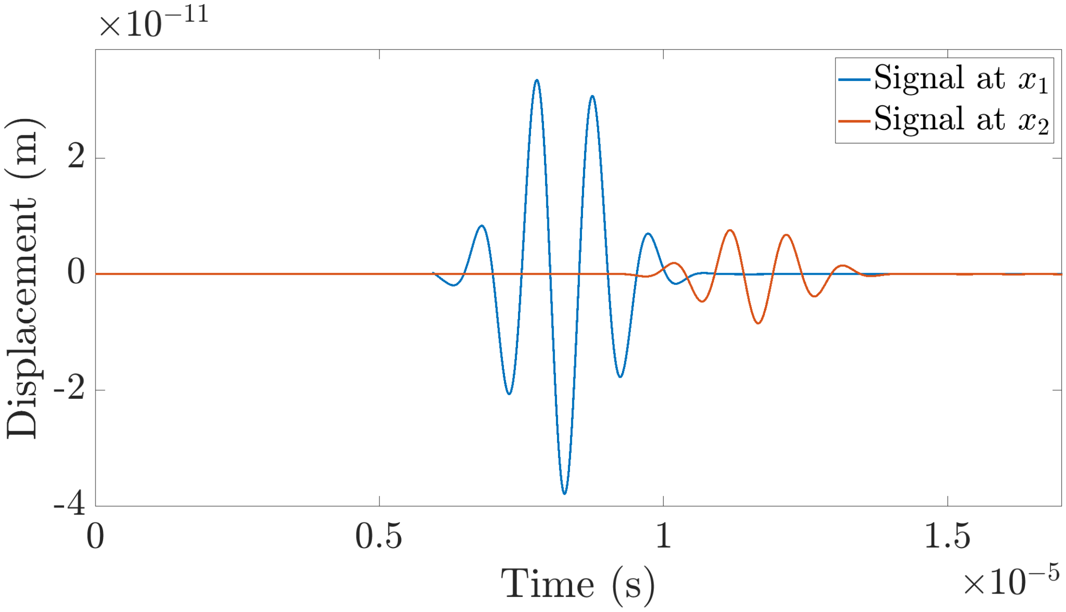

Figure 2.8: Rayleigh wave signals, travelling in a hypothetical material $C_L = 6055.3$ m/s, $C_T = 3162.3$ m/s and $p_L = 0.5$ and $p_T = 0.25$ at 1 MHz. The propagation distance between the two signals $x_2 - x_1 = 10$ mm.

in Figure 2.8. Both signals appear to be of good quality, showing that this attenuation method does not generate noise in the model. Furthermore, the α value for the Rayleigh wave signals shown in Figure 2.8 was found to be 148.8 m^{-1}, which is close to the value predicted by DISPERSE. Therefore, this example shows that the theory and modelling method derived here were able to correctly model the attenuation of a Rayleigh wave for this particular hypothetical example. A second example, with another hypothetical material is discussed below.

2.5.2 Hypothetical example B

Let us now assume the same material parameters as in Hypothetical example A, but with $p_L = 0.9$ and $p_T = 0.7$ over a distance of 10 mm. Similarly to the example above, DISPERSE was used to predict the attenuation of the Rayleigh wave on such a material. This value was found to be 36.9 m^{-1}. Since the material parameters are the same, $\gamma = 1.915$. However, η must now be selected such that the drop in amplitude of the longitudinal and shear waves, purely by the presence of η satisfies:

$$\frac{p_{L_\eta}^{\gamma}}{p_{T_\eta}} = \frac{0.9^{1.915}}{0.7} = 1.168.$$

It was found that $\eta = 325$ m^{2}s^{-1} gives $p_{L_\eta} = 0.959$ and $p_{T_\eta} = 0.791$, and therefore $\left(\frac{p_{L_\eta}^{\gamma}}{p_{T_\eta}}\right)$=1.166, which is close to the desired value.

Therefore, the required α_{Pogo} value, from either of Equations (2.26) or (2.27) is:

$$\begin{aligned}\alpha_{\text{Pogo}} =& \frac{2 \times 6055.3}{0.01} \ln(0.9/0.959) \approx \frac{2 \times 3162.3}{0.01} \ln(0.7/0.791) \\ &\approx 7.6 \times 10^4 \text{ s}^{-1}.\end{aligned}$$

When those values of η and α_{Pogo} were used in the Pogo model shown in Figure 2.7, the measured values of p_L and p_T were 0.90 and 0.70 respectively, again showing that this combination of viscosity and attenuation gave the correct drop in amplitude in both the shear and longitudinal components independently.

When a Rayleigh wave model, with $\alpha_{\text{Pogo}} = 7.6 \times 10^4$ s^{-1} and $\eta = 325$ m^{2}s^{-1} was created, the attenuation coefficient was found to be 36.5 m^{-1}, showing again that this theory and modelling method was able to correctly model the attenuation of a Rayleigh wave on this particular material.

Following these two verifications, which were completed with arbitrary p_L and p_T values, two further example calculations were completed, using material properties for steel.

2.5.3 Steel example A

As provided by DISPERSE, the material properties for steel are $E = 216.91$ GPa, $\rho = 7932$ kg/m^3, $\nu = 0.287$ which correspond to $C_L = 5960$ m/s and $C_T = 3260$ m/s. The attenuation of the longitudinal and shear waves per wavelength, are 0.002 λ_L^{-1} and and 0.004 λ_T^{-1} respectively, where λ_L and λ_T are the longitudinal and shear wavelengths respectively.

At $f = 2$ MHz, $\lambda_L = 3$ mm and $\lambda_T = 1.6$ mm. Therefore, at this frequency, $\alpha = 0.671$ m^{-1} for longitudinal waves and $\alpha = 2.454$ m^{-1} for shear waves. A propagation distance of 40 mm was chosen for this example; therefore, for this particular distance and frequency, by the definition of the attenuation coefficient in Equation (2.30),

$$\begin{aligned} p_L &= \mathrm{e}^{-0.671 \times 40e-3} = 0.9735, \\ p_T &= \mathrm{e}^{-2.454 \times 40e-3} = 0.9065. \end{aligned}$$

Also, for these material parameters,

$$\gamma = \frac{5960}{3260} = 1.828.$$

Therefore, the required value of η should be such that the resulting p_{L_η} and p_{T_η} satisfy:

$$\frac{p_{L_\eta}^{\gamma}}{p_{T_\eta}} = \frac{0.9735^{1.828}}{0.9065} = 1.050.$$

It was found that a value of $\eta = 5$ m^{2}s^{-1} gave p_{L_η}=0.9932, $p_{S_\eta} = 0.9470$ and thus $\frac{p_{L\eta}^{\gamma}}{p_{T_\eta}}$=1.043, which is close to the desired value. Hence the corresponding

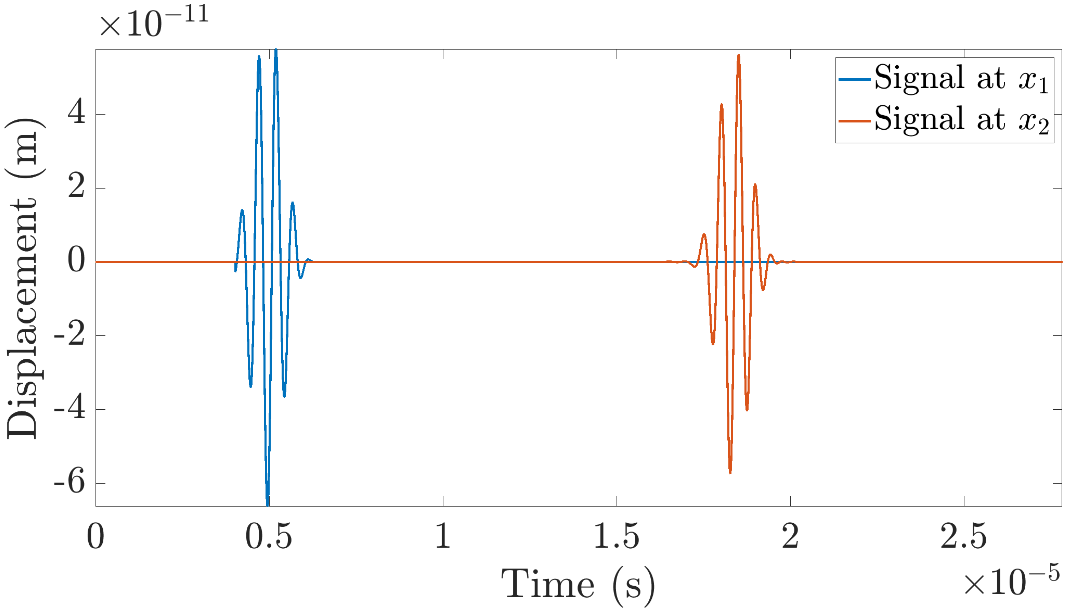

Figure 2.9: Rayleigh wave signals, travelling on steel ($p_L = 0.9735$ and $p_T = 0.9065$ at f=2 MHz). The propagation distance between the two signals is $x_2 - x_1 = 40$ mm.

value of α_{Pogo} is

$$\begin{aligned}\alpha_{\text{Pogo}} &= -\frac{2 \times 5960}{0.04} \ln\left(\frac{0.9735}{0.9932}\right) = -\frac{2 \times 3160}{0.04} \ln\left(\frac{0.9065}{0.9470}\right) \\ &\approx 6400 \text{ s}^{-1}.\end{aligned}$$

When $\alpha_{\text{Pogo}} = 6400$ s^{-1} and $\eta = 5$ m^{2}s^{-1} were implemented in the model in Figure 2.7, p_L was found to be 0.9575 and p_T was found to be 0.8998, which are both close to the desired value.

Finally, the signal obtained from a surface model with $\eta = 5$ m^{2}s^{-1} and $\alpha_{\text{Pogo}} = 6400$ s^{-1} is shown in Figure 2.9. As shown in this figure, the signal quality in this more realistic example is still preserved. The theoretical Rayleigh wave attenuation coefficient from DISPERSE, for steel at 2 MHz is 2.75 m^{-1}, while the Pogo model gave an attenuation coefficient of 2.52m^{-1}.

2.5.4 Steel example B

In this final example, the same material parameters for steel were used, but the frequency was increased to 10 MHz, resulting in $\alpha = 3.355\ \mathrm{m}^{-1}$ for longitudinal waves and $\alpha = 12.270\ \mathrm{m}^{-1}$ for shear waves. For a propagation distance of 40 mm,

$$\begin{aligned} p_L &= \mathrm{e}^{-3.355 \times 40e-3} = 0.8742, \\ p_T &= \mathrm{e}^{-12.270 \times 40e-3} = 0.6121. \end{aligned}$$

Therefore, the required value of η should be such that the resulting p_{L_η} and p_{T_η} satisfy:

$$\frac{p_{L_\eta}^{\gamma}}{p_{T_\eta}} = \frac{0.8742^{1.828}}{0.6121} = 1.278.$$

It was found that a value of $\eta = 1.4\ \mathrm{m}^2\mathrm{s}^{-1}$ gave p_{L_η}=0.9159, $p_{S_\eta} = 0.6672$, and thus $\frac{p_{L_\eta}^{\gamma}}{p_{T_\eta}}$=1.276 which is very close to the desired value. Hence the corresponding value of α_{Pogo} is

$$\begin{aligned} \alpha_{\mathrm{Pogo}} &= -\frac{2 \times 5960}{0.04} \ln\left(\frac{0.8742}{0.9159}\right) \approx -\frac{2 \times 3160}{0.04} \ln\left(\frac{0.6121}{0.6672}\right) \\ &\approx 13750\ \mathrm{s}^{-1}. \end{aligned}$$

When a model with $\eta = 1.4\ \mathrm{m}^2\mathrm{s}^{-1}$ and $\alpha_{\mathrm{Pogo}} = 13750\ \mathrm{s}^{-1}$ was created, p_L was found to be 0.8740 and p_T was found to be 0.6126, which are both close to the desired value.

When those attenuation parameters were used in a surface wave model, the attenuation coefficient of the Rayleigh wave was found to be 12.59 m^{-1}, while DISPERSE predicts an attenuation coefficient of 12.64 m^{-1}.

In all examples, the discrepancies between the DISPERSE attenuation values and the measurements are explicable by the imperfect match between the required value of the $\frac{p^{\gamma}_{L\eta}}{p_{T_{\eta}}}$ ratio, and the values that were used in each of the examples. This is demonstrated well with the final example here, where the nearly perfect match between the theoretical and achieved values of $\frac{p^{\gamma}_{L\eta}}{p_{T_{\eta}}}$ resulted in an analogously good match between DISPERSE and the value measured by the FE model.

Chapter 3

Surface waves for assessing the fatigue state of flat steel components

The work in this chapter has been reported in a journal publication [18].

3.1 Introduction

As discussed in Chapter 1, it is important to be able to characterise the fatigue state of engineering components, to ensure their safe operation and cost-effective inspection and replacement. There is a plethora of theories for predicting remaining fatigue life or fatigue state in the literature. One of the most widely known equations for predicting the remaining fatigue cycles until failure is the solution to the Paris' law differential equation [19]:

$$N_f = \int_{\alpha_0}^{\alpha_c} \frac{d\alpha}{\mathrm{C}(\Delta K)^{\mathrm{m}}}. \tag{3.1}$$

In Equation (3.1), N_f is the number of cycles required for failure, ΔK is the range of stress intensity factors that the component is subjected to, α_0

and α_c are the initial and final crack lengths respectively, and C and m are material dependent constants. It is clear that this equation requires the presence of fatigue cracks to yield a remaining fatigue life prediction, meaning it can not be used prior to crack initiation. However, the stage prior to crack initiation can last up to 40%-90% of component's life [20], meaning that Equation (3.1) can not be used for a significant portion of a component's service life. Also, Equation (3.1) may be impractical to use, as C and m must be found experimentally for every material [21], and ΔK is unique to every crack geometry [21, 22], all of which create further complexities in the remaining fatigue life predictions.

To improve Paris' theory the authors in [23] proposed models that take into account the initial crack growth stage by introducing an effective stress concentration factor, ΔK_{eff}, and the authors in [24] further modelled this factor. However, in a realistic loading scenario, it is often the case that multiple loading levels are used throughout a component's life, something which can not be modelled by Equation (3.1). To take this form of damage into account, the Palmgren-Miner rule can be used [25]:

$$\sum_{i=1}^{\mathrm{k}} \frac{n_i}{N_i} = 1. \tag{3.2}$$

In Equation (3.2), N_i and n_i are the maximum number of cycles and number of cycles already passed at the i^{th} stress level respectively, and k is the number of different stress levels applied to the component. In each stress level, N_i can be found from Equation (3.1). This theory was then further extended by Marko & Starkley [26], to distinguish between a change from a low to high stress and a high to low stress.

Both theories in [25] and [26] consider various loading patterns, however, they can not take into account the slow-accumulating damage that happens below the endurance limit (i.e. when $N_f \to \infty$). Although theoretically such stress levels will not cause failure in reasonable N_f values, research has shown that they still contribute to cumulative fatigue damage [27, 28]. In such cases, more accurate N_f values can be obtained using Basquin's relationship [29] for high cycle fatigue, or the Coffin-Manson [30] relationship for low cycle fatigue.

Numerous other fatigue life prediction theories exist, which follow a less deterministic approach to the above-mentioned ones. For instance, the authors in [31] and [32] separated the defects that exist in a material in different categories in groups based on their crack initiation ability, and used statistical modelling, stochastic processes and Monte Carlo simulations to predict fatigue life. Other examples which utilise probability theory and statistics to predict life include the work from Kim et. al [33], Pineau & Antolovich [34], and more recently Wang et.al [35] and Haridas et.al [36]. There are also theories which utilise continuum mechanics [37–39], fuzzy sets [40], and energy-work principles [41] to predict fatigue life.

The main issue however, with all the theoretical fatigue life or fatigue state prediction methods presented above, is that it would be far from straightforward to implement them in an industrial environment. For an engineering component, it is often the case that the number of loading cycles or the exact stress level of each is not known. Also, measurements relating to fatigue crack size and orientation, which are required for some theoretical approaches, are difficult to obtain, and the coefficients required for many of the calculations are too expensive and time consuming to derive for each material and loading scenario. Furthermore, many theories and methods focus on the detection and characterization of single, identifiable cracks, but cannot model the degradation that happens in the material during the early stages of fatigue - which as described in [42–44] involves the generation and coalescence of multiple microcracks before the formation of the larger, identifiable cracks. This makes it difficult to identify the early onset of fatigue - a stage which is also important when assessing the life of safety-critical components. Finally, some of the presented methods require a priori knowledge of N_f to yield a fatigue state prediction, which again may not be possible for a real component.

An alternative approach to characterising the fatigue status of engineering components, especially prior to crack initiation, would be the use of ultrasound as a fast, non-destructive method. It has been well established in the literature that ultrasound is sensitive to the presence of identifiable fatigue cracks - methods to detect and size them include linear time-of-flight measurements [45–48], and also non-linear methods [49–51]. However, the sensitivity of ultrasound is not limited just to its interaction with fatigue cracks, but also to the general presence of a fatigue zone. This sensitivity manifests as a change in the propagation speed of the ultrasound. This phenomenon can be explained through the well-known Granato-Lücke model [1, 52]. In these studies, the authors modelled the dislocations which are present in a material as strings with finite mass, length and damping. The dislocations are subsequently subjected to forced oscillation when an ultrasonic wave travels over them. As a result of the dislocations' inertia, the speed of the ultrasound reduces. Additionally, the energy which is required to force this oscillation is lost from the ultrasound, causing a change in the ultrasound's attenuation coefficient. This model has been studied widely and extended in the literature, with more recent advancements including a study of the ultrasound-dislocation behaviour at higher frequencies [53], and the use of the dislocation theory to describe the interaction between an ultrasonic wave and grain boundaries [3]. Additionally, a single dislocation was studied in a 2D space [2], followed by a study for a forest of 2D dislocations [4], and finally, a full, 3D study [5].

All studies mentioned above demonstrate that the interaction between an ultrasonic wave and the dislocations in a material will cause a change in the wave propagation speed. Given that fatigue is a phenomenon which alters the dislocation state of a material [54, 55], it is expected that the speed of a wave in a material will vary as the fatigue state of the material evolves. Indeed, multiple studies have confirmed this [56–61], by observing that the speed of a wave decreases monotonically with an increase in fatigue cycles. The authors in [56–61] were able to justify this behaviour by linking the equations in [1] with qualitative dislocation density information obtained via transmission electron microscopy (TEM). In their studies, the authors in [56–58] used axial shear waves generated by a specialised Electromagnetic Acoustic Transducer (EMAT) ring, as they completed their measurements on cylindrical surfaces, while the authors in [59–61] used through-thickness measurements.

An alternative approach to mitigate the issues discussed above, such as those of the unknown material parameters, loading sequences and amplitudes, and constants required for each theoretical model is proposed here, which also mitigates the low sensitivity issues in [59–61]. Rayleigh waves, generated by piezoelectric transducers, can be used as an alternative method for assessing the fatigue state of steel components; given that fatigue is usually a near-surface phenomenon, using Rayleigh waves, whose propagation is restricted to a region around the surface of a material, will yield maximum changes in propagation speed and hence maximum sensitivity. This is contrary to the smaller changes in speed obtained by the use of bulk waves [59–61] in through-thickness measurements, whose small magnitude is a result of the waves spending very limited time inside the near-surface fatigue region. Here it is worth noting that in [60] the magnitude of the change appears to be bigger - this is because the entire sample is being fatigued in this study, and therefore the fatigue is not concentrated just near the surface of the material. Additionally, a Rayleigh wave approach is simpler to implement than the method used by [56–58], can be used on flat or near-flat surfaces, and does not suffer from some of the EMAT issues, such as the limited operating frequency and sensitivity to the changes between the distance of their surface and the material [62]. Furthermore, the work here is on the characterisation of thermal instead of mechanical fatigue, whose detection, to the author's knowledge, has not been pursued in detail specifically using ultrasonic methods, and is also a more common issue in nuclear plants. Also, compared with longitudinal waves, the use of Rayleigh waves does not require prior knowledge of the thickness of a component - this is particularly advantageous for fatigue scenarios where the loading is causing the component's thickness to degrade, or in applications where component thicknesses are not known with high degrees of precision.

To investigate the suitability of Rayleigh waves for fatigue assessment purposes, this study compared the change in ultrasonic speed between longitudinal bulk and Rayleigh waves. The longitudinal wave results were obtained through the creation of C_L C-scans of five purposely fatigued plates, each at different fatigue states, with the aid of an immersion tank. For the same plates, Rayleigh wave speed B-scans were created though the use of a perspex wedge setup and a simple scanning frame. Following this comparison, the monotonic drop of the Rayleigh wave speed was explained through a microstructural examination of the fatigued plates, using electron back-scatter diffraction (EBSD) and novel processing of the EBSD scans to obtain a qualitative measure of the dislocation density inside the fatigue region [63, 64], and comparison of this behaviour with the Granato-Lücke model [1, 52].

Finally, this study investigated a method for representing the speed changes caused by fatigue damage, using an "effective solid" approach, in finite element modelling. To the author's knowledge, currently there does not exist a method to represent the effects of fatigue damage on the time-of-flight of ultrasonic waves, in an FE domain - such a method would however be useful in FE simulations of potentially fatigued components, where precise time-of-flight values are the important result of the simulation.

3.2 Theory

This section briefly discusses the microstructural origin and evolution of fatigue damage in metals, focusing on the behaviour of the dislocation state of the material as fatigue progresses. The dislocation behaviour is then linked with the theory which predicts the changes in ultrasonic speed when a wave travels through a fatigued region. Additionally, a brief summary of how EBSD imaging can be used to extract dislocation density information is also presented.

3.2.1 Fatigue & ultrasound

Fatigue is a phenomenon in which a material fails under cyclic stresses and strains, not because those are above its ultimate tensile strength, but rather because every cycle creates an infinitesimal amount of slowly accumulating damage, which eventually leads to failure [65,66]. The origins of fatigue damage in metals and alloys lie in the formation of slip-bands inside their grains. Slip bands are areas of localised plastic deformation which form as a result of the different stress level exhibited by each grain during cyclic loading, arising from the different mechanical properties that every grain has [67]. These slip bands act as stress concentrators which draw the dislocations that are in the material towards them. As a result of the localised change in material properties caused by the additional dislocations, the slip bands multiply and deepen [44, 68], drawing even more dislocations towards them. Additionally, more dislocations are generated from the slip lines which comprise the slip bands [68], through the Frank-Read mechanism [69], leading eventually to microcrack formation. Finally, once microcracks have formed from the slip bands, more dislocations are emitted from them [70,71]. As the cyclic loading continues, the microcracks grow, leading eventually to failure [72].

The multiple mechanisms which cause dislocation generation and multiplication have interesting implications for how an ultrasonic wave behaves when it travels through a fatigue region, which is, as described above, a region with altered dislocation state. Contrary to voids or inclusions, dislocations are material imperfections which respond dynamically when an ultrasonic wave encounters them. Granato & Lücke have studied this phenomenon in depth, by treating dislocations as strings of finite length, mass and damping [1]. The authors in [1] then combined the stress-strain Newton's laws and Koehler's differential equations for describing the motion of a dislocation under an applied stress [73], and solved the resulting system of differential equations, to find the equation of a stress field satisfying both. A brief summary of this analysis is presented below.

Let x and z be the horizontal and vertical directions in a Cartesian coordinate system, as shown in Figure 2.1. Equation (3.3) shows the usual linear elastic equation of a solid, derived from Newton's laws [1]:

$$\frac{\partial^2 \sigma}{\partial x^2} = \rho \frac{\partial^2 \epsilon}{\partial t^2}, \tag{3.3}$$

where σ is the stress and ϵ is the strain term, which contains both the linear elastic strain, and the dislocation strain.

The motion of a dislocation with length l, pinned at its ends, lying parallel to the z axis, which is forced to bow outwards, like a guitar string being displaced laterally, by a distance ξ due to an applied stress can be described by Equation (3.4) :

$$\mathrm{A}_1\frac{\partial^2\xi}{\partial t^2} + \mathrm{A}_2\frac{\partial\xi}{\partial t} - \mathrm{A}_3\frac{\partial^2\xi}{\partial z^2} = b\sigma, \qquad \xi(x,0,t) = \xi(x,l,t) = 0, \tag{3.4}$$

where A_1 is the mass of the dislocation per unit length, A_2 is the damping per unit length, A_3 is the dislocation's tension per unit length and b is the Burger's vector.

Additionally, the authors in [1] show that the dislocation strain, ϵ_{dl} can be calculated as follows:

$$\epsilon_{dl} = \frac{\Lambda b}{l}\int_0^l \xi(z)\,dz, \tag{3.5}$$

where Λ is the dislocation density. Also, the strain term in Equation (3.3) is simply equal to the stress divided by the material's shear modulus, G. Combining Equations (3.3) and (3.5) yields:

$$\frac{\partial^2\sigma}{\partial x^2} = \rho\left(\frac{1}{G}\frac{\partial^2\sigma}{\partial t^2} + \frac{\Lambda b}{l}\frac{\partial^2}{\partial t^2}\int_0^l \xi(z)\,dz\right). \tag{3.6}$$

Having assumed dislocations lying perpendicularly to the wave propagation direction, the authors were able to obtain analytical solutions for the required σ and ξ, which would only satisfy the system of Equations (3.5) and (3.6) if the propagation speed and attenuation of the elastic wave are indeed affected by the presence of the dislocations.

The closed form of the equations describing the propagation speed and attenuation coefficient are still complicated and possibly impractical to be used in a realistic scenario. However, they can be reduced to a simpler form under a low frequency assumption. The resulting simplified form is shown in

Equations (3.8) and (3.7) respectively.

$$\alpha = K_1 \Lambda \mathrm{L}^4 f^2, \tag{3.7}$$

$$\Delta C = \frac{C_f - C_h}{C_h} = -K_2 \Lambda \mathrm{L}^2, \tag{3.8}$$

where L is the dislocation loop length. K_1 and K_2 are constants and C_h and C_f the wave propagation speed in the reference area and in the area with additional dislocations, respectively. Here it is worth noting that the low frequency assumption holds true in realistic cases. This is because, in studies where the interaction between dislocations and ultrasound was investigated, the frequency terms became relevant when the wavelength was comparable to the dislocation length. For metals, this only happens in the GHz range [74, 75].

Further developments have been made to the theory presented in this section, to account for higher frequencies [53], different damping mechanisms [76], grain boundary behaviour [3], different kinds of dislocations and other wave polarisations [2,4,5]. Some studies also focused on deriving a representation of the field which an oscillating dislocation emits [77, 78]. However, the general behaviour of Equations (3.8) and (3.7) remains the same in all subsequent studies, apart from some constants.

During the experimental measurements it was found that it was very challenging to obtain attenuation values with sufficient repeatability to be used in fatigue state predictions. Therefore, this study focused on the general behaviour predicted by Equation (3.8), as well as its verification.

3.2.2 Electron backscatter diffraction

EBSD imaging was used to produce an independent assessment of fatigue damage for comparison against the theoretical model. EBSD analysis provides the ability to estimate the dislocation density of a given material, by constructing the shear stress field maps, σ_{12}, in an area on that material. Generating such stress field maps is a results of recent advancements in the ultramicroscopy community.

EBSD works by utilising the physical phenomena around electron scattering. In such a measurement, an electron beam is directed on the surface of a well-polished material, which is tilted by 70° with respect to the horizontal. When the electrons collide with the surface of the material, the collision point acts as a secondary source of (scattered) electrons. Depending on the crystal plane which causes the scattering, the electrons travel along defined areas known as Kikuchi lines. Those electrons then arrive at a scintillator screen placed nearby - the scintillation is then recorded by a camera and the EBSD microscope can image the Kikuchi line patterns. Those geometric patterns are then automatically converted to orientation data, as each pattern corresponds to a specific crystallographic plane [79, 80]. More recently, the authors in [81, 82] explained how shifts in the geometric patterns can be correlated to strain and hence stress maps. Finally, [83] derives an expression which can utilise shear stress maps to estimate the dislocation density.

Let us assume the presence of a single dislocation within an circular area (A_0) of a material, as well as an arbitrarily selected elemental area within that area (dA), as shown in Figure 3.1.

The dislocation will cause the stress in the area to increase around it, and therefore, the probability P of the presence of a high stress area due to the

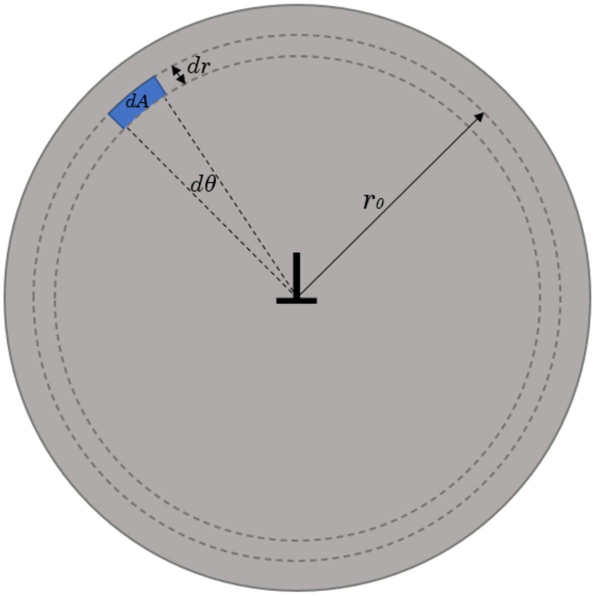

Figure 3.1: Schematic of a circular area in a material containing a single dislocation denoted by $\perp$.

dislocation is

$$P = \frac{dA}{A_0}, \qquad dA = r_0 dr d\theta. \tag{3.9}$$

Additionally, the shear stress near a dislocation can be written as

$$\sigma_{12} = \frac{DK_{12}(\theta)}{r_0}, \tag{3.10}$$

where

$$D = \frac{Gb}{2\pi(1-\nu)}, \tag{3.11}$$

and

$$K_{12} = \cos(\theta)\cos(2\theta). \tag{3.12}$$

Combining Equations (3.9) and (3.10) yields

$$P(\sigma_{12}, \theta) = \frac{D^2 K_{12}^2(\theta)}{A_0} \frac{d\sigma_{12}}{\sigma_{12}^3}. \tag{3.13}$$

The dependence of K_{12}^2 on θ can be removed by using the average value of the $K_{12}^2(\theta)$ function, denoted as $\langle K_{12}^2 \rangle$, which is given by

$$\langle K_{12}^2 \rangle = \int_0^{2\pi} K_{12}^2(\theta) \ d\theta = \int_0^{2\pi} \cos(\theta) \cos(2\theta) \ d\theta = \frac{\pi}{2}, \tag{3.14}$$

which when combined with Equation (3.13) gives the probability of a high stress area due to the presence of a dislocation simply as a function of the shear stress:

$$P(\sigma_{12}) = \frac{\pi D^2 \langle K_{12}^2 \rangle}{2A_0} \frac{d\sigma_{12}}{\sigma_{12}^3}. \tag{3.15}$$

The authors then explain that it is beneficial to use the second moment of this probability, ν_2 rather than the probability density function itself, to calculate the dislocation density:

$$\begin{aligned} v_2(\sigma_{12}) &= \int_{-\sigma}^{+\sigma} P(\sigma_{12}) \sigma_{12}^2 \ d\sigma_{12} = \frac{\pi D^2 \langle K_{12}^2 \rangle}{2A_0} \int_{-\sigma}^{+\sigma} \frac{d\sigma_{12}}{\sigma_{12}} \\ &= \frac{(Gb)^2}{8\pi(1-\nu)^2} \Lambda \ln\left(\frac{\sigma_{12}}{\sigma'}\right), \end{aligned} \tag{3.16}$$

where $1/A_0$ has been substituted by the dislocation density, as there is only one dislocation within A_0, and σ' is a constant. The latter result comes from Groma [84], where the author discusses the issues with calculating the usual second moment of $P(\sigma_{12})$, for which the integral would have to be evaluated over the entire real line, and how integrating with finite limits still yields useful results. Therefore, one can estimate Λ at a location on the surface of a material, simply by knowing σ_{12} at that location, and $v_2(\sigma_{12})$. It is possible for the Scanning Electron Microscope (SEM) to construct the $P(\sigma_{12})$ function from the σ_{12} maps, calculate the $v_2(\sigma_{12})$ value and hence estimate Λ at a given location.

3.3 Experimental methods

This subsection presents the experimental techniques for obtaining the speed of longitudinal and Rayleigh waves. For all measurements, a set of five fatigued plates was used, which were subjected to thermal fatigue under carefully controlled conditions. The plates were provided to the author by their industrial partner, Jacobs. A reference plate, containing no fatigue damage was also used as a control. An example of a fatigued plate is shown in Figure 3.2.

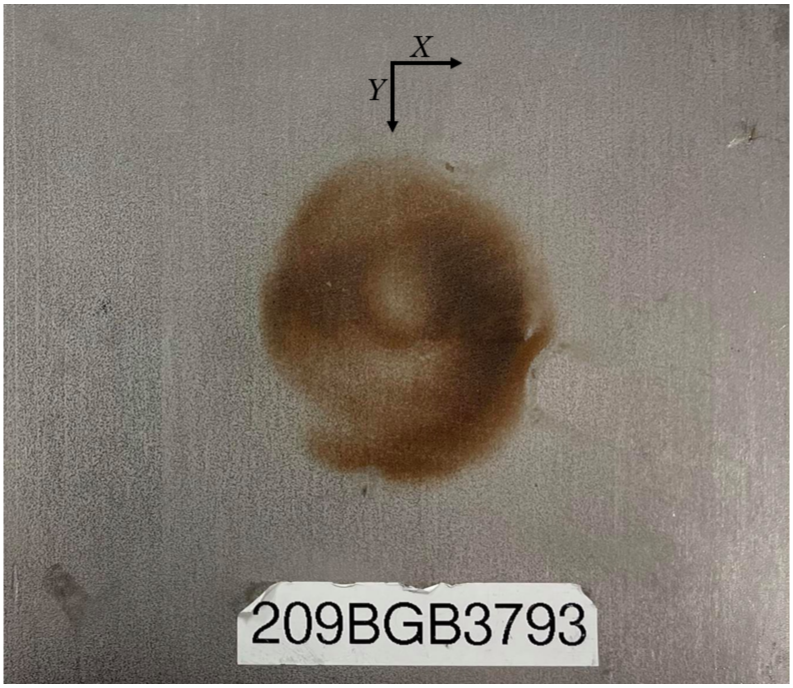

Figure 3.2: Photograph of one of the fatigued steel plates, showing the fatigue area. Additionally, a coordinate system, which is used to present the results in Section 3.4.2 is shown. The origin of the coordinate system is centred approximately where the first Rayleigh wave measurement is taken, and the positive Y axis signifies the scanning direction.

As shown in Figure 3.2, the fatigued plate contains a clear oxidisation spot, where the fatigue damage is concentrated. Each plate is 100 mm × 100 mm × 8 mm in size, with a fatigue spot whose diameter is approximately 50 mm. It is worth noting that due to steel being a good conductor of heat, the size of the fatigue spot is larger than the oxidisation spot. The plate is made from austenitic steel (≈0.04 wt. % carbon). It was subjected to thermal fatigue at 0.167 Hz (6 second cycle) by Trueflaw (Espoo, Finland) [85] under controlled conditions. The plate was heated for 3 seconds from room temperature to 302 °C, then cooled rapidly to room temperature in 1.2 seconds, and finally kept at that temperature for 1.8 seconds. This heating and cooling cycle was repeated multiple times, until the required number of cycles, and hence fatigue damage level, was reached for each plate. Table 3.1 shows the reference number of each plate, with the corresponding number of thermal fatigue cycles to which every plate has been subjected.

Table 3.1 shows each plate's usage factor (UF), where UF is defined as the number of fatigue cycles that a material has been subjected to (N) divided by N_f. Trueflaw assume $N_f = 100,000$ for these particular samples.

Table 3.1: Trueflaw plate's serial numbers, number of fatigue cycles (N) and usage factor (UF), assuming $N_f = 100,000$.

Plate	00	84	91	04	99	93
N	0	17200	34400	51600	68800	86000
UF	0	0.172	0.344	0.516	0.688	0.860

3.3.1 Longitudinal wave measurements

The longitudinal bulk wave speed in each of the five fatigued plates was measured with the aid of an immersion tank. This method is well established in NDE research for speed measurements, as it provides excellent signal quality and very high signal-to-noise ratio. A schematic of the experimental setup is shown in Figure 3.3. As shown in Figure 3.3, the sample was placed directly under an immersion transducer. Both the transducer and the sample

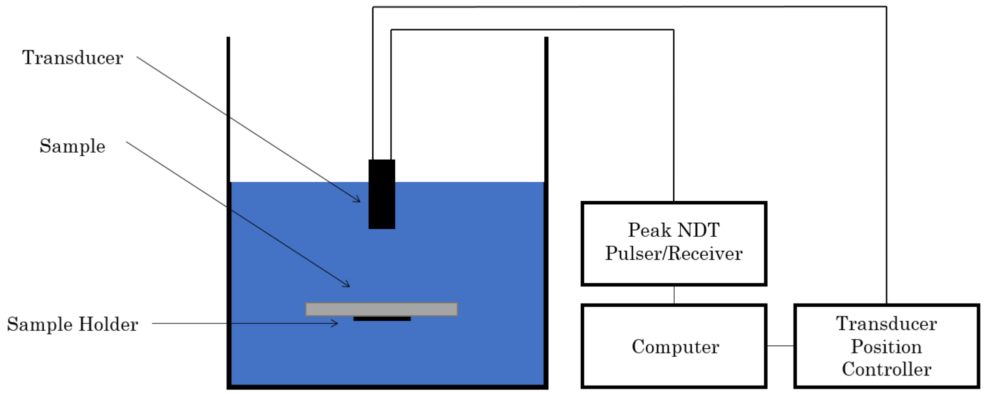

Figure 3.3: Schematic of the longitudinal wave measurements experimental setup. The setup is comprised of an immersion tank with a flat sample holder, where the steel samples were placed, a pulser/receiver and a transducer position controller.

were immersed in a water bath, with the water acting as the couplant between the transducer and the sample. The transducer was set up in a pulse echo configuration. Both the pulser/receiver and the position controller were guided by a computer. During a scan, the position controller continuously moved the transducer, while the pulser/receiver sent longitudinal waves. The sole front-wall and multiple back-wall reflections were then received by the pulser/receiver, and processed on the computer. The time of arrival between any successive reflections was subsequently used to calculate the speed of the longitudinal wave speed at that particular point on the plate.

For the measurements, an unfocused, General Electric immersion transducer (GAMMA 113-226-300), with a centre frequency of 10 MHz and an active element size equal to 0.25 inches (≈ 6.4 mm) was used. The scanning step size was set to 0.25 mm (≈ 0.43 longitudinal wavelengths) in both directions, and at each point, the signal was obtained from an average of 16 measurements. This number was found to be the optimal number of averages to give a clean signal without compromising the frame's scanning speed. The first and second back wall reflections were used for the speed measurements. In this measurement, an autocorrelation based method [86,87] was used to calculate the longitudinal wave speed.

Let $s(t)$ be the truncated signal obtained from the water tank (the signal containing only the first and second back wall reflections). Equation (3.17) gives the autocorrelated signal, $s^*(t)$:

$$s^*(\tau) = \int_{-\infty}^{\infty} \overline{s(t)} s(t+\tau)\, dt, \tag{3.17}$$

where $\overline{s(t)}$ is the complex conjugate of $s(t)$ and τ is a delay constant. The autocorrelated signal was then used to calculate the time-of-flight between the two consecutive back wall reflections, and hence the longitudinal wave speed at each point. It is possible to obtain similar results from simple, time-domain analysis, however, autocorrelated signals have even better signal-to-noise ratios, and are less sensitive to dispersion/disruption phenomena [86,87]. For the thickness of the plate, the quoted value of 8 mm given by Trueflaw was assumed to be uniform at all positions on the plate. Independent thickness variations using digital calipers showed a variation in the thickness of less than 0.025% of the quoted value.

3.3.2 Rayleigh wave measurements

The Rayleigh wave speed in each of the five fatigued plates was measured using a wedge setup, and a simple plate holder.

The experimental method for exciting Rayleigh waves here follows the technique used in past studies [88,89]. Piezoelectric longitudinal wave transducers with a centre frequency of 10 MHz were used in the experiments in this section. The Rayleigh waves were excited on the plate using perspex wedges whose angle were selected with the aid of the very well known Snell's law. An illustration of this law is shown in Figure 3.4.

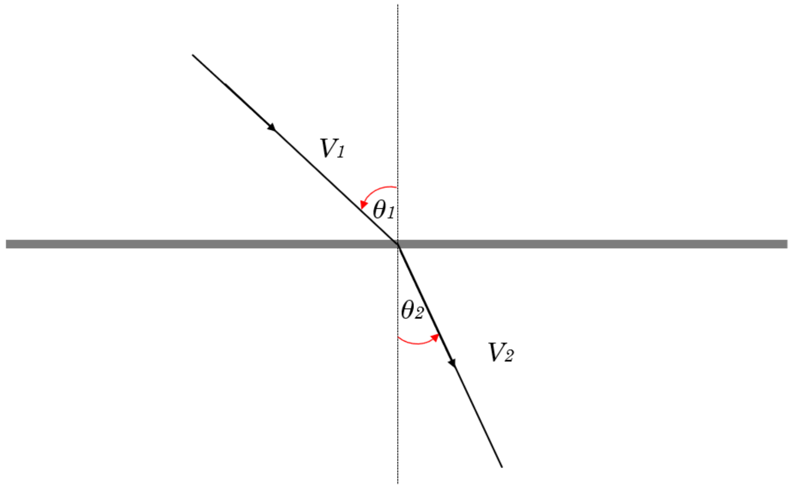

Figure 3.4: Schematic of Snell's law, showing the change in the propagation direction of an ultrasonic wave, caused by a change in the propagation medium.

Mathematically, this can be expressed as:

$$\frac{\sin(\theta_1)}{V_1} = \frac{\sin(\theta_2)}{V_2}, \tag{3.18}$$

where V_1 and V_2 are the ultrasonic wave propagation speeds in each medium respectively.

For the creation of a Rayleigh wave, the angle of the wedge, θ_R, (and hence, the longitudinal wave's travel angle), was selected to be such that when the longitudinal wave arrived at the interface between the wedge and the plate, the angle of refraction was such that the wave converted to a Rayleigh wave, i.e. $\theta_2 = 90°$. Therefore, θ_R was found from:

$$\theta_R = \arcsin\left(\frac{C_R}{C_L}\right), \tag{3.19}$$

where, for these experiments, C_R corresponds to the Rayleigh wave speed on steel and C_L corresponds to the longitudinal wavepseed of perspex. For a perspex wedge with $C_L = 2700$ m/s and a steel plate with $C_R = 2980$ m/s, $\theta_R \approx 65°$. Here it is worth noting that small variations in θ_R due to the variations in C_L in any real material are counteracted by the transducer beam spread. The transducer generates a longitudinal wave which is converted to a Rayleigh wave as it reaches the material travelling at the θ_R angle. The Rayleigh wave travels over the material, is received by the other transducer and reaches the Handyscope (TiePie Engineering, De Hemmen, Netherlands) after some further amplification. A schematic of the experimental setup is shown in Figure 3.5.

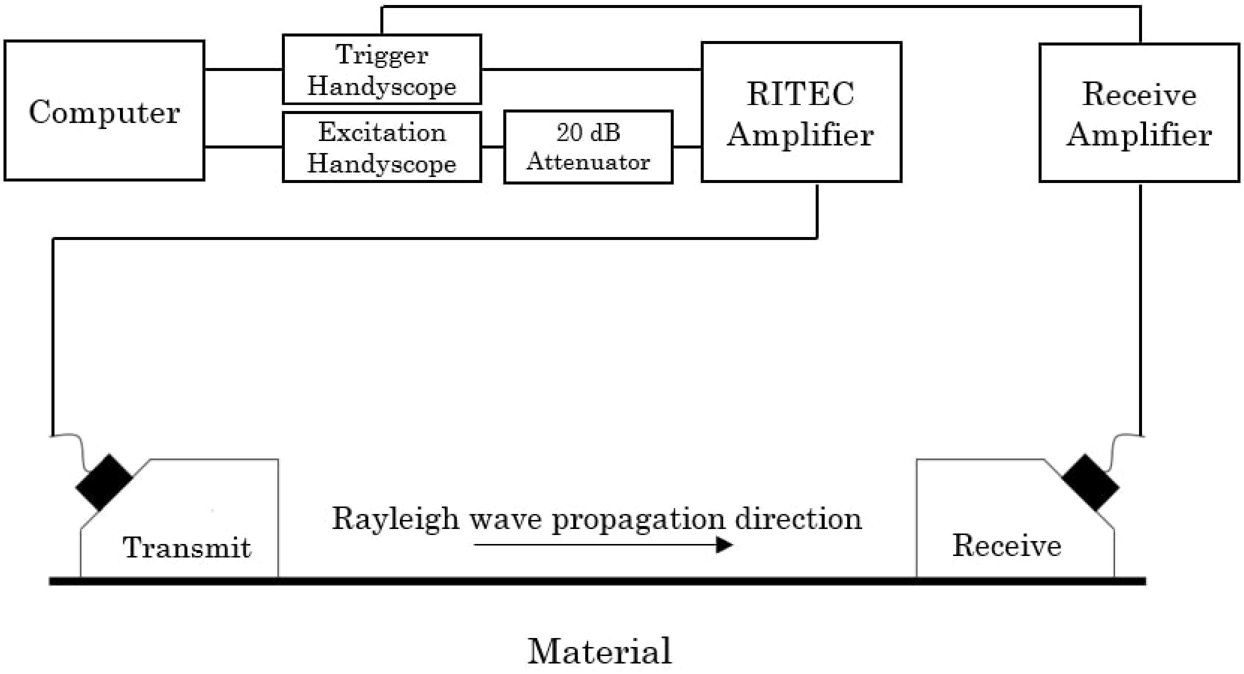

Figure 3.5: Schematic of the experimental setup, used to excite Rayleigh waves on steel. The signal is generated by the Handyscope, and reaches the transmitting transducer after being amplified.

In preliminary experimental measurements it was found that the high attenuation of the incident longitudinal wave, and the weak nature of Rayleigh waves, required multiple amplification steps to overcome. First, the longitudinal wave transducers were excited with the aid of a Ritec (Warwick, RI, USA) amplifier and a double Handyscope setup, as shown in Figure 3.5. The first Handyscope acted as a trigger, sending a 5 V square wave to the Ritec. Simultaneously, the second Handyscope sent a 5 cycle, 5 V Hann-windowed toneburst, whose length was slightly shorter than the width of the trigger signal. This signal was attenuated using a 20 dB attenuator, to comply with the Ritec's limits. The signal then travelled through the Ritec and the wedge setup, before being received by the receive amplifier, where it was further amplified by 60dB. The signal was finally collected by one of the Handyscopes.

To calculate accurate C_R values, it was necessary to obtain two Rayleigh wave measurements - this is because it is not possible to know with confidence the exact point where the longitudinal wave is converted to a Rayleigh wave, and hence the distance which the wave has travelled. The first Rayleigh wave signal was recorded by clamping the wedges together, while the second was obtained by separating the wedges with a block of known width, ΔX. The difference in the time of arrival between the two signals, divided by the width of the block, gave the C_R value for each point.

Each of the plates was scanned across its centreline, in the positive Y direction (shown in Figure 3.2), with the first scan taking place approximately where the origin was defined in the same figure. Also, the wedges were manufactured and then aligned on the plates in a way such that the first Rayleigh wave signal was entirely contained within the fatigue spot, while the second, where the separating block was used, only travelled slightly outside the fatigue region. C_R measurements were taken in 4 mm steps in the Y direction.

To ensure accurate stepping size, and also no movement/misalignment of the wedges during the measurements, a plate holder was manufactured. This is shown in Figure 3.6 - the holder was comprised of a plastic base with four

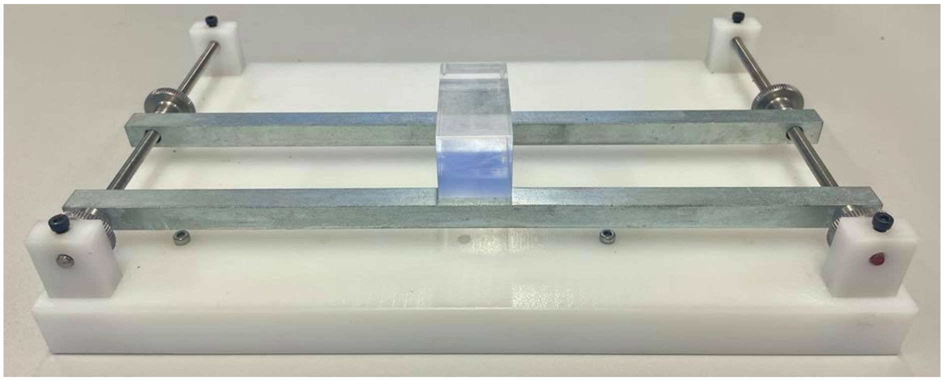

Figure 3.6: Photograph of the holder used in the Rayleigh wave scans. The plates were placed under the metal bars, with the wedges being subsequently placed on top of the plates, in-between the bars. The photograph also shows the spacing block

plastic protrusions. Each pair or the plastic protrusions was connected via a screw thread (0.8 mm pitch), and a metal ring was screwed through the thread. The screw thread also passed through two metal bars, which acted both as alignment aids for the wedges, and balancing areas for the separating block.

Due to the multiple amplification stages, it was also necessary to filter the signals with a bandpass filter with low and high cutoff frequencies of 8 MHz and 12 MHz respectively. An example of the Rayleigh wave signal, after filtering, both with the wedges touching, and with the separating block is shown in Figure 3.7.

In the processing of the Rayleigh wave signals it was found that the autocorrelation method used in subsection 3.3.1 yielded poor results. This is possibly due to the large amount of noise introduced by the multiple amplification stages, and potential changes in the shape of the signal - this is also shown in Figure 3.7 where the shape of the signal is slightly distorted. However, the peaks still remain clearly visible. Therefore, the time of arrival of each of the Rayleigh wave signals was calculated from the peak of its Hilbert

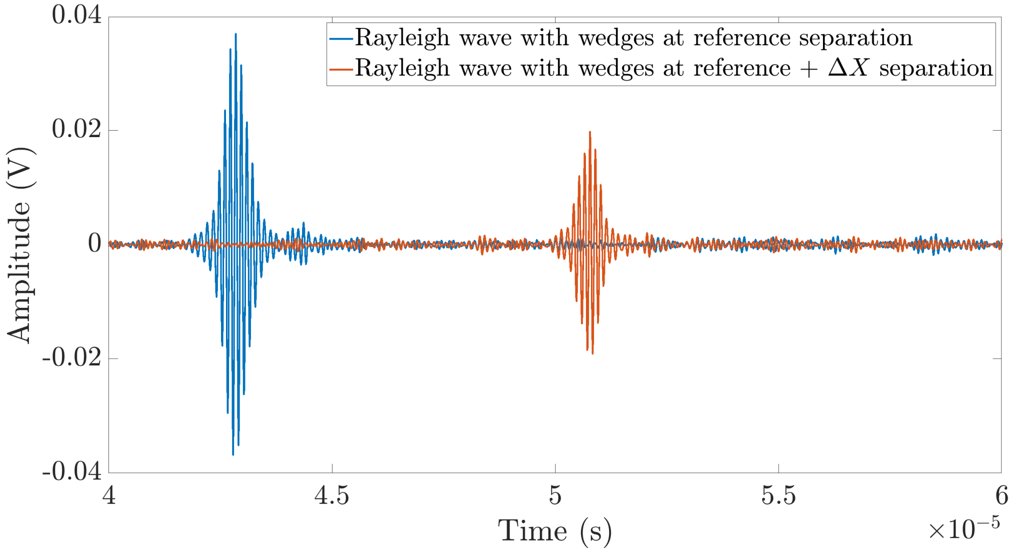

Figure 3.7: Example of the Rayleigh waves obtained with the method described in this section. A signal from both the reference separation, and from the reference separation plus the spacing block's width are shown.

envelope.

3.3.3 Electron backscatter diffraction

To verify the monotonic reduction in ultrasonic wave speed as fatigue progresses, the dislocation density and ultrasonic speed in a steel sample at high and low dislocation states was measured. It is well known that fatigue causes the overall dislocation density in a material to increase [54, 55], and therefore the high and low dislocation density states are analogous to high and low fatigue states respectively.

To achieve this, first the dislocation density of a 20 mm x 20 mm steel sample was measured using EBSD. The sample was taken from the healthy region of one of the Trueflaw plates, and was expected to have a high dislocation density, as all Trueflaw plates had been subjected to cold rolling prior to fatiguing. For its preparation, it was ground using Silicon Carbide paper, progressively from 600 to 4000 grits. Subsequently, the ground sample was polished with 1 μm diamond paste and oxide polishing suspension (OPS) polishing for 45 minutes, respectively, similarly to [63,64]. This metallurgical prepared sample was placed in a Tescan Clara Scanning Electron Microscope (Brno, Czechia), in which 20 keV acceleration voltage and 10 nA current were set. The Oxford Instrument EBSD system, Symmetry 2, was used to acquire relatively large EBSD maps, i.e., 1200 μm $\times$ 840 μm, with a step size of 1 μm at 150× magnification. Following the imaging, a C_L C-scan was created, using the technique described in 3.3.1.

After the initial C_L scan was created, the sample was annealed at 1000°C for 45 minutes, followed by furnace cooling, to reduce the dislocation density, and the C_L and dislocation density measurements were repeated.

3.4 Experimental results & discussion

This subsection firstly presents the experimental results from the longitudinal and Rayleigh wave measurements completed on each of the five fatigued plates. The behaviour observed in these measurements is subsequently verified against the theory using EBSD imaging, the results of which are also presented here.

3.4.1 Longitudinal wave measurements

The method described in 3.3.1 enabled the creation of a C_L map for each plate. For reference, a C_L map was also created for a blank, reference plate containing no fatigue damage. The results are shown in Figure 3.8.

As shown in Figure 3.8, there is a clear low-speed region in all but the reference plate. The region is of roughly circular shape, which is consistent with the shape of the oxidisation mark on the plate. Additionally, as expected,

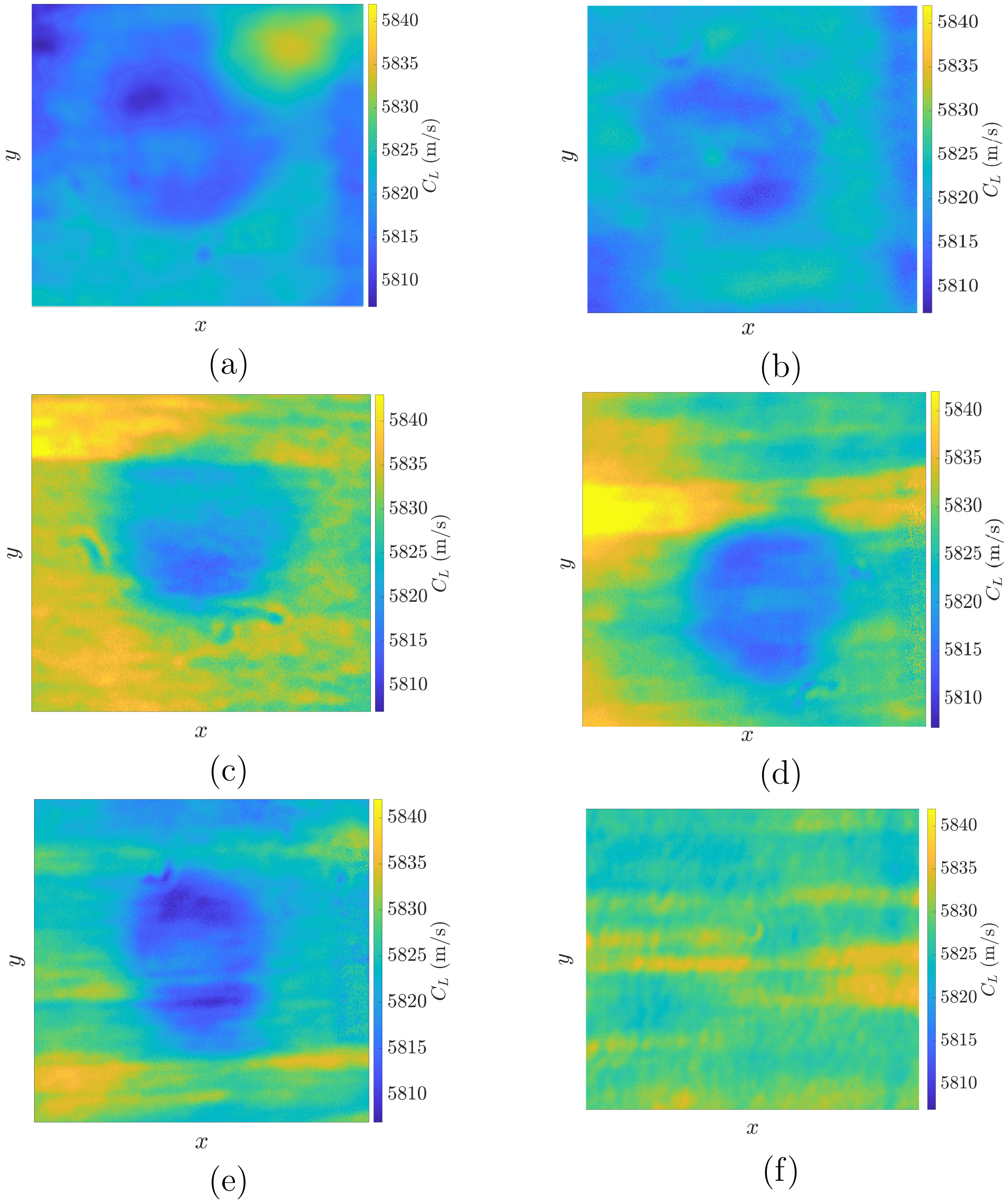

(a)

(b)

(c)

(d)

(e)

(f)

Figure 3.8: C_L C-scans maps, obtained by 0° through-thickness reflection immersion testing. The results are presented in decreasing fatigue order, with subfigures (a)-(e) corresponding to plates 93, 99, 04, 91 and 84 respectively. Finally, Subfigure (f) corresponds to the reference plate (plate 00). Each plate is approximately 100 mm×100 mm in size, and the fatigue spot has a diameter of approximately 50 mm.

the reference plate in Figure 3.8f shows no signs of a low speed area.

Ranking the plates in fatigue order is not visually obvious - there is some indication of the most fatigued area becoming increasingly slower at higher fatigue levels, however, this is not strong enough to confidently indicate a different fatigue state. To achieve a more rigorous fatigue indication, it was first necessary to define a healthy and a fatigue region in each plate, from which healthy (C_{L_h}) and fatigued (C_{L_f}) longitudinal speed values could be extracted. This process was necessary as material inhomogenity creates zones of irregularities in the ultrasonic wave speed, which do not allow for simple, visual ranking of the plates in fatigue order. The fatigue region was always defined as the region of most severe damage in the plate i.e. the region with the lowest C_L values. The healthy region was defined to be away from the boundary of the fatigue spot, at a representative area, ensuring that it did not contain any sudden changes in C_L, which could be a result of inherent material inhomogenity and not fatigue. Both C_{L_h} and C_{L_f} were calculated by using the arithmetic mean of all the C_L values in their respective area. The change in longitudinal speed, ΔC_L was then calculated from Equation (3.20):

$$\Delta C_L = \frac{C_{L_f} - C_{L_h}}{C_{L_h}}. \tag{3.20}$$

It is convenient to plot the ΔC_L value for each plate against its usage factor (UF) value. The results are shown in Figure 3.9. In Figure 3.9, the % change in longitudinal wave speed, $\Delta C_L(\%) = \Delta C_L \times 100$ is plotted. In terms of the error in the C_L calculations, this was found to be two orders of magnitude smaller than the order of the changes in longitudinal speed due to fatigue.

As shown in Figure 3.9, ΔC_L decreases with an increased UF, meaning that the longitudinal wave travels slower as fatigue progresses. Additionally, this

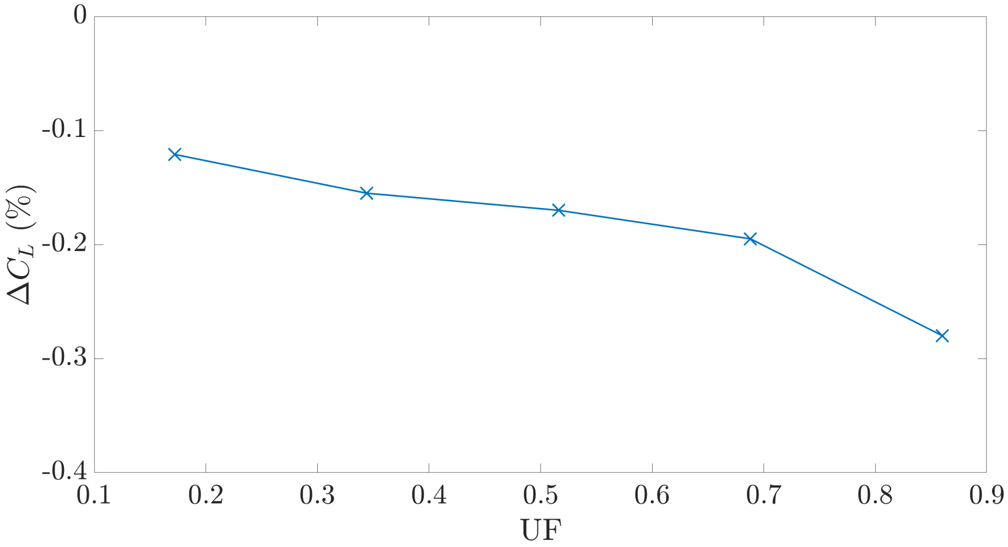

Figure 3.9: Evolution of the change in longitudinal wave speed, ΔC_L, with an increase in UF.

change is monotonic, and ΔC_L decreases rapidly as UF approaches 1, which is consistent with the theory and past studies [56–61]. Also, these observations confirm that thermal fatigue has a similar effect on C_L as mechanical fatigue.

However, as shown in Figure 3.9, the magnitude of ΔC_L is small. In an industrial environment, if a chart based on Figure 3.9 was used to correlate a ΔC_L value from a component to a specific UF value, it would be difficult to do so with confidence, as even a small, benign change or error in either C_{L_f} or C_{L_h} would yield a ΔC_L value corresponding to a significantly different UF value. Also, as shown in Figure 3.8, when a material is not homogeneous, it is not straightforward to define its healthy region. Additionally, the use of longitudinal waves requires accurate knowledge of the material thickness, which may not be possible for some industrial applications where the components are subjected to loading which gradually damages them, or where the components are not made with a high degree of accuracy. Therefore, in subsection 3.4.2 Rayleigh waves are used for a similar assessment, both to increase the change in speed values, and to eliminate the need for using the component thickness.

3.4.2 Rayleigh wave measurements

The results of scanning the five fatigue plates and the reference plate using Rayleigh waves are shown in Figure 3.10.

Again, variation of C_R in the reference plate appears random and there are no signs of a low C_R area. In all five fatigue plates however, the presence of a fatigue zone is clear and is signified by a region of low C_R values. The wave speed can be seen to vary by a small amount in the first 2-3 C_R measurements, which visually lie outside the fatigue region. After those points, C_R can be seen to decrease to a minimum, before recovering as the wedges exit the fatigue area. The change in Rayleigh wave speed, ΔC_R was calculated from Equation (3.21):

$$\Delta C_R = \frac{C_{R_f} - C_{R_h}}{C_{R_h}}, \tag{3.21}$$

where C_{R_h} and C_{R_f} are the Rayleigh wave speed in the healthy and fatigue areas respectively. The healthy Rayleigh wave speed for each plate was defined as the mean of the first 3 measurements from the respective subfigure of Figure 3.10. The fatigued wave speed for each plate was defined as the minimum C_R value in the plate's respective subfigure in Figure 3.10. Again, it is convenient to plot the ΔC_R value of each plate against is UF. The results are shown in Figure 3.11, again plotted as a percentage change ($\Delta C_R(\%) = \Delta C_R \times 100$). Figure 3.11 also shows the ΔC_L values from Figure 3.9, to better visualise the increase in the changes in speed observed through the use of Rayleigh waves. In terms of the error in the C_R calculations, this was again found to be two orders of magnitude smaller than the order of the changes in Rayleigh

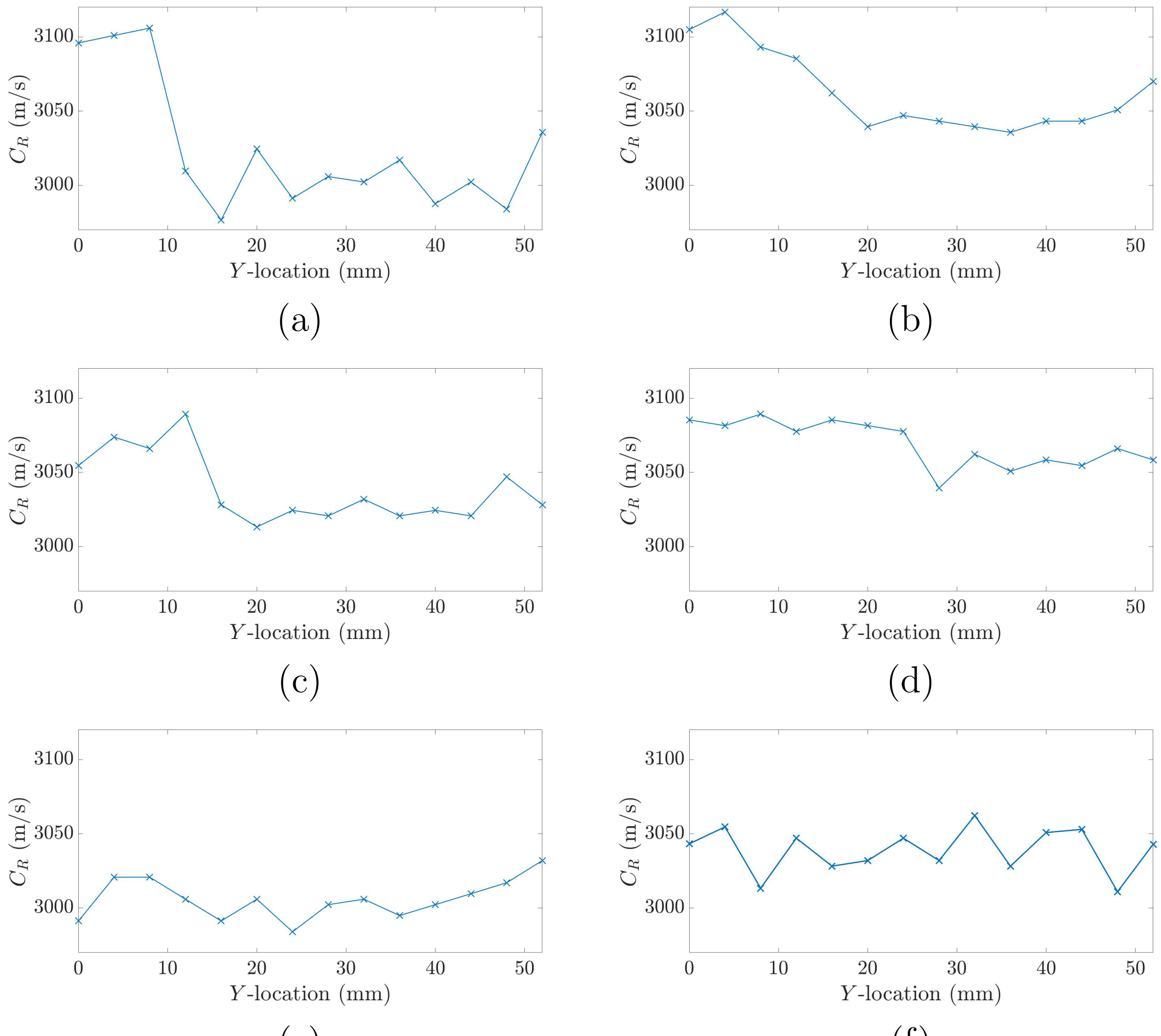

(a) (b) (c) (d) (e) (f)

Figure 3.10: B-scans showing the variation of C_R for the five fatigued plates and the reference plate (f). The scans were obtained by moving the wedges at 4 mm increments along the centreline of the plate. The $X - Y$ coordinate axes are shown in Figure 3.2 for one fatigue spot, but the variation of the origin between the other spots is expected to be very small. The results are presented in decreasing fatigue order, with parts (a)-(e) showing plates 93, 99, 04, 91, and 84 respectively.

speed due to fatigue.

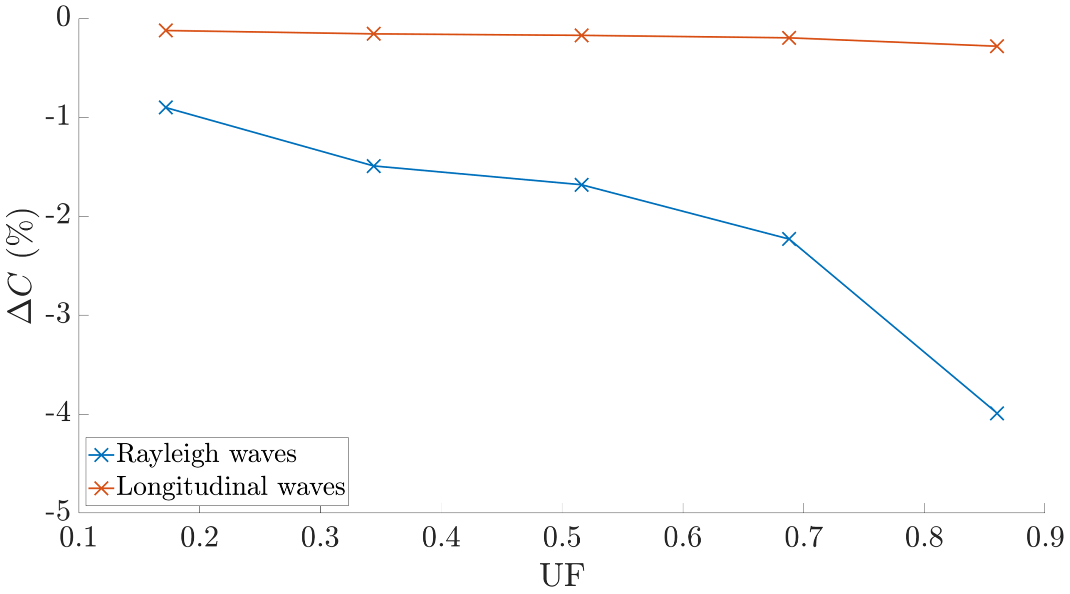

Figure 3.11: Evolution of the change in Rayleigh wave speed, ΔC_R, with an increase in UF. The respective ΔC_L values from Figure 3.9 are also plotted to facilitate the comparison between the change in speed of both waves.

Similar to Figure 3.9, the change in speed decreases monotonically as fatigue progresses. The shape of the plot has also been preserved, showing the larger gradient increase between the second-to-most and most fatigued spot. However, as expected, the absolute values are significantly amplified, as the Rayleigh wave travels entirely across the fatigue area, compared with longitudinal waves. The combination of the monotonic evolution of ΔC_R values with UF, and their significantly larger magnitudes can potentially allow for a more confident fatigue state assessment, as small errors in C_{R_h} or C_{R_f} do not significantly change the UF prediction, contrary to the similar approach using longitudinal waves. Additionally, using this method eliminates the need for knowing a component's thickness, as discussed previously.

3.4.3 Electron backscatter diffraction imaging

The resulting dislocation density and C_L maps both prior and after annealing are shown in Figure 3.12. By following the process described in subsection 3.3.3 process speed maps of a steel sample both at high and low dislocation densities were obtained, which correspond to high and low fatigue states respectively.

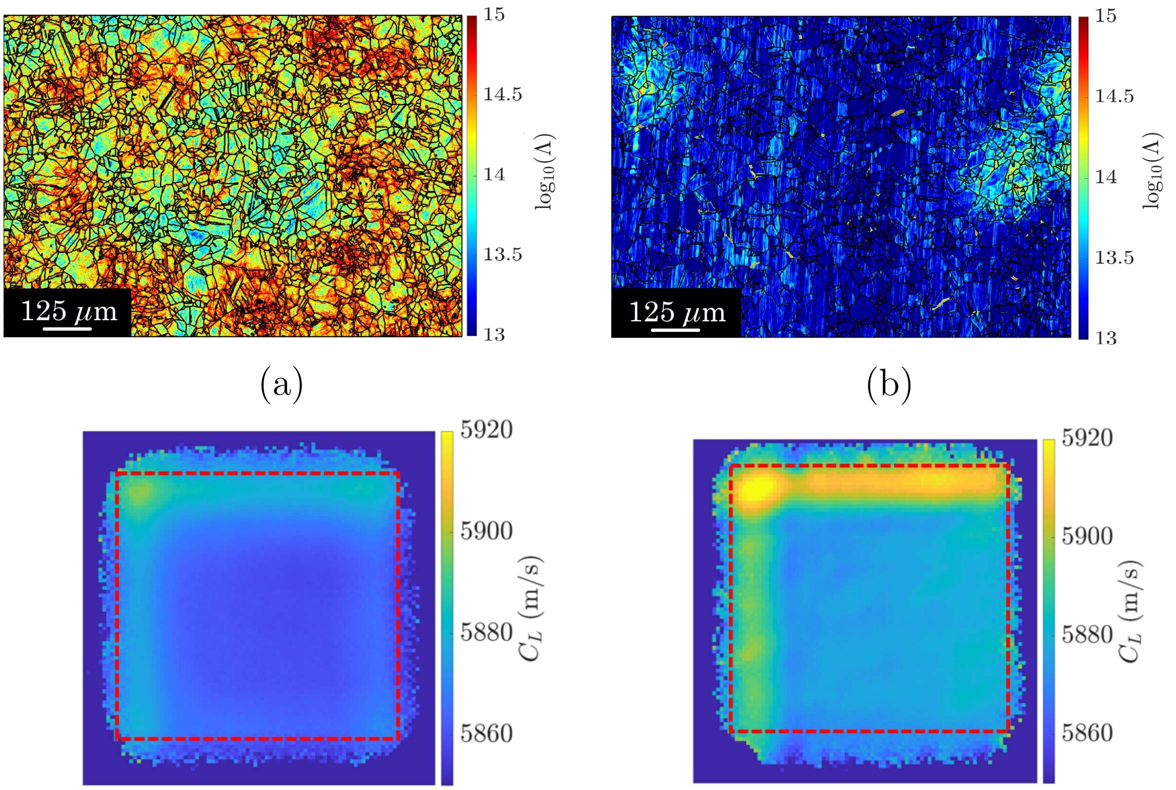

(a) (b)

(c) (d)

Figure 3.12: Dislocation density maps, obtained using EBSD, of the steel sample prior (a) and (b) after annealing, obtained using EBSD. The corresponding C_L maps are shown in (c) and (d). In (c) and (d), the dashed square represents the approximate boundary of the steel sample, which is 20 mm × 20 mm in size.

The mean dislocation density prior to annealing was $10^{14.29}$ m^{-2} (subfigure 3.12a), while after annealing, this value was reduced to $10^{13.21}$ m^{-2} (subfigure

3.12b). In terms of the speed, as shown when comparing subfigure 3.12c with subfigure 3.12d, there is a noticeable increase in the wave propagation speed, in all the points of the C-scan.

This observation verifies that a reduction in Λ increases the propagation speed of an ultrasonic wave. Therefore, as fatigue generally increases dislocation density, it will cause the propagation speed to reduce as per Equation (3.8). This explains the monotonic relationship between the UF and the ΔC_L or ΔC_R. It is finally worth noting that only looked at changes in dislocation density and not dislocation length were considered- this is because in [90] the authors observed that large deformations are required for L to change significantly, and therefore, the changes in speed become a function solely of Λ.

3.5 Finite element modelling

In this section a method through which the effects of fatigue in terms of ultrasonic time-of-flight can be implemented within a 2D FE model is presented, followed by a validation of this method using experimental data.

The phenomenon of wave propagation in the presence of fatigue damage, prior to crack initiation, is relatively unexplored in terms of FE modelling. Previous work includes studies for FE modelling for simulating creep-fatigue growth [91–93], as well the combination of theoretical approaches and FE results for predicting the service life of bonded joints [94], and crack growth in them [95]. However, to the author's knowledge, there currently does not exist an FE model which represents the effect which fatigue damage has on wave propagation speed, or which models the effect of fatigue on ultrasound, prior to crack initiation.

In the modelling, an equivalent-solid approach was used, which has been proposed in the theoretical derivations in [5]. This approach uses simple changes in the material properties in the FE domain to encapsulate the complex behaviour between the wave and the microstructural features of a real material. An analogy with the work that has been completed by Horne [96] was also implemented - in his work, the author used FE simulations to predict the equivalent reduction in E in areas which were subjected to creep damage. This was achieved by creating FE domains with elliptical voids, to simulate the pores which creep creates, and then using the simulation data to extract the equivalent stiffness matrix, for a domain with no elliptical voids. It was found that the presence of creep reduced the E value by approximately 10%-20%. As a starting point, here similar values of E reduction were used, before using an iterative approach to obtain the real E values to represent the fatigue damage. This iterative approach is discussed below, alongside a description of the FE model. The equivalent-solid approach here is analogous to the approach in Chapter 2, where energy loss terms in FE were used to achieve the required attenuation values, however, the focus here is in speed rather than in attenuation.

3.5.1 Setting up the FE model

A schematic of the FE model used in the study here is shown in Figure 3.13. As shown in the schematic, a rectangular FE domain was created, to represent a 2D cross-section of the fatigued plates. The fatigue damage zone was placed in the lower part of the domain, and monitor nodes were placed to its left and right. The distance d was selected to be the average distance between the two Rayleigh measurements described in subsection 3.3.2. The length of the fatigue zone was set to be equal to 50 mm, which is the size of the fatigue zone as provided by Trueflaw. For longitudinal wave simulations, a source line was defined at the top of the FE domain, while for Rayleigh wave simulations, the source line was defined to be at the left of the FE domain, on the bottom boundary. Finally, Absorbing Layers (ALs) were implemented at the top, left and right of the FE domain, to eliminate any unwanted boundary reflections, using the method described in [97].

For exciting longitudinal waves, the nodes comprising the source line were displaced in the Z direction. A Gaussian amplitude window was applied to the source line, to better represent the physics of a real transducer. For exciting Rayleigh waves, the method described in [98] and described in detail in Chapter 2 was followed.

For the meshing, 2D triangular elements were used. These elements are of low order and possess three nodes each. For both longitudinal and Rayleigh wave simulations, 20-30 elements per Rayleigh wavelength were used, as per the recommendations in [14]. A typical model size for the longitudinal wave simulations was of the order of 10^7 degrees of freedom.

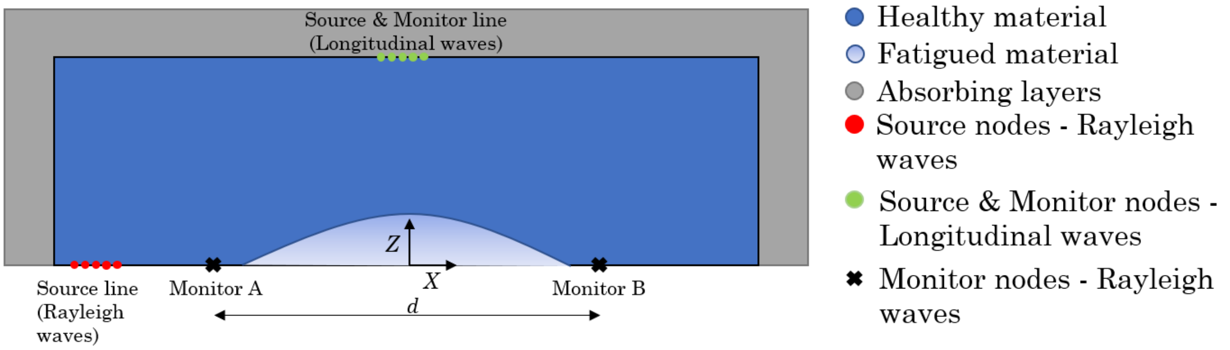

Figure 3.13: Schematic of the model used in the FE simulations. The fatigue zone comprised part of the bottom area of the FE domain, and is represented as an area of gradually reducing E. The schematic also shows the origin of the coordinate system used in this section.

It was assumed that fatigue affects 10% of the material thickness, similar to the findings in [96]. This implies that for the 8 mm thick plates that were used in this study, the fatigue zone thickness, t_f, was equal to 0.8 mm.

This is further supported by comparing the findings in Figures 3.9 and 3.11 - the changes in C_R are approximately one order of magnitude larger than the changes in C_L. Given that also the Rayleigh wave travel distance is approximately one order of magnitude times larger than the plate thickness, this implies that the fatigue zone affects approximately 10% of the plate thickness. It is worth noting that the extent of how the fatigue affects this 10% band of the material is not expected to be uniform, but rather to be more severe at the centre of the fatigue spot, with a gradual taper towards the healthy area near the edges of the fatigued area.

Although implementing fatigue as a change in a material's Young's modulus has physical meaning [99], it would not be realistic to assume that the effective Young's modulus exhibits a step change in its magnitude near the fatigued surface. Therefore the fatigue change was implemented as a gradual change in E, from the healthy value, E_h, to a fatigued value, E_f. It was then necessary to decide on the variation of the Young's modulus profile from E_h to E_f from the healthy portion of the material to the fatigued surface. To construct a Young's modulus profile with physical significance, the strain profile which was provided from Trueflaw for one of the plates was utilised. Trueflaw were able to calculate the strain along the thickness of the plate using simulation results from the commercial FE package ANSYS (Canonsburg, Pennsylvania). The strain profile provided by Trueflaw is shown in Figure 3.14.

As shown in Figure 3.14, the value of the strain is high at the point which lies on the fatigued surface ($Z = 0$ mm in Figure 3.13). The strain values initially decline rapidly, up to approximately $Z = 0.2$ mm, before gradually tending to 0, as the Z value approaches 0.8 mm, which is the end of the fatigue zone as per the assumptions.

With the aid of the strain profile in Figure 3.14, an analogous Young's mod-

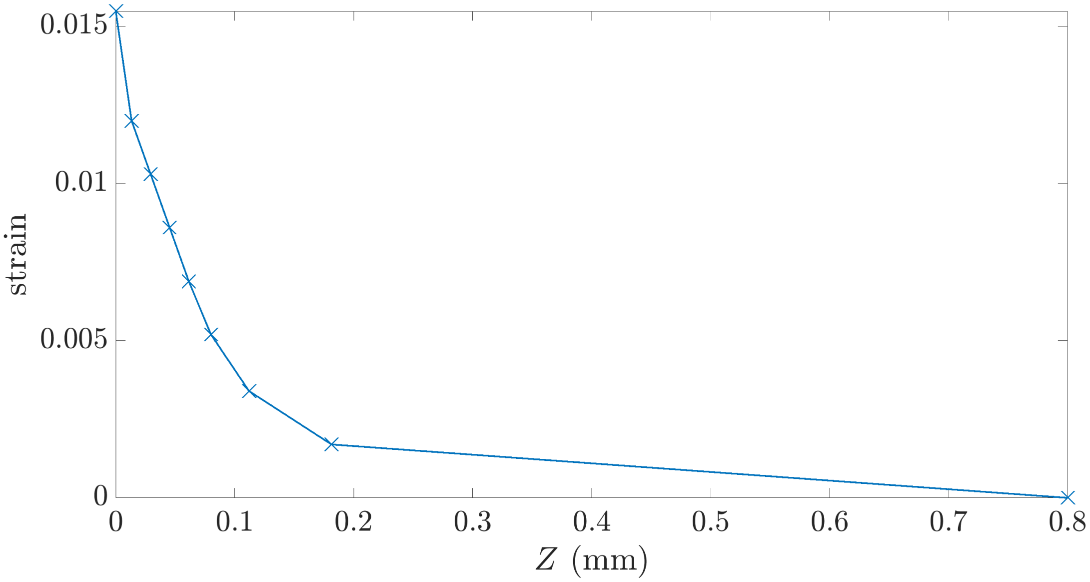

Figure 3.14: Plot of strain versus distance (Z) from the surface. The strain in the plate has initially a large magnitude, at the point which lies exactly on the fatigued surface ($Z = 0$ mm), and can be seen to decrease as one moves away from this surface. The data in this figure was provided by Trueflaw.

ulus profile was derived. To achieve this, first the percentage difference from the maximum strain point was calculated for all the other points in Figure 3.14. Then, E_h, which is the Young's modulus value for all $Z > 0.8$ mm, was chosen to be 200 GPa, and, due to the 10% maximum drop in E which was assumed, E_f was chosen to be 180 GPa. All Young's modulus values in-between were calculated by applying the same percentage change between the point of interest and E_f, as for the corresponding strain profile point and the strain profile point at $Z = 0$ mm. It is worth noting that there is no strong physical justification in this approach, however, the fine details in the shape of the profile and the variation of E will only have a minor effect on an ultrasonic wave - in recognition that strain corresponds to damage level, the change in E is assumed to be in proportion to this. The resulting E profile is shown in Figure 3.15.

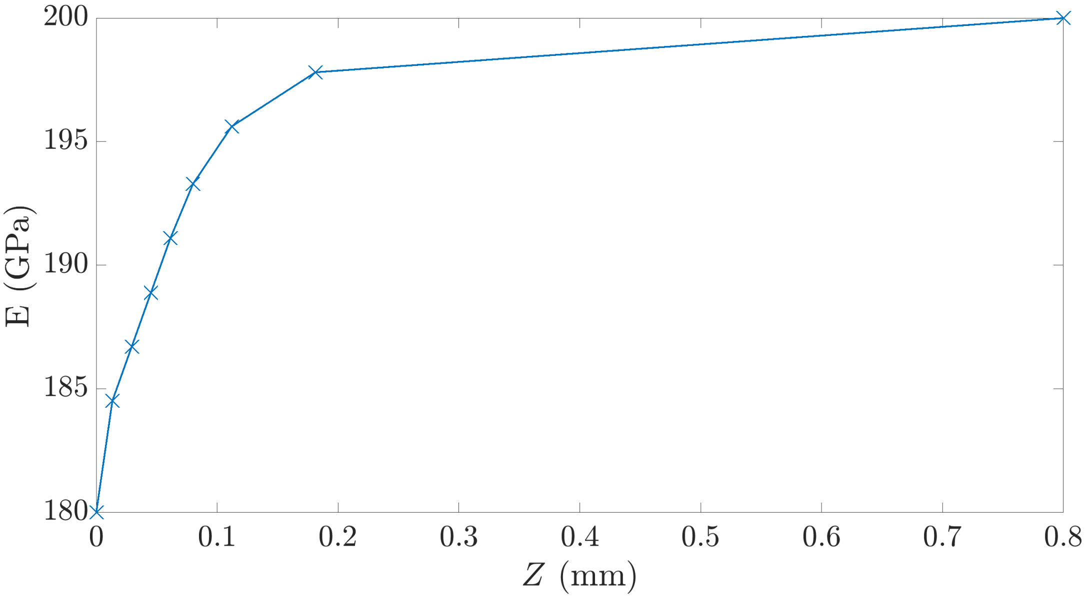

Figure 3.15: E profile, representing the variation of the Young's modulus inside a fatigued plate. The minimum E value lies on the fatigued surface ($Z = 0$ mm), and E can be seen to recover to the healthy Young's modulus value, E_h as Z approaches 0.8 mm, which is the end of the fatigue zone. The profile here has been derived by imitating the shape of the strain profile in Figure 3.14.

The graph in Figure 3.15 gives eight distinct Young's modulus values. To implement this in the FE model in Pogo, eight material layers of gradually decreasing Young's modulus were defined. At $Z > 0.8$ mm, the Young's modulus value was set to E_h (which is the highest E value in Figure 3.15), at 0.7 mm $< X <$ 0.8 mm, the Young's modulus value was set to be the second highest value of Young's modulus in Figure 3.15, and so forth. Here it is worth noting that these layers were only applied for -25 mm $< X <$ 25 mm, creating a damaged area with a length of 50 mm. Additionally, a Tukey window, with a Tukey parameter r=0.5 was applied to all the layers, to ensure a smooth joining between the fatigued region and the rest of the domain, as per Equation(3.22):

$$w(X) = \begin{cases} \frac{1}{2}\{1 + \cos\left(\frac{2\pi}{\mathrm{r}}[X - \mathrm{r}/2]\right)\} & 0 \leq X < \frac{\mathrm{r}}{2} \\ 1 & \frac{\mathrm{r}}{2} \leq X < 1 - \frac{\mathrm{r}}{2} \\ \frac{1}{2}\{1 + \cos\left(\frac{2\pi}{\mathrm{r}}[X - \mathrm{r}/2]\right)\} & 1 - \frac{\mathrm{r}}{2} \leq X \leq 1. \end{cases} \tag{3.22}$$

The implementation of such a window both avoids the creation of unwanted reflections due to acoustic impedance mismatch issues at the boundary, but is also more realistic, as steel conducts heat well, and therefore it is expected that a smooth damage profile is also present inside the plates themselves. A detail of the FE domain, showing the area of gradually reducing E created with the method described in this paragraph, is shown in Figure 3.16.

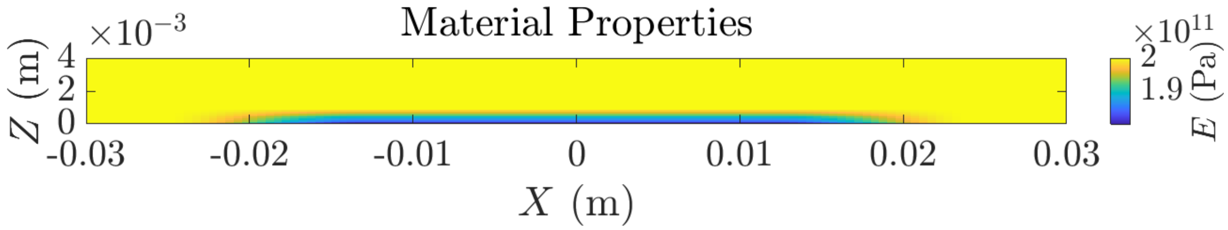

Figure 3.16: Detail of the FE model, showing the variation of E, created to represent the fatigue region. The gradually decreasing E layers can be seen, as well as the smooth joining with the healthy material, created by the implementation of a Tukey window.

Using this approach, it is also possible to calculate the theoretical, C_{L_f} value. This will be equal to the thickness of the model divided by the time of flight of the longitudinal wave. The time of flight will be equal to the sum of the time of flights in each individual material layer; those can be found by dividing the thickness of each layer by the (known) longitudinal velocity in that layer.

This can be expressed as:

$$C_{L_f} = \frac{t_{\text{model}}}{\sum_{i=1}^{\text{N}} \frac{t_i}{C_{L_i}}}, \tag{3.23}$$

where t_i and C_{L_i} are the thickness and longitudinal wave speeds of that layer respectively, t_{model} is the thickness of the entire domain and N is the number of material layers. In terms of material properties, and using the results in [7, 15] for relating C_L to the density and elastic constants, the above equation can be expressed as

$$C_{L_f} = \frac{t_{\text{model}}}{\sqrt{\frac{1-\nu}{\rho(1+\nu)(1-2\nu)}} \sum_{i=1}^{\text{N}} \frac{t_i}{\sqrt{E_i}}}. \tag{3.24}$$

A final consideration was to investigate whether the centre frequency of the simulation (10 MHz) would yield appropriate results. To investigate this, the value of t_f was fixed at 0.8 mm, and the frequency was varied. A plot showing the variation of ΔC_R against the Rayleigh wavelength (normalised by t_f) is shown in Figure 3.17.

As shown in Figure 3.17, the Rayleigh wavelength should be at most equal to t_f, for the ΔC_R to converge. This is expected, however, as the theory suggests that most of a Rayleigh wave's energy lies within one wavelength, in the Z direction. Therefore, at lower frequencies, where their energy lies outside the fatigue zone too, ΔC_R is not meaningful.

As an additional verification step, t_f was doubled to 1.6 mm and the same process was followed; this was to allow for even lower λ_R/t_f values at similar frequencies. The results are plotted in Figure 3.18. Similarly to Figure 3.17, the change in speed values only converge once the wavelength is at most equal to λ_R.

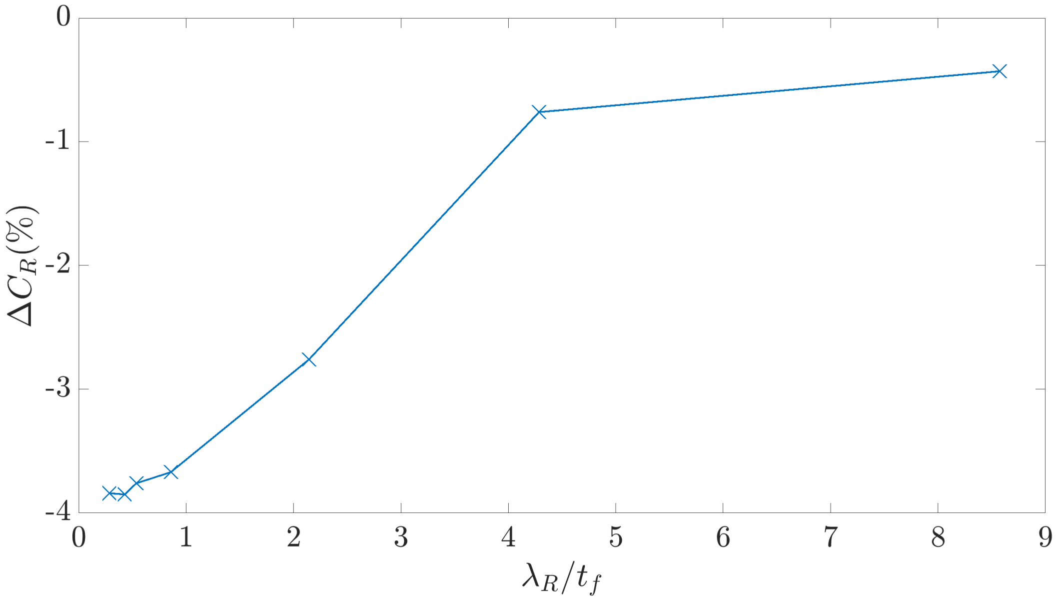

Figure 3.17: Variation of ΔC_R with a change in frequency. The ΔC_R values are plotted against the Rayleigh wavelength, normalised by the thickness of the fatigue zone. For this set of results, $t_f = 0.8$ mm

In this study, with t_f equal to 0.8 mm and a centre frequency of 10 MHz, $\lambda_R/t_f \approx 0.38$, and therefore this limiting condition was satisfied.

3.5.2 Results & discussion

The method of using the shape of the strain profile to derive an equivalent E profile provided a good basis for the analysis. However, this method remains a simplification which possibly does not encapsulate all the physical complexity of the evolution of E as fatigue progresses. Additionally, only one strain profile was provided by Trueflaw. Therefore, it was necessary to modify the profile derived in the previous section, and generate a profile for each of the five fatigued plates.

To achieve this, a gradient-multiplicator method was implemented. Let the vector containing the profile derived in the previous section, and shown in

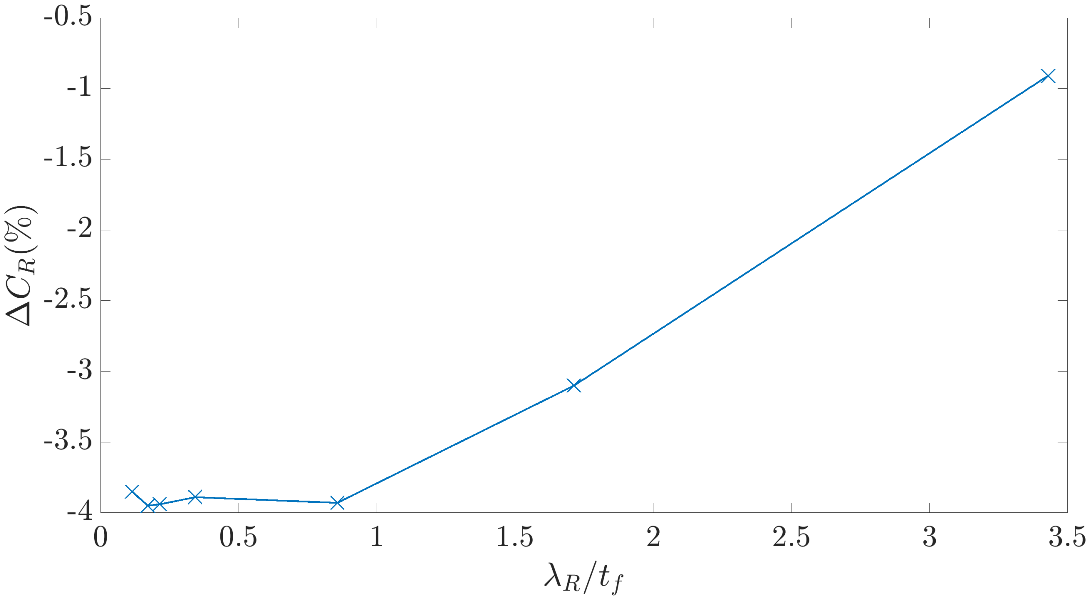

Figure 3.18: Variation of ΔC_R with a change in frequency. The ΔC_R values are plotted against the Rayleigh wavelength, normalised by the thickness of the fatigue zone. For this set of results, $t_f = 1.6$ mm

Figure 3.15, be $\mathbf{E}_{\text{ref}}$. Let also the subscript 1 denote the first entry in a vector. First, the difference between $\mathbf{E}_{ref_1}$ and all the other values in $\mathbf{E}_{\text{ref}}$ was calculated, creating a difference vector, $\mathbf{E}_{\text{diff}}$. Then, a method to modify $\mathbf{E}_{ref}$ to create a more or less severe profile, would be to subtract $n \times \mathbf{E}_{\text{diff}}$ from $\mathbf{E}_{\text{ref}_1}$, where n can be thought of as a gradient-multiplicator i.e. :

$$\mathbf{E}' = \mathbf{E}_{ref_1} - n \times \mathbf{E}_{diff}, \tag{3.25}$$

where $\mathbf{E}'$ is the modified profile vector. If $n = 1$, then the profile remains unchanged. A value of $n > 1$ implies a more severe change in the Young's modulus profile from E_h to E_f (hence, more severe fatigue), and similarly, a value of $n < 1$ implies a less severe change in the Young's modulus profile.

As there are no reference n values for these kinds of FE simulations, it was

Table 3.2: ΔC_R values from experimental measurements, and the required n values required to achieve the same ΔC_R values in Pogo. This table also shows what percentage drop from E_h each value of n corresponds to. Here, as per the above-mentioned assumptions, $n = 1$ corresponds to a 10% maximum reduction between the E profile in the FE model and the healthy E value.

Plate	93	99	04	91	84
$\Delta C_R(\%)$	-3.99	-2.23	-1.68	-1.49	-0.90
n	1.37	0.80	0.61	0.55	0.32
$\Delta E(\%)$	-13.29	-7.68	-6.43	-5.72	-3.50

necessary to derive them for each plate. To achieve this, an iterative approach was used, where the n value for each plate was found, such that the ΔC_R value from the FE simulation was matched to the respective ΔC_R value of the blue curve in Figure 3.11. Table 3.2 shows the experimental ΔC_R values, the value n which was required to achieve the ΔC_R value in Pogo, and the corresponding percentage change in E (ΔE) which each value of n implies. It was then necessary to assess how well this method of implementing fatigue damage with respect to changes in speed compared with the ΔC_L measurements. To complete this assessment, a bulk wave model was created, as described in subsection 3.5.1. The question here was to check how well the experimental and FE values of ΔC_L matched, using the profiles derived from the ΔC_R measurements. The results are shown in Figure 3.19.

As shown in Figure 3.19, there is good agreement between the ΔC_L values obtained from the simulations and the experiments. The agreement is best at UF values below 0.7, while there is a small discrepancy in the ΔC_L value at the highest UF value - however, the change in the gradient of the UF vs ΔC_L plot observed in the experiments graph can also be seen in the FE graph, implying that the FE domain still behaves like the physical plate. The difference in the value of ΔC_L at this point is possibly due to the large UF

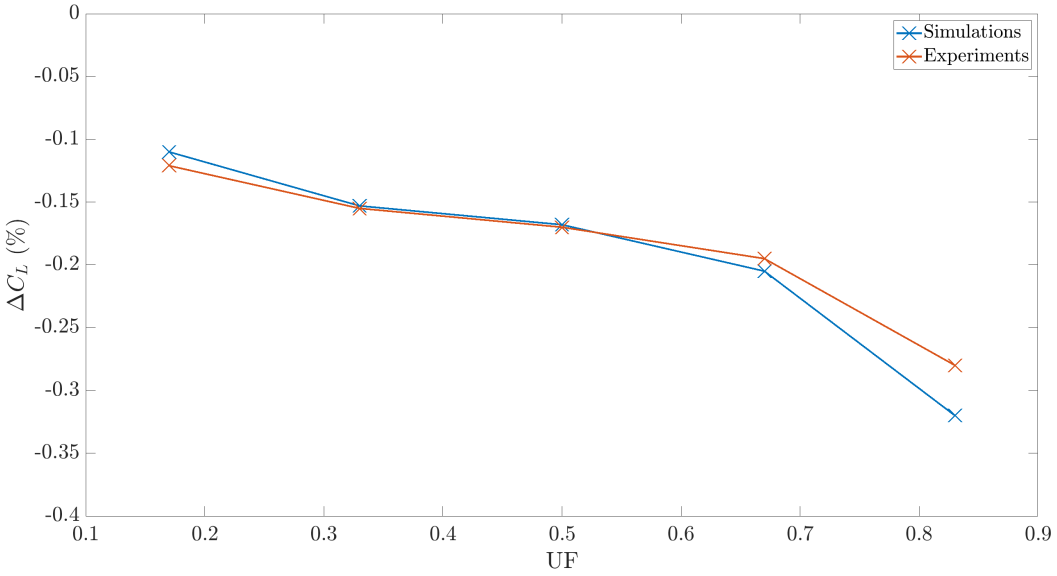

Figure 3.19: Comparison between the ΔC_L values obtained from the immersion measurements and the FE model. The results for each plate are plotted against their respective UF values.

itself. At large UF values, there is the possibility that other, larger defects have been developed in the material, and therefore the changes in speed might not arise purely from the dislocation multiplication.

Additionally, the overall agreement of the FE model with the ΔC_L values shows that using a Young's modulus profile as a method of representing fatigue damage is accurate in terms of modelling the propagation speed of ultrasound. This is because the profiles were derived from the ΔC_R values, but then matched the ΔC_L measurements, which were obtained independently. This method is simple to implement, and can have useful implications for the FE modelling of engineering components, where NDE methods rely on accurate time-of-flight measurements, but are also subjected to fatigue damage. Prior modelling of such components can provide correction factors which can be used in the experimental measurements, to provide more accurate time-of-flight measurements. It may be noted that in the model here, a pure change in E was assumed as the means of representing fatigue damage, which implies that shear waves should also be well represented in terms of speed changes - however, the literature suggests otherwise [5]. A potential solution is to also create a Poisson's ratio profile, such that shear waves are also represented well in the FE model, however, this requires a full study on the effects of fatigue on the Poisson's ratio of metals and alloys such as steel. For the present study, such further refinement was not pursued, as the stiffness reduction method was able to capture the effects of fatigue on the time of flight of longitudinal and Rayleigh waves accurately.

Finally it is worth noting that, given that the values of n in Table 3.2 gave a good match between the FE model and the experimental results, it is expected that if the inverse approach was used, a similarly good match would be obtained (i.e., if the n values were derived such that the FE simulations matched the longitudinal wave results, and were subsequently used in a Rayleigh wave model, a good match between the experimental and FE ΔC_R would have been achieved). It was chosen that the n values were to be derived from the Rayleigh wave experiments, as the larger ΔC_R values allowed the effect of small changes in n to be visible in the simulation results, and hence more accurate n values were obtained.

Chapter 4

Creeping waves for assessing the fatigue state of pipe geometries

4.1 Introduction

In the previous chapters the theory and implementation of a method for characterising the fatigue state of flat steel components was presented. Here, an attempt to extend those findings in pipe geometries is presented and discussed, as well as the limitations found during this investigation.

Pipe geometries are often a geometry of interest in the NDE field. Namely, multiple techniques have been developed to inspect pipes in the power [100, 101], chemical [101] and petroleum [102–104] industries. In terms of fatigue damage, the authors in [105] investigated the behaviour of drill pipes under fatigue and corrosion fatigue, while Han et al. [106] calculated the stress intensity factors in cracks caused by bending fatigue. In more theoretical studies, Paffumi et al. [107] used numerical methods and an elasto-plastic fatigue model to simulate the fatigue crack propagation in authentic steel pipes, while in [108] the authors used probabilistic methods to predict the number of cycles to failure for a steel pipe. However, the methods in their papers are concerned with large, individual cracks, and do not provide a method to characterise the fatigue state as a whole, either before, or after crack initiation and growth.

As discussed in the previous chapter, some valuable work has been completed by [60] and [61], using bulk shear waves. However, as these methods use through-thickness shear waves, the waves spend very limited time in the fatigued region, and therefore, the observed changes in speed and attenuation are smaller in magnitude compared with if a surface wave was used. It is worth noting that in [60], the changes appear to be bigger - however, the authors here were sending a wave through the length of a test piece on a tension-compression machine, and therefore the wave spends its entire travel time within a fatigued zone. In terms of using waves which travel on pipe surfaces, [56] and [57] used axial shear waves propagating in the circumferential direction of a pipe, and measured the changes in speed and attenuation as fatigue progressed - arriving at the same monotonic reduction in speed and the more complicated behaviour of the attenuation coefficient which was discussed in the previous chapter.

However, the scenario of being presented with a component which is fatigued along its entire thickness, or the scenario of fatigue existing on the outer surface of a pipe are both less likely to occur in industrial applications - rather fatigue in those cases is present around the inner surface of the pipe due to the cyclic pressure and temperature of the fluids which travel through it. Therefore, here an attempt was made to create a method which generated a wave travelling around the inner surface of the pipe to maximise the travel time inside the fatigue area, ensuring that this method did not need direct access to the inner surface - this is because such a method would require the component to go out of service and even sectioning of the pipe.

A potential solution, which maximises the travel time of the wave around the inner surface of the pipe, and satisfies these constraints, is the use of creeping waves, excited by mode conversion upon the incidence of a shear wave on the inner surface. Creeping waves are similar to Rayleigh waves, in the sense that they travel on the surface of a material and their amplitude exponentially decays away from the surface, however, their existence requires the presence of a curved and not a flat surface, as explained in [109] and [110]. While the creeping wave travels along the curved surface, it leaks energy in the form of shear waves into the bulk of the material. It can be noted that in the limit, as the radius of curvature becomes large, the energy radiation (and hence effective attenuation of the creeping waves) drops and the waves become Rayleigh waves. Creeping waves have been used in the past for various NDE applications - Nagy et al. [110] and Doherty & Chiu [111] used creeping waves for inspecting weep holes for the presence of identifiable fatigue cracks, while Qu et al. [112] used creeping waves for detecting notches in thick annuli. Studies involving FE modelling have also been completed; for instance, the authors in [113] used a commercial FE software to investigate the effect of cracks normal to the inner radius of an annulus to the amplitude of a creeping wave.

Here, the use of creeping waves excited by sending a shear wave from the outer towards the inner surface, as described in [110], is proposed for assessing the fatigue state of steel pipes, by utilising the results of the previous chapters and the leaky nature of creeping waves. Since it has already been demonstrated that the presence of fatigue reduces the propagation speed of an ultrasonic wave, creeping waves are expected to exhibit the same behaviour. As creeping waves will leak energy into the bulk of the material while travelling around the inner surface of a pipe, and those leaky waves can be recorded on the outside

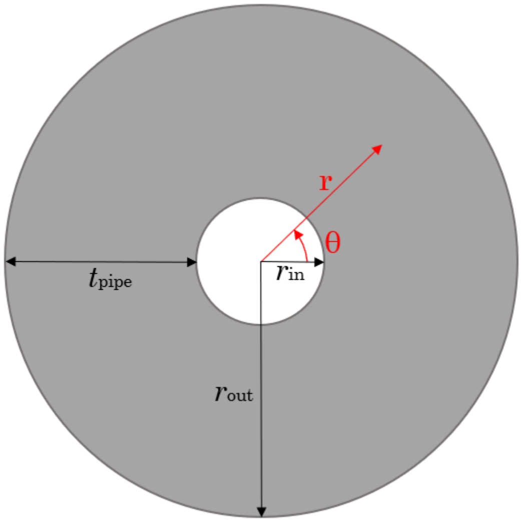

Figure 4.1: Polar coordinate system and pipe dimensions. The positive axis direction for the coordinate system are shown in red, while the pipe dimensions are shown in black.

radius of the annulus, their arrival time can be compared with the expected values from the case where fatigue was not present. This method maximises the travel time of the wave inside the fatigue region, since the creeping wave is restricted to propagating along the inner surface, where most of the fatigue damage is concentrated, without the need to access the inner surface.

4.2 Theory & FE modelling

4.2.1 Mathematical formulations

The theory presented here has already been established in [112] and [114]. Let us assume a circular annulus, with inner radius r_{in}, outer radius r_{out} and thickness $t_{\text{pipe}} = r_{\text{out}} - r_{\text{in}}$, in a standard (r, θ) polar coordinate system, as shown in Figure 4.1.

Let u_r and u_θ be the radial and circumferential components of the displacement in the annulus respectively. Let also σ_r, σ_θ and $\sigma_{r\theta}$ be the radial, circumferential and shear stresses in the annulus respectively. The equations of motion for such an annulus, are [114]:

$$\frac{\partial \sigma_r}{\partial r} + \frac{\sigma_r - \sigma_\theta}{r} + \frac{1}{r}\frac{\partial \sigma_{r\theta}}{\partial \theta} = -\rho\omega^2 u_r, \tag{4.1}$$

$$\frac{\partial \sigma_{r\theta}}{\partial r} + \frac{1}{r}\frac{\partial \sigma_\theta}{\partial \theta} + 2\frac{\sigma_{r\theta}}{r} = -\rho\omega^2 u_\theta. \tag{4.2}$$

If stress free boundary conditions are assumed, i.e.

$$\sigma_r = \sigma_{r\theta} = 0 \quad \text{at} \quad r = r_{\text{in}}, r_{\text{out}}, \tag{4.3}$$

and displacement potentials are also introduced, similarly to the method presented in Chapter 2, it can be shown that [112, 114]

$$u_r^{(\text{n})} = W_r^{(\text{n})}(\overline{r})\mathrm{e}^{jk_{\text{cr}}r_{\text{out}}\theta}, \tag{4.4}$$

and

$$u_\theta^{(\text{n})} = W_\theta^{(\text{n})}(\overline{r})\mathrm{e}^{jk_{\text{cr}}r_{\text{out}}\theta}, \tag{4.5}$$

where k_{cr} is the wavenumber of the creeping wave, defined as its angular frequency divided by its speed.

In the equations above, n denotes the n$^{\text{th}}$ creeping wave mode arising from the solutions of the equations of motion. The displacement amplitudes, $W_r^{(\text{n})}(\overline{r})$ and $W_\theta^{(\text{n})}(\overline{r})$ are then given by

$$\begin{aligned} W_r^{(\text{n})}(\overline{r}) = \frac{1}{r}\Bigg[& A_1^{(\text{n})}\frac{\hat{\omega}_{\text{n}}\overline{r}}{\gamma}J'_{\hat{k}}\left(\frac{\hat{\omega}_{\text{n}}\overline{r}}{\gamma}\right) + A_2^{(\text{n})}\frac{\hat{\omega}_{\text{n}}\overline{r}}{\gamma}Y'_{\hat{k}}\left(\frac{\hat{\omega}_n\overline{r}}{\gamma}\right) \\ & + j\hat{k}A_3^{(\text{n})}J_{\hat{k}}(\hat{\omega}_{\text{n}}\overline{r}) + j\hat{k}A_4^{(\text{n})}Y_{\hat{k}}(\hat{\omega}_{\text{n}}\overline{r})\Bigg] \end{aligned} \tag{4.6}$$

and

$$\begin{aligned} W_{\theta}^{(\mathrm{n})}(\overline{r}) = \frac{1}{r}\Big[& j\hat{k}A_1^{(\mathrm{n})}J_{\hat{k}}\left(\frac{\hat{\omega}_{\mathrm{n}}\overline{r}}{\gamma}\right) + j\hat{k}A_2^{(\mathrm{n})}Y_{\hat{k}}\left(\frac{\hat{\omega}_{\mathrm{n}}\overline{r}}{\gamma}\right) \\ & -A_3^{(\mathrm{n})}\hat{\omega_{\mathrm{n}}}\overline{r}J'_{\hat{k}}(\hat{\omega}_{\mathrm{n}}\overline{r}) - A_4^{(\mathrm{n})}\hat{\omega_{\mathrm{n}}}\overline{r}Y'_{\hat{k}}(\hat{\omega}_{\mathrm{n}}\overline{r})\Big], \end{aligned} \tag{4.7}$$

where $\overline{r} = r/r_{\mathrm{out}}$, $\hat{k} = k_{\mathrm{cr}}r_{\mathrm{out}}$, $\hat{\omega} = [\omega t_{\mathrm{pipe}}(1 - \frac{r_{\mathrm{in}}}{r_{\mathrm{out}}})]/C_T$. Also, $J_{\hat{k}}()$ and $Y_{\hat{k}}()$ are the first and second kind Bessel functions of order $\hat{k}$, and $A_1 - A_4$ are constants to be found from the boundary conditions.

4.2.2 Setting up the FE model

In terms of exciting a creeping wave the method described in [110] was followed, as the method described there assumes no direct access to the inner surface of the annulus. The authors in this study present two methods for exciting creeping waves on the surface of a circular hole embedded in a large plate. Both methods rely on the fact that shear waves are well coupled to leaky Rayleigh waves, which belong to the same category as creeping waves, and therefore the authors explain that if a shear wave passes sufficiently close to a curved surface, it will excite a creeping wave. The first method involves generating a shear wave wavefront, whose centre coincides with the centre of the hole whose length is at least 50% bigger than the radius of the hole. As the wavefront approaches the hole, most of the energy is reflected, however, the portion of the wave which grazes the hole excites a creeping wave. This method may be practical for plates with embedded holes, however, for annuli where the space is more limited, this method may not be feasible. Alternatively, the authors here present a method in which a shear wave is sent at an angle such that the main lobe of the shear wave grazes the hole, again resulting in the excitation of a creeping wave. This is the method which was used in this study, as it is better suited to the limited space within an annulus.

To assess the suitability of this method for fatigue state monitoring, preliminary FE investigations using Pogo were completed, and the simulation data was visualised using PogoPro [6]. First, an FE domain in the shape of an annulus was created, which was meshed using 2D triangular elements. The mesh size was set to approximately $\lambda_T/25$. A source line, with a length of 5 mm, centred at $\theta = 90^\circ$ was defined, as well as a monitor line with the same length, centred at $\theta = 270^\circ$.

To excite an optimal creeping wave, the centre of the shear wavefront must be such that it passes very close to the inner surface, without necessarily being incident upon it. To achieve this a focus point close to but not directly on the inner surface was selected. The distance of each source node on the source line was calculated from this focus point, and was then converted to time-delays which were prescribed to the source nodes, resulting into the shear wave beam being steered to the focus point. A schematic of the FE domain, showing the source and monitor lines, as well as an indicative location for the focus point, is shown in Figure 4.2.

It was also necessary to define absorbing layers to attenuate both the incident shear wave, as if not absorbed would create multiple reflections when colliding with the outer wall of the annulus, as well as any other unwanted reflections. The simplest method to achieve this would have been to introduce flat absorbing layers as shown in Figure 4.3. To achieve the best possible absorption, it would have been necessary to bring the absorbing layers as close as possible to the inner surface, however, this comes with the risk that the absorbing layer interferes with the creeping wave. Also, flat absorbing layers leave a larger portion of the pipe “free”, which may results in less than optimal absorption, especially at lower frequencies.

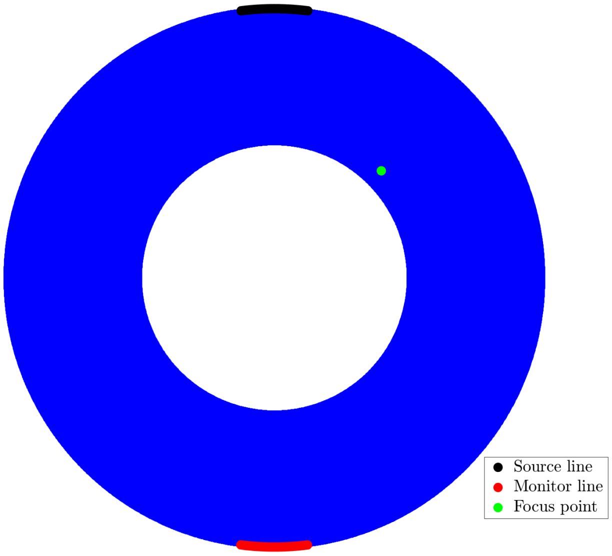

Figure 4.2: Schematic of the FE domain used to excite creeping waves on the inner surface of an annulus. The source line is shown in black, the monitor line is shown in red, and an indicative location of a focus point, where the shear wave beam is steered is shown in green, In this schematic, the focus point is located at $(r_{\text{in}} + t_{\text{pipe}}/8,\ 45°)$ in polar coordinates.

To mitigate this issue, it was decided to use elliptical absorbing layers instead of flat. This was achieved by modifying the pre-defined Pogo feature which creates circular absorbing layers, to accept a positive constant representing the eccentricity of the ellipse. A value of this constant equal to 1 would yield circular absorbing layers, while a value less or more than one would create ellipses with their major axes either parallel or perpendicular to the x direction respectively. An example of such an absorbing layer is shown in Figure 4.4.

For thick-walled annuli, the use of elliptical absorbing layers is not of imminent importance, as the large thickness allows for sufficient space for wave absorption. The issue of maximising the absorbing layer area becomes more important with thin-walled annuli. In those, due to the limited space it is very important to ensure that the maximum area is covered by absorbing

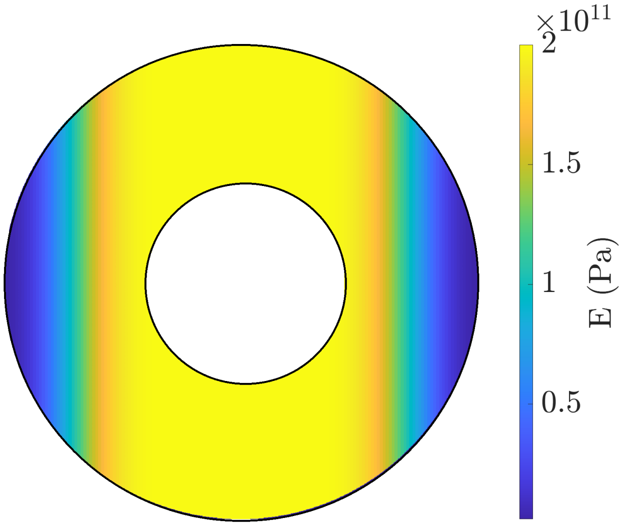

Figure 4.3: Example of flat absorbing layers applied to an annulus. The absorbing layer is shown as an area of gradually reducing E. Here, $r_{\text{in}} = 10$ mm and $r_{\text{out}} = 25$ mm.

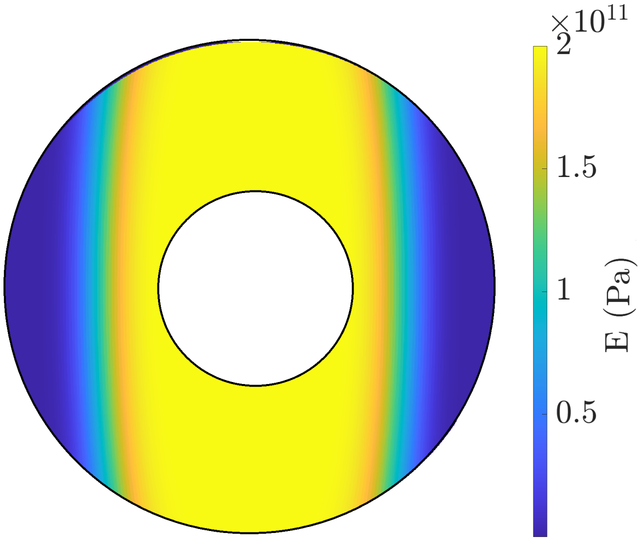

Figure 4.4: Example of an elliptical absorbing layer applied to an annulus. The absorbing layer is shown as an area of gradually reducing E. As shown here, the absorbing layer approaches the inner surface approximately where the creeping wave is first generated, and also covers a larger area of the pipe compared with 4.3. Here, $r_{\text{in}} = 10$ mm and $r_{\text{out}} = 25$ mm.

layers, without them interfering with the creeping wave measurements. Figures 4.5 and 4.6 show an illustration comparing the effect of using flat versus elliptical absorbing layers in a thin-walled annulus. By comparing them, it is clear that using elliptical absorbing layers gives larger area coverage while simultaneously not approaching the propagation path of the creeping wave.

4.2.3 Geometrical considerations

The theory suggests that the dimension of the inner surface of the annulus with respect to the wavelength is very important with regards to the creation of a creeping wave, as Equations (4.6) and (4.7) show a dependence of the displacement on the geometry of the annulus. Hence, R was defined to be the ratio between the shear wavelength, λ_T and the inner radius,

$$R = \frac{\lambda_T}{r_{\text{in}}}, \tag{4.8}$$

to investigate what the effect of the wavelength or the inner radius is on the creation of a creeping wave, and whether there are any limiting conditions in R which prohibit the excitation of a creeping wave.

The investigation of the effect of the R value on the excitation was approached in two ways. First, the frequency of the simulations was fixed to 5 MHz and the pipe's inner radius was varied from 10 mm to 25 mm. Following this investigation, the annulus' inner radius was fixed to 20 mm, and the frequency was varied from 3 MHz to 6 MHz. Finally, the circumferential and radial location of the focus point was also investigated in an analogous fashion, i.e. by fixing one parameter and varying the other. To investigate whether the circumferential location of the focus point has an effect on the generated creeping wave, the radial location was fixed to (r_{in}+$t_{\text{pipe}}/8$, θ) and θ location

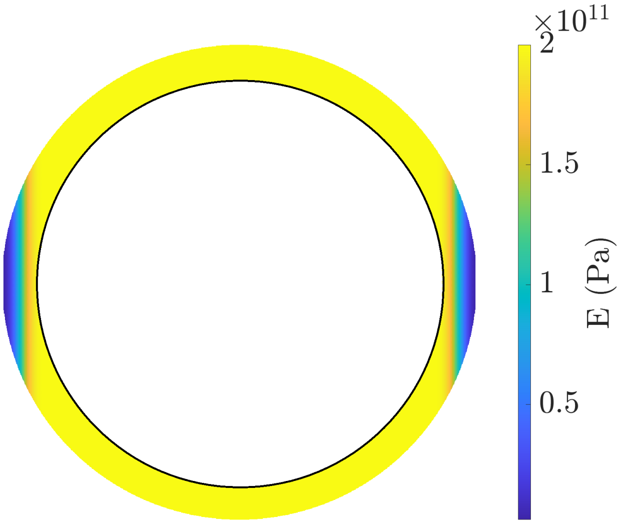

Figure 4.5: Example of flat absorbing layers applied to an thin-walled annulus. The absorbing layer is shown as an area of gradually reducing E. Here, $r_{\text{in}} = 20$ mm and $r_{\text{out}} = 25$ mm.

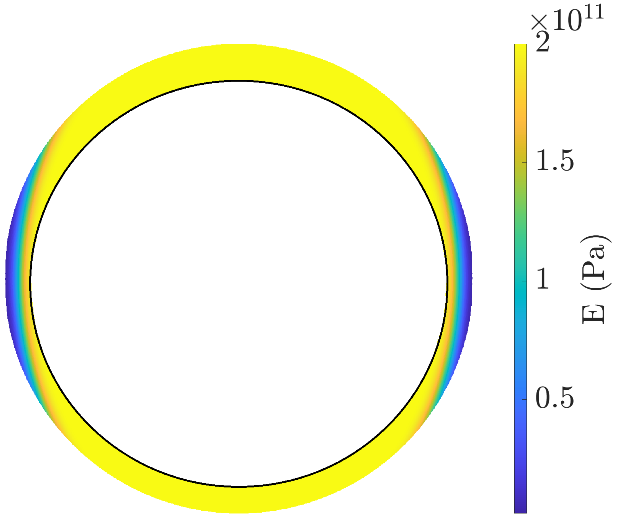

Figure 4.6: Example of an elliptical absorbing layer applied to an thin-walled annulus. The absorbing layer is shown as an area of gradually reducing E.Here, more area of the annulus has been covered by the absorbing layer compared with 4.5. Here, $r_{\text{in}} = 20$ mm and $r_{\text{out}} = 25$ mm.

was varied. Following the completion of this set of simulations, an analogous investigation was completed to determine whether the radial location of the shear wave focus point had an effect on the quality of the creeping wave, and subsequently, the wave leaking from it. For this set of simulations, the circumferential location of the focus point was kept at $\theta = 45°$.

4.3 Calibration results & discussion

For the purposes of better visualising and understanding the method of exciting the creeping waves on the inner surface of a pipe, Figure 4.7 shows wave field plots before, during and after the creeping wave excitation. Namely, subfigure 4.7a shows the shear wave, travelling at an angle before it hits the rough surface, subfigure 4.7b shows the shear wave just after it has collided with the inner radius and a creeping wave has been excited, and subfigure 4.7c shows the field after the shear wave has been absorbed by the absorbing layers, and the creeping wave is travelling along the inner radius, leaking energy in the shape of a spiral as predicted by [110].

4.3.1 Optimal f and r_{in} combinations for the excitation of a creeping wave

The resulting leaky waves from each simulation, received on the outer surface monitor line, are shown in Figure 4.8, when fixing the frequency at 5 MHz and varying r_{in}, while results from fixing r_{in} at 20 mm, and varying the frequency, are shown in Figure 4.9.

Even though Figures 4.8 and 4.9 show the wave leaking from the creeping wave, as recorded on the outer surface, the quality of these leaky signals is directly linked to the presence of a creeping wave, and its amplitude and signal-to-noise ratio are also linked to the same parameters of the creeping

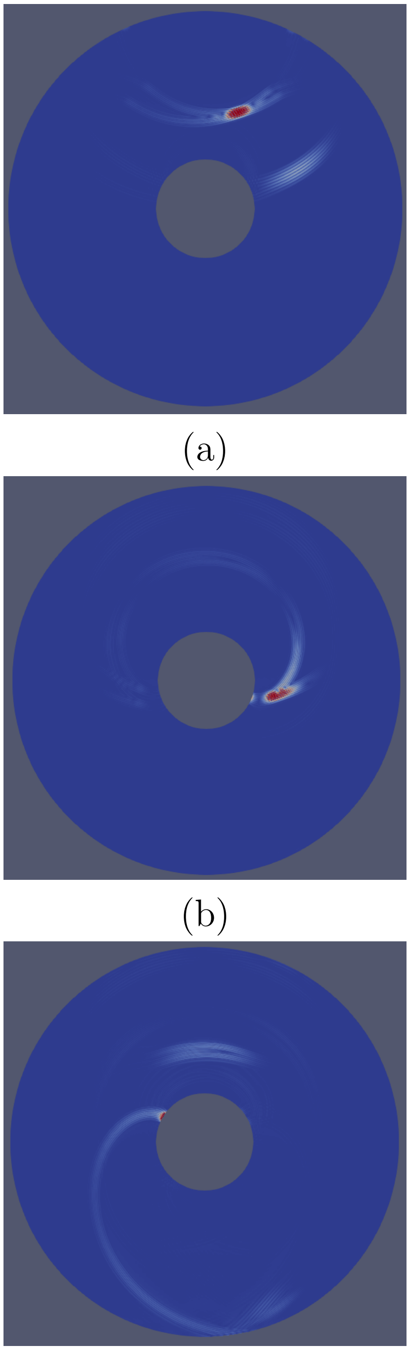

(a)

(b)

(c)

Figure 4.7: Illustration of the steps for generating a creeping wave. In (a) a shear wave travels at an angle before it collides with the inner surface - a weak longitudinal wave can also be seen ahead of it. In (b), the shear wave has collided with the inner surface, and a creeping wave has been excited at the collision point. Finally, (c) shows the creeping wave travelling around the inner surface, while energy leaks from it. The QR code directs to an animation of this process.

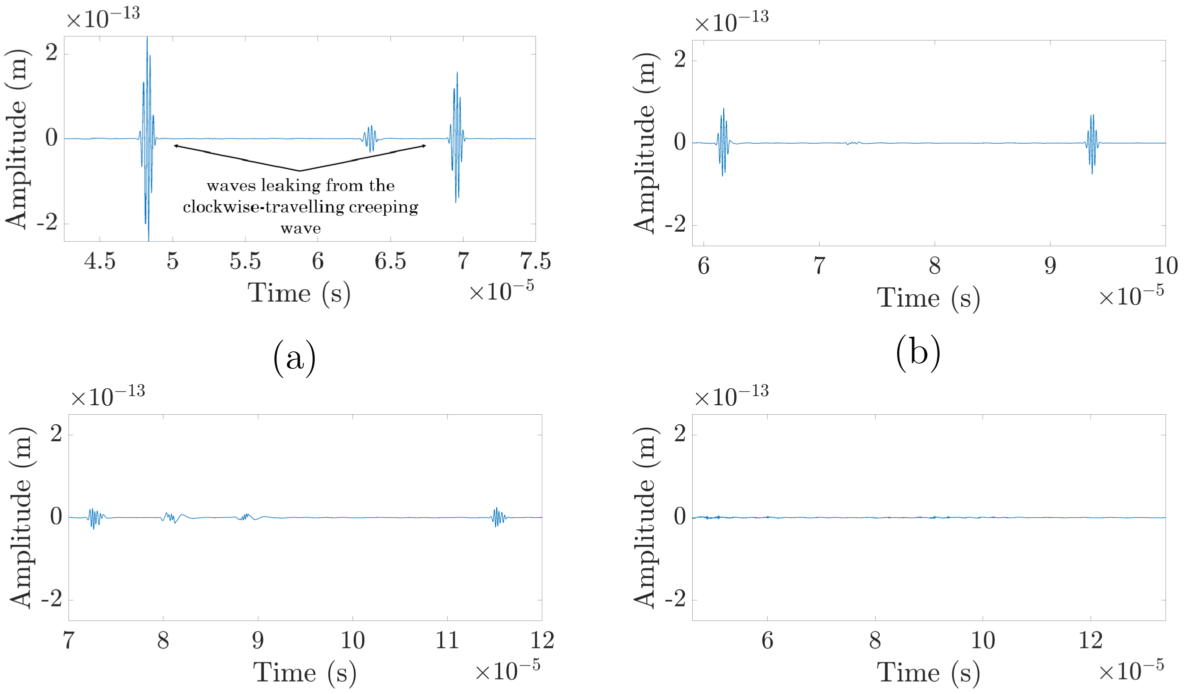

(a) (b) (c) (d)

Figure 4.8: Comparison of the wave leaking from the creeping wave, at different R values, where the variation in R has been obtained by varying the inner radius. In all simulations here, f = 5 MHz and r_{out}=40 mm. The R values for (a) is 0.064 (r_{in}=10 mm), for (b) is 0.043 (r_{in}=15 mm), for (c) is 0.032 (r_{in}=20) mm and for (d) is 0.026 (r_{in}=25 mm). In (a) this leaky wave is labelled - the analogous waveforms in the subfigures here and in the next figures are also the waveforms corresponding to the leaky wave.

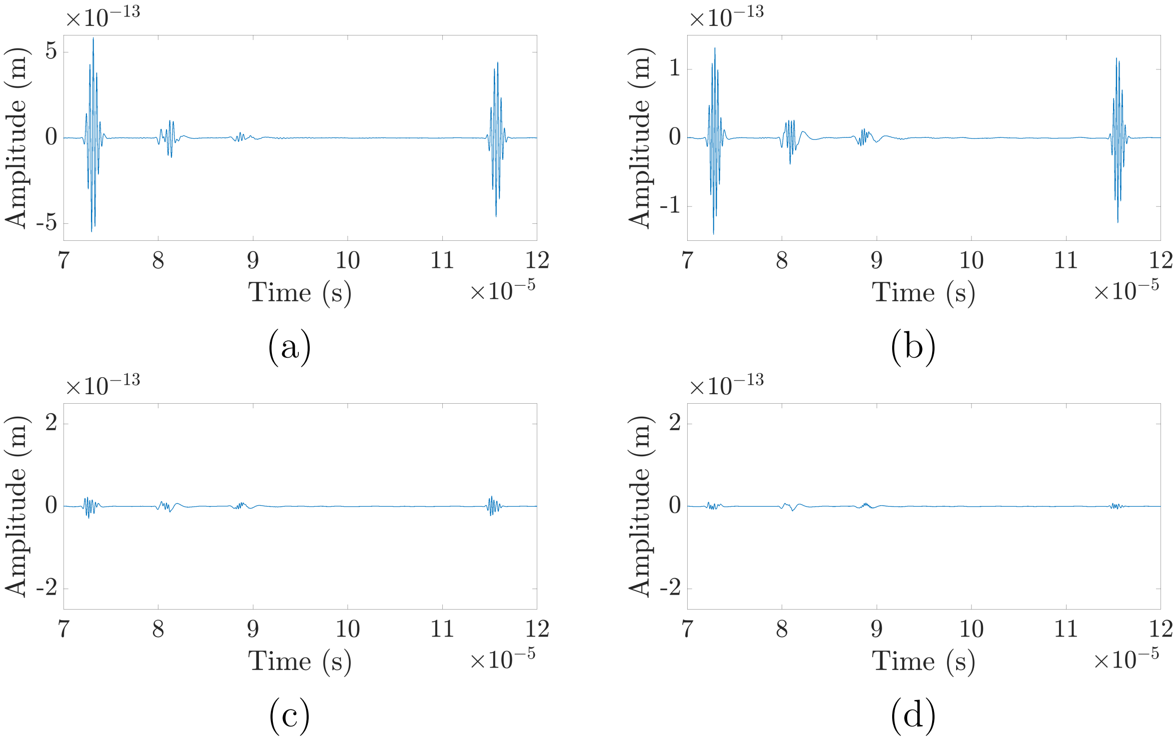

Figure 4.9: Comparison of the wave leaking from the creeping wave, at different R values, where the variation in R has been obtained by varying the centre frequency of the incident wave. In all simulations here, $r_{\text{out}} = 40$ mm and $r_{\text{in}} = 10$ mm. The R values for (a) is 0.053 (f=3 MHz), for (b) is 0.040 (f=4 MHz), for (c) is 0.032 (f=5 MHz) and for (d) is 0.027 (f=6 MHz).

wave. As shown in Figures 4.8 and 4.9, the R value is crucial for the excitation of a creeping wave. It appears that the generation of a good quality creeping wave requires a value of R greater than approximately 0.04. The physical reason relates to the necessary conditions for the creation of a creeping wave, and namely, the presence of a sufficiently curved surface. Physically, a large inner radius would appear flat to a small wavelength which would cause reflection rather than mode conversion. Therefore, larger inner radius values require lower frequency incident shear waves for a creeping wave to be excited on their surface.

One more interesting feature can be seen in Figures 4.8 and 4.9. An additional waveform can be seen between the two main leaky wave waveforms. Visualising the FE results showed that this is again a wave leaking from a creeping wave, travelling in the counter-clockwise direction. This creeping wave has been excited by the tail of the shear wave being incident upon with the inner surface at a location to the left of the $\theta = 90°$ point. Its lower amplitude can be explained by the fact that the incident tail of the shear wave in this case carries significantly less energy than the main lobe of the wavefront which travels towards the focus point. Additionally, the amplitude, signal-to-noise ratio and peak clarity of this wave is noticeably worse in most subfigures in Figures 4.8 and 4.9. There are two potential reasons for this - first, the creation of this wave is an unavoidable consequence, and therefore no effort is made to tailor the excitation parameters for it. Additionally, the processing method from which the main leaky wave signal is obtained is based around itself, and is potentially not ideal for this secondary leaky wave. However, as this additional leaky wave is smaller in amplitude, it does not interfere with any speed measurements of the main leaky wave.

4.3.2 Optimising the location of the focus point

Here the results relating to whether the radial and circumferential locations of the focus point have an effect on the quality of the resulting creeping wave are presented, provided that the R condition is satisfied. For this investigation, a pipe with $r_{\text{out}} = 40$ mm and $r_{\text{in}} = 10$ mm was selected and a shear wave centre frequency of 5 MHz, giving an R value of 0.08, which as discussed in the subsection above, is sufficient for the excitation of a creeping wave.

The resulting leaky wave signal, monitored on the outer surface, when varying the circumferential location of the focus point and fixing its radial position is shown in Figure 4.10. For varying the radial position and fixing the circumferential, the results are shown in Figure 4.11.

As shown in Figure 4.10, there is a large range of θ values which give a creeping wave of good quality, and subsequently a good leaky wave, as all θ values between 0° and 60° yielded clean leaky waves, with distinguishable peaks from which the speed can be easily extracted. The circumferential location appears to be slightly more restrictive, with values of $r_{\text{in}} + t_{\text{pipe}}/6$ or less giving a good quality creeping wave. This means that the focus point should be located at most approximately 10 λ_T away from the inner radius. This 10 λ_T distance appears to be significantly larger than what the theory suggests the allowable range to be - however, both this and the fact that there is a large number of permissible θ values can be explained by the phenomenon of beamspread. Even though the wave is focused at a particular point, the wavefront has a finite size, and therefore, collides with the inner radius continuously as it travels towards the focus point. Therefore, as long as the focus point is not radially directly below, or close to directly below the source line, and circumstantially within $10\lambda_T$, the quality of the resulting creeping and leaky waves is good enough for the purposes of speed measurements.

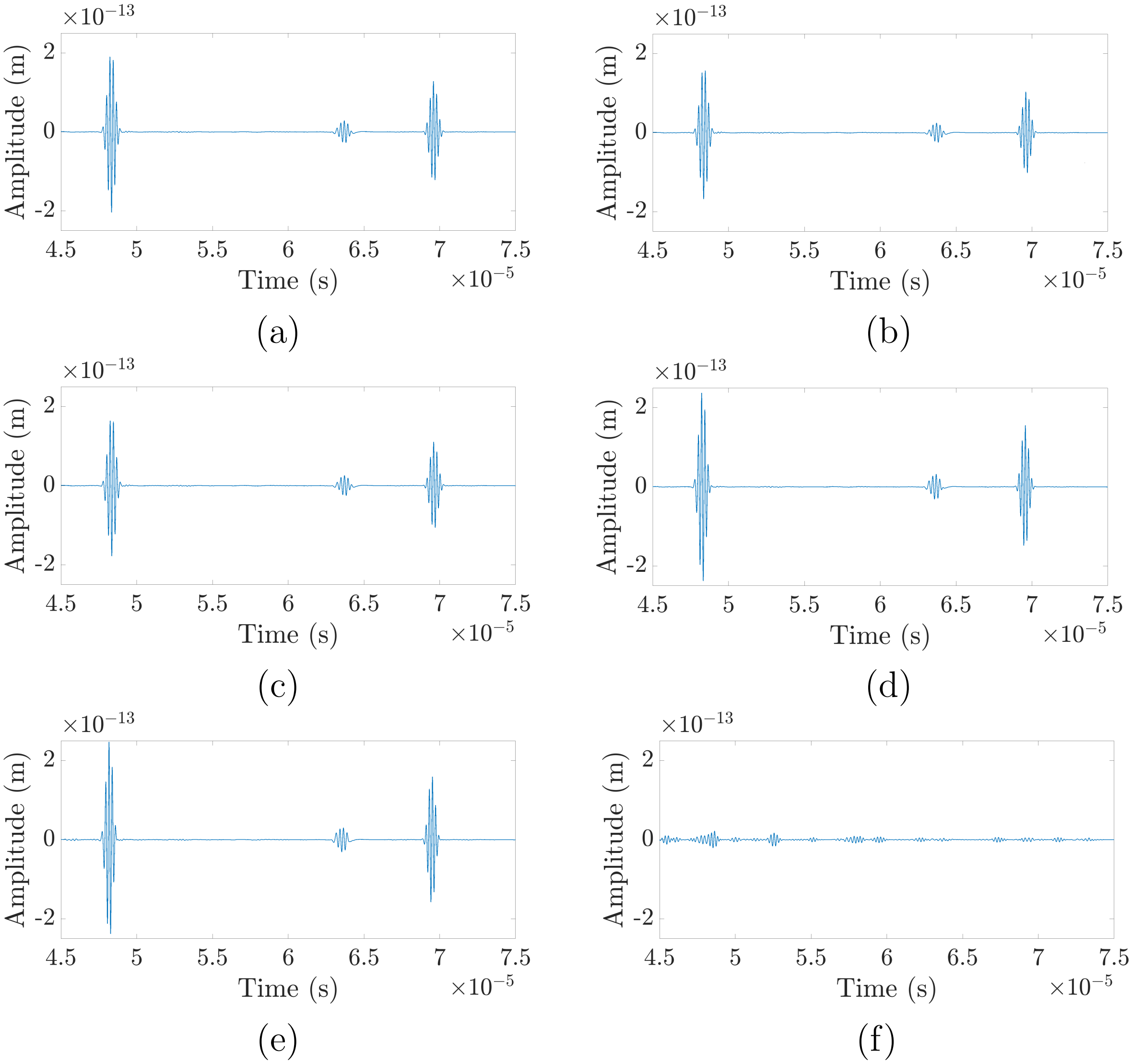

(a) (b) (c) (d) (e) (f)

Figure 4.10: Comparison of the wave leaking from the creeping wave, where the creeping wave was excited by focusing it at $(r_{\text{in}} + t_{\text{pipe}}/8, \theta_{\text{inc}})$, and θ_{inc} was varied. In all simulations results here, $r_{\text{out}} = 40$ mm, $r_{\text{in}} = 10$ mm and $f = 5$ MHz. The θ_{inc} values for each subfigure is as follows: (a) $\theta_{\text{inc}} = 0°$, (b) $\theta_{\text{inc}} = 15°$, (c) $\theta_{\text{inc}} = 30°$, (d) $\theta_{\text{inc}} = 45°$, (e) $\theta_{\text{inc}} = 60°$, (f) $\theta_{\text{inc}} = 75°$.

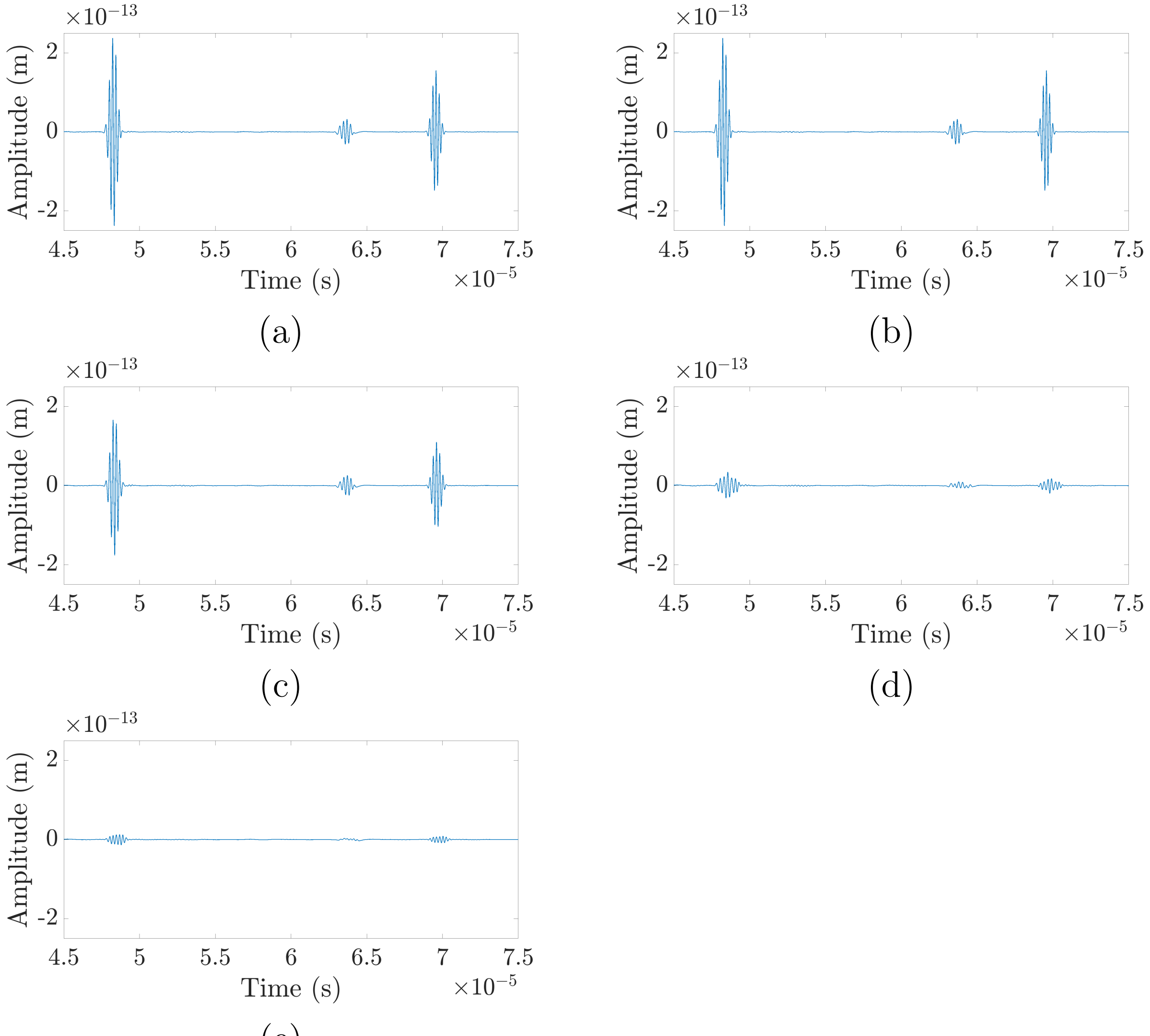

(a)

(b)

(c)

(d)

(e)

Figure 4.11: Comparison of the wave leaking from the creeping wave, where the creeping wave was excited by focusing it at $(r_{\text{in}} + t_{\text{pipe}}/p_{\text{inc}}, 45°)$, and p_{inc} was varied. In all simulations here, $r_{\text{out}} = 40$ mm, $r_{\text{in}} = 10$ mm and $f = 5$ MHz. The p_{inc} value for each subfigure is as follows: (a) p_{inc}=10, (b) p_{inc}=8, (c) $p_{\text{inc}} = 6$, (d) $p_{\text{inc}} = 4$, (e) $p_{\text{inc}} = 2$.

4.4 Introducing fatigue damage - idealised FE simulation conditions

Following the investigation of the effect of the location of the focus point on the quality of the creeping wave, fatigue damage was introduced to the annulus model, in an analogous method to the one described in Chapter 3, i. e. the modelling parameters were altered to capture the effect of fatigue on the speed of ultrasonic waves. A ring-shaped area of gradually reducing Young's modulus was introduced around the inner radius of the pipe, covering 10% of the pipe's thickness. This area was comprised of eight layers of reducing Young's modulus values, up to a minimum value equal to 90% of the healthy E value. Figure 4.12 shows a schematic of this ring-shaped E profile. The values of E in the profile were derived using the same method as in Chapter 3, where the known strain profile of the fatigued plates was converted into a E profile. In all simulations, elliptical absorbing layers of suitable eccentricity and thickness were implemented.

Initially, through-thickness measurements simulations were completed using longitudinal bulk waves. To achieve this, the same setup was used as in Figure 4.2, with the absence of the focus point - rather the source nodes were all excited in the vertical direction, to create a longitudinal wave. Also, the source nodes were also defined to act simultaneously as monitor notes, and the monitor line centred at the $\theta = 270°$ position was removed. The resulting signal from this setup, both without and with the presence of the fatigue profile are shown in Figure 4.13.

The speed of the longitudinal wave travelling through the thickness of the healthy annulus, obtained from the signal shown in Figure 4.13 was found to be 5543 m/s. For the same pipe, when the damage described above was introduced, the longitudinal wave speed was reduced to 5529 m/s, which

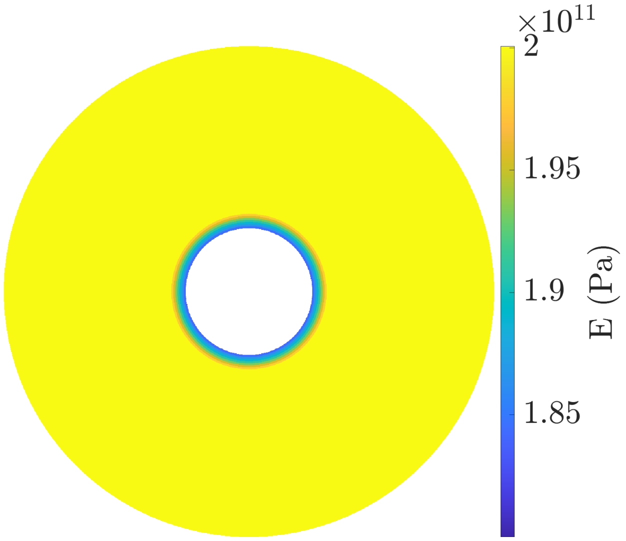

Figure 4.12: Schematic of the E profile used to represent fatigue damage in the FE model. The fatigue is represented as a ring of gradually reducing Young's modulus values. The maximum change from the healthy E value to the E value in the most fatigued layer in this figure is equal to a 10% change from the healthy value.

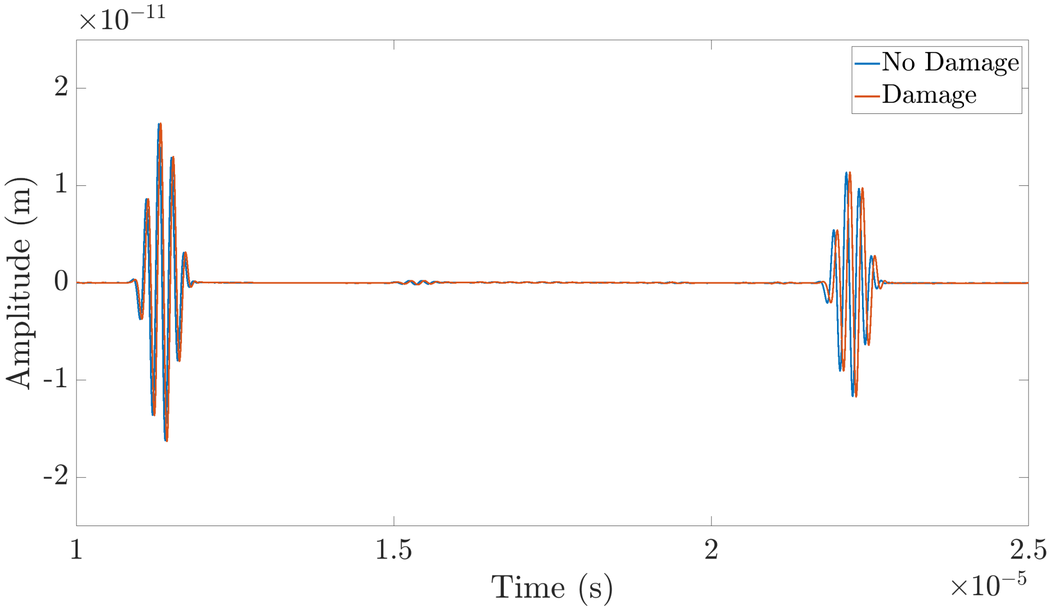

Figure 4.13: Longitudinal wave FE signal, obtained from a through-thickness simulation of a longitudinal wave generated at the $\theta = 90°$ position. For this FE model, $r_{\text{in}} = 10$ mm and $r_{\text{out}} = 40$ mm.

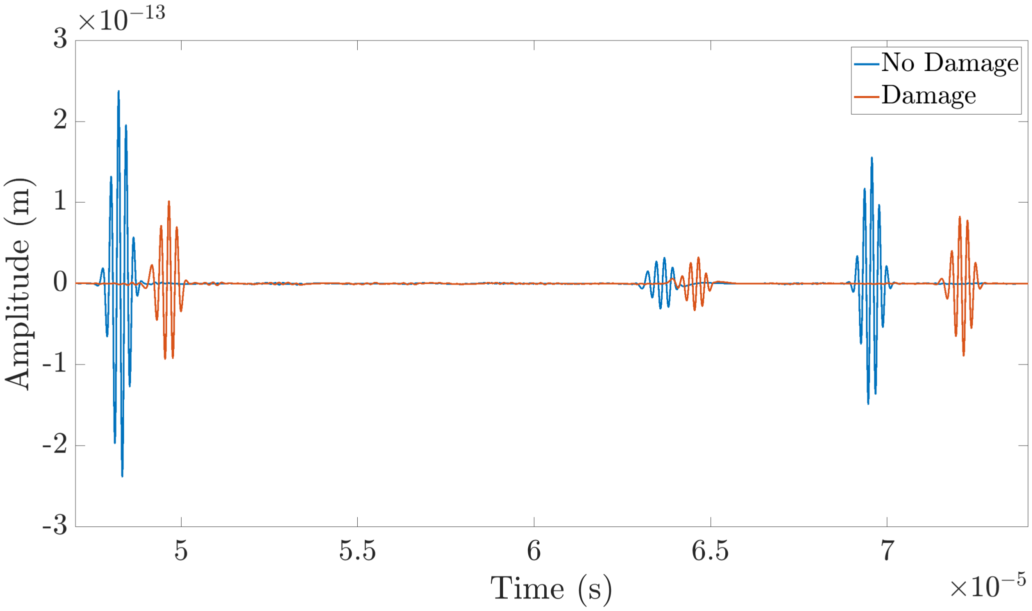

Figure 4.14: Leaky wave FE signal, obtained from simulation of a creeping wave generated by the incidence of a shear wave with the inner radius of the pipe. The focus point was defined to be at $(r_{\text{in}} + t_{\text{pipe}}/8,\ 45°)$. For the FE model used to obtain these signals, $r_{\text{in}} = 10$ mm, $r_{\text{out}} = 40$ mm and $f = 5$ MHz.

corresponds to a 0.26% reduction in wave speed. This is of the same order of magnitude as observed in the plate simulations.

Following this investigation, the measurements were repeated on the same healthy and damaged annulus, using creeping waves and the setup shown in Figure 4.2. The resulting leaky waves, monitored at the $\theta = 270°$ are shown in Figure 4.14.

The speed of the leaky (and hence the creeping) wave travelling around the inner surface of the annulus, obtained from the signal shown in Figure 4.14 was found to be 2943 m/s. For the same annulus, when the damage was introduced, the creeping wave speed was reduced to 2805 m/s - a reduction of approximately 4.7%. This demonstrates well how the creeping wave method generates significantly larger changes in speed in the presence of the fatigue,

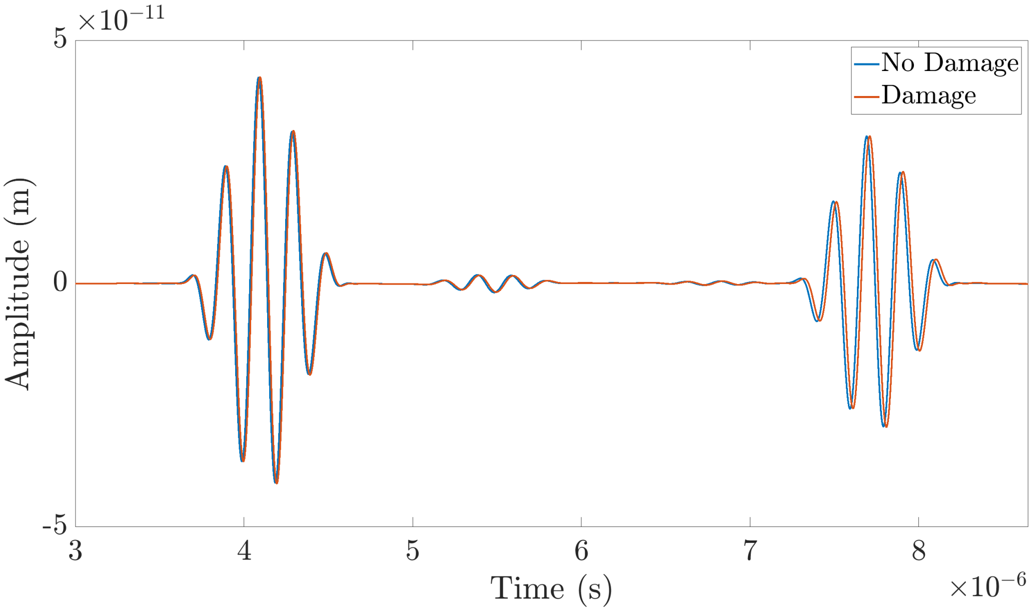

Figure 4.15: Longitudinal wave FE signal, obtained from a through-thickness simulation of a longitudinal wave generated at the $\theta = 90°$ position. For this FE model, $r_{\text{in}} = 10$ mm, $r_{\text{out}} = 20$ mm and f=5 MHz.

as the creeping wave is restricted to spend all of its propagation time within the fatigued area. For this particular example, the changes in speed were amplified by approximately seventeen times.

It is often the case that some industrial applications may require the inspection of pipes with thinner walls than the results presented so far in this chapter. To investigate this, analogous simulations were repeated on a thinner-wall pipe, with $r_{\text{in}} = 10$ mm and $r_{\text{out}} = 20$ mm. The choice of reducing the inner and not the outer radius was made to keep the shear wave frequency at 5 MHz, and allow for a more direct comparison between the thick and thin-walled annuli. The signal from the longitudinal bulk wave measurements is shown in Figure 4.15, while the leaky wave signal is shown in Figure 4.16.

The change in longitudinal speed when damage is introduced in the thin-walled pipe, as calculated from the signals in Figure 4.15 is -0.26% as ex-

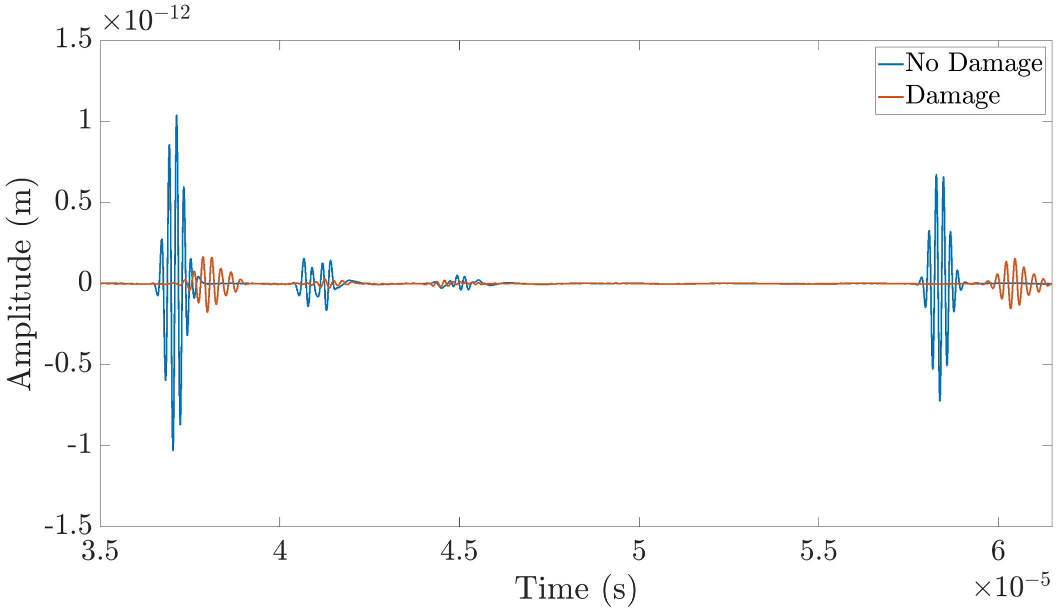

Figure 4.16: Leaky wave FE signal, obtained from simulation of a creeping wave generated by the incidence of a shear wave with the inner radius of the pipe. The focus point was defined to be at $(r_{\text{in}} + t_{\text{pipe}}/8,\, 45°)$. For this FE model, $r_{\text{in}} = 10$ mm, $r_{\text{out}} = 20$ mm and $f = 5$ MHz.

pected. This number remains the same as for the thick-walled pipe, as both the inner radius and the fatigue thickness were scaled by the same value. The change in the creeping wave speed was found to be -5.32%, which is approximately equal to a 20× increase in the change in speed between the longitudinal and creeping wave measurements. It is worth noting that the change in creeping wave speed is larger compared with the thick-walled pipe, due to the fact that the creeping wave now spends even more time inside the fatigued area, as both the source and monitor lines are located closer to the inner radius for a thin-walled pipe.

4.5 Introducing fatigue damage - more realistic FE conditions

In the previous subsection it was shown how the use of creeping waves greatly amplifies the changes in speed due to the presence of near-surface fatigue, compared with through-thickness longitudinal wave measurements. This investigation was completed with the aid of idealised FE domains, where absorbing layers were used to ensure that any unwanted waves and reflections were absorbed and would not interfere with the leaky wave measurements. Here, analogous creeping wave simulations were repeated, with the absorbing layers removed. The through-thickness simulation results were not repeated, as the presence of the absorbing layers is away from the source and it was therefore expected that their removal would not have affected the quality of the signal.

Starting from the thick-walled pipe (r_{in} = 10 mm and r_{out} = 40 mm) and no fatigue damage, it was observed that the signal received at the monitor line contained multiple waveforms which were of noticeably larger amplitude compared with the signal in Figure 4.14. This signal is shown in Figure 4.17.

By visualising the simulation in Paraview, three main contributors to the additional waveforms in Figure 4.17 were identified:

- Reflections from the incident shear wave, which is scattered both when it approaches and collides with the inner surface, and also when it arrives at the outer surface (marked in red).
- Creeping waves which travel on the outer surface, generated by the source line while while generating the shear wave (marked in green).
- Additional leaky waves, resulting from inner surface creeping waves,

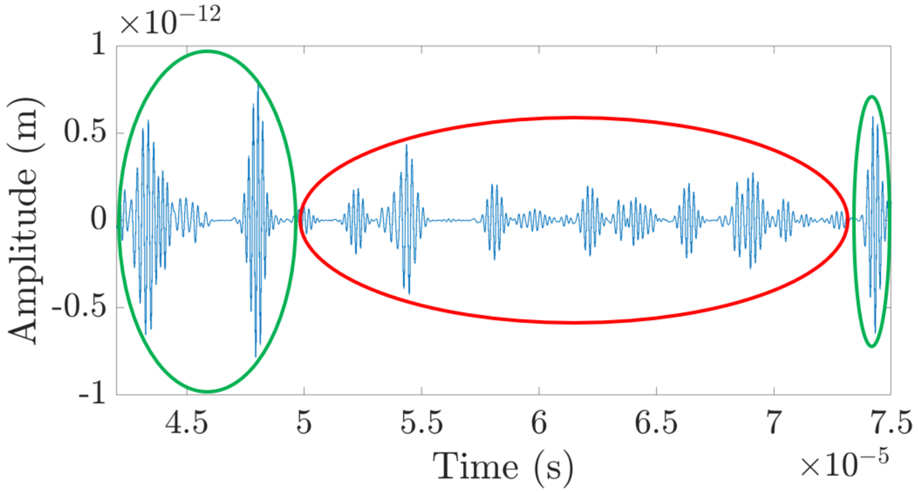

Figure 4.17: Leaky wave FE signal, obtained from simulation of a creeping wave generated by the incidence of a shear wave with the inner radius of the pipe. The focus point was defined to be at ($r_{\text{in}} + t_{\text{pipe}}/8$, 45°). For this FE model, $r_{\text{in}} = 10$ mm, $r_{\text{out}} = 40$ mm and $f = 5$ MHz. Here, the absorbing layers were removed. Shear wave reflections are marked in red and outer surface creeping waves are marked in green.

which are excited when any of the scattered shear waves approach the inner radius under the right conditions for creeping wave generation (not visible in Figure 4.17, due to their small amplitude).

An illustration of each of these features is shown in Figure 4.18 - examples of shear wave reflections are contained within the red circles, examples of outer surface creeping waves are contained within the green circles, and arbitrarily generated inner surface creeping waves are contained within yellow circles. It is clear that the unavoidable existence of those reflections and surface waves renders the leaky wave undetectable.

A potential solution to this issue would be to identify a method which would absorb the shear wave after it has excited the creeping wave. To achieve this an external material to the annulus model was attached in the simulation, as shown in Figure 4.19. The external material was added almost to the entirety

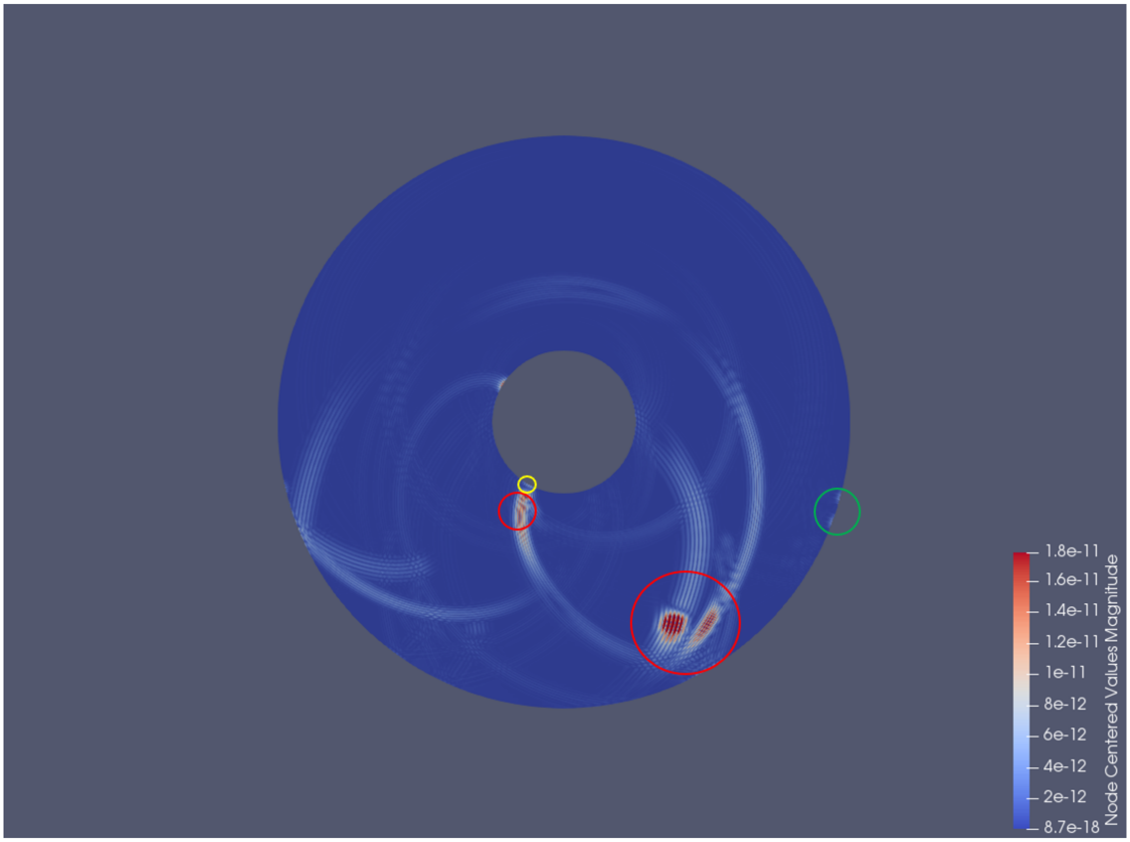

Figure 4.18: Wave field in the annulus, after the incidence of the shear wave with its inner surface. Examples of shear wave reflections are contained within the red circles, examples of outer surface creeping waves are contained within the green circles, and inner surface creeping waves are contained within yellow circles.

of the outer surface, leaving gaps only around the source and monitor lines. The purpose of this external area was to be filled with a suitable absorbing material, so that it can act as an absorbing patch.

Initially, the patches were filled with absorbing layer material. The signal obtained from this configuration is shown in Figure 4.20. The leaky wave signal appears to be clean, and its quality resembles that of the signals in Figure 4.14. This implies that the use of external patches is effective at suppressing the waves in Figure 4.17 which rendered the leaky wave undetectable.

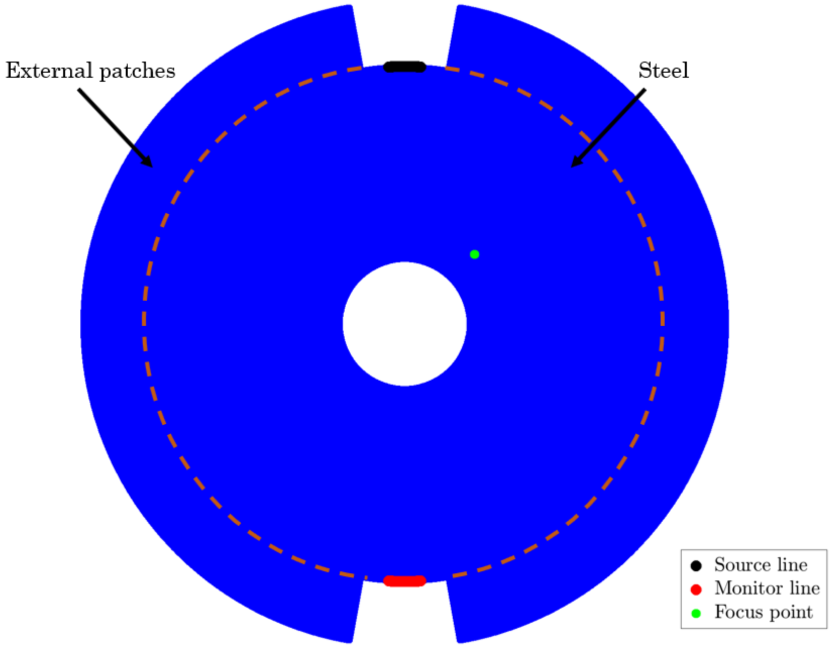

Figure 4.19: Schematic of the FE domain used to excite creeping waves on the inner surface of an annulus, with external patches attached. The source line is shown in black, the monitor line is shown in red, and an indicative location of a focus point, where the shear wave beam is steered is shown in green. The dashed line indicated the boundary between the steel annulus and the external patches.

However, in an experimental setup, some coupling will be required to facilitate the transmission of the waves between the annulus and the patches. To simulate this, a thin layer of STOPAQ (Stadskanaal, The Netherlands) ($E =$ 1.37 GPa, $\rho = 970$ kg/m^3, $\nu = 0.443$) was defined between the annulus and the material, as shown in Figure 4.21.

The signal obtained from using AL filled patches, with STOPAQ coupling is shown in Figure 4.22. For the particular case in Figure 4.22, the couplant thickness was set to $\lambda_T/5$. It is clear that the coupling has an adverse effect on the effectiveness of the absorbing layers, as the unwanted waves are not able to cross this boundary and have been recorded by the monitor line. Further simulations, where the thickness of the coupling was varied, revealed

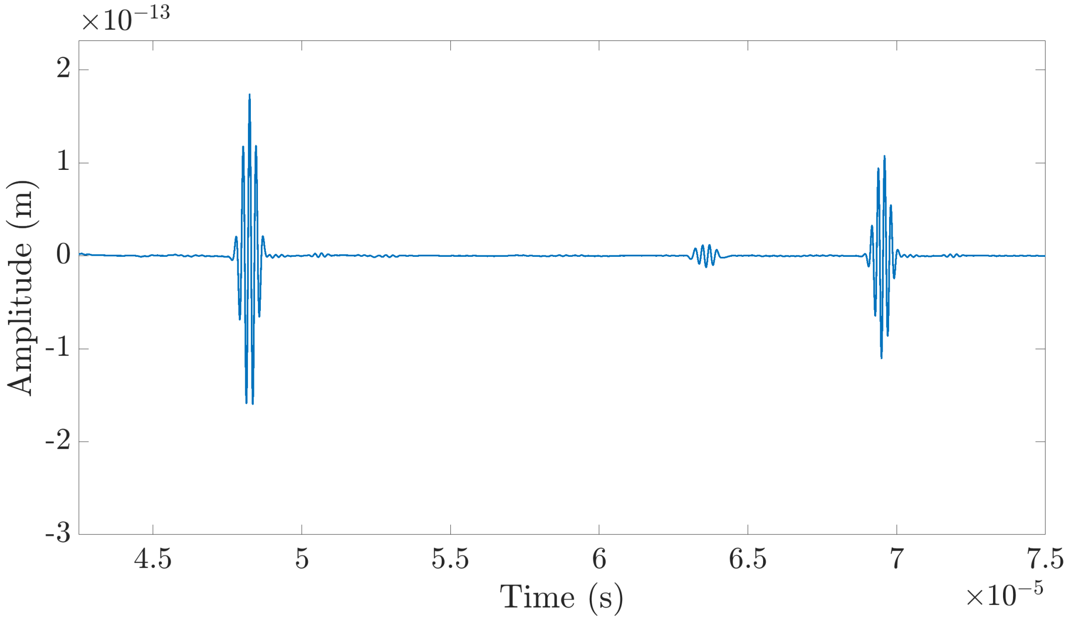

Figure 4.20: Leaky wave FE signal, obtained from simulation of a creeping wave generated by the incidence of a shear wave with the inner radius of the pipe, under the configuration shown in Figure 4.19. Here, the external patches were filled with AL material.

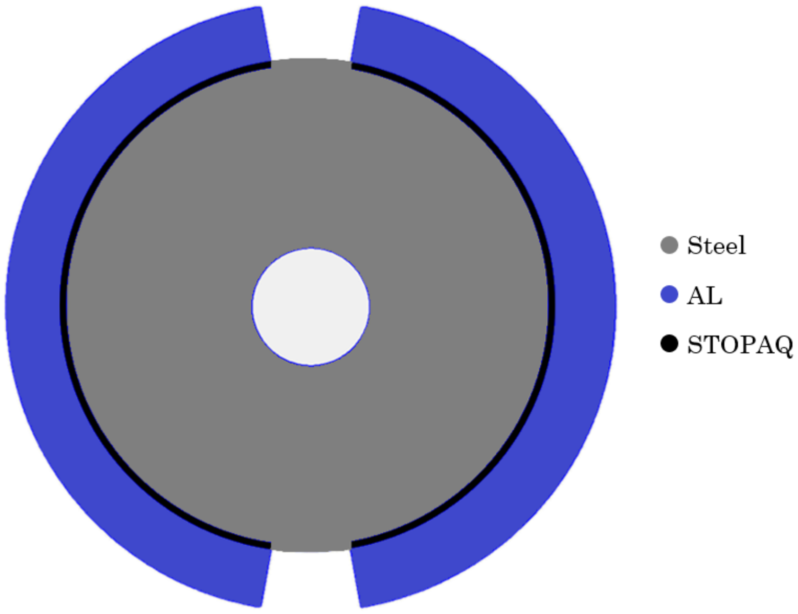

Figure 4.21: Schematic showing the materials used to investigate the effect of adding a coupling layer between the steel annulus and the idealised absorbing layers.

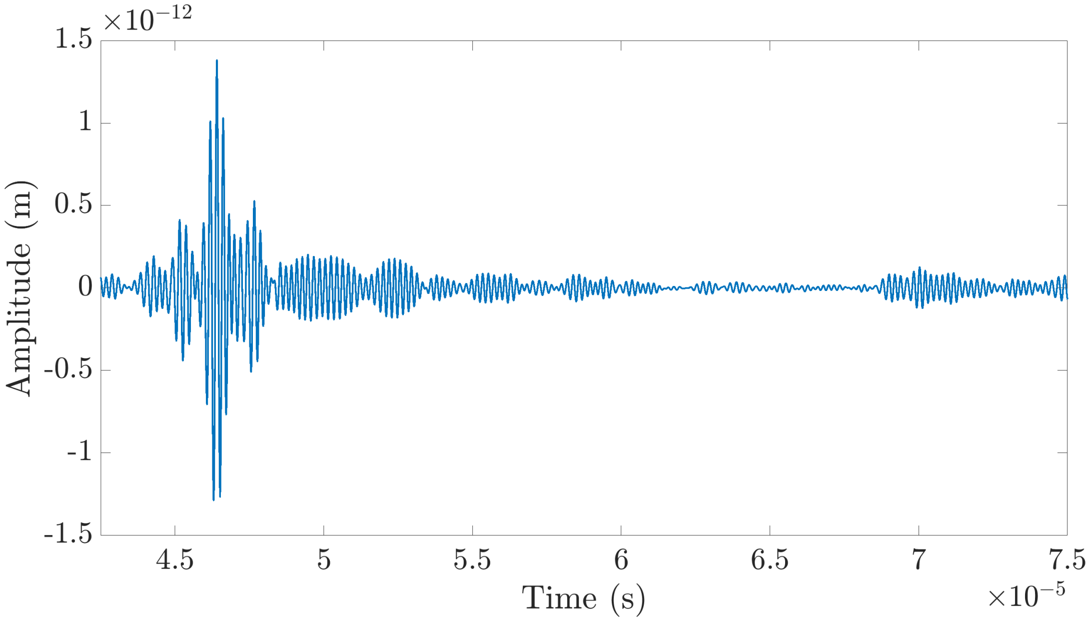

Figure 4.22: Leaky wave signal, generated from the FE configuration shown in Figure 4.19. Here, the external patches were filled with absorbing layer material, and a thin layer of STOPAQ coupling was defined between the annulus and the patch.

that in order for the wave to be able to pass through the couplant barrier to a degree which renders the leaky wave visible again, this thickness must be reduced to $\lambda_T/45$, which for steel is approximately equal to 25 μm. Such a small thickness would be unrealistic to achieve in an experimental setup uniformly, especially with the high viscosity substances required for shear wave coupling.

As a final check for this patch method, STOPAQ was introduced to the entire patch region in the model, without any coupling (i.e. assuming perfect coupling between the patch and the annulus), since STOPAQ has been used as an absorbing material in past studies [115] on plates, and could potentially be useful in pipe geometries.

It was found that the transmission between the annulus and the absorbing patches area was poor. The signal obtained from defining STOPAQ patches

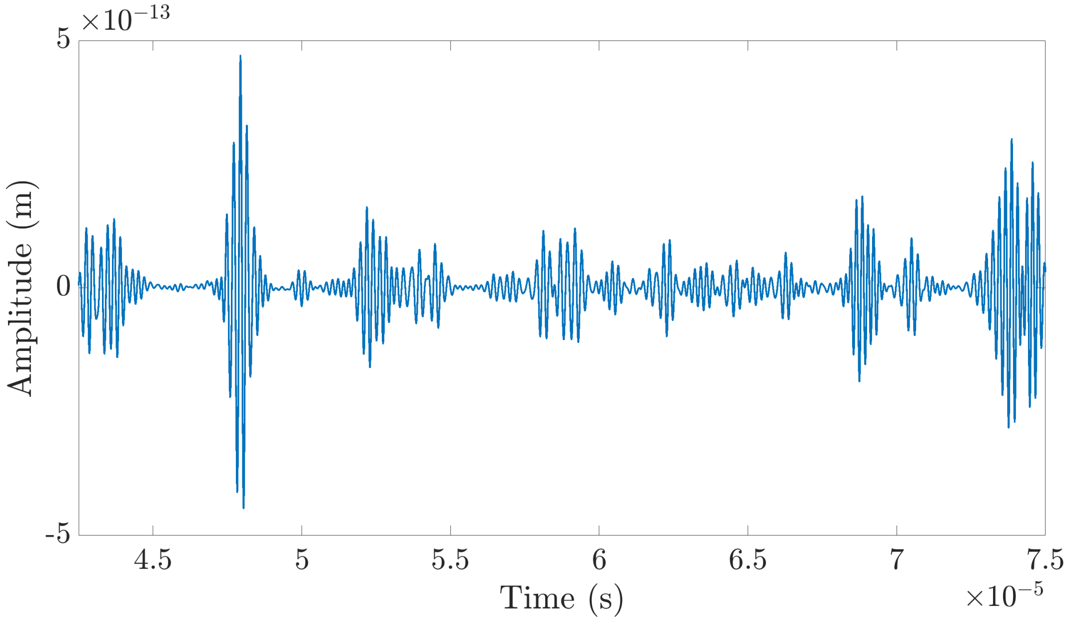

Figure 4.23: Leaky wave signal, generated from the FE configuration shown in Figure 4.19. Here, the external patches were filled with STOPAQ.

is shown in Figure 4.23.

The signal in Figure 4.23 resembles that of Figure 4.17 closely, although some of the waveforms appear to have reduced amplitude. This implies that the STOPAQ patches were partially effective - there was some absorption of the incident shear wave, however, this was far from the required amount to make the leaky wave visible. The most probable reason for this is the large impedance mismatch between STOPAQ and steel, which prevents the transmission of waves between them. Given the results for the thick-walled pipes, there was no need to repeat simulations for the thin-walled pipes, as it had already been demonstrated that thinner pipes generate more complex noise patterns.

From this study it was concluded that the use of creeping waves for fatigue state assessment in realistic scenarios is not feasible. This is due to the inherent weak nature of the leaky wave, which is rendered easily masked by the presence of other waves. Given that the excitation of the creeping wave by definition requires the presence of a shear wave, and the space in an annulus is confined, it is unavoidable that the scattered shear wave will interfere with the leaky wave. As a result, it was decided not to proceed further with the creeping wave methods.

4.6 Alternative approach - beating of creeping waves

Here, an alternative approach to that of creeping waves is discussed, as the investigation above showed that the weak nature of the leaky wave compared with the incident shear wave required to excite it makes its monitoring impractical in realistic scenarios. A potential solution would be to excite a creeping wave without the use of an incident wave. It has already been shown that a similar excitation is possible by Masserey & Fromme [116]. In their study, the authors study a behaviour known as beating, in which the energy of a Rayleigh wave is transferred between the two surfaces of a plate, when the centre frequency of the Rayleigh wave falls within a specific range. To aid with the explanation of this phenomenon, an example of the dispersion curves showing the first anti-symmetric (A_0) and first symmetric S_0 modes is shown in Figure 4.24, for a 5 mm thick steel plate.

As shown in Figure 4.24, at low frequencies, the two Lamb wave modes have significantly different phase velocities, while at higher frequencies, they converge to a single speed, which in the high frequency limit is equal to C_R. However, there is a region in-between where the speeds are close, but not identical. This region was the region of interest in the study in [116] - as the authors explain, Rayleigh waves on a plate can be thought of as a superposition of the A_0 and S_0 Lamb wave modes. In this particular region,

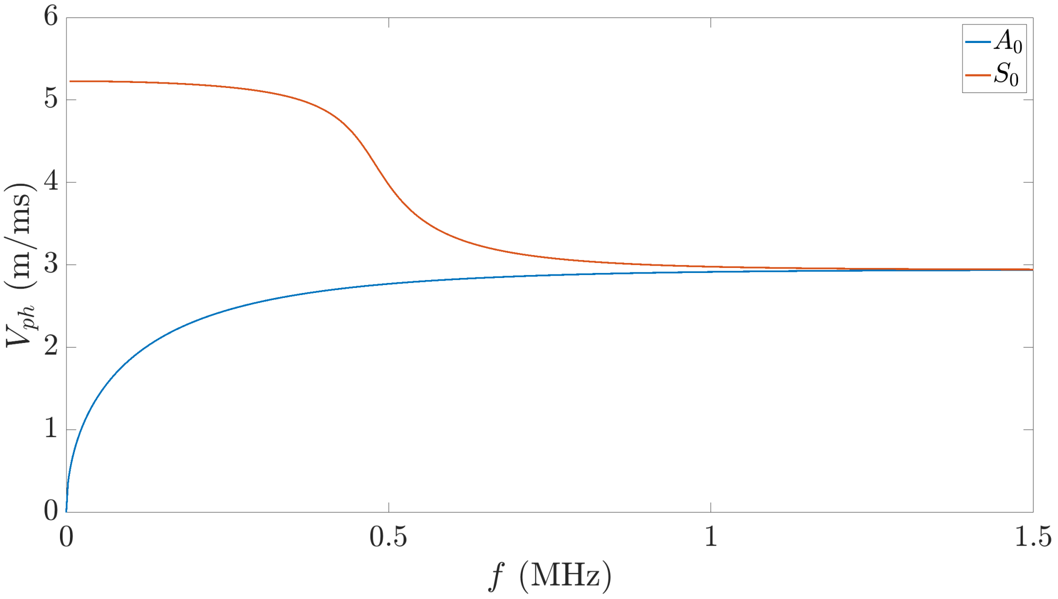

Figure 4.24: Dispersion curves, showing the A_0 and S_0 modes for a 5 mm thick steel plate. In this figure, V_{ph} is the phase speed.

the slight difference in phase speed of A_0 and S_0 results in a continuous phase shift between them causing energy to be transferred between the surfaces of the plate. This energy transfer happens over a distance known as the beat-length, L_s, which is equal to

$$L_s = \frac{2\pi}{k_{A_0} - k_{S_0}}, \tag{4.9}$$

where k_{A_0} and k_{S_0} are the wavenumbers of the A_0 and S_0 modes respectively.

To the author's knowledge, the phenomenon of beating has not been studied for creeping wave travelling around curved surfaces. Similar studies for defects around holes have been completed, [117,118], however, those focused on the detection of identifiable cracks using pulse-echo configurations and not creeping waves.

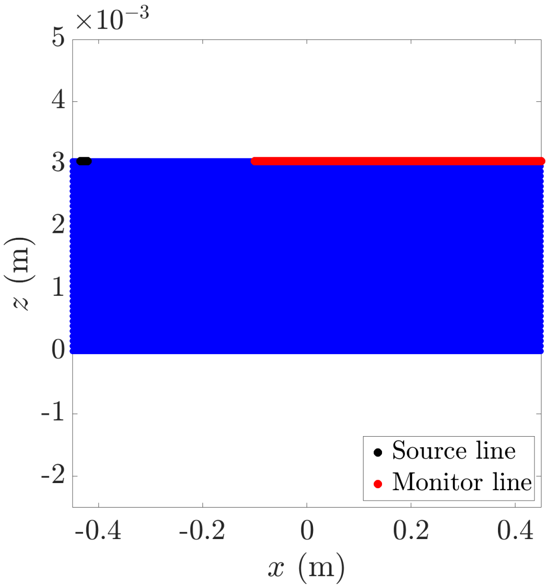

Figure 4.25: Schematic of the FE model used to recreate the results in [116]. The rectangular FE domain has dimensions 900 mm × 3 mm, with source and monitor lines placed on the upper surface.

Initially, an attempt was made to recreate the results in [116], by creating a rectangular FE domain as shown in Figure 4.25. The domain was 900 mm × 3 mm in size, as per the dimensions in the plate in [116]. A source line, with a length equal to 5 λ_R (calculated from the centre frequency) was defined on the upper surface, along with a monitor line, starting at $x = -100$ mm and ending at $x = 450$ mm. A clean Rayleigh wave signal was excited, using the method described in detail in Chapter 2.

The centre frequency of the Rayleigh wave was set to 2 MHz. The normalised maximum z displacement of each of the monitor nodes, defined as the ratio of the maximum amplitude of each node divided by the largest of the maximum amplitudes recorded across the monitor line, was recorded and plotted against its respective x location. The results are shown in Figure 4.26.

The phenomenon of beating is clear in Figure 4.26, as the z amplitude can be seen to vary periodically. The distance over which this happens is approxi-

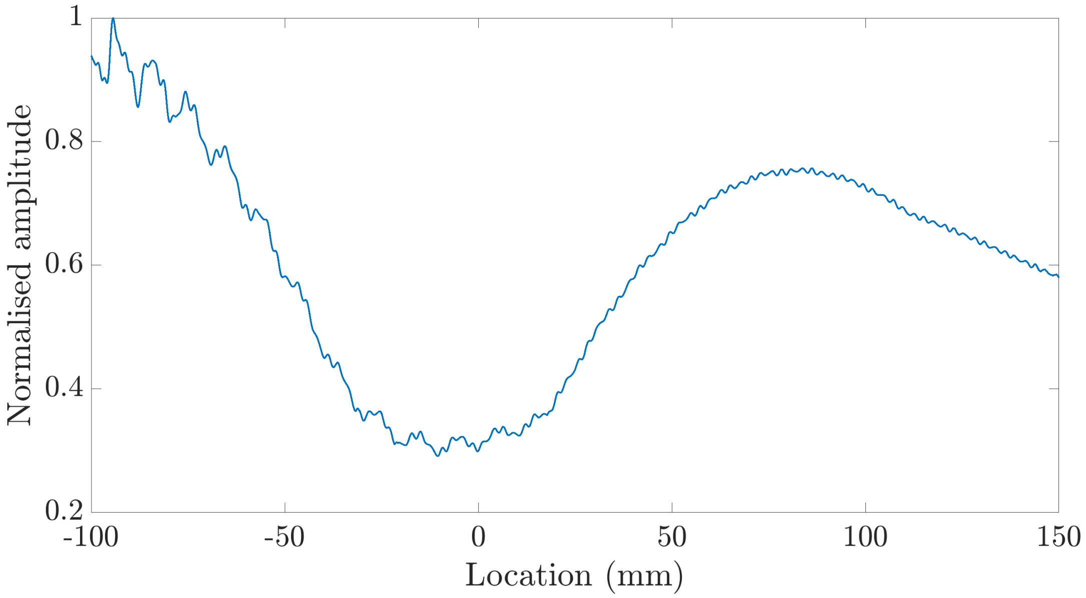

Figure 4.26: Variation of the maximum z displacement of a Rayleigh wave along the monitor line shown in Figure 4.25, for a 3 mm thick plate with f=2 MHz and -100 mm $\leq x \leq 150$ mm.

mately equal to 200 mm, which agrees with the experimental results in [116]. This both verifies the result, and demonstrates Pogo's ability to simulate the beating behaviour of Rayleigh waves. Therefore it was feasible to proceed with the investigation of this phenomenon in curved surfaces.

For the investigation, an annulus with a wall thickness of 3 mm was chosen. Although this might not be representative of a realistic pipe in an industrial environment, the small thickness allows for the choice of a reasonable model size and frequency combination, to achieve beating. The A_0 and S_0 speeds for a plate with 3 mm thickness were used in the calculations, similarly to [116]. For such a plate, at 2.25 MHz the speed of the A_0 mode is 2936.01 m/s and the speed of the S_0 mode is 2950.01 m/s, giving $L_s \approx 270$ mm.

Initially, an annulus with $r_{\text{in}} = 50$ mm and $r_{\text{out}} = 53$ mm was selected. A 5 mm long source line was defined at the top, and then equispaced monitor

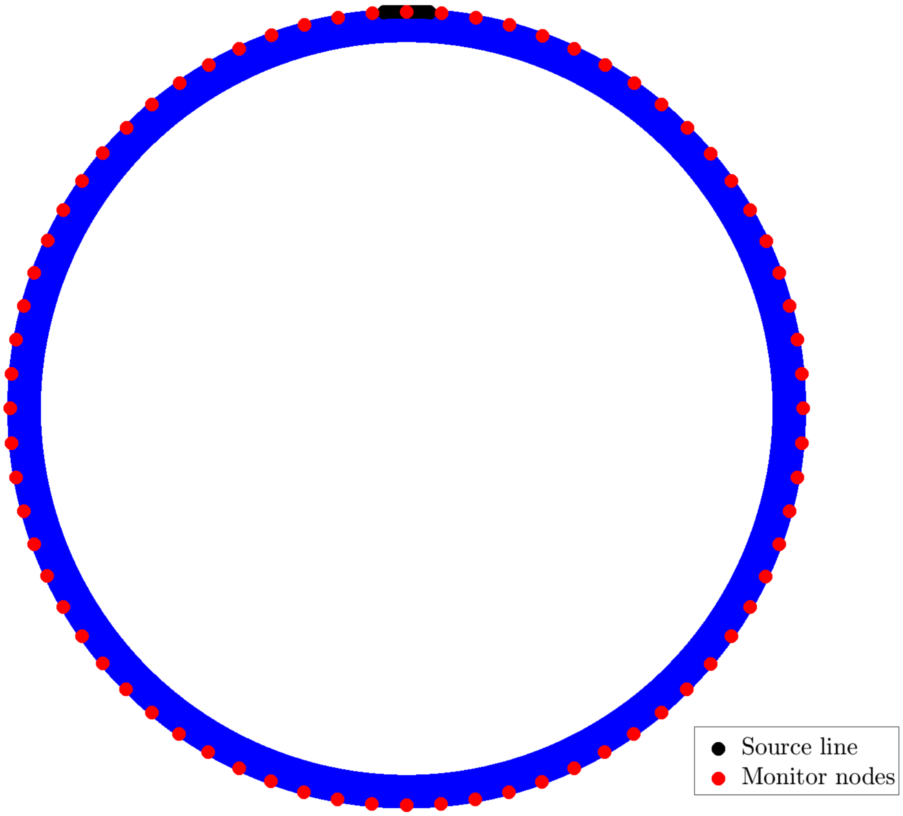

Figure 4.27: Schematic of the setup used to measure L_s in an annulus. The source line is shown in black and the monitor points are shown in red.

nodes around the outer surface were defined to investigate whether the same L_s would be measured for plates in the annulus and whether full energy transfer between the two surfaces would be achieved, which is a requirement for the end goal of using this method for fatigue state characterisation. A schematic of the setup is shown in Figure 4.27.

The amplitudes and phases of the nodes on the source line were defined as per [98], to ensure the creation of a clean outer surface wave. The amplitude of the outer surface creeping wave was monitored at the circumferential location. Then, the maximum amplitude of each signal was recorded, and a plot showing the variation of the maximum amplitude along the outer surface was created. The plot for the model with $r_{\text{in}} = 50$ mm and $r_{\text{out}} = 53$

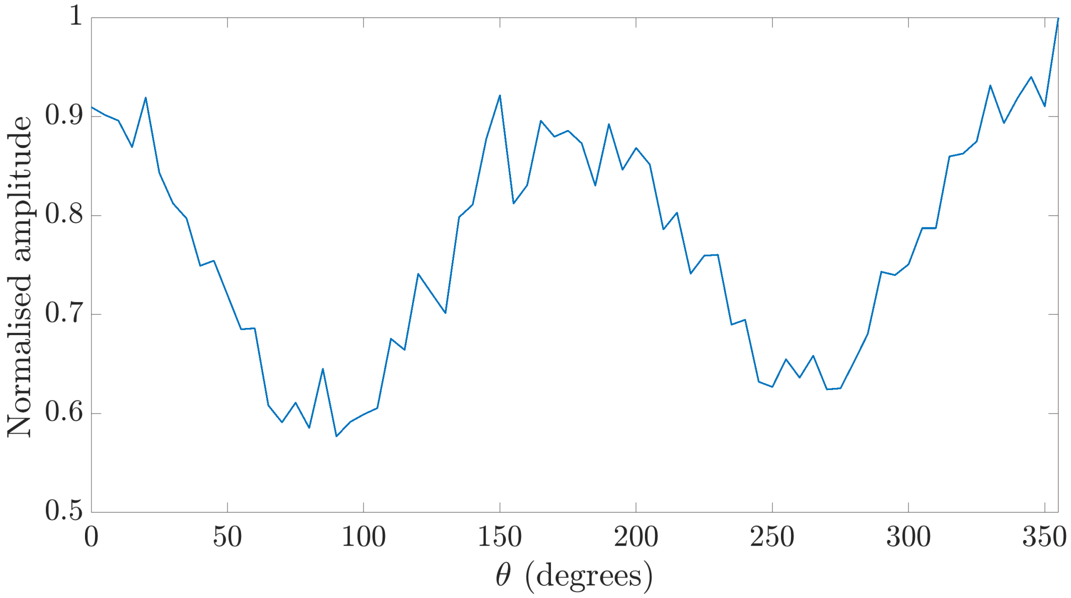

Figure 4.28: Variation of the amplitude of the creeping wave around the outer surface of the annulus model, for an annulus with $r_{\text{in}} = 50$ mm and $r_{\text{out}} = 53$ mm.

mm is shown in Figure 4.28. Also, as the creeping wave is created at the top of the model and is travelling in the clockwise direction, let us move the origin of the coordinate system to the source line position, and define the clockwise direction as positive, for the purposes of presenting the results in this subsection.

If no beating was taking place, one would expect very small variation of the amplitude of the creeping wave along the travel surface - any potential variation would possibly be a reduction in the amplitude, due to the leaky nature of the creeping wave. However, it is clear that the variation in amplitude shown in Figure 4.28 resembles the phenomenon of beating. The maximum amplitude of the wave occurs at the origin, as expected, and then gradually drops to a minimum value. The amplitude then increases up to a maximum, and this behaviour repeats. The average distance between two consecutive maxima (converted to a linear scale) is approximately equal to

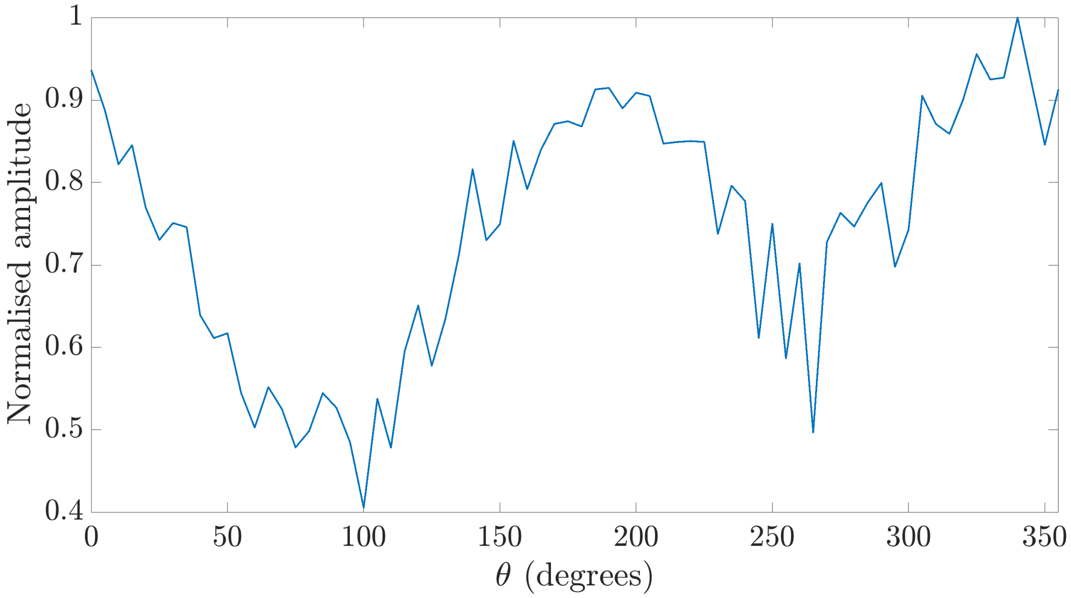

Figure 4.29: Variation of the amplitude of the creeping wave around the outer surface of the annulus model, for an annulus with $r_{\text{in}} = 60$ mm and $r_{\text{out}} = 63$ mm.

200 mm, which is fairly close to the theoretical value. However, the bigger issue here is that the energy does not drop to zero as with plate beating - this is possibly due to the curved nature of the surface. The drop in amplitude is approximately 31.8% compare with the amplitude just after the wave has been generated.

To further investigate this claim, a pipe with a larger inner radius was created ($r_{\text{in}} = 60$ mm and $r_{\text{out}} = 63$ mm) - this is because a larger inner and outer radii implies a smaller curvature, and hence the model closer resembles a plate (as a plate is a limiting case of an annulus with an infinite inner radius). The variation of the amplitude of the creeping wave is shown in Figure 4.29.

As shown in Figure 4.29, the beating effect is still prominent. The beat-length was again found to be approximately equal to 210 mm, however, the drop in amplitude is increased to 58.8% compared the initial value. This observation potentially confirms the speculation that the curved nature of the surface impedes full energy transfer between the surfaces, as it appears that a larger and hence less curved pair of surfaces results in greater energy transfer. Additionally, the beatlength has slightly increased, and is closer to the theoretical value of 275 mm, which is potentially more evidence that curved surfaces impede full energy exchange between the surfaces. However, as this will be an issue in all pipe models, the beating method was deemed not suitable for the purposes of this study.

4.7 Alternative approach II - SH$_0$ waves

In the NDE field, longitudinal and vertically polarised shear waves are most commonly used in inspection techniques. However, shear waves in 3D can exist with a different polarisation - in vertical shear waves, the wave propagation is in the x direction and the particle motion is in the z direction. Shear horizontal waves have the same propagation direction, however, the particle motion is in the y direction. Therefore, their displacement vector, $\mathbf{u}_{\mathrm{SH}}$ can be written as

$$\mathbf{u}_{\mathrm{SH}} = (u_{x_{\mathrm{SH}}}, u_{y_{\mathrm{SH}}}, u_{z_{\mathrm{SH}})} = (0, f(z)\mathrm{e}^{k_{\mathrm{SH}}x-\omega t}, 0), \tag{4.10}$$

where $f(z)$ is a fixed amplitude distribution in the z direction, and k_{SH} is the wavenumber of the shear horizontal mode. Therefore, this mode propagates purely in the x direction, but only generates shearing in the out-of-plane direction. A detailed derivation of the displacement and other properties of shear horizontal waves can be found in [15] and [119].

Since shear horizontal waves possess, by definition, a shearing motion, they could potentially excite creeping waves too. For setting up an FE model to investigate this, the same configuration as the one shown in Figure 4.2 was

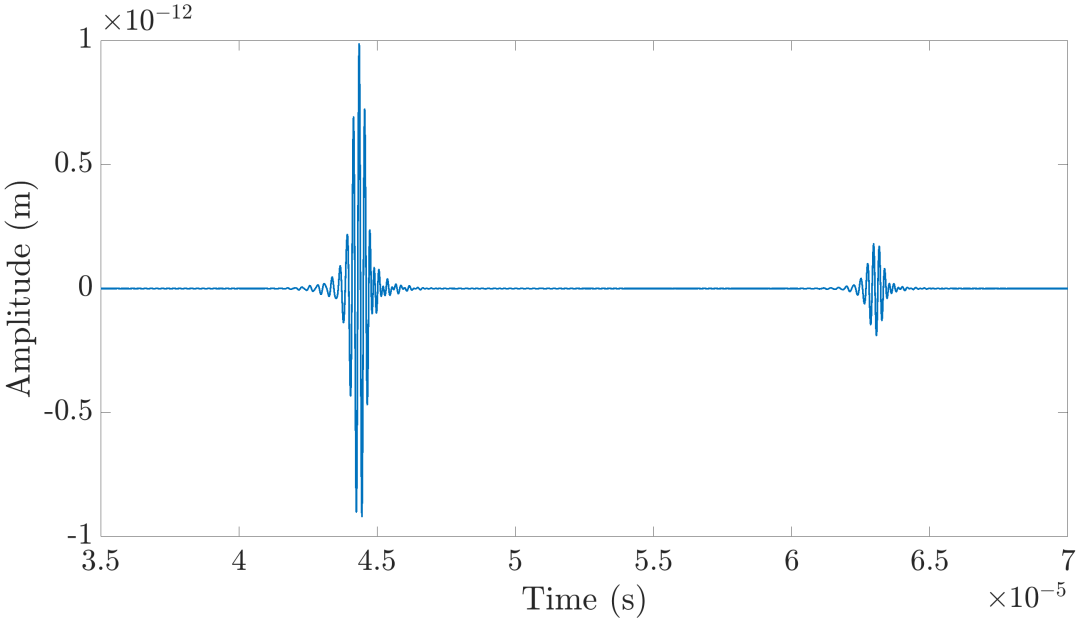

Figure 4.30: Signal received on the monitor line, for an annulus with $r_{\text{out}} = 40$ mm and $r_{\text{in}} = 10$ mm, and the use of SH3 elements, which allow for the simulation of SH waves. The signal represents the out of plane displacement of the nodes.

used, with a source and monitor lines at the $\theta = 90°$ and $270°$ positions respectively. The element type in Pogo was set to SH3, which is a type of element able to simulate out of plane displacements in 2D models i.e. displacements displacements out of the plane of the corss-section of the model. The size of the model was kept at $r_{\text{out}} = 40$ mm and $r_{\text{in}} = 10$ mm, which is a radius combination which gave good results for the creeping wave simulations using conventional shear waves. Similarly, the focus point was kept at the optimal location for this geometry, at $(r_{\text{in}} + t_{\text{pipe}}/8, 60°)$. The signal received on the monitor line is shown in Figure 4.30.

It is not immediately clear in Figure 4.30 whether the signal is a leaky wave or arises from elsewhere. However, it appears that the two waveforms arrive at different times compared with the respective ones in Figure 4.14, indicating that they may arise from a different source, as the geometries of the models

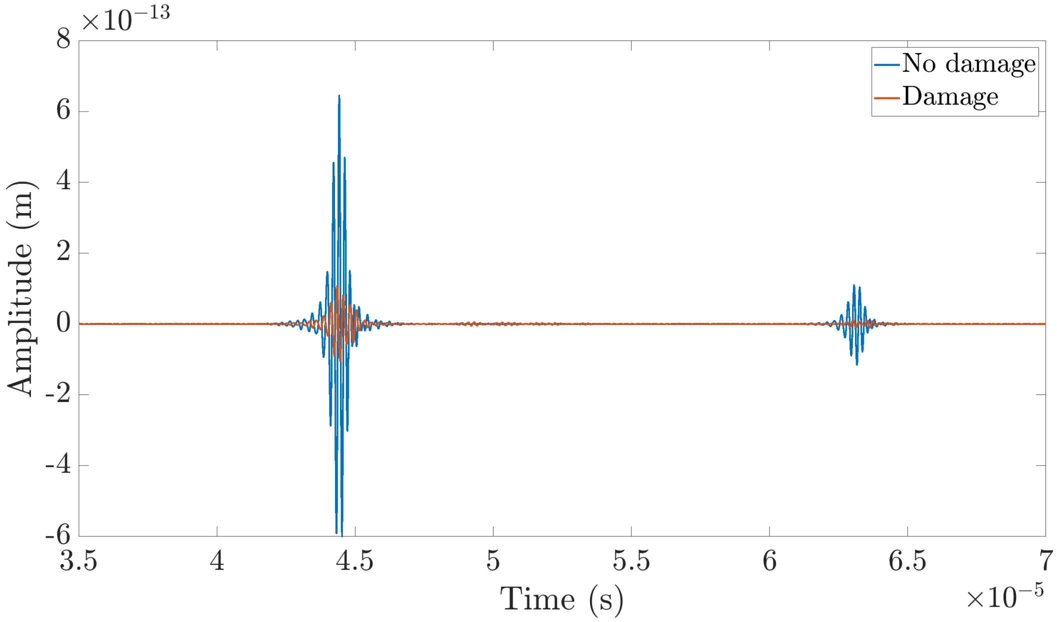

Figure 4.31: Comparison of the signal received on the monitor line, for an annulus with $r_{\text{out}} = 40$ mm and $r_{\text{in}} = 10$ mm, and the use of SH3 elements, which allow for the simulation of SH waves, with and without the presence of fatigue damage. The signal represents the out of plane displacement of the nodes

from which the signals in Figures 4.14 and 4.30 were recorded are identical, and therefore, the leaky wave is expected to arrive at the same time.

To investigate this further, the E profile was introduced to the model to investigate whether it would cause the same time shift in the signal as in Figure 4.14. The resulting signal, along with a comparison with Figure 4.30 is shown in Figure 4.31.

It is clear that the shift caused by the presence of the E profile in Figure 4.31 is significantly smaller than the shift shown in Figure 4.14, indicating that the waveforms are indeed not caused by energy leaking from a creeping wave travelling on the inner surface of the annulus.

Further visualization of the model in Paraview (not depicted here) revealed that these waveforms arise from the multiple reflections of the incident shear wave, with no evidence of a creeping wave being excited. This potentially can be attributed to the poor coupling between SH waves and creeping waves, as the former do not possess any in plane motion, while the latter possess purely in plane motion. One may expect though that the creeping wave could potentially excite Love waves, which still are surface waves in which the particle motion is purely out of the plane [120]. However, the excitation of Love waves requires the presence of layers of gradually reducing sound speed below their propagation surface [120]. Therefore, there exists no reason for the incident SH wave to excite a Love wave, given that the annulus is comprised of a single material in the undamaged case, or materials whose sound speed gradually increases from the inner surface for the damaged case. As an easy verification of this a source node was placed directly on the inner surface, which was excited in the out of plane direction. This model indeed showed no evidence of a Love wave being excited.

4.8 Alternative approach III - noise suppression methods

The use of noise suppression methods was also briefly considered in this study. This method works by utilising multiple sources and the principle of superposition, to suppress an unwanted wave at a desired location. Let us assume an annulus with two source lines, centred at P and Q as well as two monitor nodes, located at M_1 and M_2, as shown in Figure 4.32.

For the particular scenario which the noise suppression attempts to improve here, the aim is to determine excitation signals, S_{P} and S_{Q} such that the resulting signals interfere destructively at M_1 while preserving a signal of good quality in M_2. The specific location of the suppression point is not important,

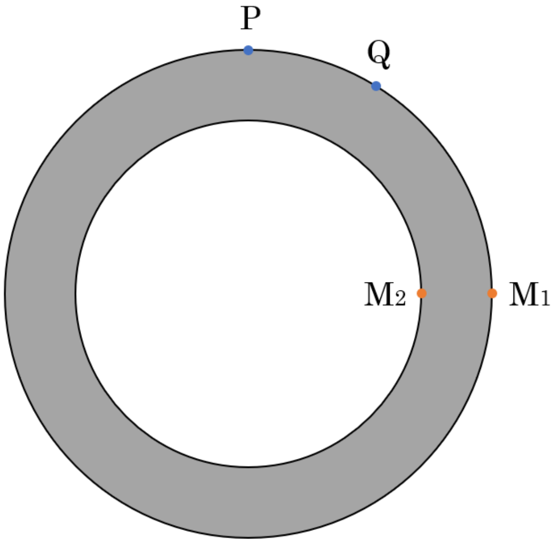

Figure 4.32: Schematic showing the location of the centres of the sourcelines, P and Q and the locations of the monitor nodes, M_1 and M_2, for a noise suppression model

and the location here was selected arbitrarily, without loss of generality. To calculate S_{P} and S_{Q}, let us assume that initially both sourcelines receive the same excitation signal S_0. This implies that

$$\begin{aligned} S_{\mathrm{P}} M_{1_{\mathrm{P}}} + S_{\mathrm{Q}} \mathrm{M}_{1_{\mathrm{Q}}} &= \mathrm{M}_1 S_0, \\ S_{\mathrm{P}} M_{2_{\mathrm{P}}} + S_{\mathrm{Q}} \mathrm{M}_{2_{\mathrm{Q}}} &= \mathrm{M}_2 S_0, \end{aligned} \tag{4.11}$$

where the subscripts at P and Q at M_1 and M_2 denote the source from which the signal has originated. The simultaneous Equations in (4.11) arise from the principle of linearity i.e. the signal recorded at M_1 and M_2, multiplied by the excitation signal, when both sources were excited by S_0, should be equal to the respective product for when each sourceline is excited separately. For the creeping wave simulations, the desired result is no signal at the outer surface ($\mathrm{M}_1 = 0$), and a well-behaved signal in the inner surface. Let us denote the latter by X - the simultaneous equations now become

$$
\begin{aligned}
S_{\mathrm{P}} M_{1_{\mathrm{P}}} + S_{\mathrm{Q}} M_{1_{\mathrm{Q}}} &= 0, \\
\frac{S_{\mathrm{P}} M_{2_{\mathrm{P}}}}{S_0} + \frac{S_{\mathrm{Q}} M_{2_{\mathrm{Q}}}}{S_0} &= \mathrm{X}.
\end{aligned}
\tag{4.12}
$$

An annulus with $r_{\text{in}} = 60$ mm $r_{\text{out}} = 70$ mm was used to investigate the efficacy of this method. The desired location for diminishing the outer surface wave and retaining a good quality inner surface wave was set to be at $\theta = 0°$. To determine S_{P} and S_{Q}, two FE models were created with the above mentioned dimensions, one with a sourceline only at M_1 and one with a sourceline only at M_2. For both models S_0 (the excitation signal) was set to be a 5-cycle Hann-windowed toneburst, with a centre frequency of 0.5 MHz. This allowed for the measurement of $\mathrm{M}_{1_{\mathrm{P}}}$ and $\mathrm{M}_{2_{\mathrm{P}}}$ for the model where only source P was used, and for $\mathrm{M}_{1_{\mathrm{Q}}}$ and $\mathrm{M}_{2_{\mathrm{Q}}}$ for the model where only source Q was used. Signal X was set to be identical to S_0, but time-delayed to the correct location at M_1. This set of simulations subsequently allow the solution of (4.12) for determining S_{P} and S_{Q}. These signals, after suitable windowing to remove unwanted noise, are shown in Figure 4.33.

Figure 4.34 shows the resulting wave field at three instances, when the signals on Figure 4.33 were implemented in an FE model, at their respective sourceline locations. Subfigure 4.34a shows the wave field prior to the arrival of the outer surface wave to the 0° position, Subfigure 4.34b shows the field approximately when the outer surface wave is at that position, and finally, Subfigure 4.34c shows the field at an instance after the outer surface wave has passed the desired suppression position. By comparing Subfigure 4.34b to the other two, it is clear that this method had greatly reduced the amplitude of the outer surface wave.

However, it is also clear that the suppression is far from perfect, and, as shown before, the amplitude of the leaky wave is two orders of magnitude smaller

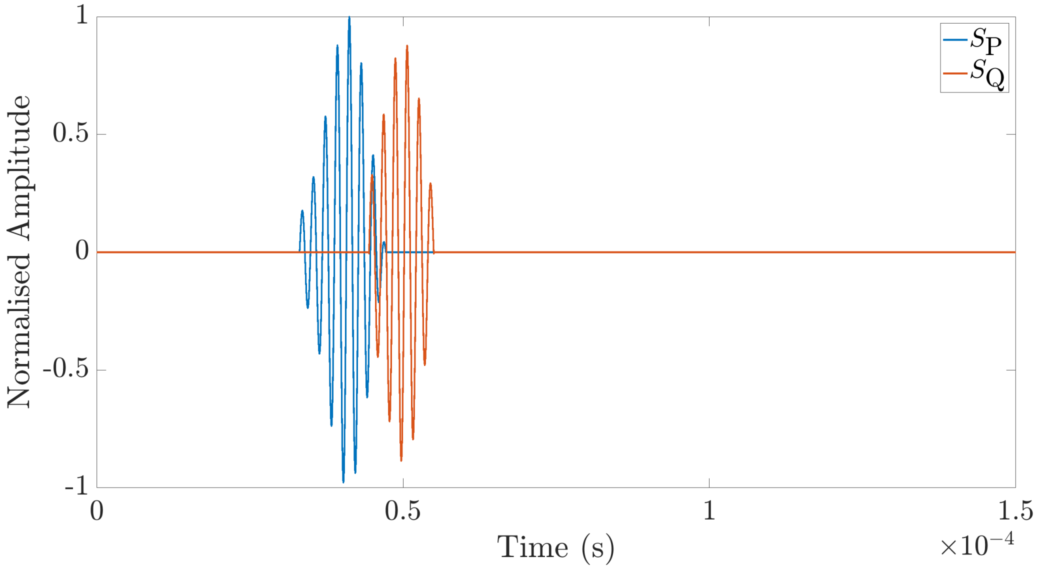

Figure 4.33: Signals S_P and S_Q, such that when used simultaneously, the outer surface wave in a pipe with $r_\mathrm{in} = 60$ mm $r_\mathrm{out} = 70$ mm at the $\theta = 0^\circ$ position diminishes.

than the outer surface wave - therefore, unless nearly perfect suppression is achieved, the leaky wave will still not be visible on the outer surface. Additionally, this method would have to be fine-tuned to each pipe geometry and inspection location. Such a refinement and geometrical dependence in a method is potentially impractical in an industrial scenario, and therefore this method was not pursued further.

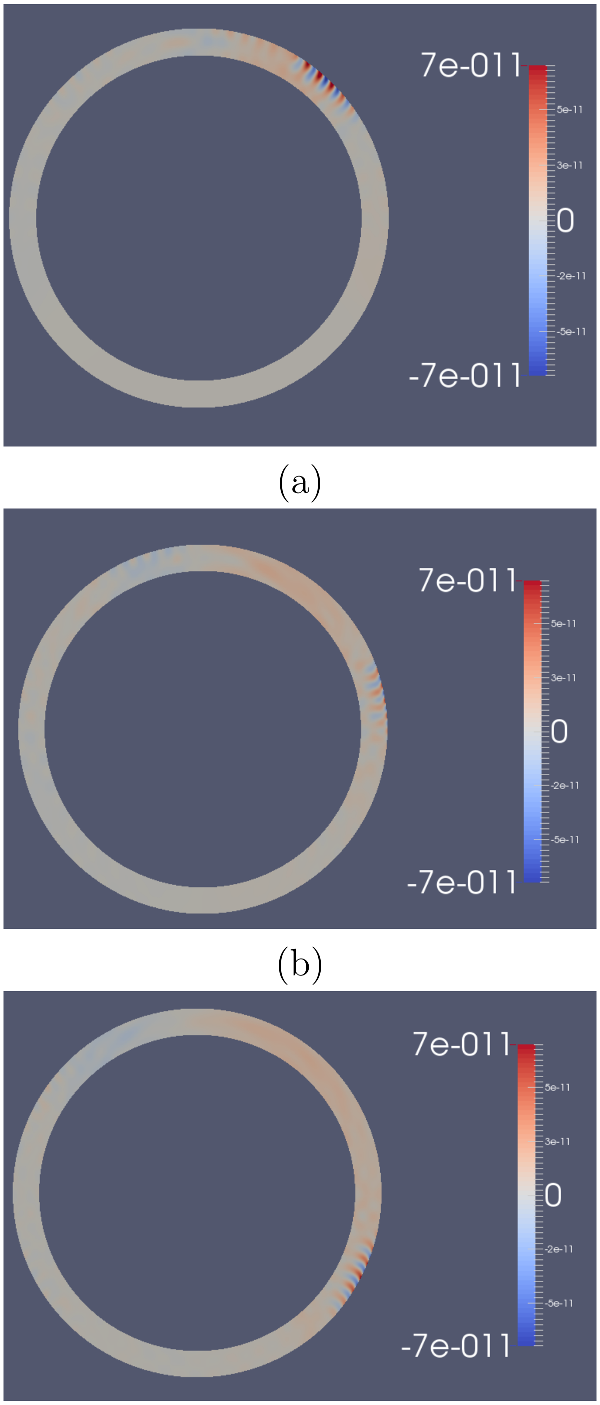

(a)

(b)

(c)

Figure 4.34: Evolution of the x component of the outer surface wave field as the wave travels along the outer surface of an annulus. The desired suppression area is at the $\theta = 0^\circ$ in (a) the field is shown prior to the arrival of the wave at the desired suppression location, in (b) the field is shown at the suppression location and in (c), the field is shown after the suppression location. The QR code directs to an animation of this process.

Chapter 5

Shear waves for assessing the fatigue state of flat & cylindrical components

The work in this chapter has been reported in a journal publication [121].

5.1 Introduction & theory

In this chapter, an alternative approach for assessing the fatigue state of steel pipes is presented, as in Chapter 4 it was demonstrated that surface wave methods produced unsatisfactory results; here, the use of bulk shear waves is proposed for such fatigue state characterisations. The initial studies completed by Granato & Lücke [1,52], regarding the interaction of ultrasound with dislocations did not consider various wave polarisations, and also used an idealised "material cell", where all dislocations lie perpendicular to the wave polarisation. More recent studies, however, have been able to consider multiple wave polarisations and random dislocation forests within a material cell.

Maurel et al. [2] studied the effect of a single dislocation (either screw or edge) on the propagation of a shear wave, in a 2D space. This study was subsequently extended by the same authors in [4], where the authors introduced a forest of random dislocations, again in 2D, deriving expressions for the changes in speed and the attenuation coefficient of an elastic wave travelling through them. Here the authors also introduced the idea of an equivalent-solid, i.e. the replacement of the dislocation-filled material with an equivalent homogenous dislocation-free one, with altered material properties such that the effect of the dislocations is expressed via the material alteration. Finally, the authors in [5] discussed the results from a 3D study, where the effect is shown on the propagation of an elastic wave with generalised polarisation due to the presence of a 3D forest of randomly oriented dislocations.

5.1.1 Theoretical motivation

The methods and findings from [5] will be briefly discussed below, as this is the more generalised study in the series of gradually increasing in complexity results from the same authors as in [5], and therefore the methods and results are analogous to [2] and [4]. The authors start from the elastic equation for a solid containing dislocation realisations, and use averaged Green's functions and perturbation theory to consider the mean effect of the presence of multiple dislocation realisations on the mean wavenumber of a wave travelling over such realisations. The effect of the dislocations is represented as a perturbation in the constitutive tensor of elasticity (C_{ijkl}) - this is an alternative approach to that of Granato & Lücke [1], who derived analogous expressions by considering dislocations as pinned strings with finite mass, drag and damping. The resulting expressions for the effective wavenumber are rather complicated and contain multiple terms which are potentially difficult to measure in reality, however, under a low frequency assumption, they reduce to:

$$\Delta C_w = \frac{C_{w_f} - C_{w_h}}{C_{w_h}} = Z_w \frac{\mu b^2}{\Gamma} \Lambda \mathrm{L}^2, \tag{5.1}$$

where C_{w_h} and C_{w_f} are the ultrasonic speeds at the reference and altered dislocation (and hence in this thesis, fatigued) states respectively, Z_w is a constant depending on whether the incident wave is shear or longitudinal, and $w = L$ for longitudinal and $w = T$ for shear waves. Also,

$$\Gamma = \frac{\rho b^2}{2\pi} \left(1 - \frac{1}{\gamma^2}\right) C_T^2 \ln \left(\frac{\epsilon'}{\epsilon'_0}\right). \tag{5.2}$$

In Equation (5.2), ϵ' and ϵ'_0 are the long and short distance cutoff lengths. Again, the terms in Equation (5.1) might be difficult to quantify in an industrial inspection, however, an important observation is that the ratio between the changes in shear and longitudinal wave speed is a constant:

$$\frac{\Delta C_T}{\Delta C_L} = \frac{Z_T}{Z_L}, \tag{5.3}$$

where the change is shear wave speed, ΔC_T, is defined as

$$\Delta C_T = \frac{C_{T_f} - C_{T_h}}{C_{T_h}}. \tag{5.4}$$

Provided that $Z_T = \frac{4}{5\pi^4}$ and $Z_L = \frac{16}{15\pi^4\gamma^2}$

$$\frac{\Delta C_T}{\Delta C_L} = \frac{3\gamma^2}{4}, \tag{5.5}$$

or, equivalently,

$$\frac{C_{T_f} - C_{T_h}}{C_{L_f} - C_{L_h}} = \frac{3\gamma}{4}. \tag{5.6}$$

Given that γ is approximately 1.8 for steel, this means that for a given dislocation state, the changes in speed for a shear wave are approximately 2.5x bigger than for longitudinal waves, if their speed is measured after they have propagated through the same fatigue area. This observation has two useful implications - firstly, if an inspection is completed by using through-thickness measurements and shear waves, the changes in speed will be amplified by approximately 2.5 times. Additionally, if those measurements are combined with analogous longitudinal wave measurements, and the ratio between the speeds is found to be 2.5 instead of 1, this can distinguish between a reduction in thickness and a fatigue spot, provided that those are not combined. This is because a change in thickness would cause the same perceived change in speed in all types of through-thickness waves, and thus the ratio would be equal to 1. However this is a preliminary observation; it would require more work to pursue this as a viable approach for thickness-variation inspections

5.1.2 EMATs for C_T measurements

EMATs work by utilising the principles of electromagnetic theory. A schematic of an EMAT, showing its basic components is shown in Figure 5.1 - it is worth noting that Figure 5.1 shows an exemplar setup of an EMAT, and that multiple other configurations exist.

As shown in Figure 5.1, EMATs are comprised of a permanent magnet and a conductive coil which is located below the magnet. There are three methods in which an EMAT is able to create ultrasonic waves - the magnetisation force, magnetostrictive phenomena, and the Lorenz force [122]. The magnetisation force is the stress created to a magnetised material, when also influenced by the presence of an external magnetic field. When this field is periodic, the stress is subsequently periodic, leading to the creation of an ultrasonic wave. Magnetostriction is the phenomenon in which an external magnetic

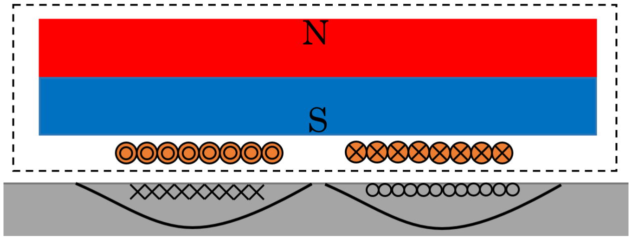

Figure 5.1: Schematic of the basic components of an EMAT. The red and blue areas denote the north and south pole of a permanent magnet, below which the cross section of a copper coil is shown. The directions of the current and magnetic field are denoted as ◦ for out of the page and × for into the page. The casing of the EMAT is denoted by the dashed line.

field forces the magnetic domains inside a material to align, causing strain on its surface. This strain-disturbance then propagates through the thickness of the material in the form of a wave [123]. However, it has been shown that in steel, the Lorenz force mechanism is the dominant driving force for the creation of ultrasonic waves [124, 125]. This is also shown in Figure 5.1 - when an alternating current flows through the coil, it generates eddy currents on the surface of a material. Those eddy currents interact with the magnetic field from the permanent magnet, with this interaction manifesting as a Lorenz force acting on the electrons of the material. If the eddy current density is denoted by $\mathbf{J}$ and the permanent magnet's field density by $\mathbf{B}$, the Lorenz force density, $\mathbf{F_L}$ can be found using Equation (5.7).

$$\mathbf{F_L} = \mathbf{J} \times \mathbf{B}. \tag{5.7}$$

The now disturbed electrons interact with the rest of the material causing a through-thickness disturbance [126].

EMATs are therefore capable of generating through-thickness shear waves that reverberate between the walls of a material. The echoes created by the reverberation allow us to measure the speed of these waves, and subsequently, any effect that a fatigue zone has on it. Although the phenomenon of shear waves creating larger frictional forces and hence being able to more easily force dislocations to oscillate has been experimentally verified in past studies [127], to the author's knowledge, through-thickness measurements have not been used for fatigue state characterisation via C-scanning. Such maps are however desirable for fatigue state assessments, as they provide a visual verification of the presence of a fatigue area, which would not be possible with a few point measurements, leading to potential errors especially in the C_{L_h} value. Such a speed C-Scan is currently very difficult to achieve with conventional piezoelectric contact transducers.

Here an alternative approach to create C_T C-scans was utilised - the use of shear wave generating EMATs mounted on a specialised frame, which is able to move them in pre-defined increments, similarly to how immersion transducers move in an immersion tank. The next section presents how this setup can be used to achieve C_T scans for the Trueflaw plates to verify the theory in Equation (5.3). Following this verification, some findings in extending this method to curved surfaces are presented, as an alternative method to creeping waves to increase the change in speed.

5.2 Shear waves for fatigue characterisation of plates

5.2.1 Experimental methods

Initially, at attempt was made to to replicate the longitudinal wave C-scans in Chapter 3 using shear waves. Shear wave speed C-scans, using contact transducers, are far from straightforward to achieve. Longitudinal wave C-scans are significantly easier to obtain due to the fact that water can support such waves and hence immersion tanks can be used in combination with a stepper controller, as described in Chapter 3, to achieve these results. The requirement of high-viscosity coupling for standard piezoelectric shear wave transducers prohibits the use of such a continuous-motion setup, and also, the couplant adversely affects the signal quality and repeatability of measurements.

As explained in the previous subsection, EMATs do not require any mechanical coupling to produce ultrasonic waves inside a material, contrary to pieazoelectric transducers. Hence, they can be used for the creation of shear wave C-scans, analogous to the ones created by an immersion tank with the use of a suitable setup. In this study here, a 3-axis frame controlled by stepper motors was utilised for the creation of such C-scans. The EMAT was mounted on a bespoke holder, and the frame allowed for controlling the x, y and z coordinates of the EMAT, similarly to the frame used for the longitudinal waves measurements. A schematic of the experimental setup is shown in Figure 5.2

Prior to the generation of C-scans, the ability of the EMAT to produce a signal strong and clean enough for repeated speed measurements was investigated. For this investigation, a 2.25 MHz EMAT was used with a circular Printed Circuit Board (PCB) coil, which was produced by the NDE lab at Imperial College [126,128]. An example of the signal produced by this EMAT is shown in Figure 5.3. The signal was obtained by placing the EMAT on an 8 mm thick steel sample, and recording the back wall echoes from it. Each of the peaks of the wavepackets in Figure 5.3 represents a back wall reflection. The signal in Figure 5.3 appears to have distinguishable peaks and therefore can be used for speed measurements. The EMAT is also able to record multiple reflections, allowing for averaging of C_T values if desired.

To investigate the repeatability of the speed measurements from the EMAT,

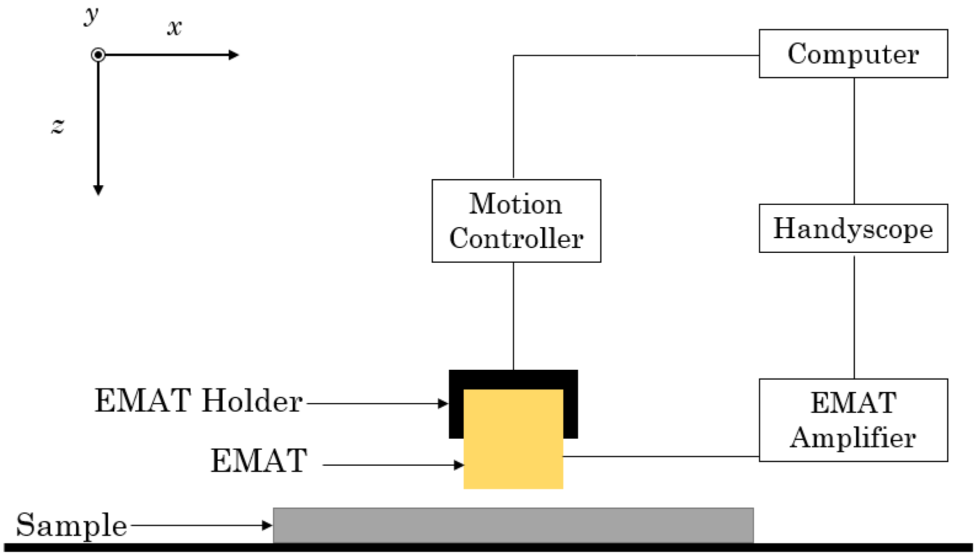

Figure 5.2: Experimental setup used to obtain shear wave C-scans. The EMAT is excited by a Handyscope, and its position is controlled through a 3-axis stepper motor frame.

it was placed at an arbitrary point on the steel plate, from which 100 signals were acquired. Using the same autocorrelation method presented in Chapter 3, 100 C_T values were obtained, the variation of which is shown in Figure 5.4.

From the data shown in Figure 5.4 it appears that the EMAT is performing well - the mean C_T value is 3331.1 m/s, and the maximum variation from the mean is 0.012%, which is far smaller than the expected changes in speed due to fatigue. Therefore, this rendered this EMAT suitable for fatigue state investigations.

As a final check of any potential error sources in this method, 50 C_T measurements were taken at a single point, but the EMAT was removed and replaced by hand at the same position between each measurement. This allows for the assessment of any errors associated with placement and misaligment of the EMAT. The results are shown in Figure 5.5.

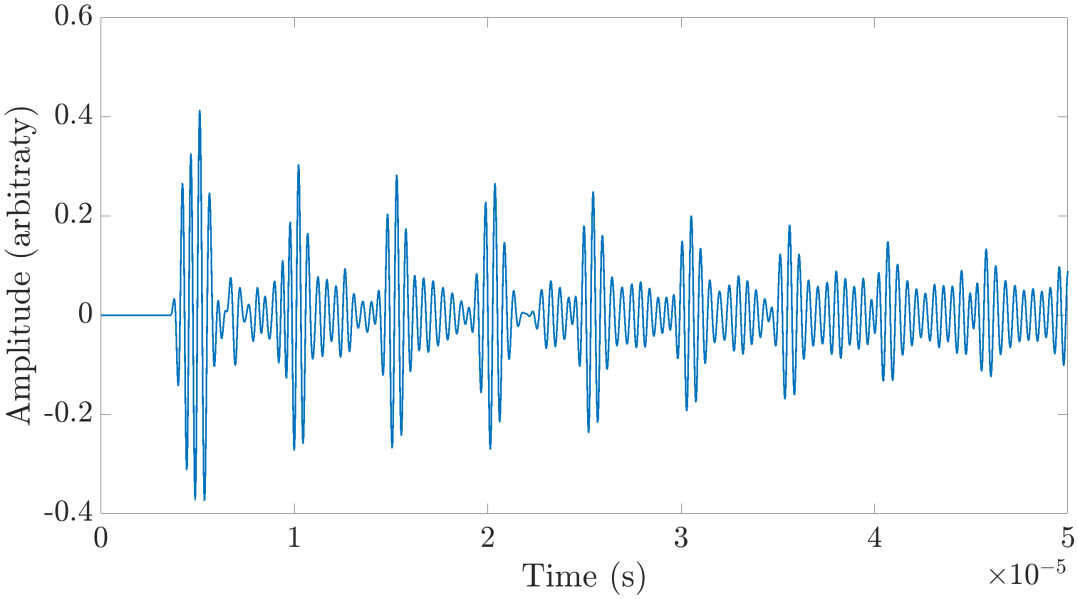

Figure 5.3: Example of the signal obtained from the EMAT, with a centre frequency of 2.25 MHz.

As shown in Figure 5.5, the variation in speed is small - the maximum absolute deviation from the mean C_T value of 3150.3 m/s is 0.014%. This variation is again far smaller than the expected ΔC_T values. Both variations are an order of magnitude smaller than the expected variation in speed due to fatigue, rendering therefore the EMAT suitable for such measurements, at least in this present context which is believed to be appropriate to inspections in the electric power generation industry. These results are an indication that shear waves generated by EMATs are of similar quality to those obtained from the more established immersion testing, which gives the best performance for longitudinal wave measurements.

5.2.2 Results & discussion

To obtain C_T C-scans for the flat samples, the frame controller was programmed to move the EMAT in 0.5 mm steps, starting from the bottom left of the fatigued plate, and ending at the top right. The scanning direction

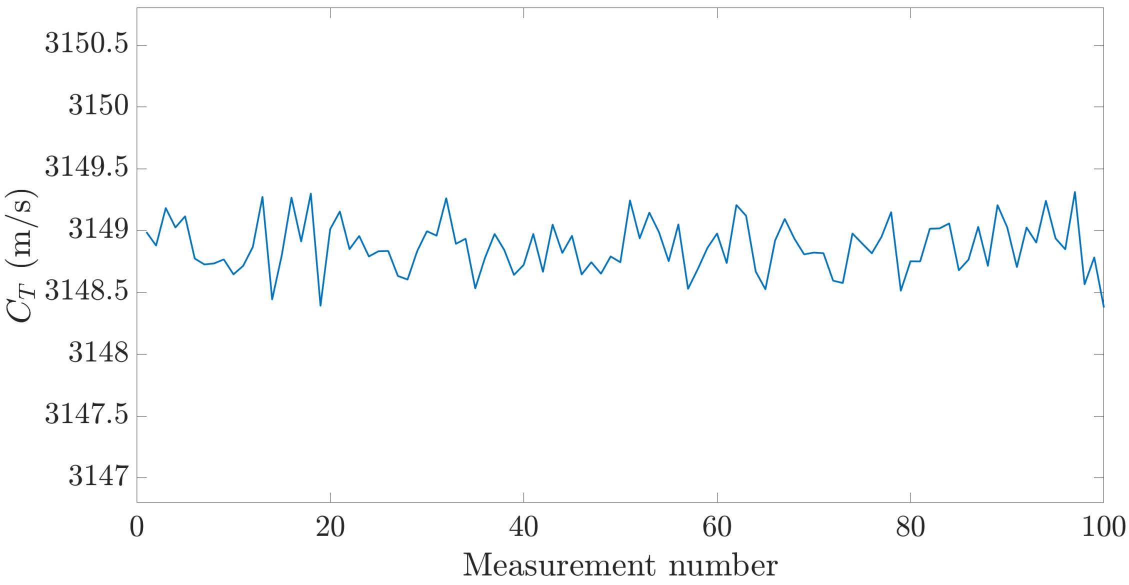

Figure 5.4: Variation of C_T on a fixed arbitrary point on a steel plate, obtained by processing the signal from the EMAT in Figure 5.3.

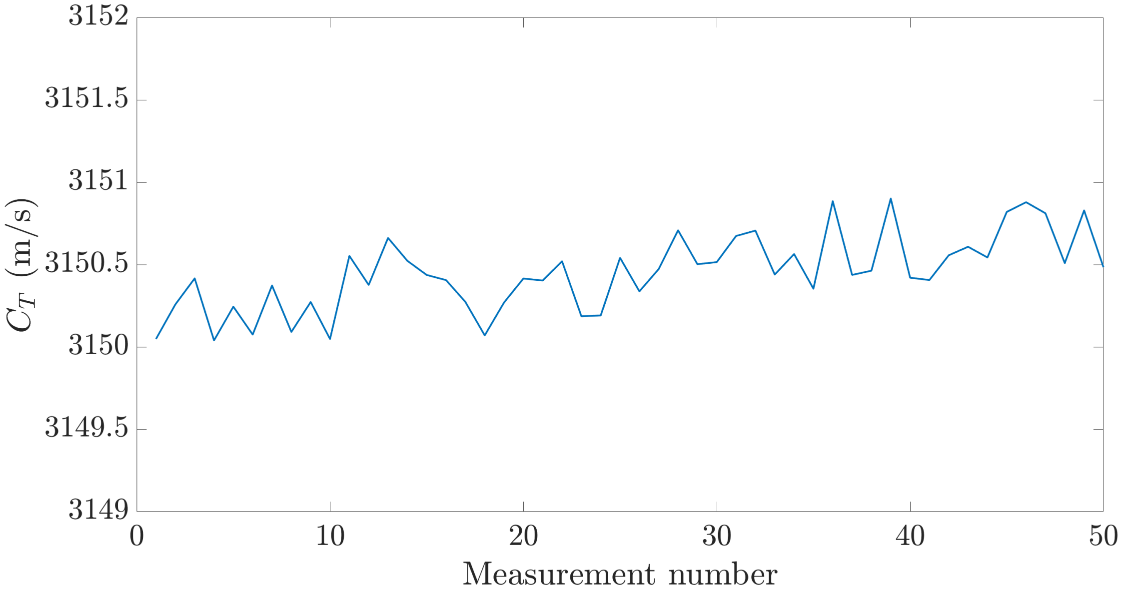

Figure 5.5: Variation of C_T when the EMAT was removed and replaced on the same point of a steel plate.

was alternated between the positive and negative x direction for each new line. For each point, the signal was recorded and the C_T value at the particular point was calculated, allowing for the creation of C_T C-scans for all fatigued plates, similar to the ones obtained using the immersion tank and longitudinal waves. The results are shown in Figure 5.6.

The presence of a low C_T area is evident in the C-scans of all the plates apart from the reference one. The area is circular in shape as expected, and additionally, each subfigure shows some of the same speed features present in its respective C_L map, increasing the confidence in the reliability of this scanning technique. To illustrate this, and for the convenience of the reader, Figure 5.7 shows both the longitudinal and shear wave speed maps of plate 93.

Multiple common features can be seen when comparing subfigures 5.7a and 5.7b. For instance, a high speed area is evident at both C-scans at the top right corner. The lowest speed area is located on the left quadrant of the fatigue spot, and finally, the healthy region appears to be “faster” in the bottom half of the C-scan. Analogous features, such as the small high speed spot in the middle of the fatigue spot for plate 99, and the “breakage” of the fatigue spot of plate 84 into 2 smaller fatigue areas can be seen across the comparison of each plate’s C_L and C_T C-scans.

The C_T C-scan of plate 00 in subfigure 5.6f has a very useful implication in assessing the level of accuracy in speed measurements of the method presented in this chapter, to the more established C_L measurements using an immersion tank presented in Chapter 3. In subfigure 3.8f, the mean C_L value is 5828.2 m/s and the standard deviation is 2.48 m/s, which is equal to 0.042% of the mean C_L value. The analogous C_T scan in subfigure 5.6f has a mean C_T value of 3158.7 m/s with a standard deviation of 1.47 m/s, which is equal to 0.047% of the mean C_T value. The proximity of the normalised standard deviation of

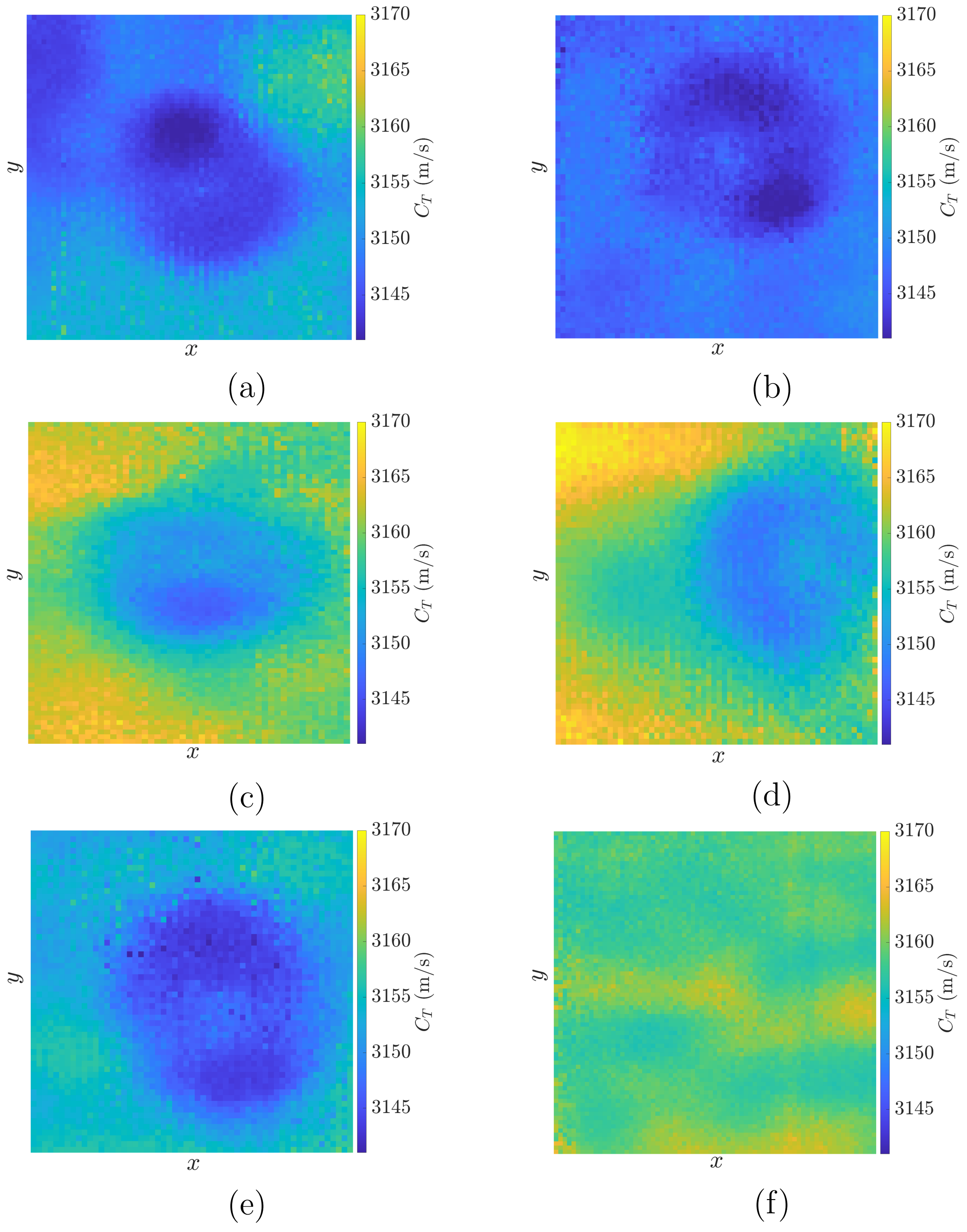

(a) (b) (c) (d) (e) (f)

Figure 5.6: C_T C-scans maps, obtained by 0° EMAT raster scanning. The results are presented in decreasing fatigue order, with subfigures (a)-(e) corresponding to plates 93, 99, 04, 91 and 84 respectively. Finally, Subfigure (f) corresponds to the reference plate (plate 00). Each plate is approximately 100 mm × 100 mm in size, and the fatigue spot has a diameter of approximately 50 mm.

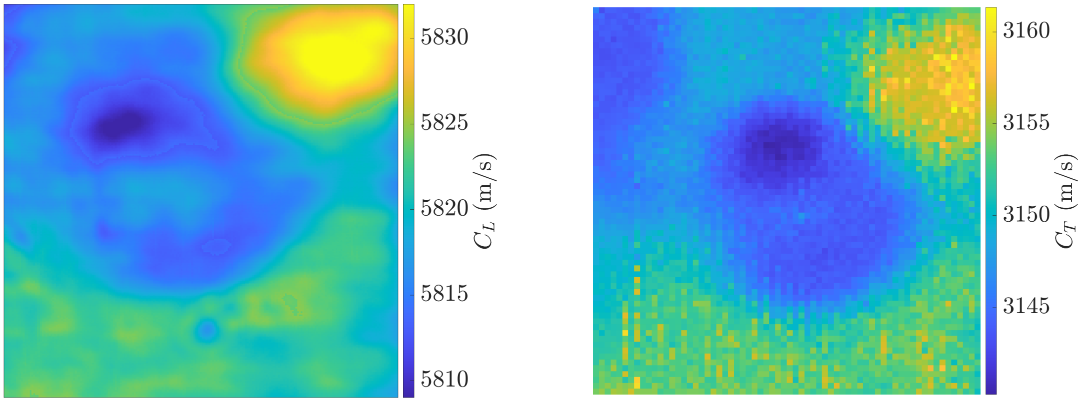

(a) (b)

Figure 5.7: Longitudinal (a) and shear (b) wave speed C-scans of plate 93. Subfigure (a) is a repeat of subfigure 3.8a, and subfigure 5.7b is a repeat of subfigure 5.6a. Here, the colourbar scales have been adjusted, compared to the original subfigures, to allow for better visualisation of the speed features. The plate is approximately 100 mm × 100 mm in size, and the fatigue spot has a diameter of approximately 50 mm.

the two scanning methods further increases the confidence in the shear wave scanning frame, as it shows that on a reference plate, where a more significant part of the variation in speed comes from potential equipment/processing errors rather than the specimen itself, the fluctuations in speed are very similar to what is achievable by immersion scanning.

For calculating the ΔC_T value, an analogous technique to the calculation of the ΔC_L value was used. Similarly to the longitudinal wave C-scans, a healthy area was selected in each subfigure of Figure 5.6, from which the average speed value was used as the C_{T_h} for that particular plate. The C_{T_f} was again defined as the area of minimum speed inside the fatigue spot.

A plot showing the variation of the ΔC_T value as the UF increases is shown in Figure 5.8. Again, the percentage change in shear wave speed, $\Delta C_T(\%) = \Delta C_T \times 100$ is plotted. The change in shear wave speed is still monotonic as fatigue progresses. Also, the shape of the graph in Figure 5.8 resembles that of

Figure 3.8, where the segment joining the most and second-to-most fatigued points exhibits a sharper increase in gradient. However, the magnitude of the changes is noticeably larger for shear waves, as supported by the theory [5], and the justification obtained with the aid of EBSD imaging in Chapter 3.

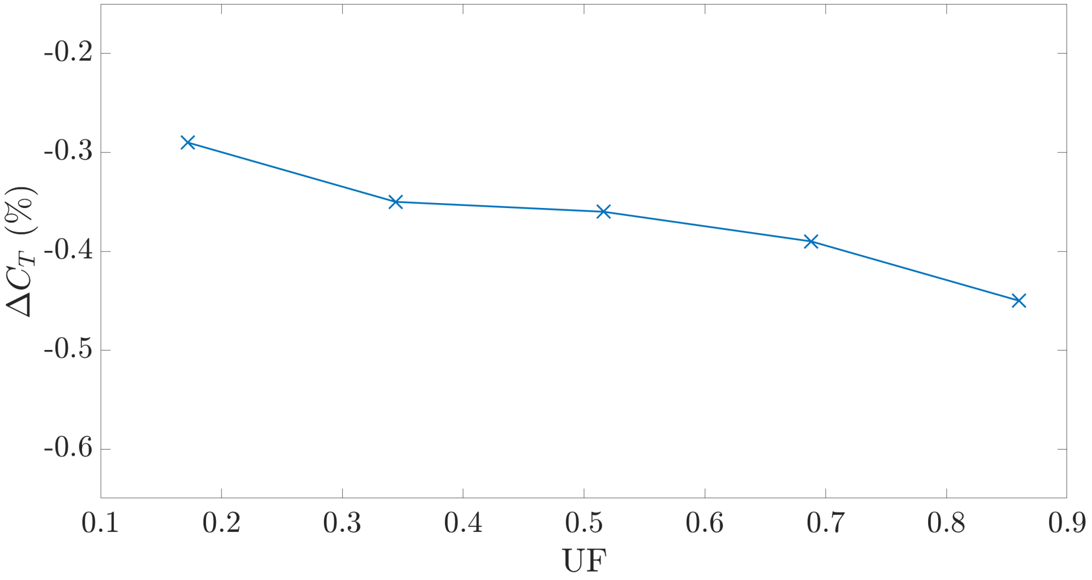

Figure 5.8: Evolution of the change in shear wave speed, ΔC_T, with an increase in UF. An increase in UF implies an increase in the number of cycles to which a material has been subjected, therefore, the monotonic nature of this figure shows that as fatigue progresses, the propagation speed of a shear wave reduces.

Each ΔC_T value was then divided by the respective ΔC_L in Figure 3.9, with the ratio being plotted in Figure 5.9. For the particular plates used in this study, C_L was found to be equal to 5824.4 m/s and C_T to be equal to 3154.7 m/s from the mean of the five C_{L_h} and C_{T_h} values respectively. Therefore, from Equation (5.5) the theoretical value of this ratio is expected to be approximately 2.56. The mean value of $\Delta C_T/\Delta C_L$ in Figure 5.9 is 2.05 - however, it appears that all but the last point have a $\Delta C_T/\Delta C_L$ value of 2 or more. Again given that it had previously been observed that the

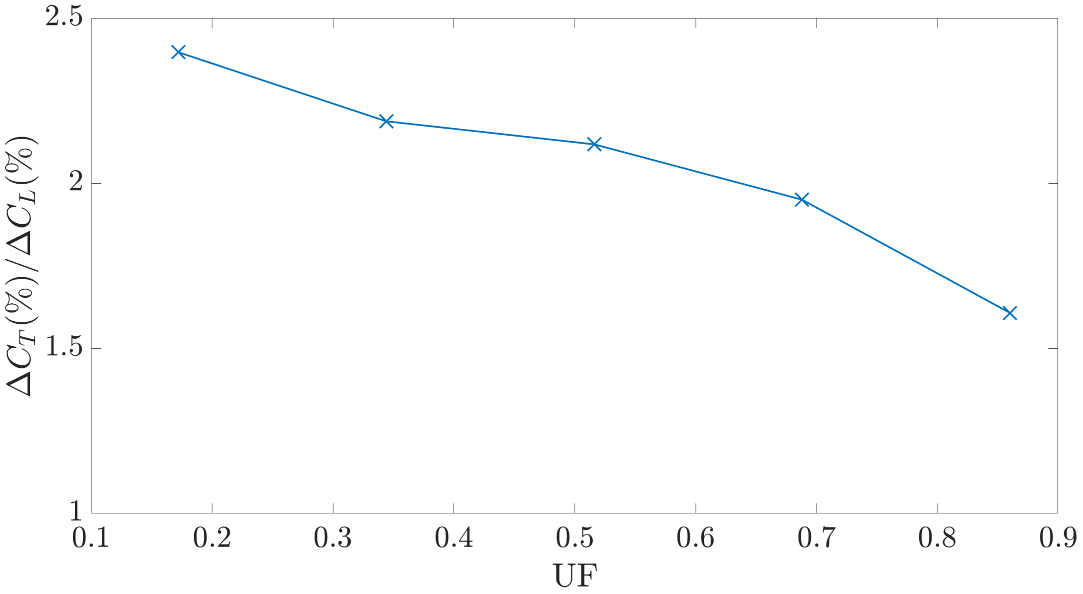

Figure 5.9: Variation of the $\Delta C_T(\%)/\Delta C_L(\%)$ with the UF.

results from this particular plate also do not match the FE simulations, and also that the UF of this plate is close to the crack formation stage [20], it is potentially sensible to disregard the last point - this increases the value of the ratio to 2.17, which is closer to the theoretical value. It is also worth noting that, even when disregarding the last point in Figure 5.9, there still appears to be some variation of the $\Delta C_T/\Delta C_L$ value, even though Equation (5.5) suggests that this value should remain constant. This can potentially be attributed to two reasons; first, experimental errors which affected the ΔC_L or ΔC_T values, and also, any secondary effects which fatigue causes on the propagation speed of ultrasonic waves which can not be attributed to the evolution of the dislocation state of the material and hence are not captured by the theory in [1–5].

Additionally, in Figure 5.9 the $\Delta C_T/\Delta C_L$ values were calculated for the maximum reduction in speed - however, the theory in Equation (5.5) would hold true regardless of which comparison point is selected. Therefore, both

C_L (Figure 3.8) and C_T (Figure 5.6) maps were converted into ΔC_L and ΔC_T maps respectively, which were subsequently divided to get a $\Delta C_T/\Delta C_L$ map for each plate - an example of such a map, showing the $\Delta C_T/\Delta C_L$ map of Plate 99 is shown in Figure 5.10.

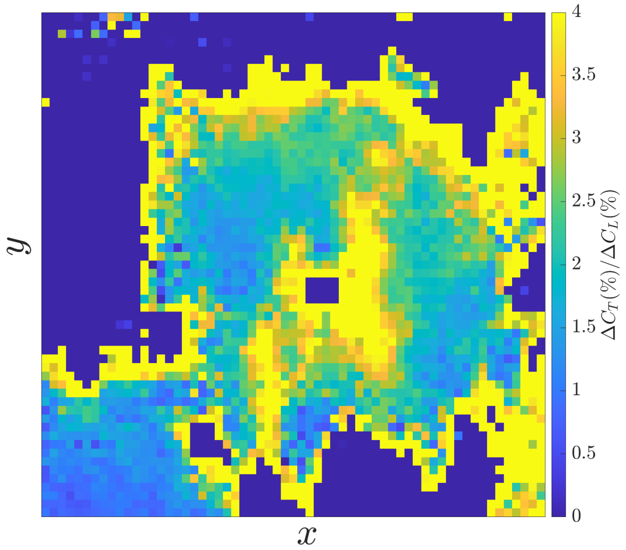

Figure 5.10: $\Delta C_T(\%)/\Delta C_L(\%)$ C-Scan of plate 99, obtained by converting Figures 5.6b and 5.6b into percentage change in speed maps, aligning them and dividing each point.

There are a few interesting features in Figure 5.10. Firstly the value of the ratio inside the fatigue spot is always greater than 1, with most areas having a value of this ratio being approximately equal to 2. Additionally, the large blue and yellow areas show that good values for C_{L_h} and C_{T_h} had been selected - this is because those areas are in the healthy region, and therefore $\Delta C_T/\Delta C_L = 0/0$ which yields very large positive or negative values depending on the sign of the small difference between the value at each of the points in the healthy area and C_{L_h} or C_{T_h}. A similar effect can be seen in the middle of the spot. However, this is possibly the result of uneven fatigue, because as shown both in Figures 3.8b and 5.6b, there is indeed an area of higher speed roughly in the middle of the fatigue spot, potentially indicating uneven heating of the plate. Finally, an area where the $\Delta C_T/\Delta C_L$ value is approximately equal to one is shown at the bottom left corner of Figure 5.10, which is located at the same location as the low speed area in Figures 3.8b and 5.6b. This is potentially a very good example of how this method was able to distinguish between fatigue and change in thickness - given that both C_L and C_T maps show a low speed area at the bottom right, but the ΔC_L and ΔC_T values approximately equal one, and not $3\gamma^2/4$. As it is already known that no other fatigue damage exists on any of the plates, this value of the ratio implies the presence of an area with altered thickness.

Therefore, two important findings here have been presented here. Firstly, that through-thickness shear wave C-scans can be used for fatigue detection, with the aid of a suitable setup, showing clear visual indications of fatigue which manifest as a change in the propagation speed of the shear wave. The theory suggests that these changes are $3\gamma^2/4$ times (which is approximately equal to 2.5 times) greater than those observed using longitudinal waves, something which was verified here. This has a useful implication where longitudinal and shear waves scans can be completed on the same component, as it allows the distinction between changes in speed caused by pure thickness changes and pure fatigue damage.

5.3 Shear waves for fatigue characterisation of pipes

In the previous section it was demonstrated how through-thickness shear wave speed measurements can be used for fatigue state characterisation of flat samples. This was a useful verification, allowing the expansion of this method to other fatigue scenarios. The aim here was to extend this method to pipe geometries, since the obstacles of using creeping waves have already been demonstrated in Chapeter 4.

5.3.1 Experimental methods

For this investigation, a pipe containing two fatigue spots was used, which were fabricated by Trueflaw using the same method for making the fatigue spots on the plate samples. One spot has a UF of 0.8 and the other spot has a UF of 0.24. The pipe has an inner radius of 98 mm, a wall thickness of 7 mm and an axial length equal to 200 mm.

First it was necessary to establish whether the EMAT used in the previous section would be able to produce accurate enough C_T measurements on the curved surface of the pipe. To assess this, the same technique was followed, where the EMAT was positioned on a fixed point and 100 C_T measurements were obtained at that particular point. The variation of the speed in this experiment is shown in Figure 5.11.

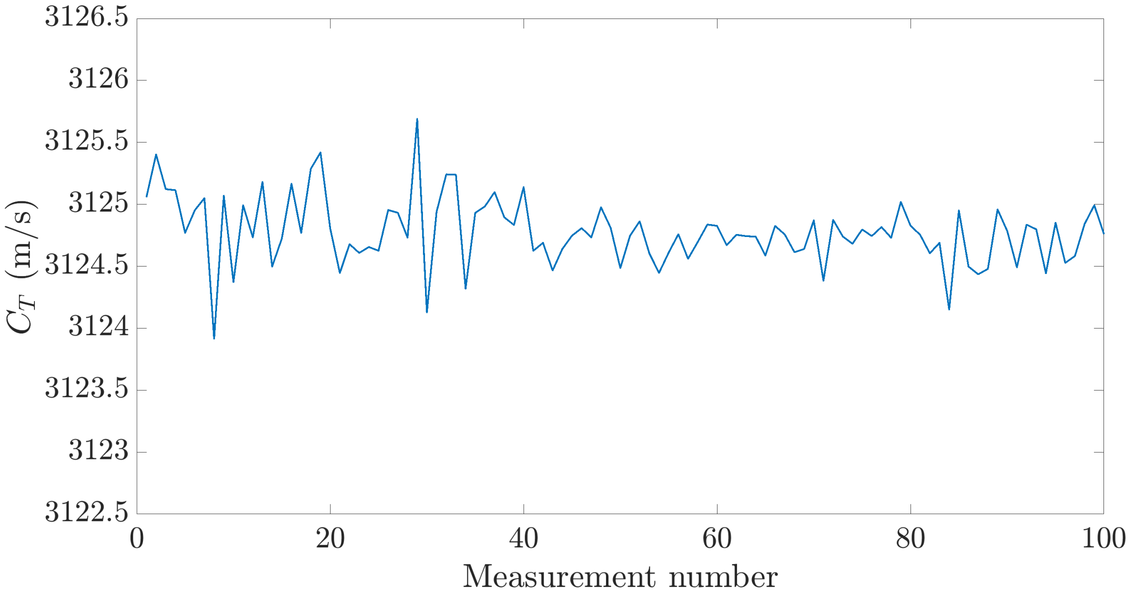

Figure 5.11: Variation of C_T on a fixed point on a steel pipe, obtained by using the signal from a flat EMAT.

From the data shown in Figure 5.11 it appears that the EMAT is performing very well - the mean C_T value is 3333.1 m/s, and the maximum variation from the mean is 0.029%, which is larger than the variation on the flat plates, however, it still remains approximately one order of magnitude lower than the expected changes in speed due to fatigue. Therefore, this rendered this flat EMAT suitable for fatigue state investigations on the pipe sample.

Following this verification, the pipe was placed on an indexing head, below the scanning frame setup. A photograph showing this setup is shown in Figure 5.12. The indexing head is a device which is usually used for indexing pipes in workshops, by allowing the operator to turn the pipe by the desired number of degrees accurately. The frame was programmed to move in the positive y direction while taking C_T measurements in 2 mm intervals, pause at the end of the pipe, and then move in the negative y direction again taking C_T measurements every 2 mm. During the pause, the pipe was rotated manually by 1°. This semi-automated method allows for the creation of C_T C-scans for the pipe, which would not have been possible otherwise.

5.3.2 Results & discussion

The fatigue spots are positioned towards the left hand end of the pipe in Figure 5.12 - therefore, the EMAT's starting position was selected to be just to the left of the polished area in the pipe in the same figure. The EMAT completed line scans, alternating between the positive and negative y directions, until sufficient pipe area had been scanned. The resulting C-scan is shown in Figure 5.13.

As shown in Figure 5.13, both fatigue spots are clearly visible. It is also very clear that the left fatigue spot corresponds to a lower UF, as denoted by the lower C_T values in its vicinity. In terms of change in speed, the ΔC_T value for the left spot is -0.24% and for the right spot is -0.38% ,

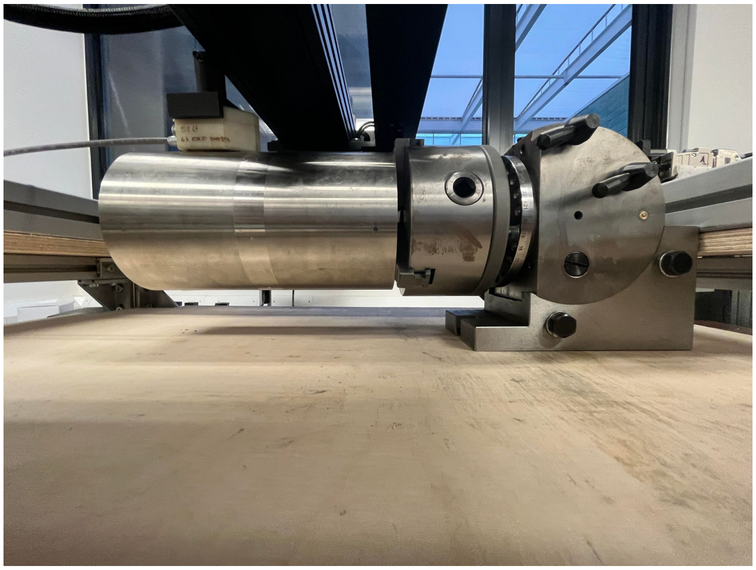

Figure 5.12: Setup used for obtaining a C_T C-scan of the area around the fatigue spots in the pipe shown. The EMAT, which is mounted on the scanning frame can move in the axial direction, while the pipe can be manually rotated using the indexing head each time the EMAT finishes the measurements on one line, to achieve a semi-automated C-scan.

calculated using the same approach of defining a healthy and a fatigued area. It also appears that the low C_T spots "leak" outside their boundaries. This potentially indicates that heat was leaking from the heating element, used to create the fatigue spots on the inner surface of the pipe, to the rest of the pipe during the fatiguing process. This is potentially due to the curved nature of the surface, as it is more prominent in the circumferential direction, and the associated difficulty to get a complete seal between the heating element and the material. The leakage is more prominent on the high UF spot. This could be attributed to two reasons - first, the higher number of cycles allows for more opportunities for heat to escape the designated fatigue area. Additionally, on the right-hand side of this fatigue spot, Trueflaw has created a third fatigue area which further increases the possibility of heat to leak in the region between the two spots. This third spot is not shown in Figure 5.13 as recording EMAT signals of adequate quality was not possible, due

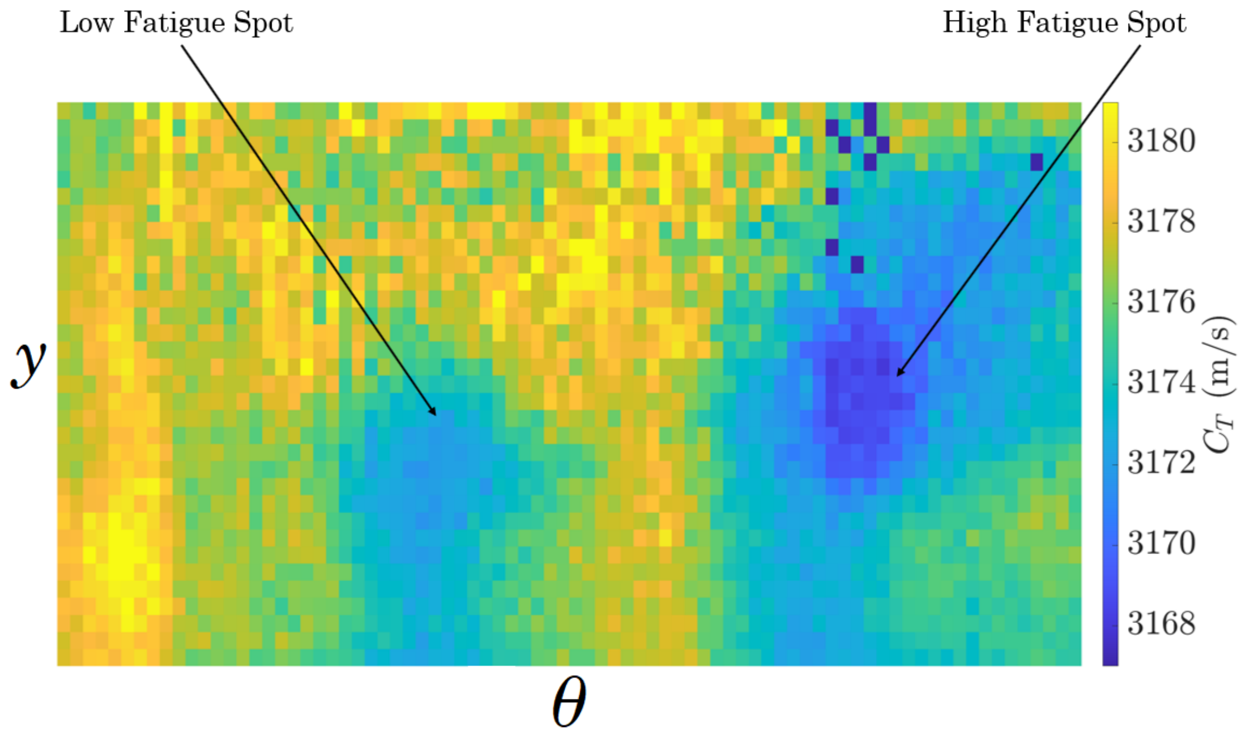

Figure 5.13: C_T C-scan of the area containing the fatigue spots, obtained by scanning the pipe shown in Figure 5.12. The size of the area scanned here is approximately 150 mm × 100 mm.

to that sample already having identifiable cracks, the presence of which had been reported by Trueflaw.

Again, it appears that an increase in fatigue cycles results in an increase in the magnitude of the ΔC_T value. In terms of comparison with the previous results, the graph in Figure 5.8 predicts a ΔC_T value of approximately -0.3% and -0.4% for UF values of 0.24 and 0.80. It appears that there is a good match at the high UF value, but a poorer match for the low UF value. Here, it is worth re-iterating that even though the changes in speed are monotonic, past studies have shown that even very small changes in the chemistry of the steel result in greatly different ΔC plots. Trueflaw does not disclose any information about the chemistry of the steel. Therefore, it is suggested that the absolute ΔC_T values are so sensitive to even small changes in the concentration of the different elements in steel, that a comparison between the plate and pipe results is not potentially meaningful, and that these discrepancies could be attributed to potential changes in the steel's chemistry.

5.3.3 Potential extension to pipes with larger curvatures

In the previous subsection, the ability to obtain a C_T C-scan of a pipe with the aid of an indexing head and a flat EMAT was presented and discussed. A flat EMAT was used in the particular pipe geometry, since it was previously established that the accuracy of the shear wave measurements was not compromised to the point where it introduced an unacceptable uncertainty in the measurements. However, it was observed that the maximum variation in the C_T measurements from their mean value increased from 0.012% to 0.029%, implying that if it is desirable to obtain C_T C-scans on a pipe with smaller inner and outer diameters, and hence larger curvature, there is a possibility that a flat EMAT will not be able to produce results which are of acceptable precision.

To mitigate this, a prototype of an EMAT whose bottom surface was curved to match the curvature of the particular pipe in this study was constructed - this was achieved by using additive manufacturing techniques. As shown in Figure 5.14 all the surfaces of the EMAT were manufactured in the usual way, apart from the bottom surface which was designed to fit the curvature of the pipe sample.

An example of the signal obtained using this EMAT prototype is shown in Figure 5.15. The signal has a similar signal-to-noise ratio as the signal in Figure 5.3, and the peaks are distinguishable for the purposes of speed

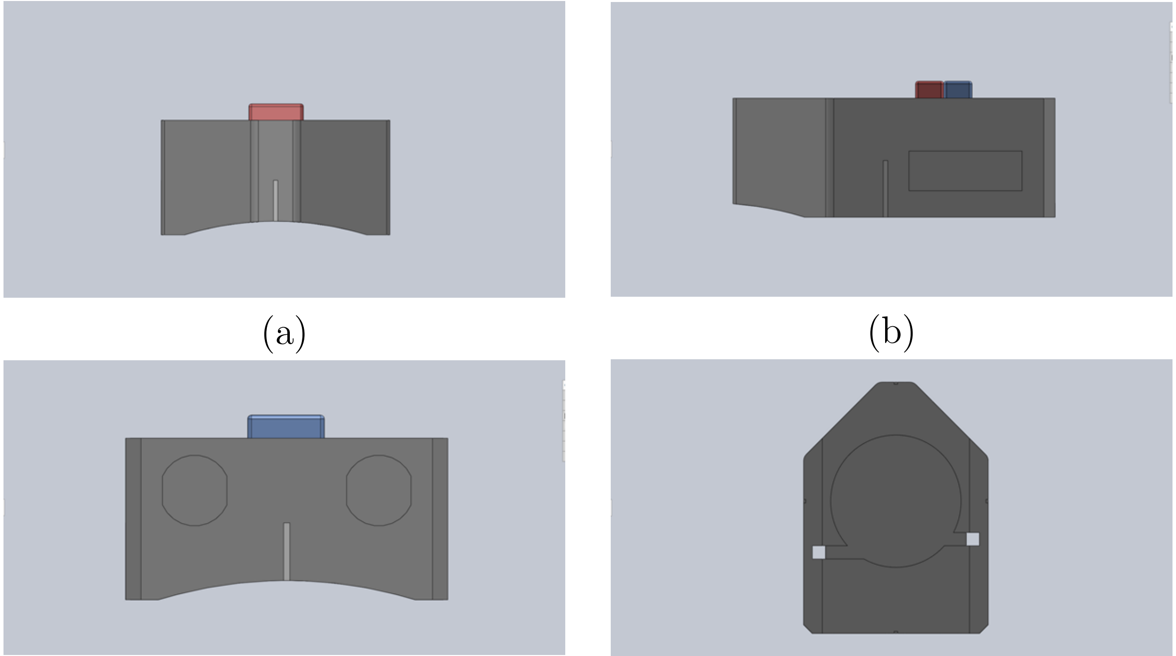

(a) (b)

(c) (d)

Figure 5.14: Computer-Aided Design (CAD) schematic of the curved surface EMAT prototype. The schematic was created using SolidWorks (Vélizy-Villacoublay, France). Subfigures (a)-(d) show the front, side, back and bottom views of the EMAT respectively.

measurements. The variation in the amplitude is potentially the result of a focusing effect, caused by the curved nature of the pipe surface.

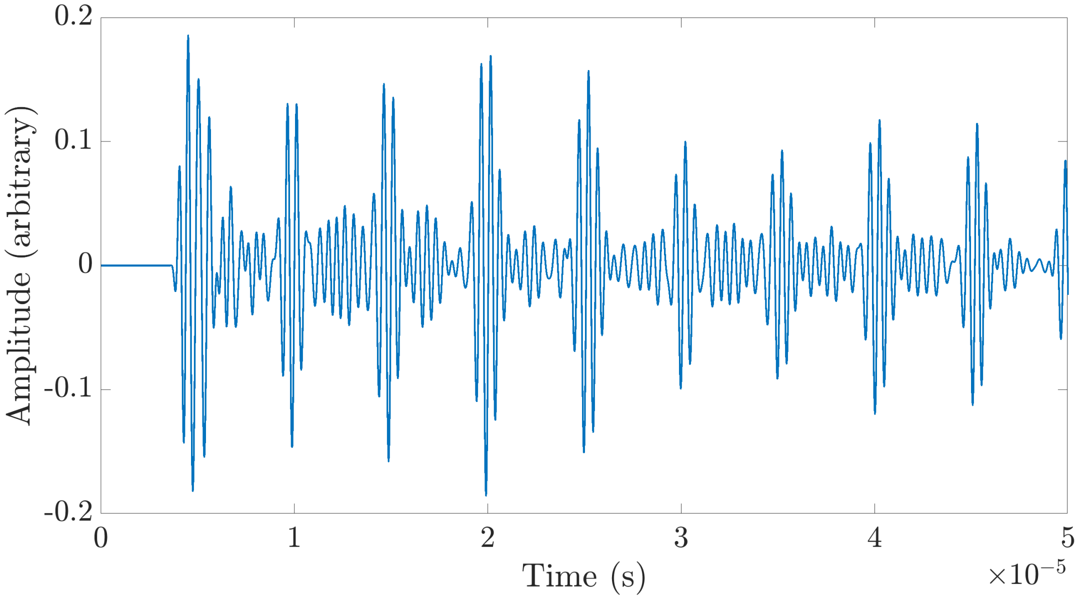

Figure 5.15: Example of the signal obtained from the curved EMAT prototype, when placed on the pipe sample shown in Figure 5.12.

To compare the performance of this EMAT with the flat version on the curved surface of the pipe, the same accuracy test as before was completed, in which 100 C_T measurements were taken from a single location on the pipe. The variation of the shear wave speed using the curved EMAT is shown in Figure 5.16.

In Figure 5.16, the maximum variation of the speed from the mean C_T value is 0.027%, which not only meant that this EMAT is suitable for fatigue state assessment measurements, but is already a small improvement compared with the accuracy of the flat EMAT, on this particular pipe geometry.

One additional test was completed to compare the performance of the curved prototype to the flat EMAT. A healthy area on the pipe was selected, and a B-scan was performed from that point to the end of the pipe. This line

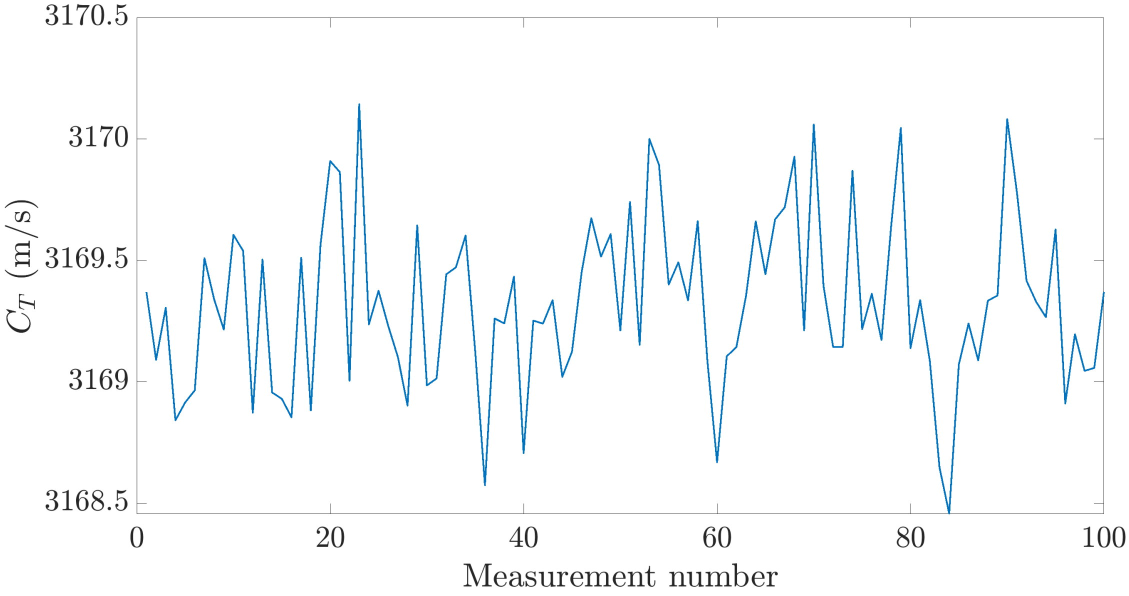

Figure 5.16: Variation of C_T on a fixed point on a steel pipe. The measurements were taken using a 2.25 MHz EMAT prototype, with a curved surface.

scan was repeated 5 times for each of the flat and curved EMATs, and the resulting speed values were averaged for each point of measurement along the B-scan. A comparison of the variation of the shear wave speed across this arbitrary line is shown in Figure 5.17.

It appears that both EMATs yield similar results - initially there is an increase in shear wave speed which is followed by a sharp drop. After this area of fluctuation, C_T remains approximately constant towards the end of the scan. The mean difference between the curved and flat EMAT results is 1.32 m/s, which is less than 0.05% of the mean C_T along this particular line. It is worth re-iterating that this B-scan was completed along a healthy line, and any C_T variation observed in Figure 5.17 is a result of thickness fluctuations and not fatigue.

Therefore, this curved EMAT prototype is able to replicate the results of

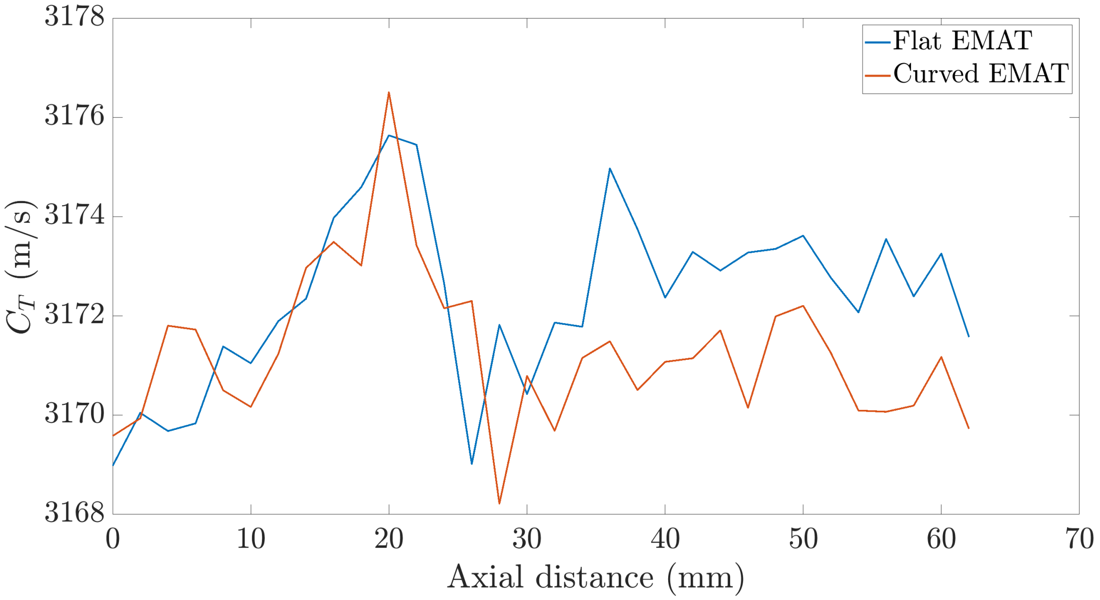

Figure 5.17: Comparison of the variation of C_T along a healthy axial line of the pipe specimen, between the flat and curved EMATs.

the flat EMAT, with an error smaller than 0.05%, and also exhibit a small increase in accuracy. There is definitely scope for improvement, if in the future it is desirable to inspect pipes for which the flat EMAT can not be used reliably. The most important change would be to use a flexible PCB coil instead of manually winding the main coil of the EMAT, to avoid coil overlap and potential fluctuations between the distance of each layer of the coil. Additionally, the positioning and strength of each permanent magnet of the EMAT is important in achieving the best signal to noise ratio. In terms of pipes with larger dimensions, flat EMATs can be used reliably as it was demonstrated that the loss in accuracy is far smaller than the expected changes in speed that are to be measured.

5.4 Thickness considerations

The fatigue state assessment presented in this chapter involves the use of through-thickness measurements, and therefore accurate knowledge of the thickness of a component is crucial in calculating the ΔC_L and ΔC_T values. It is however possible that for real components their thickness is not constant and varies randomly.

In these cases, the method presented here requires an additional step to be implemented. It becomes necessary for reference time-of-flight measurements to be taken prior to the component beginning its service life. Such measurements should be taken at arbitrary areas for components where fatigue is expected to be uniform, and at susceptible areas in cases where fatigue is expected to be concentrated at specific regions. Equations (3.20) and (5.4) can be easily converted to their equivalent time-of-flight form:

$$\Delta C_L = \frac{C_{L_f} - C_{L_h}}{C_{L_h}} = \frac{t_{L_h} - t_{L_f}}{t_{L_f}}, \tag{5.8}$$

$$\Delta C_T = \frac{C_{T_f} - C_{T_h}}{C_{T_h}} = \frac{t_{T_h} - t_{T_f}}{t_{T_f}}, \tag{5.9}$$

where t_{L_h} and t_{L_f} are the healthy and fatigued longitudinal wave time of flights, and similarly for t_{T_h} and t_{T_f} for shear wave time of flights. In all measurements in this thesis a constant healthy speed for the ΔC_L and ΔC_T measurements (and thus constant healthy time-of-flight values) was assumed for each component. However, when a reference time-of-flight map is available, each point on a time-of-flight map obtained after a component has started its service life should be compared against its respective point in the reference rather than an average. Such a comparison not only provides more accurate C-scans, but also solves the issue of the unknown variation in thickness. This does make an assumption that the thickness will not change throughout the component's life, however, the typical damage mechanisms for applications where fatigue is important do not include ones which cause wall loss, such as corrosion or erosion, for the current context of interest for nuclear power plant components

Demonstrating the effectiveness of this additional step for components of unknown thickness variation would require the generation of such a map prior to purposely fatiguing the sample for a few thousand thermal cycles. Due to time restrictions this was difficult to achieve in the timescales of a doctoral project. Therefore, a simple numerical verification is presented below.

Let us assume, without loss of generality, that in Figure 5.18, t_{T_h} was obtained for a flat plate, with a thickness of 10 mm and $C_T = 3000$ m/s. This map was created by visualising a matrix containing the suitable t_{T_h} values in Matlab. As shown in Figure 5.18, the map contains a low t_{T_h} square in its middle, which can be thought of as an area of reduced thickness. The t_{T_h} values in this square were defined to be 10% higher than the expected t_{T_h} value, which is equivalent to an 11.11% increase in C_T as per the definition of ΔC_T.

Let us also assume that the same area has been subjected to fatigue damage, causing the shear wave speed to reduce by 0.3%. This is equivalent to multiplying all the values in the low t_T area in Figure 5.18 by 0.997.

Now, for converting the t_{T_h} map in Figure 5.18 into a ΔC_T map - if the reference scan had not been obtained, one would assume $t_{T_h} = 3.33$ μs for the entirety of the plate, which would yield the ΔC_T the C-scan shown Figure 5.19.

As shown in Figure 5.19, an area of altered ΔC_T is present - however, the reduction in thickness has completely diminished the effect of the fatigue. This is expected, as the reduced t_{T_h} region would increase C_T by a factor of 1.11, while the fatigue would reduce it merely by 0.997. As a result, the

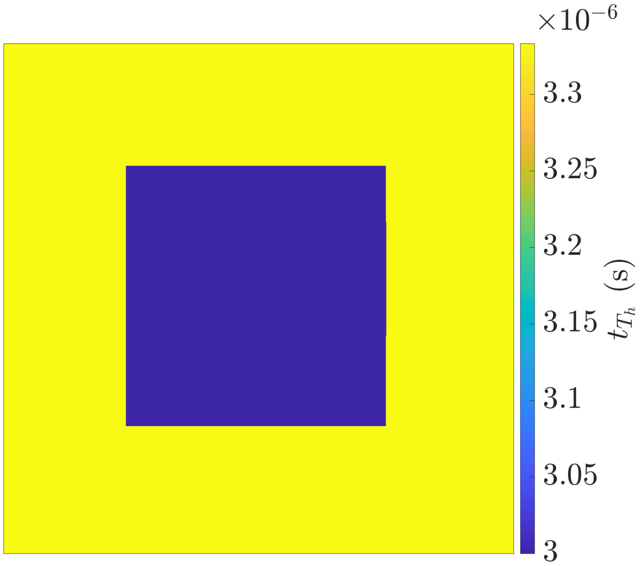

Figure 5.18: t_{T_h} map of a flat plate, containing an area with increased thickness and hence reduced t_{T_h} values.

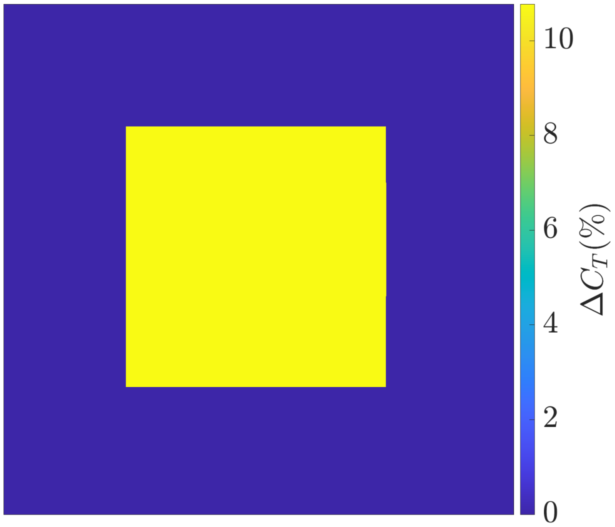

Figure 5.19: ΔC_T map of a flat plate, containing an area with increased thickness, obtained by assuming $t_{T_h} = 3.33\mu$s

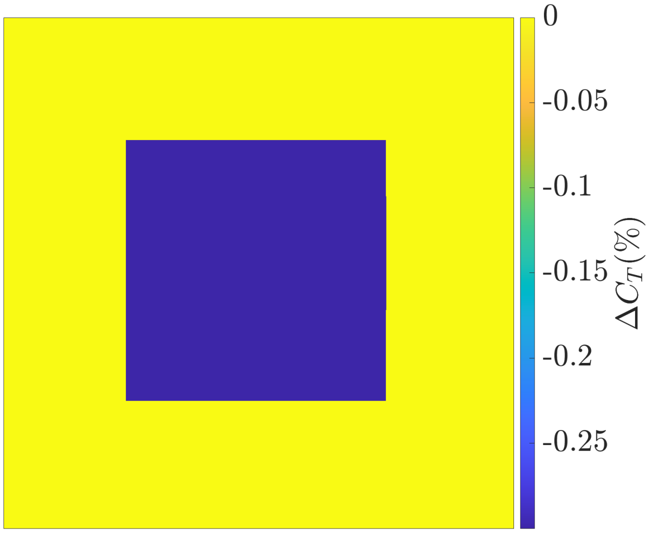

Figure 5.20: ΔC_T map of a flat plate, containing an area with increased thickness, obtained by using Figure 5.18 as a reference scan for the plate

total change in speed would be equal to a factor of 1.1078 (equivalent to 10.78%).

However, if each point in the C-scan is compared against its respective one in Figure 5.18, the C-scan in Figure 5.20 is obtained, which indeed reveals the correct ΔC_T value.

Chapter 6

Attenuation of Rayleigh waves due to surface roughness

The work in this chapter has been reported in a journal publication [98].

6.1 Introduction

When using surface waves to assess the fatigue state of engineering components, it is possible that the wave might be attenuated by other reasons, such as surface roughness, which could lead to erroneous UF predictions. Surface roughness may be inherent to the surface, as a result of its manufacturing technique, and can also gradually be amplified due to the operating conditions of a component. As a result, it is necessary to understand the effects of surface roughness on the attenuation of Rayleigh waves, to separate that effect from attenuation due to fatigue.

All real surfaces unavoidably possess a degree of roughness [129]. The attenuation of Rayleigh waves due to the presence of this surface roughness has been well studied analytically, however, it has proven difficult to experimentally validate the existing theory over a wide range of roughness parameters. This is either because the regions which fulfil the required mathematical assumptions are difficult to reproduce in the physical world, or because the attenuation values predicted by the theory would render the waves undetectable in an experimental investigation.

Early experimental work on the attenuation of Rayleigh waves includes the study by Salzmann et. al [130], where the authors used lasers to measure the effects of frequency and temperature on the attenuation of Rayleigh waves when propagating over quartz crystals. This was followed by the study from Maris [131], where the author considered crystallographic surfaces of arbitrarily-oriented crystals, and derived analytical expressions for the attenuation of Rayleigh waves travelling over them, with temperature and viscosity effects also being considered. Further experimental studies on quartz attenuation include the work of Daniel & de Klerk [132] and Gibson & Meijer [133], while the author in [134] measured the attenuation of Rayleigh waves in a superconducting Pb film. However, all of these studies focused on specific attenuation phenomena and did not take into account the explicit effect of roughness, which would cause attenuation even at perfect, lossless materials.

Some of the first analytical expressions for the attenuation of Rayleigh waves from rough surfaces come from Urazakov & Fal'kovskii [135]. The authors utilised the solutions to the Rayleigh equation [136] and obtained expressions for the attenuation by extending the stress free boundary condition from a flat to a rough surface. Maradudin & Mills used two statistical parameters, the root-mean-squared (RMS) height, δ, and the correlation length, Λ to characterise rough surfaces, and utilised a Green's function approach in solving the relevant Rayleigh equations to obtain expressions for the attenuation [137]. Both studies were completed in three dimensions, and considered low-roughness ($\delta/\Lambda < 0.3$), and both predicted that the attenuation is proportional to the fifth power of the frequency in the low frequency limit. Additionally, Maradudin & Mills demonstrated that the attenuation is proportional to δ^2 in the same limit. Subsequently to these studies, Eguiluz & Maradudin [138] published updated analytical expressions, which took into account the attenuation caused by the scattering of Rayleigh waves into bulk waves, which both confirmed the f^5 proportionality in the low frequency limit, but also derived a proportionality of the attenuation to δ^2/Λ^2. At the same time, studies were also completed for other types of surface waves [139, 140].

More recently, Kosachev & Gandurin [141] studied the attenuation caused by the rough surface of a hexagonal, anisotropic crystal at a generalised crystal orientation, to expand on the isotropic case studied in [138] - with their generalised, anisotropic results reducing to the same f^5 relationship when the anisotropic terms are ignored. Finally, Chukov used the Rayleigh-Born approximation in the low frequency limit as an alternative to the small perturbation method in [138], arriving at the same power relationships, while also deriving expressions for the relationship between the attenuation coefficient and δ, Λ and f, in two-dimensions.

Here it is worth observing that the theory is restricted to specific δ, Λ and λ_R combinations, and particularly those belonging to the very low frequency Rayleigh regime ($\lambda_R \gg \Lambda$). Additionally, there is little experimental validation of the theory. Therefore, the above-mentioned considerations motivate two research problems which this study attempted solving - firstly, to create an FE model to validate the existing analytical expressions in the Rayleigh region, as an accurate alternative to experimental measurements, and secondly, to extend the results, by FE modelling, to other more practically useful scattering regimes and statistical parameter combinations. Finally, the aim was to create a unified approach in studying the phenomenon of rough surface scattering, where the results can be obtained using the same FE modelling philosophy, removing the need to use different mathematical tools and assumptions in different scattering regimes and roughness severity scenarios.

To obtain a statistically meaningful attenuation result from FE modelling it is necessary to average over a large number of attenuation values obtained from statistically identical surfaces for each δ, Λ and f combination. Accurate modelling also requires a model large enough to accommodate a suitable scattering distance. The theory presented above has been derived in three-dimensions, however, simulating multiple combinations of δ, Λ and f would incur significant computational burden. Therefore, this study was completed in two-dimensions, with the results also providing useful implications for the 3D theory. This is because the mathematical approach and methods used for the derivation of the 3D theory are identical for 2D - namely, Huang & Maradudin [142] used the same small perturbation approach to conclude that in the low frequency limit, the attenuation is proportional to $\delta^2 \Lambda f^4$. The same relationship was also derived by Chukov, under the Rayleigh-Born approximation [143].

Following the validation of the theory in the Rayleigh regime, this study looked at validating the theory in the two other scattering regimes, the stochastic ($\lambda_R < \Lambda$) and geometric ($\lambda_R \ll \Lambda$). To the author's knowledge, the theory about the attenuation of Rayleigh waves due to surface roughness is very limited in this regime. Therefore, a useful analogous study was used to aid the investigations. The authors in Van Pamel et al. [144] studied the attenuation behaviour of an elastic wave, where the scattering occurred due to the inhomogeneous nature of the medium i.e. the waves would attenuate due to the presence of grain boundaries inside the model. This is analogous to the study here, as the wave's motion is still impeded by an obstacle whose statistical size determines the attenuation behaviour. The authors also compared this behaviour between 2D and 3D scattering. In the Rayleigh regime, the authors found a reduction of the power dependence of the attenuation from f^5 to f^4, which is consistent with [143] , [142], and [145]. In the stochastic regime however, there was no change in the power dependence between the attenuation coefficient and the statistical parameters of the grains, regardless of the number of dimensions. Therefore, for the stochastic regime in surface roughness scattering, it is suggested that the 3D power relationship derived by Kosachev et. al. [146] also holds true in two dimensions and the attenuation is expected to vary with $\delta^2\Lambda^{-1}f^2$. This power relationship is also inferred in [142] and is discussed in more detail below. Finally, for the geometric regime, it is already known that the attenuation is frequency independent [144,147], however, it remains relatively unexplored in the literature.

6.2 Theory

Here, the theory relating to this study is presented. The theory is split into two distinct categories. In Section 6.2.1 the theory related to the characterisation and generation of random, statistically rough surfaces is presented, and in Section 6.2.2 the equations relating both to the absolute and asymptotic attenuation expressions are presented and discussed.

6.2.1 Rough surfaces

An important parameter to characterise a rough surface is its δ value. This is a measure of the height variation of the rough surface, relative to a flat surface. Let x be the direction along which the surface lies, and z be the direction perpendicular to this. Also, let h be the shortest distance between any point on the rough surface and the reference surface at $z = 0$. In this case, the profile of the rough surface can be described by

$$z = h(x). \tag{6.1}$$

Here, rough surfaces with a mean height variation of zero were used, i.e. $< h >= 0$, where the angle brackets denote the ensemble average value of the quantity in their argument. For surfaces with $< h >= 0$, the RMS height can be calculated from:

$$\delta = \sqrt{< h^2 >}. \tag{6.2}$$

For characterising the lateral spacing between the peaks and valleys of a rough surface, the correlation length, Λ was used, which is formally defined as the distance over which the correlation function drops to 1/e from its initial value. The correlation function, $C(\mathrm{R})$, for two points spaced by R is defined as:

$$C(\mathrm{R}) = \frac{< h(x)h(x+\mathrm{R}) >}{\delta^2}. \tag{6.3}$$

Here, a Gaussian $C(R)$ was chosen:

$$C(\mathrm{R}) = \exp\left(-\frac{\mathrm{R}^2}{\Lambda^2}\right). \tag{6.4}$$

A Gaussian $C(\mathrm{R})$ was not only chosen because it has been widely studied and is well understood [129, 148, 149], but also because it has been shown that such roughness can occur naturally [150, 151]. This means that the choice of Gaussian roughness does not restrict the analysis to an idealised domain.

As described in Section 6.1, multiple simulations at each set of statistical parameter combinations of interest have to be conducted to obtain a meaningful attenuation value. To achieve this it was necessary to generate multiple random rough surfaces and the moving average method presented in [129] and [148] was utilised. Under this approach, the random rough surface was generated as follows: first a number of pseudo-random numbers, with Gaussian distribution was generated using Matlab, and the moving average approach in [129, 148] combined with Equations (6.2) and (6.4) transformed these into correlated numbers, corresponding to distinct $h(x)$ points to create a rough surface with the desired δ and Λ.

Figure 6.1 shows the effect of varying δ in random rough surfaces, which have been derived with the method described above. Figure 6.2 shows the effect of varying Λ in random rough surfaces. In all examples, the respective histogram is shown, showing the distribution of the discrete z values of each rough surface

As shown in Figure 6.1, doubling the δ value while keeping Λ constant has the effect of generating higher peaks and lower valleys in the rough surface,

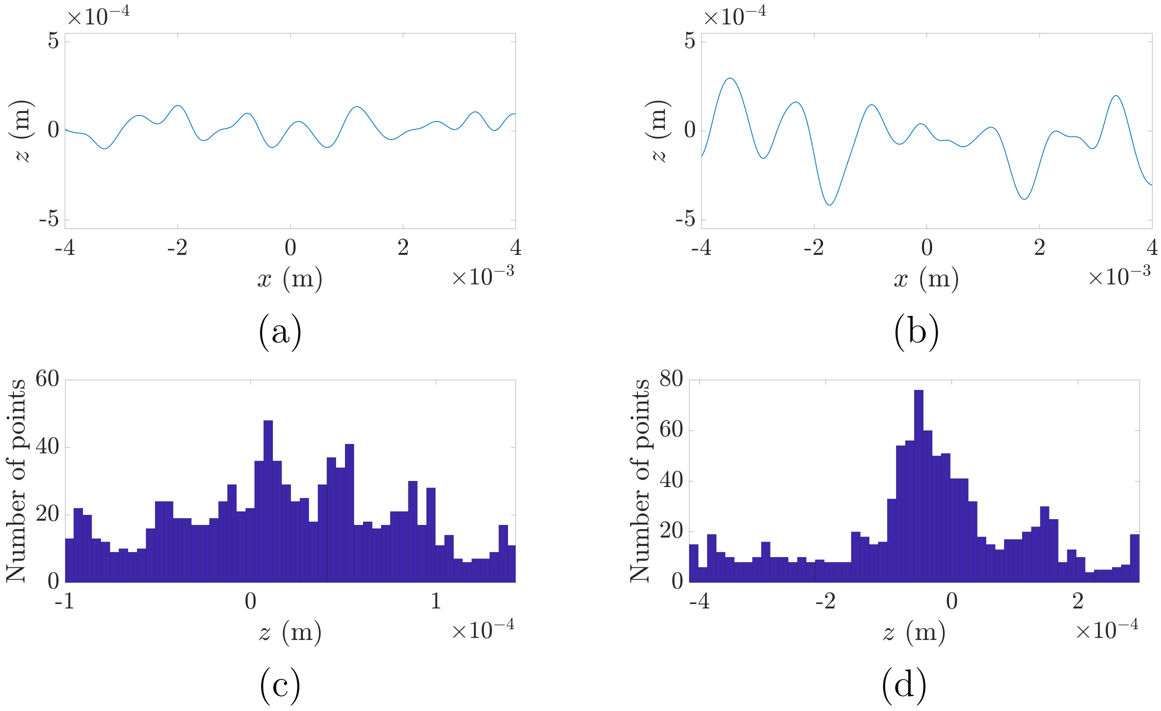

(a)

(b)

(c)

(d)

Figure 6.1: Comparison between the height profiles and the height distributions of two random rough surfaces with the same Λ (400 μm) and different δ. In (a) and (b), the height profile of surfaces with $\delta = 100$ μm and $\delta = 200$ μm is shown respectively. The histograms in (c) and (d) show the height distribution of the points comprising the rough surfaces in (a) and (b) respectively.

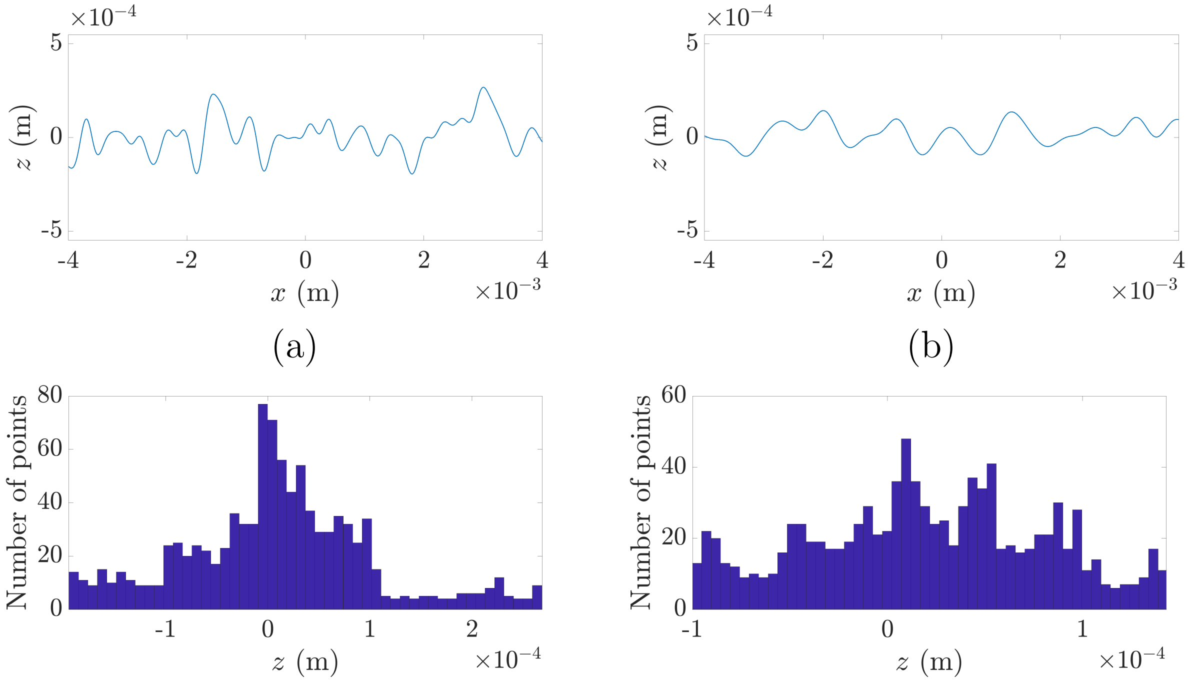

(a) (b)

(c) (d)

Figure 6.2: Comparison between the height profiles and the height distributions of two random rough surfaces with the same δ (100 μm) and different Λ. In (a) and (b), the height profile of surfaces with $\Lambda = 200$ μm and $\Lambda = 400$ μm is shown respectively. The histograms in (c) and (d) show the height distribution of the points comprising the rough surfaces in (a) and (b) respectively.

while keeping the spacing between the approximately constant. In Figure 6.2, where δ is kept constant at 200 μm and Λ is halved, it can be seen that this has the effect of keeping the height variation approximately the same, but the spacing between each peak and valley is reduced. Finally, with respect to all the histograms in Figures 6.1 and 6.2, it can be seen that the distribution of the height points is approximately Gaussian, with a mean of zero, which is consistent with the choice of $C(R)$ and reference surface height.

6.2.2 Absolute attenuation coefficient values

Starting from the theory in [138, 142], the usual dispersion relationship, for a Rayleigh wave propagating on a flat surface of an isotropic material is

$$\omega = C_R q, \tag{6.5}$$

where q is the wavenumber. In this chapter the wavenumber is denoted by q instead of the usual k, for uniformity with the derivations and results in [138, 142].

When a Rayleigh wave travels over a rough surface, Equation (6.5) becomes

$$\omega = C_R q + \Delta\omega, \tag{6.6}$$

as per the perturbation method used to study this phenomenon in [138]. In the above equation, $\Delta\omega$ is a complex frequency perturbation, whose imaginary part gives the attenuation exhibited by the wave, due to the presence of the rough surface. Therefore, $\Delta\omega$ can be written as

$$\Delta\omega = \nu_1 + j\nu_2, \tag{6.7}$$

where ν_1 and ν_2 are the real and imaginary parts of $\Delta\omega$ respectively. If the attenuation length l_α is defined as the distance over which the Rayleigh wave energy drops to 1/e from its initial value, it can be shown that

$$l_\alpha = \frac{C_R}{2\nu_2}. \tag{6.8}$$

The authors in [138] then demonstrate that ν_2 can be written as

$$\frac{\nu_2}{\omega} = \left(\frac{\delta^2}{\Lambda^2}\right)\omega_2. \tag{6.9}$$

In Equation 6.9, ω_2 is not another frequency term, but rather a complicated function encapsulating material and Rayleigh wave properties, as well as the statistical information of the surface.

Finally, by combining Equations 6.8 and 6.9, the attenuation length can be found from:

$$l_\alpha^{-1} = 2\left(\frac{\delta^2}{\Lambda^2}\right)q\omega_2. \tag{6.10}$$

In our study, the attenuation coefficient, α was used as a measure of attenuation instead of the attenuation length; α is defined as the length over which a wave's amplitude drops to 1/e from its initial value. This choice was made because both in an FE and in an experimental study it is more straightforward to measure a wave's amplitude rather than its energy. It was then necessary to convert between the two attenuation measures - let us assume that there are two points in space, A and B, spaced l_α apart:

Let also the energy of the wave at points A and B be E_A and E_B respectively. By the definition of the attenuation length,

$$E_A = \mathrm{e}E_B. \tag{6.11}$$

It is also known that the energy of a wave is proportional to the square of its amplitude, A [15]. Therefore,

$$E_A = cA_A^2, \tag{6.12}$$

$$E_B = cA_B^2, \tag{6.13}$$

where c is a constant of proportionality.

Dividing (6.12) by (6.13) yields :

$$\frac{E_A}{E_B} = \frac{A_A^2}{A_B^2}. \tag{6.14}$$

Substituting (6.11) in (6.14) yields

$$\frac{A_A^2}{A_B^2} = \mathrm{e}. \tag{6.15}$$

For the same distance, the attenuation coefficient, α, is

$$\alpha = \frac{1}{l_\alpha} \ln\left(\frac{A_A}{A_B}\right). \tag{6.16}$$

Multiplying each side by 2 gives

$$2\alpha = \frac{1}{l_\alpha} \ln\left(\frac{A_A^2}{A_B^2}\right). \tag{6.17}$$

Substituting (6.15) yields

$$2\alpha = \frac{1}{l_\alpha} \ln(\mathrm{e}). \tag{6.18}$$

Therefore, for a known attenuation length l, the corresponding attenuation coefficient is:

$$\alpha = \frac{1}{2l_\alpha}. \tag{6.19}$$

Finally, Equations (6.10) and (6.19) can be combined, to arrive at the theoretical expression giving the attenuation coefficient of a Rayleigh wave propagating over a statistically rough surface:

$$\alpha = \left(\frac{\delta^2}{\Lambda^2}\right) q\omega_2. \tag{6.20}$$

Equation (6.20) is the analytical relationship which this study attempted to verify.

6.2.3 Asymptotic power relationships

Apart from the analytical α relationship in Equation (6.20), the verification of the asymptotic power relationships which exist between α and δ, Λ and f in the three scattering regimes were also investigated. To achieve this, it was necessary to look into the ω_2 term of Equation (6.20) in more detail.

As discussed in the previous subsection, the ω_2 term is a function which is unique to every material, Rayleigh wave, and statistical roughness scenario. For the 3D case, the authors in [138] have shown that in the Rayleigh regime, $\omega_2 \propto (\omega\Lambda)^4$, and hence, $\alpha_{3\mathrm{D}_R} \propto f^5\delta^2\Lambda^2$, where the subscripts 3D and R denote the presence of three-dimensional roughness, and the Rayleigh region respectively. Similarly, the authors in [142,152] demonstrated that in two dimensions, in the Rayleigh regime, $\omega_2 \propto (\omega\Lambda)^3$ and thus that $\alpha_{2\mathrm{D}_R} \propto f^4\delta\Lambda^2$, where the subscripts 2D and R denote the presence of two-dimensional roughness. This is also evident in Figure 6.3, where the ω_2 function is plotted against $q\Lambda$, for $q\Lambda$ values less than 1, which by definition correspond to the Rayleigh regime.

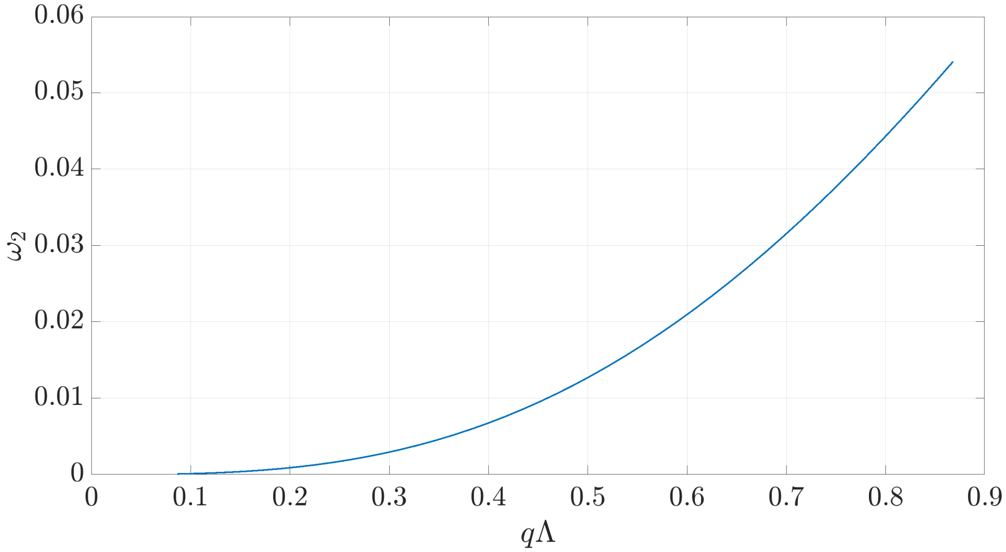

Figure 6.3: ω_2 versus $q\Lambda$, for $q\Lambda$ values corresponding to the Rayleigh regime. The cubic relationship between ω_2 and $q\Lambda$ can be seen here.

For values of $q\Lambda$ greater than 1, corresponding to the stochastic regime, the analogy between this study and the study in [144] was used to predict the power relationships between α and δ, Λ and f. In this study, the authors investigated the phenomenon of scattering from the grains of an inhomogenous material, and demonstrated that the power relationship between α and the variables of interest is independent of the number of dimensions. The analogy in their study to the one presented here lies in both the fact that the stochastic regime was defined again as the region where $q\Lambda > 1$ and also that the characteristic size of the "obstacle" was measured by its correlation length. It can be therefore suggested that this independence holds true in this study as well i.e. that the power relationships between α and δ, Λ and f are the same in two and three dimensions. A 3D analysis has been completed by [146], and based on extending their findings from 3D to 2D, it is expected that $\alpha_{2\mathrm{D}_S} \propto \delta^2 \Lambda f^2$. This power relationship can also be inferred by the observations regarding the behaviour of the ω_2 function in the stochastic regime. Figure 6.4 shows how ω_2 varies with $q\Lambda$ in this region. It is clear

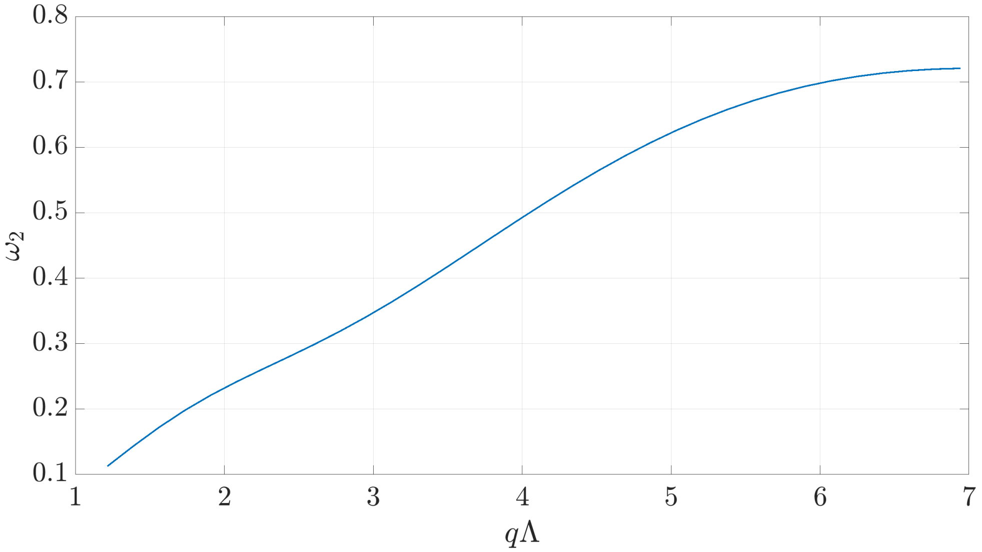

Figure 6.4: ω_2 versus $q\Lambda$, for $q\Lambda$ values corresponding to the stochastic regime. The linear relationship between ω_2 and $q\Lambda$ can be seen here.

that the variation is approximately linear, thus $\omega_2 \propto q\Lambda$, and, by substituting this in Equation (6.20), the same result of $\alpha_{2\mathrm{D}_S} \propto \delta^2 \Lambda f^2$ is achieved. Here it is also worth noting that the absolute values of the ω_2 function, which were numerically calculated using the equations in [142] agree well with the results in the same article.

The geometric regime is relatively unexplored in terms of rough surface scattering - to the author's knowledge there do not exist analytical expressions for the power relationships between the attenuation coefficients and the rough surface parameters for $q\Lambda \gg 1$. Therefore a different approach to the analysis presented here was used, and powers were treated as unknowns to be found and verified in the FE study. For this regime, dimensional analysis was used, utilising the principle of similitude, which stipulates that different phenomena can be described by the same dimensionless variables if they can be reduced to analogous forms [136]. Namely, for attenuation and scattering phenomena, the same dimensionless analysis can be implemented if the statistical parameters of the scatterer (δ and Λ) and the energy loss terms (α) are normalised by the wavelength of the scattered wave.

For the specific case of this study, this means that the general form of such a power relationship is

$$\alpha_n \propto \delta_n^{m_\delta} \Lambda_n^{m_\Lambda}, \tag{6.21}$$

where $\alpha_n = \alpha\lambda_R$ (normalised attenuation coefficient), $\delta_n = \delta/\lambda_R$ (normalised RMS height), and $\Lambda_n = \Lambda/\lambda_R$ (normalised correlation length). Additionally, here m_{k} denotes the power to which the variable k is raised.

Assuming non-dispersive Rayleigh waves, the wavelength is inversely proportional to the frequency, and therefore:

$$\delta_n^{m_\delta} \propto f^{m_\delta}, \tag{6.22}$$

$$\Lambda_n^{m_\Lambda} \propto f^{m_\Lambda} \tag{6.23}$$

and

$$\alpha_n \propto f^{-1}. \tag{6.24}$$

Combining Equations (6.22),(6.23) and (6.24) with Equation 6.21, yields the following generalised expression:

$$\alpha \propto \delta^{m_\delta} \Lambda^{m_\Lambda} f^{m_f}, \tag{6.25}$$

where

$$m_f = m_\delta + m_\Lambda + 1. \tag{6.26}$$

Here, no assumptions about the rough surface, the Rayleigh wave or the scattering regime were made, hence Equation 6.26 holds true regardless of the number of dimensions or the scattering regime. This can also be confirmed by the fact that the power relationships for both $\alpha_{2\mathrm{D}_R}$ and $\alpha_{2\mathrm{D}_S}$ obey

Table 6.1: Expected asymptotic power relationships, between the attenuation coefficient and the RMS height, correlation length and frequency. In this table, q is the wavenumber, δ is the RMS height, Λ is the correlation length and f is the frequency.

Regime	Rayleigh	Stochastic	Geometric
Limits	$q\delta < q\Lambda < 1$	$q\delta < 1 < q\Lambda$	$1 < q\delta \ll q\Lambda$
$\alpha(\delta, \Lambda, f)$	$\delta^2 \Lambda f^4$	$\delta^2 \Lambda^{-1} f^2$	$\delta^{m_{\delta_G}} \Lambda^{-1-m_{\delta_G}}$
$\beta(\delta_n, \Lambda_n)$	$\delta_n \Lambda_n^2$	δ_n	$\delta_n^{m_{\delta_G}-1} \Lambda_n^{-m_{\delta_G}}$

Equation (6.26). Additionally, for the geometric regime it is already known that α is independent of f ($m_f = 0$) [147]. If the other powers are expressed in terms of m_{δ_G}, equation (6.26) implies that $m_{\delta_G} = -1 - m_{\Lambda_G}$, and $\alpha_{2D_G} \propto \delta^{m_{\delta_G}} \Lambda^{-1-m_{\delta_G}}$, where the subscript G denotes the geometric regime. The powers here were treated as unknowns to be found by the FE analysis. Here it is finally worth noting that for all derivations $\delta < \Lambda$ was assumed which follows numerous past rough surface scattering studies [150, 153–155].

A summary of all the power relationships is shown in Table 6.1. In Table 6.1 the dimensionless variable β is also introduced, where $\beta = \alpha_n \Lambda / \delta$. This variable was also defined to later allow for plotting all of the results against a single variable, in the stochastic and geometric regimes. This would have not been possible simply using α, as α is always a function of at least two other variables. Assuming that m_{δ_G} is zero, this would reduce the dependence of β simply to δ_n, allowing for the creation of a single plot with all numerical data relating to the stochastic and geometric regimes.

6.3 FE modelling

This section presents the method used to generate the FE models which were subsequently used in all numerical simulations in this study. As discussed before, one of the aims of this study was to use FE as a unified method to study rough surface scattering from numerous rough surface and frequency combinations, contrary to the various mathematical approaches needed to treat each of the scattering regimes - hence necessary steps to ensure that the results were achieved efficiently and had statistical meaning were taken. The aim was to minimise the size of the model, ensuring that the rough surface was inserted in a way that did not cause additional attenuation or was unrealistic. This process along with the method to calculate the attenuation coefficient, and an estimate of the computational resources required for this study, is presented below.

Even though rough surfaces can be statistically equivalent if they have the same δ and Λ values, each of them has a unique $h(x)$ profile. Therefore, it was necessary to average over multiple α values from multiple unique surfaces for each δ, Λ and f combination, to ensure that the result was statistically meaningful. To achieve this, Monte Carlo simulations were performed with 100 realisations per δ, Λ and f combinations using the high-fidelity GPU-based FE solver Pogo, and the visualisation software PogoPro [6]. For the material, the properties of Inconel 718 (Young's modulus, $E = 208.73$ GPa, Poisson's ratio, $\nu = 0.303$ and density, $\rho = 7800$ kg/m^3) were used. For a material with known material properties, the Rayleigh wave speed can be estimated from Equation (2.16). For the Inconel 718 material parameters used in the simulations, C_R was found to be approximately 2892 m/s.

A schematic of the FE domain is shown in Figure 6.5. As shown in Figure 6.5, the rough surface was inserted to form part of the lower portion of a

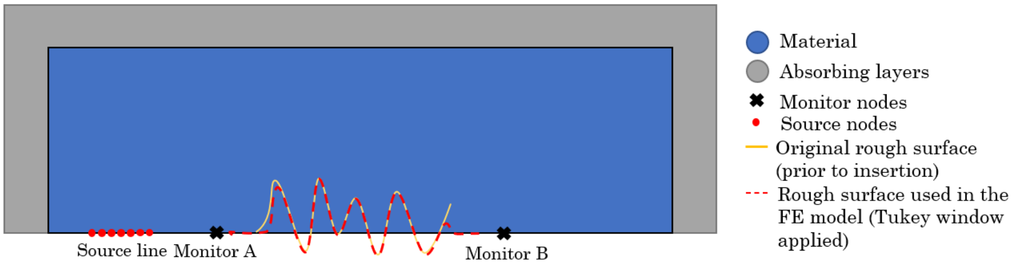

Figure 6.5: Schematic of the FE model. A Tukey window was applied to the original rough surface, which was generated using the method described in subsection 6.2.1 (in yellow), before it was inserted to form the lower boundary of the FE domain (in red). The scale of the rough surface is exaggerated for better visualisation.

rectangular, 2D FE domain. The length of the rough surface was selected to be at least equal to 50Λ, to ensure ergodic stability [129]. A Tukey window, $w(x)$ was applied to the rough surface prior to insertion - this has the effect of smoothing the boundary between the rough surface and the flat sides of the domain. As a result, the Tukey window serves two purposes - first to prevent a rough joint which would artificially increase the α value obtained from the model, and second, to eliminate any discontinuities between the edges of the rough surface and the domain. An equation for the $w(x)$ which was used is given below:

$$w(x) = \begin{cases} 0 & |x| \geq \frac{L_R}{2} \\ 1 & |x| \leq \frac{L_R}{2} - \frac{l_w}{2} \\ \frac{1}{2}\left[1 - \cos\left(2\pi \frac{|x| - \frac{L_R}{2}}{l_w}\right)\right] & \text{otherwise,} \end{cases} \tag{6.27}$$

where L_R is the length of the rough surface, and l_w is the tapering length (i.e. the length of the rough surface which will be affected by the window). For the simulations here, $l_w = \frac{L_R}{10}$ was used. The smoothing effect was achieved by multiplying $h(x)$ with $w(x)$.

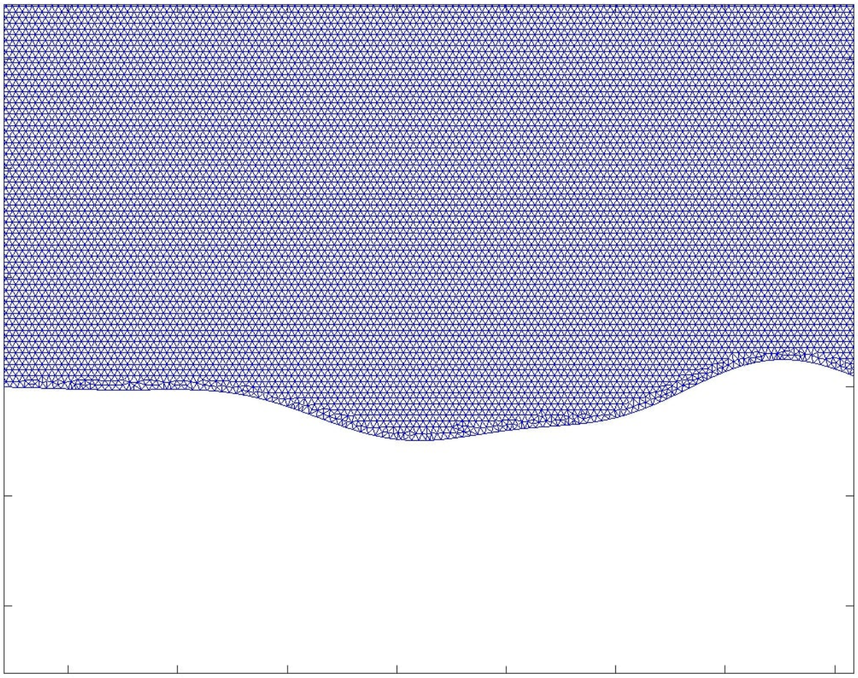

Figure 6.6: Detail of the FE domain's meshing, after the Tukey-windowed rough surface has been applied to its lower boundary.

For the meshing 2D triangular elements were used. The mesh size was set to approximately $\lambda_R/25$, with λ_R being calculated each time at the centre frequency. This level of mesh refinement is necessary to avoid numerical stability errors and errors in the C_R measurements [14], and also similar mesh refinement levels can be found in analogous studies [156]. An example of the meshing generated by Pogo is shown in Figure 6.6.

Two interesting features can be observed in Figure 6.6. Firstly, the smooth joining between the rough surface and the rest of the domain can be seen. Secondly, the mesh appears irregular near the rough surface and the boundary of the domain, but very quickly reverts to a normal form away from them, demonstrating Pogo's ability for effective meshing of irregular areas. Here it is worth acknowledging that meshing unavoidably truncates the fractal nature of a real rough surface [157]. Weierstrass functions, which exhibit self similarity have been used in past theoretical roughness studies [158].

However, it was expected that, since the fractal nature lies well below the wavelength, this truncation would not have a measurable effect on the results of this study [154, 159].

In terms of exciting the Rayleigh wave, a source line comprised of multiple source nodes was defined to the left of the rough surface as shown in Figure 6.5. The length of the source line was set to be equal to $3\lambda_R$, with λ_R being calculated again from the centre frequency. For measuring the amplitude of the Rayleigh wave, monitor nodes were defined just before and just after the rough surface. This study again required the excitation of Rayleigh waves with good signal-to-noise ratio and minimal excitation of other modes, both of which could interfere with the attenuation measurements. Therefore, the method described in detail in Chapter 2 was implemented for the excitation of Rayleigh waves in this study.

To obtain the α value from each realisation, the Rayleigh wave's z amplitude was recorded just before and just after the rough surface. The attenuation coefficient was then calculated from Equation (2.30), where in this case A_{x_1} and A_{x_2} were the z amplitudes of the Rayleigh wave just before and just after the rough surface respectively.

As explained above, for each δ, Λ and f combination the numerical average of 100 α values obtained from 100 unique surfaces was used, and hence an equal number of FE domains were generated and solved. One Nvidia GTX 1080Ti with 11 GB of memory was used, and each set of 100 domains took approximately 1.5 hours to solve. This level of efficiency allows multiple sets of simulations to be solved, to cover a wide range of roughness and frequency scenarios, providing more insight in the validation of the theoretical models. A study of similar depth, and with such a large range of statistical parameters would not have been possible in three dimensions due to computational expenses and limitations. However, the 2D study presented here provides useful and meaningful insight in the verification of the existing 3D theory, as the 2D [142] and 3D [138] theory have been derived under the same assumptions and using similar methods. Additionally, the 2D work here identifies the most important regimes where 3D investigations may be conducted, without the need to use computational time and resources in identifying those.

It is also worth noting that the same method described here was used to generate all the FE models required for this study, regardless of the scattering regime. This strengthens the universality of the findings here, as the need to study each regime study has been eliminated - something which is prominent in the theoretical studies.

An example of a Rayleigh wave field generated by implementing this method is shown in Figure 6.7. As shown in Figure 6.7, a clean Rayleigh wave has been generated. The minimal head waves which lie above the Rayleigh wave have a very small amplitude, and also lie away from the measuring locations, therefore they would not interfere with the attenuation measurements. The rough surface, to the right of the Rayleigh wave can also be seen.

6.4 Results & discussion

Here the results from the FE study are presented - subsection 6.4.1 shows a comparison between the analytical and FE α values, while subsection 6.4.2 presents the results relating to the power relationships between α and δ, Λ and f. Finally, subsection 6.4.3 shows a master plot, where the attenuation for simulations with multiple frequency and roughness combinations was plotted.

In terms of the roughness parameters used, the investigation started in the Rayleigh regime with δ values in the range of $10 - 25$ μm. These reflect roughness values which correspond to the roughness of metal parts made by

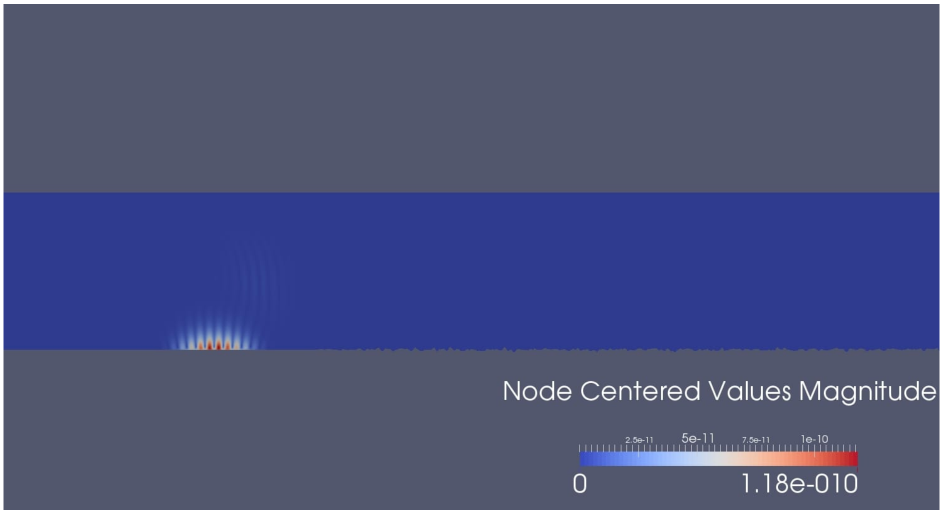

Figure 6.7: Example of a Rayleigh wave field, travelling in the positive x-direction created using the method described in this section. The colour scale in the figure represents the absolute magnitude of the displacement at each node. The Rayleigh wave's centre frequency is 6 MHz and the rough surface has δ=25 μm and Λ=50 μm. The QR code directs to an animation of this process.

additive manufacturing [160–162]. The correlation length was subsequently selected to fulfil the $\delta < \Lambda$ condition, as required by the limits of the Rayleigh regime defined in Table 6.1.

For obtaining the results, first it was necessary to establish that reliably obtaining the amplitude was possible, i.e. that the rough surface has not distorted the signal to the point where the peak of its Fast Fourier Transform (FFT) is no longer distinguishable. For the purpose of investigating this, it was assumed that the δ/Λ ratio can be thought of as an approximate roughness measure, where small δ/Λ values imply low roughness, and δ/Λ values approaching 1 imply high roughness. A comparison of both the time and frequency domain signals obtained from a low and high roughness case is shown in Figures 6.8 and 6.9 respectively.

As shown in Figure 6.8, both the time and FFT signals are of good quality. There appears to be a small frequency shift in the FFT of the signal after the rough surface in 6.8b, however, this is also an effect of the rough surface [138, 142]. In Figure 6.9, both time and FFT signals are visibly noisier - however, the peaks of the signals are clearly distinguishable, both in the time and frequency domain and hence Equation (6.20) was expected to yield accurate results. As a result, it was decided not to post-process the signals to remove any of the noise.

As explained in the previous chapter, the unique nature of the rough surfaces, due to their random generation, requires averaging of the α values each δ, Λ and f combination, to ensure that the results are statistically stable and meaningful. This number of averages was selected to be equal to 100 - therefore each of the points in the results figures is an ensemble average of 100 realisations with the statistical parameters and frequency corresponding to that point. This number of averages was selected as it lies within the 50-200 range which has been used by the researchers in past similar stud-

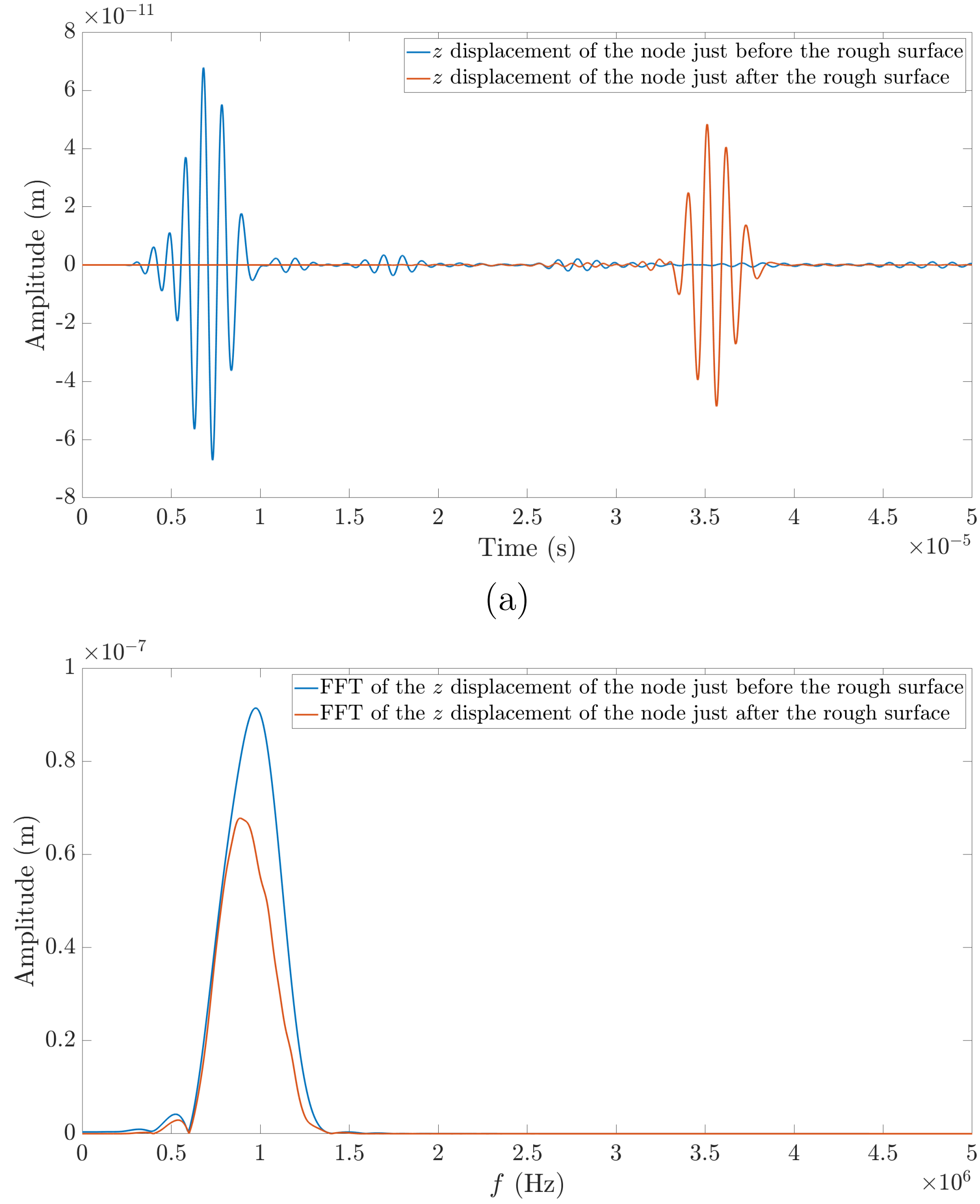

(a)

(b)

Figure 6.8: z displacement of a Rayleigh wave, just before and just after encountering a rough surface, where $\delta/\Lambda \approx 0.1$ for the rough surface (a), and corresponding FFTs (b).

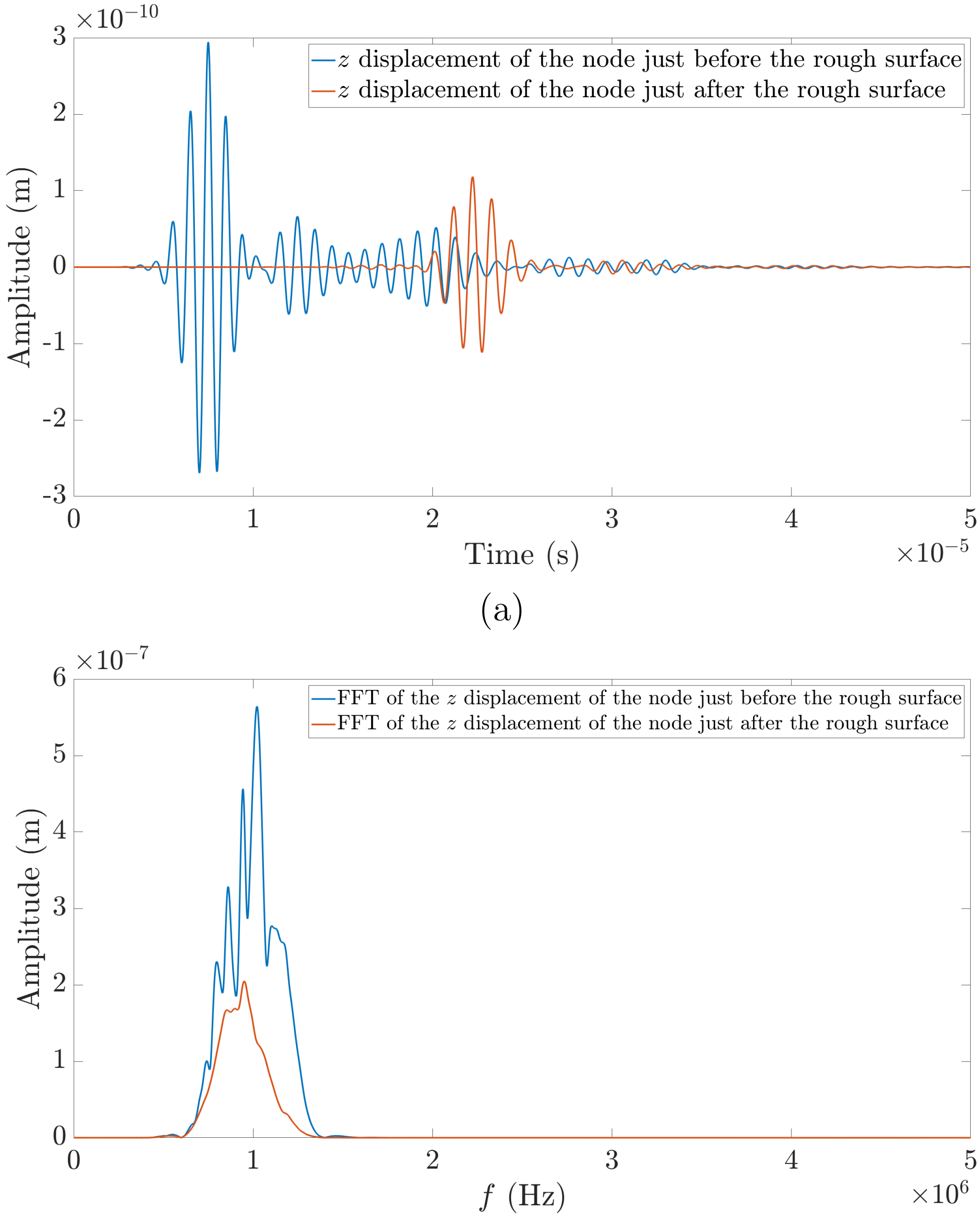

(a)

(b)

Figure 6.9: z displacement of a Rayleigh wave, just before and just after encountering a rough surface, where $\delta/\Lambda \approx 0.33$ for the rough surface (a), and corresponding FFTs (b).

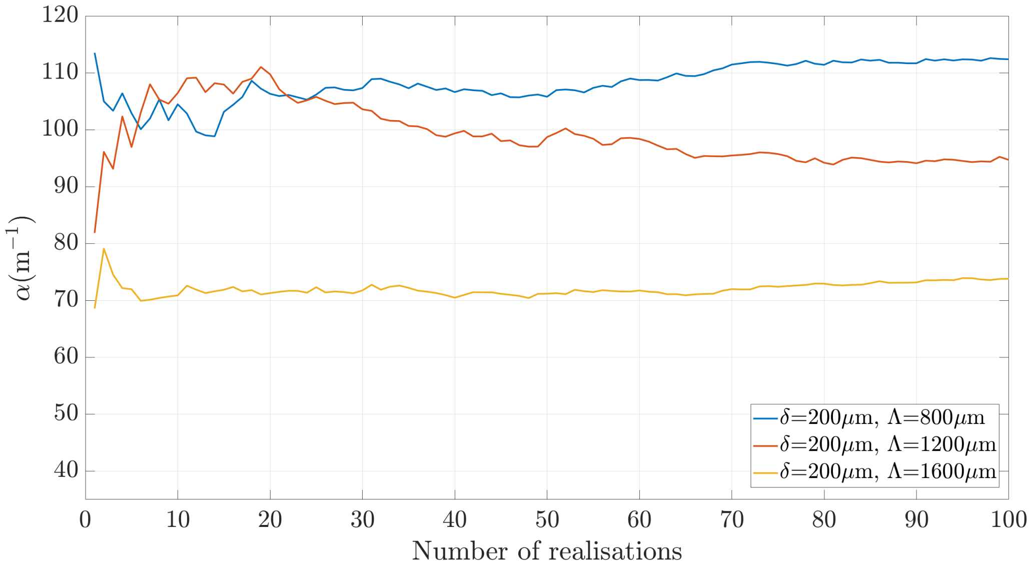

Figure 6.10: Variation of α as the number of realisations increases, for three δ/Λ values. For the dataset presented here, $f = 10$ MHz.

ies [153, 154, 156]. A verification that 100 realisations were sufficient was also presented, by competing a convergence analysis similar to that of [163]. This analysis was completed by plotting the average value of the attenuation coefficient, as the number of realisations increased, and observing the number at which α settled. Figure 6.10 shows the convergence of the attenuation coefficient as the number of realisations increases, for three δ/Λ combinations.

As shown in Figure 6.10, the rate of convergence of the attenuation coefficient depends on the degree of roughness. Again, if δ/Λ is assumed to be a measure of roughness, the simulations on Figure 6.10 relating to the least rough case ($\delta/\Lambda = 0.125$) appears to have converged after 15-20 realisations. The two rougher cases with the higher δ/Λ values converge at a higher number of realisations - however, in all three cases the attenuation coefficient value converges before the 100 realisation limit, which further supports such a choice.

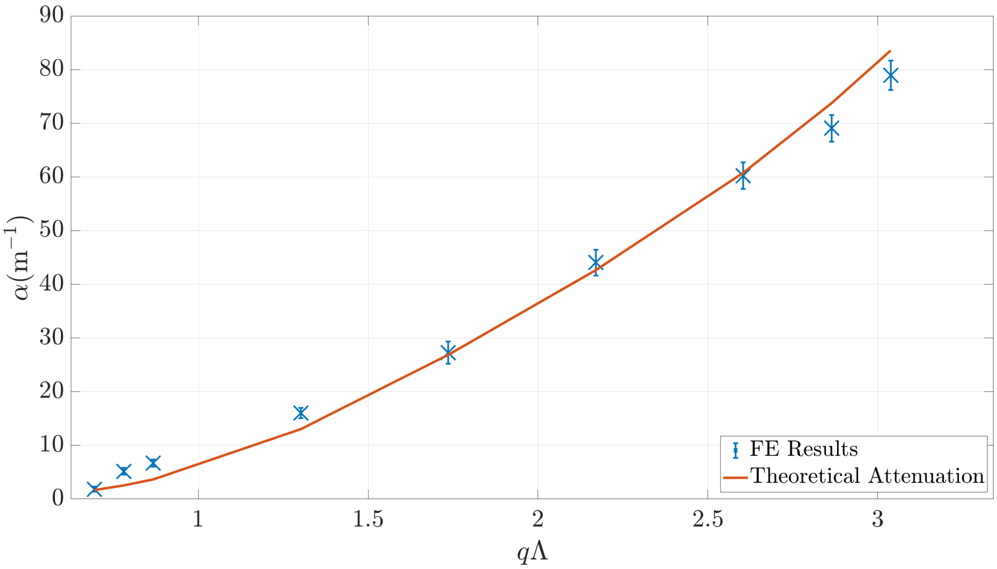

Figure 6.11: Comparison of the α values predicted by Equation (6.20), for the rough surface of Inconel 718 with $\delta = 200\ \mu$m and $\Lambda = 800\ \mu$m, with FE results. The continuous line shows the theoretical variation of α, while the FE results are plotted as “×”, with error bars corresponding to to SEs.

6.4.1 Quantitative results

A comparison between the theoretical attenuation values predicted by Equation (6.20), for Inconel 718, and roughness characterised by $\delta = 200\ \mu$m and $\Lambda = 800\ \mu$m is shown in Figure 6.11. For this set of results f was varied in the range of 0.4-1.75 MHz. However, in the horizontal axis of Figure 6.11, the dimensionless quantity $q\Lambda$ is plotted - since in the simulation Λ was fixed and q varies linearly with f for a given non-dispersive material, plotting against $q\Lambda$ is analogous to plotting against the frequency. Additionally, this allows for a more direct comparison with [142], which also use $q\Lambda$ in their analysis.

In Figure 6.11, as well as in Figures 6.12, 6.13 and 6.14 the mean attenuation coefficient value is plotted as “×”, including error bars. The length of the error bars is equal to ± 2 standard errors (SEs), where SE is defined as:

$$\mathrm{SE} = \frac{\sigma_d}{\sqrt{n}}, \tag{6.28}$$

where σ_d is the standard deviation of the attenuation coefficient, and n is the number of realisations used in computing that standard deviation.

It is clear that the FE results in Figure 6.11 follow the theory, with the agreement being evident in more than one scattering regimes - the results appear to agree well with the theoretical curve both in the Rayleigh $q\Lambda < 1$ and the stochastic $q\Lambda > 1$ regimes, as per the definitions in Table 6.1. Additionally some of the points in Figure 6.11 lie in the transition between the stochastic and geometric regimes ($q\Lambda \gg 1$).

Here it is also worth noting that some small discrepancies can be seen between the theory and the FE results, mostly towards the larger $q\Lambda$ values. However, since two different approaches are compared, it would be inappropriate to interpret these discrepancies as the FE results not matching the theory. There are three possible sources of these discrepancies - errors in the FE simulations, poor convergence of the results at the 100 realisation limits and approximations in the theory. Regarding the first concern, it has been shown by recent studies that the results from FE modelling possess a high degree of accuracy. The accuracy of FE results is discussed in detail in [164–166], therefore the errors in FE study are expected to be small. Regarding the insufficient convergence, the convergence study in Figure 6.10 shows that α converges well below the 100 realisation limit, suggesting again that errors related to this are expected to be small. Therefore, it is possible - indeed likely, that the approximations and assumptions made by the theory are a bigger contributor to the discrepancies shown in Figure 6.11. It can hence be concluded that the agreement of the FE modelling results and the theory are a good indicator that the model follows it well, and can proceed to deeper analysis of each scattering regime.

6.4.2 Asymptotic results

In this section the results relating to the power relationships between α and δ, Λ and f, in each of the Rayleigh, stochastic and geometric regimes are presented. To calculate the power relationship between α and the variable of interest, the attenuation coefficient was plotted against that variable in a log-log scale, and a best fit line, in the least square sense was plotted through the resulting points. The power was then found from the gradient, m of the best fit line.

Here it is worth noting that the power relationships from δ and Λ were calculated from the plotting of the attenuation coefficients against their normalised forms (δ_n and Λ_n) respectively. However, the power of either δ_n or Λ_n to which α_n is proportional, is the same as the power to which either δ or Λ is proportional to α - this is because in both cases, the frequency and hence wavelength (which is the normalisation variable) is fixed and therefore all values are normalised by a scalar, which does not affect the power relationship.

6.4.2.1 Rayleigh regime

The results relating to the geometric region are shown in Figure 6.12. Figure 6.12a shows the simulation results relating to the δ^2 relationship. To produce Figure 6.12a, the frequency of the simulations was set to 0.5 MHz ($\lambda_R = 5800\ \mu$m), and Λ was set to 80 μm. Then, δ was varied from 30 μm to 80 μm. The gradient of the best fit line in Figure 6.12a is 1.77, which is fairly close to 2.

Figure 6.12b shows the simulation results relating to the Λ relationship. To produce Figure 6.12b, the frequency of the simulations was set to 0.5 MHz ($\lambda_R = 5800$ μm) and δ was set to 20 μm. Then, Λ was varied from 50 μm to 90 μm. The gradient of the best fit line in Figure 6.12b is 0.94. Again even though the power relationship has been calculated for $\alpha_n(\Lambda_n)$, it remains the same for against Λ, for the same reason explained in the previous paragraph.

Figure 6.12c shows the simulation data, relating to the f^4 relationship. To generate the datapoints in Figure 6.12c, the rough surfaces were defined to have $\delta = 10$ μm and $\Lambda = 20$ μm. The frequency was varied from 1.75 MHz to 2.25 MHz, and at each frequency point, a Monte Carlo simulation of 100 realisations was completed. The gradient of the best fit line in Figure 6.12c is 3.77, which is close to the expected value of 4.

It appears that the powers obtained from the FE simulations here match the theoretical powers in Table 6.1 well. Again, this power relationship can be derived by combining the behaviour of the ω_2 function in Figure 6.3 and Equation (6.20) - in The Rayleigh regime, Huang & Maradudin have shown that $\omega_2 \propto (q\Lambda)^3$, and therefore, based on Equation (6.20), expected that $\alpha_{2\text{D}_R} \propto \delta^2 \Lambda f^4$. Physically, as $q\Lambda$ tends to zero, the Rayleigh wavelength becomes so large compared with the roughness, that the wave is no longer obstructed by it and hence, the attenuation coefficient also tends to zero.

6.4.2.2 Stochastic regime

The results relating to the stochastic region are shown in Figure 6.13. To produce Figure 6.13a, the frequency of all simulations was set to 1 MHz ($\lambda_R = 2900$ μm), and Λ to 800 μm. Then, δ was varied from 100 μm to 400 μm, satisfying the stochastic region's condition. The gradient of the best fit line was found to be 2.15.

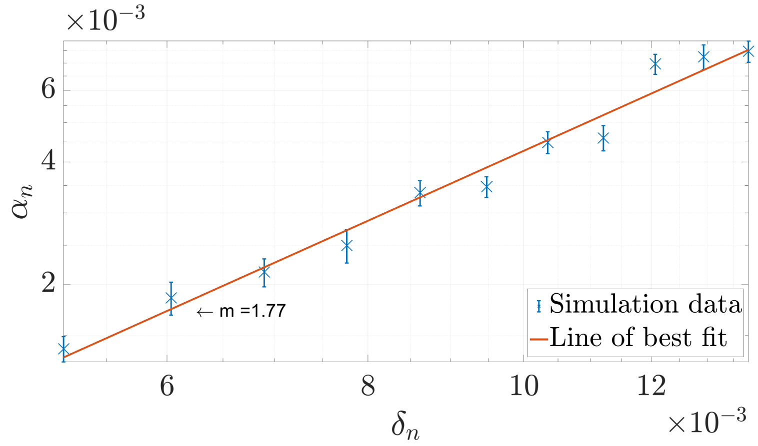

(a) α_n vs δ_n plot, Rayleigh regime.

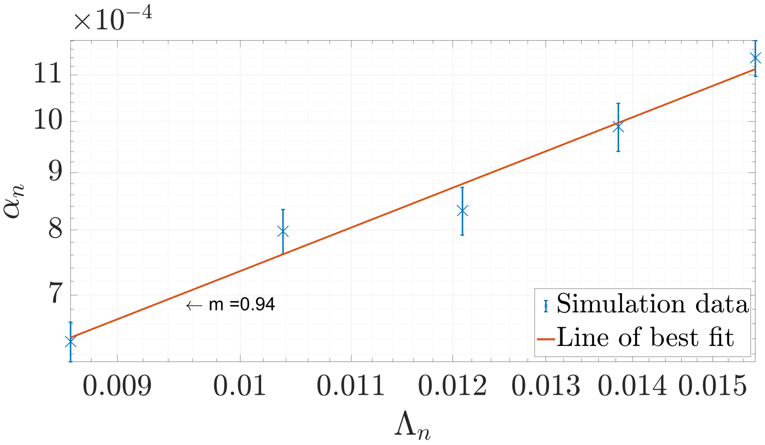

(b) α_n vs Λ_n plot, Rayleigh regime.

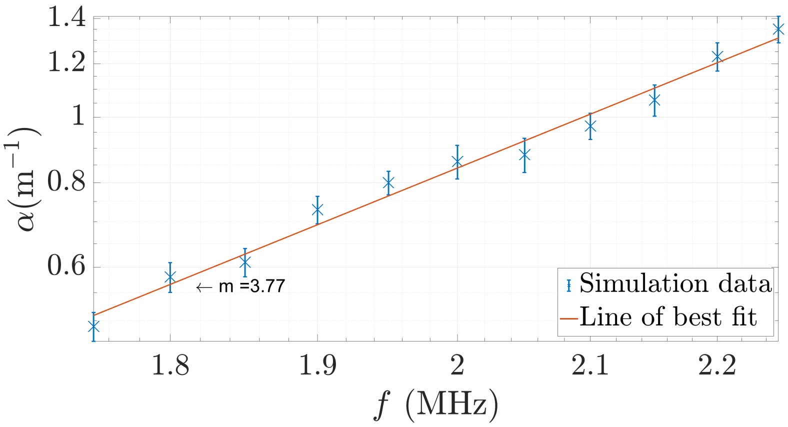

(c) α vs f plot, Rayleigh regime.

Figure 6.12: The FE results relating to the Rayleigh regime. The FE results, plotted as "×" and the line of best fit through them are shown. The gradient of the best fit line, m, is also shown. Values of the attenuation coefficient (either absolute or normalised) are plotted on the vertical axis, whereas the variable whose power relationship is investigated is plotted on the horizontal axis.

Figure 6.13b was generated by setting the frequency again to 1 MHz. Then, δ was fixed to 200 μm, and Λ was varied from 400 μm to 1600 μm. The gradient of the best fit line was found to be -1.25.

Finally, Figure 6.13c shows the FE results relating to the f^2 relationship. For this set of simulations, δ was set to 200 μm and Λ was set to 800 μm. The gradient of the best fit line is 1.94.

It appears that the FE model also follows the theory relating to the power relationships well in the stochastic regime too. Again, the power relationships can be attributed to the behaviour of the ω_2 function in Figure 6.4. In the stochastic regime, ω_2 can be seen to very linearly with $q\Lambda$ and therefore, if this linear variation is substituted in Equation (6.20), expected that $\alpha_{2\mathrm{D}_S} \propto \delta^2\Lambda^{-1}f^2$, which was also verified by the FE study here.

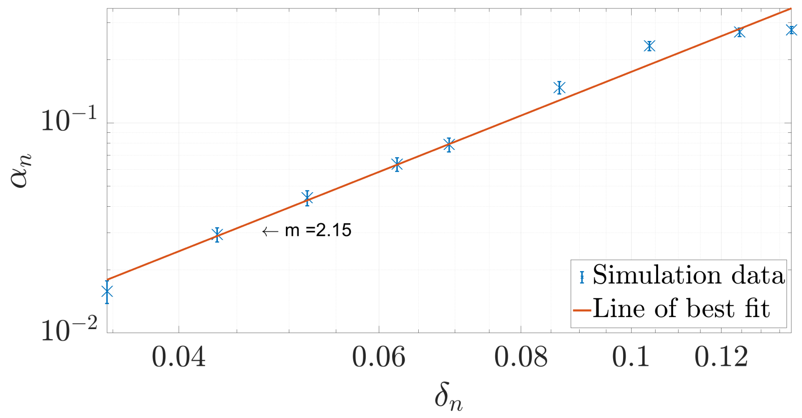

(a) α_n vs δ_n plot, stochastic regime.

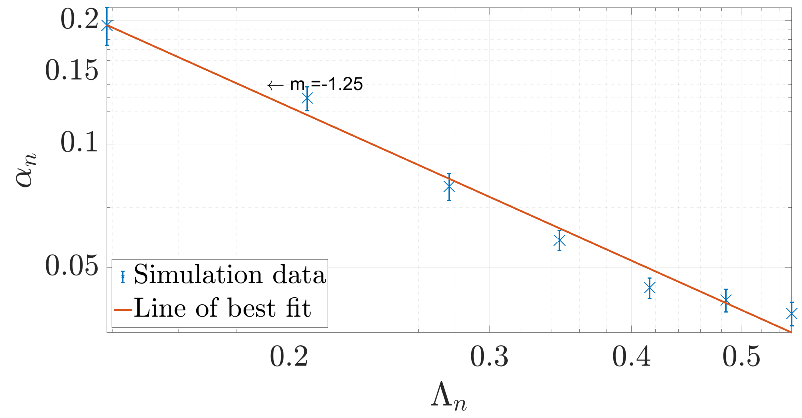

(b) α_n vs Λ_n plot, stochastic regime.

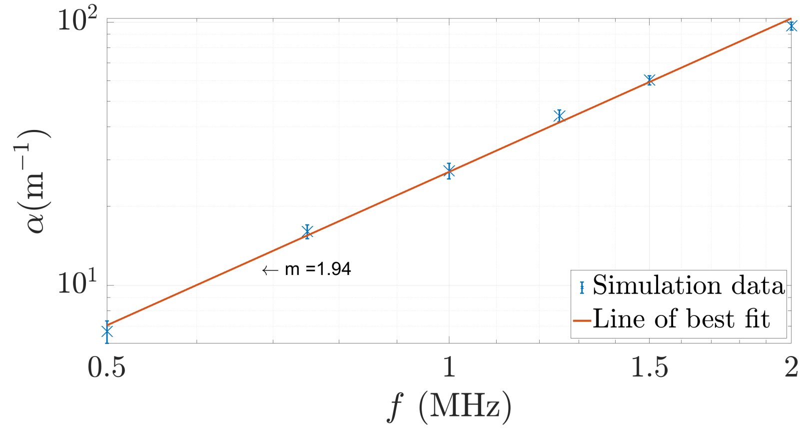

(c) α vs f plot, stochastic regime.

Figure 6.13: The FE results relating to the stochastic regime. The FE results, plotted as "×" and the line of best fit through them are shown. The gradient of the best fit line, m , is also shown. Values of the attenuation coefficient (either absolute or normalised) are plotted on the vertical axis, whereas the variable whose power relationship is investigated is plotted on the horizontal axis.

6.4.2.3 Geometric regime

The results relating to the geometric region are shown in Figure 6.14.

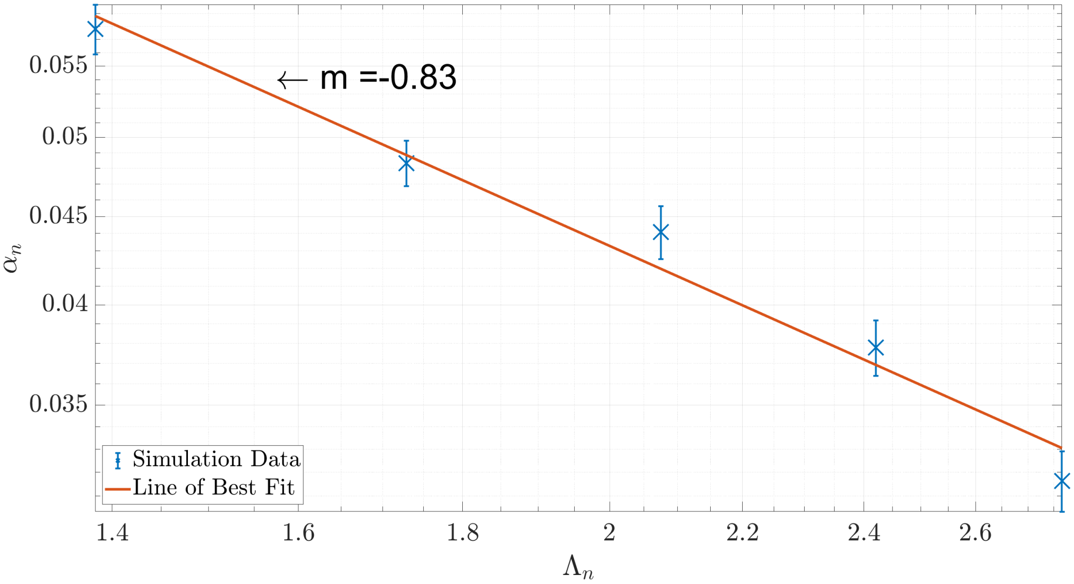

Figure 6.14: α_n vs Λ_n plot, geometric regime. The figure shows the FE results, plotted as ×, and the line of best fit through them. The gradient of the best fit line, m, is also shown on the figure. Values of the attenuation coefficient (either absolute or normalised) are plotted on the vertical axis, while the variable whose power relationship is investigated, is plotted on the horizontal axis.

The geometric region is a region where the RMS height is greater than $\frac{\lambda_R}{2\pi}$, as per the definition made in Table 6.1. Therefore, the frequency in this set of simulations was set to 5 MHz ($\lambda_R = 580$ μm), δ was set to 200 μm and Λ was varied from 800 μm to 1600 μm to fulfil the necessary conditions. The gradient of the best fit line in Figure 6.14 which relates to the power relationship between the attenuation coefficient and the correlation length is -0.83.

The negative gradient of the best fit line in Figure 6.14 implies that an increase correlation length decreases the attenuation coefficient. This is because, in the geometric regime, the wavelength has become so small compared with the parameters of the rough surface, that it travels following the profile of it, without getting scattered from it. The only obstacle is the number of "bumps" that it will encounter - since the correlation length is inversely proportional to the number of "bumps" in a given length, a long correlation length implies few obstacles, and hence little attenuation.

From the dimensional analysis, it was found that $m_{\Lambda_G} = -1 - m_{\delta_G}$. Since the FE results here show that $m_{\Lambda_G} \approx -1$, this implies that $m_{\delta_G} \approx 0$, i.e. that the attenuation coefficient in the geometric regime is not only independent of f, but also independent of δ. This result is further investigated and discussed in subsection 6.4.3.

6.4.3 Master plot & summary of results

In Table 6.1, the generalised attenuation coefficient was also introduced, β. This generalised attenuation coefficient reduces the number of variables to which the normalised attenuation coefficient is a function of, and therefore allows for plotting of the results from multiple FE simulations, in the stochastic and geometric regimes, against only δ_n. The results of this analysis are shown in Figure 6.15.

In Figure 6.15, two asymptotes are plotted. The asymptote with m=1 corresponds to the stochastic regime, while the asymptote with m=-1, corresponds to the geometric regime. The point of intersection is at $q\delta = 1 \iff \delta_n = 1/2\pi$, as per the definitions of the stochastic and geometric regimes in Table 6.1. It appears that the datapoints from the FE results follow both these asymptotes in their relevant regimes, further confirming that the FE models follows the theory. The transition point between the stochastic and geometric regimes is also visible at $\delta_n = 1/2\pi$. One further interesting result inferred by this master plot is that it confirms both that $m_{\delta_G} = 0$ and $m_{\Lambda_G} = -1$.

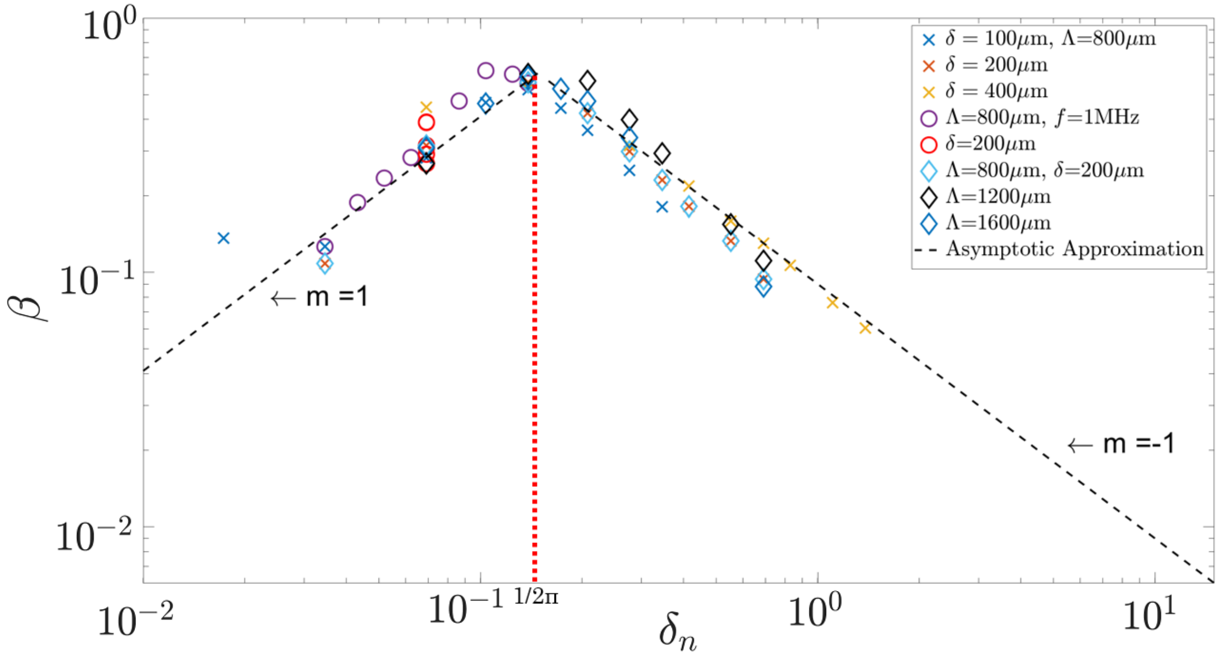

Figure 6.15: β vs δ_n master plot. Here, generalised attenuation coefficient values are drawn for a large combination of frequencies and roughness parameters. The datapoints cover both the stochastic and geometric regions, where the above proposed ad hoc approximation predicts that $\beta \propto \delta_n$ and $\beta \propto \delta_n^{-1}$ respectively, with the transition occurring at the $\delta_n = 1/2\pi$ point. The Monte Carlo results with a fixed Λ (= 800 μm) are plotted as ×, the results with a common f (=1 MHz) are plotted as ∘, and the results with a fixed δ (= 200 μm) are plotted as ◇. The dashed black lines show the asymptotic approximation for both scattering regimes, while the red dashed line indicated the transition point between them.

This is because, on the right-hand side Figure 6.15, corresponding to the geometric regime, expected, from the dimensional analysis that $\alpha_{2\mathrm{D}_G} \propto \Lambda^{-1-m_{\delta_G}}$ and $\beta \propto \delta_n^{m_{\delta_G}-1}\Lambda_n^{-m_{\delta_G}}$. Therefore, $m_{\delta_G} - 1 = -1$ and $m_{\delta_G} = 0$. Also, since $m_{\delta_G} = 0$, $\alpha_{2\mathrm{D}_G}$ is independent of Λ, as demonstrated in the previous section. Finally, from Equation (6.26), $m_{f_G} = 0$, as suggested by [144, 147].

A summary of the power relationships obtained from this FE study, compared with the power relationships predicted by the theory is shown in Table 6.2. Comparing Tables 6.1 and 6.2, it is clear that there is good agreement in the asymptotic power relationship coefficient, across the Rayleigh and stochastic regimes. For the geometric regime the respective powers were evaluated, and their correctness verified using the master plot. This has two implications - firstly, the well-established theory regarding scattering in the Rayleigh regime was verified, both quantitatively and asymptotically. Secondly, the FE model was able to also verify the asymptotic in the stochastic and geometric regimes quantitatively, while the asymptotic results confirmed the applicability of assumptions from scattering [144], to this study.

Table 6.2: Comparison of the theoretical and FE power relationships, between the attenuation coefficient and the RMS height, correlation length and frequency. In this table, q is the wavenumber, δ is the RMS height, Λ is the correlation length and f is the frequency.

Regime	Rayleigh	Stochastic	Geometric
Limits	$q\delta < q\Lambda < 1$	$q\delta < 1 < q\Lambda$	$1 < q\delta \ll q\Lambda$
$\alpha(\delta, \Lambda, f)$ (Theory)	$\delta^2\Lambda f^4$	$\delta^2\Lambda^{-1}f^2$	Λ^{-1}
$\alpha(\delta, \Lambda, f)$ (FE Results)	$\delta^{1.77}\Lambda^{0.94}f^{3.77}$	$\delta^{2.15}\Lambda^{-1.25}f^{1.94}$	$\Lambda^{-0.83}$

Chapter 7

Conclusion

7.1 Review of thesis

The work in this thesis primarily investigated the potential use of ultrasonic waves for fatigue state characterisation of steel components. Namely, for flat and near flat components the potential use of Rayleigh waves was proposed, while for pipe geometries, the use of creeping and shear bulk waves was investigated. The extensive use of surface waves in the duration of this work also motivated a study of the attenuation behaviour of Rayleigh waves when those propagate on rough surfaces.

In an industrial application, it is important to be able to assess the fatigue state of steel components - this becomes increasingly important for safety-critical components, due to the severity of the consequences shall such components fail unexpectedly due to fatigue damage. Due to the latter, industry currently uses very conservative estimates, resulting in high inspection, maintenance and replacement costs. These estimates are bound to be conservative, due to the theoretical models which currently exist not being able to accurately characterise the fatigue state of a real life component which is subjected to cyclical (but unpredictable in terms of frequency), amplitude and load level, loading.

An alternative approach would be the use of ultrasound, as the theory suggests that ultrasonic waves are sensitive to the presence of fatigue damage; this sensitivity is visible as a reduction in their propagation speed. The reduction is expected to be monotonic as fatigue progresses, and therefore, it is possible to construct plots showing the variation in speed versus the fatigue state of a component. When those are constructed, an inverted approach can be used, where the change in propagation speed of an ultrasonic wave in a component with an unknown level of fatigue damage can be correlated to a unique fatigue state through the aid of such a diagram. Past studies have investigated this phenomenon and constructed such diagrams, using bulk waves, and observed this monotonic evolution of the wave speed as fatigue progressed - however, the changes measured were small due to fatigue inherently being concentrated on the surface of a component. The work in this thesis investigated how these changes can be amplified, to increase the confidence in such measurements - this is because, even small errors in calculating the change in speed value would result in large over- or underestimation of the fatigue state of a component.

The aforementioned work also inspired a separate, in depth study of how the attenuation coefficient of Rayleigh waves is affected when they travel over a rough surface. As any real surface possesses a certain degree of roughness, it is important, especially for applications where the attenuation coefficient is to be measured accurately in an NDE inspection, to be able to identify and account for the presence of this roughness. Additionally, similarly to the fatigue state investigations discussed above, an inverted approach can be equally useful i.e. to use the attenuation information of a Rayleigh wave after it has travelled over a rough surface to assess the degree of roughness of the surface.

In Chapter 2, the theory and methods for exciting a clean Rayleigh wave in FE were presented. This was achieved by implementing the theory related to the propagation of Rayleigh waves and the features of the Pogo FE package. A method for correctly modelling the attenuation of Rayleigh waves in a material was also derived.

Chapter 3 presented the theory around the phenomenon of fatigue-ultrasound interaction. The phenomena related to this theory were subsequently verified with the use of longitudinal bulk waves. Rayleigh waves were then implemented in analogous measurements to show that the monotonic reduction in speed as fatigue progresses still holds true, but the amplitude of the changes in speed was magnified. An FE model was also derived using the experimental information, which was able to model the propagation speed effects which fatigue has on the propagation of longitudinal bulk and Rayleigh waves.

The idea of using surface waves for fatigue state characterisation was further investigated in Chapter 4, by implementing creeping waves to characterise the fatigue state of pipe geometries. This was attempted by also considering that in a realistic application, it is often the case that there is no access to the inner surface. Therefore, creeping waves were excited in an FE model on an annulus by exciting shear wave, travelling at an angle, towards a suitable location on the inner surface of the pipe. A thorough optimisation process of this method was presented as well as some results from idealised models - however, the poor performance of this method in more realistic scenarios motivated the trial of other methods too, such as the utilisation of the phenomenon of beating, the use of SH_0 waves and the implementation of noise suppression methods.

It was found that none of the methods discussed in the previous paragraph performed adequately for the purposes of this study. Therefore, Chapter 5 presented an alternative method which involved the use of bulk shear waves to obtain similar changes in speed versus fatigue state information. Shear waves are known to be more sensitive to the presence of fatigue damage, however, the difficulties related to their excitation have made them a less popular choice in the NDE community. Here, an alternative method achievable through the use of EMATs was presented, which allowed for the creation of shear wave C-scans of comparable quality to those created by longitudinal waves, with no coupling, while longitudinal waves require a water-immersion facility. This method can be used in both flat and moderately curved geometries - additionally, a method to expanding this to surfaces with smaller curvatures was also discussed.

Finally, Chapter 6 presented in detail the modelling techniques and results related to the attenuation behaviour of Rayleigh waves when they propagate over rough surfaces, in 2D. The relevant theory, as well as the creation of the FE models used in this study was explained followed by a presentation of both the analytical and asymptotic results of the study and the potential implications of these result for 3D studies.

7.2 Summary of main findings

7.2.1 Ultrasonic methods for characterising the fatigue state of steel components

For all the ultrasonic measurements related to flat surfaces, a set of five purposely fatigued plates, each at a different fatigue level, was used. Those plates were manufactured by Trueflaw and each contained a circular fatigued area in its centre.

Longitudinal wave speed C-scans were generated for each of the plates with the aid of an immersion tank. Suitable processing of these revealed that, as the theory predicts, ultrasound is sensitive to the presence of a fatigue zone as all C-scans revealed a circular low-speed area at the location of the fatigue spot. Furthermore, the contrast between that area and the surrounding material became more severe as the plates' UFs increased - as a result, the ΔC_L vs UF diagram created from these 5 plates showed a monotonic reduction in speed as fatigue progressed.

With the use of a suitable wedge setup, Rayleigh wave speed maps were also created for each plate by taking multiple Rayleigh wave speed measurements across the centreline of each plate. Again these showed the sensitivity of the ultrasound to the presence of a fatigue zone to increase with an increase in UF, however, compared with longitudinal waves, the magnitude of the changes was amplified by approximately ten times. This is because the waves spend their entire propagation inside the fatigue zone, contrary to through-thickness measurements during which waves spend a very limited time inside the fatigue zone. Therefore the use of the ΔC_R vs UF graph instead of the ΔC_L vs UF graph in an inspection scenario would yield significantly higher confidence in the fatigue state prediction - this is because a human/equipment error would have a smaller effect in the ΔC_R and therefore, the resulting fatigue state prediction.

Both longitudinal and Rayleigh wave data were combined, along with a strain profile provided by Trueflaw for one of the plates, to create an FE model able to encapsulate the effects of fatigue in the propagation speed of both types of wave. This was achieved using an equivalent solid approach - initially, the strain profile was converted into a Young's modulus profile, comprised of eight different, gradually reducing Young's modulus values. This profile was implemented in 2D Pogo, by defining an area of equal length to the diameter of the fatigue spots and height equal to 10% of the plate's thickness. In this area, eight different material layers were defined, each corresponding to one of the materials in the Young's modulus profile, with the lowest Young's modulus area being on the surface of the FE domain and the rest containing gradually increasing Young's modulus values. The Rayleigh wave change in speed data was then used to control the severity of this profile - this was achieved by using a gradient multiplication approach to the profile, and a trial and error approach, up until five unique Young's modulus profiles were obtained, each corresponding to one of the plates. When those profiles were used in a longitudinal bulk wave simulation of plates with the same dimensions, a very good match was found between the simulation results and the experimental longitudinal wave change in speed values, indicating that this method can indeed correctly model the effects of fatigue on the propagation speed of longitudinal and Rayleigh waves.

Multiple interesting observations were made when attempting to extend the use of surface waves in pipe geometries. Having assumed no access to the inner surface, creeping waves were excited on the inner surface of a pipe by firstly exciting a shear wave at the outer surface of the pipe, travelling at an angle such that it excited a creeping wave when it arrived near the inner surface. It was found that whether the shear wave would indeed excite a creeping wave was a strong function of the ratio of the wavelength of the shear wave to the inner radius of the pipe i.e. for a given inner surface, the wavelength must be large enough to perceive the surface as curve and excite the creeping wave. It was also found that the location to which the shear wave is steered is a weaker function of whether a creeping wave will be excited - this is because, as the theory suggests it is sufficient for any part of the shear wave field to pass close to the inner radius. Therefore, any sensible choice of a focusing location leads to the generation of a creeping wave.

The same Young's modulus profile approach was used in the annulus models to simulate the presence of a fatigue ring around the inner surface. When a creeping wave travels around the inner surface of the annulus, it leaks energy into the bulk of the material which can be received on the outer surface, and hence, the speed can be calculated. For idealised models, with the use of absorbing layers it was found that indeed creeping waves are very sensitive to the presence of fatigue, and for the geometries investigated here, the changes in speed from creeping waves were found to be approximately fifteen times bigger than those observed with longitudinal waves.

Unfortunately this method didn't yield satisfactory results in more realistic FE simulations, with the absorbing layers removed. The underlying reason was the weak nature of the leaky wave. As the magnitude of the leaky wave was measured to be two orders of magnitude less than that of the shear wave, its presence was masked by: (i) the multiple reflections of the shear wave after it had excited the creeping wave, (ii) the outer surface creeping waves which were unavoidably excited by the source and (iii) other inner surface creeping waves which were excited by the arbitrary motion of the reflected shear waves inside the annulus. Therefore, this idea was not pursued further, however, there is still room for optimisation especially for thicker walled pipes which may be of interest in other applications.

As a result, the study reverted back to the use of through-thickness measurements, this time using EMATs, as they are inherently more sensitive to the presence of a fatigue zone. An EMAT was mounted on a 3-axis stepper motor frame, which was pre-programmed to take shear wave speed measurements in a grid, similar to a standard immersion tank setup, in order to generate analogous shear wave speed maps for the five fatigued plates. Prior to the creation of the C-scans, the repeatability and replacement accuracy of the EMAT were tested, both of which were found to be more than sufficient for our purposes, as any associated errors were found to be much smaller than the expected changes in speed. The C-scans revealed two interesting features - first when visually comparing the C_L with the C_T scans, multiple common features could be seen. This indicates that EMATs are capable of performing such scans. Additionally, when calculating the change in speed inside the fatigue zone, it was found not only that the magnitude of the change in each plate is larger for shear than for longitudinal waves, but also that this magnification is approximately equal to $3\gamma^2/4(\approx 2.56$ for steel) as suggested by the theory.

Having observed that the use of shear waves excited by EMATs is practical for speed (and hence fatigue state) measurements, it was extended to pipe geometries. For all pipe related measurements, a pipe specimen from Trueflaw was used, which contained 2 purposely fatigued spots similar to the plates. After establishing the good performance of the EMAT on the curved surface, a semi-automated C-scan was performed on it, achieved by using the frame to move the EMAT in the axial direction, and manually rotating the pipe using a dividing head. The resulting C_T map clearly showed the fatigue spots, as well as the difference in the UF between them. Additionally, having acknowledged a small loss in signal quality and C_T accuracy due to the curved nature of the surface, a curved EMAT prototype was manufactured, whose curvature matched the outer surface of the pipe. It was found that even the use of this simple prototype improved the C_T measurements. As a result, for the case where a pipe with a large curvature is to be inspected, such an approach can potentially be successfully used in the case that a flat EMAT does not perform adequately. Therefore, using a ΔC_T vs UF graph instead of a ΔC_L vs UF graph for a cylindrical component would again yield a more confident fatigue state prediction, for the reasons discussed above.

7.2.2 Attenuation of Rayleigh waves due to surface roughness

The amount by which the rough surface affects a Rayleigh wave is a function of the surface's statistical parameters, and the wave's frequency. This phenomenon, in the literature, is split into three scattering regimes - the Rayleigh (low frequency), stochastic (low to medium frequency) and geometric (high frequency) regimes. In the Rayleigh and stochastic regimes, both quantitative and asymptotic power relationships exist between the attenuation coefficient and (i) the surface's statistical parameters and (ii) the wave's frequency, while the geometric regime has remained relatively unexplored.

Using Monte Carlo FE simulations, the existing theory was verified in 2D for the Rayleigh and stochastic regimes, while power relationships were derived for the geometric regime with the aid of dimensional analysis. The verification was achieved both qualitatively, with absolute attenuation values from the FE simulation being compared against attenuation values from analytical expressions, and asymptotically, by comparing the predicted power relationships with the ones obtained from multiple FE simulations. The simulations were also able to extend the validity of the theory in combinations of frequency and surface parameters outside the stated region of validity of the theory.

Finally, it is worth highlighting the value of the 2D study in terms of verifying the 3D theory too. Due to computational restriction, the entirety of this study was completed in 2D. However, it is highly likely that the 2D verification and extension has useful implications for the 3D scattering - this is because the small perturbation theory used to derive the 2D and 3D theory is identical, and the mathematical analysis and resulting expressions share multiple common features.

7.3 Future work

The work presented in this thesis provides a good basis for extending the proposed methods to an industrial environment. Therefore, some research for technology transfer is proposed both for the Rayleigh and shear wave inspection methods. Such a study would encompass a plethora of parameters to be optimised, including but not limited to: suitable frequencies for different components, maximum and minimum component dimensions, wedge sizes/angles for the Rayleigh wave method and curvature considerations for the shear wave method. Additionally, the sensitivity of any new conventional transducer or EMAT developed through this study would have to be thoroughly investigated.

In addition to the above, further study on the behaviour of curved EMATs obtained through 3D printing is also proposed. In this study, a simple prototype yielded good results - therefore, it is worth investigating by how much the performance of such an EMAT can be improved if the manufacturing parameters are optimised. Additionally, a study to determine the maximum curvature (and hence smallest possible pipe) is also suggested.

For implementing the technique of correlating ΔC to a specific UF, in an industrial environment, either with Rayleigh or shear waves, some calibration of the technique is required to account for the sensitivity of ΔC to the exact material composition. Namely, it would be useful to generate ΔC vs UF curves for steels with slightly different chemistries to investigate the effect of the steel's composition, and if possible, derive correction factors for industrial use. Additionally, these tests would ideally involve different plastic strain cycles that reflect those in nuclear power generation plant, or at least cycles that result in a realistic fatigue region thickness, and would cover a UF range up to something close to unity. In this way, the two probable, yet likely, main variables influencing the change in velocity with fatigue would be realistically investigated. Also, analogous studies could be completed to investigate the effect of oxidisation, and any potential implications arising when assesing non-uniform geometries.

In terms of FE modelling, it was demonstrated that a Young's modulus profile approach for representing fatigue damage yielded accurate results when comparing the simulation results to experimental measurements. However, as suggested by the theory, shear waves behave differently to longitudinal wave when encountering fatigue. As such, a step change in complexity of the FE model to encapsulate this behaviour would be to add an analogous Poisson's ratio profile to the model - at the time of writing of this thesis, and to the knowledge of the author there does not currently exist a simple way to obtain such a profile. Therefore, an experimental and numerical simulation to derive a method for obtaining such profiles is proposed.

Finally, the study presented here regarding the attenuation of Rayleigh waves when they travel over a rough surface was completed fully in 2D. Despite the results also providing very useful insights in terms of the 3D analytical and asymptotic relationships predicted by the theory, it would be useful if an analogous study was completed in 3D. An initial 3D study was not feasible due to the large number of simulations required to obtain meaningful results - however, in the light of the 2D results which revealed combinations of statistical parameters which are of interest, a 3D study has become more viable.

References

[1] A. V. Granato and K. Lücke, "Theory of mechanical damping due to dislocations," *Journal of Applied Physics*, vol. 27, no. 6, p. 583–593, 1956.

[2] A. Maurel, J. F. Mercier, and F. Lund, "Scattering of an elastic wave by a single dislocation," *The Journal of the Acoustical Society of America*, vol. 115, p. 2773–2780, 2004.

[3] A. Maurel, V. Pagneux, D. Boyer, and F. Lund, "Elastic wave propagation through a distribution of dislocations," *Materials Science and Engineering: A*, vol. 400-401, p. 222–225, 2005.

[4] A. Maurel, J. F. Mercier, and F. Lund, "Elastic wave propagation through a random array of dislocations," *Physical Review B*, vol. 70, 2004.

[5] A. Maurel, V. Pagneux, F. Barra, and F. Lund, "Wave propagation through a random array of pinned dislocations: Velocity change and attenuation in a generalized Granato and Lücke theory," *Physical Review B*, vol. 72, no. 17, 2005.

[6] P. Huthwaite, "Accelerated finite element elastodynamic simulations using the GPU," *Journal of Computational Physics*, vol. 257, p. 687–707, 2014.

[7] J. D. Achenbach, *Wave propagation in elastic solids.* North Holland Publishing Company, 1973.

[8] I. A. Viktorov, *Rayleigh and Lamb Waves (Translated from Russian).* Plenum Press, 1967.

[9] W. Hassan and P. B. Nagy, "Simplified expressions for the displacements and stresses produced by the Rayleigh wave," *The Journal of the Acoustical Society of America*, vol. 104, no. 5, pp. 3107–3110, 1998.

[10] R. D. Cook, D. S. Malkus, M. E. Plesha, and R. J. Witt, *Concepts and applications of finite element analysis.* John Wiley & Sons, 1989.

[11] S. G. Haslinger, M. J. S. Lowe, P. Huthwaite, R. V. Craster, and F. Shi, "Appraising Kirchhoff approximation theory for the scattering of elastic shear waves by randomly rough defects," *Journal of Sound and Vibration*, vol. 460, p. 114872, 2019.

[12] M. Huang, G. Sha, P. Huthwaite, S. I. Rokhlin, and M. J. S. Lowe, "Maximizing the accuracy of finite element simulation of elastic wave propagation in polycrystals," *The Journal of the Acoustical Society of America*, vol. 148, no. 4, p. 1890–1910, 2020.

[13] A. A. Zimmermann, P. Huthwaite, and B. Pavlakovic, "High-resolution thickness maps of corrosion using SH1 guided wave tomography," *Proceedings of the Royal Society A: Mathematical, Physical and Engineering Sciences*, vol. 477, no. 2245, p. 20200380, 2021.

[14] M. B. Drozdz, *Efficient Finite Element Modelling of Ultrasound Waves in Elastic Media.* PhD thesis, Imperial College of Science Technology and Medicine, 2008.

[15] J. L. Rose, *Ultrasonic guided waves in solid media.* Cambridge University Press, 2014.

[16] M. J. S. Lowe, “Matrix techniques for modeling ultrasonic waves in multilayered media,” *IEEE Transactions on Ultrasonics, Ferroelectrics, and Frequency Control*, vol. 42, no. 4, pp. 525–542, 1995.

[17] B. N. Pavlakovic, M. J. S. Lowe, D. N. Alleyne, and P. Cawley, “Disperse: A general purpose program for creating dispersion curves,” in *Review of Progress in Quantitative Nondestructive Evaluation*, 2012.

[18] G. Sarris, S. G. Haslinger, P. Huthwaite, and M. J. S. Lowe, “Ultrasonic methods for the detection of near surface fatigue damage,” *NDT & E International*, vol. 135, p. 102790, 2023.

[19] P. Paris and F. Erdogan, “A critical analysis of crack propagation laws,” *Journal of Basic Engineering*, vol. 85, no. 4, pp. 528–553, 1963.

[20] M. Makkonen, “Predicting the total fatigue life in metals,” *International Journal of Fatigue*, vol. 31, no. 7, pp. 1163–1175, 2009.

[21] H. Tada, P. C. Paris, and G. R. Irwin, *The stress analysis of cracks handbook.* ASME Press, 2000.

[22] S. A. Laham, *Stress intensity factor and limit load handbook.* British Energy Generation Ltd, 1998.

[23] J. C. Newman, “A crack-closure model for predicting fatigue crack growth under aircraft spectrum loading,” *American Society for Testing and Material*, 1981.

[24] B. F. Spencer and J. Tang, “Markov process model for fatigue crack growth,” *Journal of Engineering Mechanics*, vol. 114, no. 12, p. 2134–2157, 1988.

[25] M. A. Miner, “Cumulative damage in fatigue,” *Journal of Applied Mechanics*, vol. 12, no. 3, pp. A159–A164, 1945.

[26] S. M. Marco and W. L. Starkley, “A concept of fatigue damage,” *Transactions of the ASME*, vol. 76, no. 3, pp. 627–632, 1954.

[27] C. Bathias, “There is no infinite fatigue life in metallic materials,” *Fatigue & Fracture of Engineering Materials & Structures*, vol. 22, no. 7, p. 559–565, 1999.

[28] A. Fatemi and L. Yang, “Cumulative fatigue damage and life prediction theories: A survey of the state of the art for homogeneous materials,” *International Journal of Fatigue*, vol. 20, no. 1, p. 9–34, 1998.

[29] O. H. Basquin, “The exponential law of endurance tests,” *American Society for Testing and Materials Proceedings*, vol. 10, pp. 625–630, 1910.

[30] L. F. Coffin, *A study of the effect of cyclic thermal stresses on a ductile metal.* Knolls Atomic Power Laboratory, 1953.

[31] M. T. Todinov, “Probability distribution of fatigue life controlled by defects,” *Computers & Structures*, vol. 79, no. 3, p. 313–318, 2001.

[32] M. T. Todinov, “A probabilistic method for predicting fatigue life controlled by defects,” *Materials Science and Engineering: A*, vol. 255, no. 1-2, p. 117–123, 1998.

[33] S. S. Lee, J. H. Lee, I. K. Park, S. J. Song, and M. Y. Choi, “Statistical analysis of casting defects in microstructure for understanding the effect on fatigue property of 17-4PH stainless steel,” *Key Engineering Materials*, vol. 321-323, p. 1503–1506, 2006.

[34] A. Pineau and S. D. Antolovich, “Probabilistic approaches to fatigue with special emphasis on initiation from inclusions,” *International Journal of Fatigue*, vol. 93, p. 422–434, 2016.

[35] Q. G. Wang, D. Apelian, and D. A. Lados, "Fatigue behavior of A356-T6 aluminum cast alloys. part I. effect of casting defects," *Journal of Light Metals*, vol. 1, no. 1, p. 73–84, 2001.

[36] R. S. S. Haridas, S. Thapliyal, P. Agrawal, and R. S. Mishra, "Defect-based probabilistic fatigue life estimation model for an additively manufactured aluminum alloy," *Materials Science and Engineering: A*, vol. 798, p. 140082, 2020.

[37] V. Dattoma, S. Giancane, R. Nobile, and F. Panella, "Fatigue life prediction under variable loading based on a new non-linear continuum damage mechanics model," *International Journal of Fatigue*, vol. 28, no. 2, p. 89–95, 2006.

[38] S. Giancane, R. Nobile, F. W. Panella, and V. Dattoma, "Fatigue life prediction of notched components based on a new nonlinear continuum damage mechanics model," *Procedia Engineering*, vol. 2, no. 1, p. 1317–1325, 2010.

[39] L. Hua, W. Tian, and W. Liao, "Remaining life evaluation for remanufacturing blanks based on non-linear continuum fatigue damage model," *Journal of Mechanical Engineering*, vol. 51, no. 21, p. 132, 2015.

[40] S. P. Zhu, H. Z. Huang, and Z. L. Wang, "Fatigue life estimation considering damaging and strengthening of low amplitude loads under different load sequences using fuzzy sets approach," *International Journal of Damage Mechanics*, vol. 20, no. 6, p. 876–899, 2011.

[41] K. Tanaka and T. Mura, "A theory of fatigue crack initiation at inclusions," *Metallurgical Transactions A*, vol. 13, no. 1, p. 117–123, 1982.

[42] R. I. Stephens, A. Fatemi, R. R. Stephens, and H. O. Fuchs, *Metal fatigue in engineering*, p. 33–56. John Wiley and Sons, 2000.

[43] J. M. Barsom and S. T. Rolfe, *Fracture and fatigue control in structures: Applications of fracture mechanics*, p. 28–40. ASTM, 1999.

[44] S. Suresh, *Fatigue of materials (online)*, p. 134–143. Cambridge University Press, 2012.

[45] L. Satyarnarayan, D. M. Pukazhendhi, K. Balasubramaniam, C. V. Krishnamurthy, and D. S. Ramachandra-Murthy, "Phased array ultrasonic measurement of fatigue crack growth profiles in stainless steel pipes," *Journal of Pressure Vessel Technology*, vol. 129, no. 4, p. 737–743, 2007.

[46] C. L. Du, Y. S. Wang, D. Y. Gao, K. H. Liu, and X. L. Qing, "In-situ quantitative monitoring of fatigue crack using fastest time of flight diffraction method," *Transactions of Nonferrous Metals Society of China*, vol. 22, no. 11, p. 2679–2684, 2012.

[47] Q. Shan and R. J. Dewhurst, "Surface-breaking fatigue crack detection using laser ultrasound," *Applied Physics Letters*, vol. 62, p. 2649–2651, 1993.

[48] S. Alavudeen, C. V. Krishnamurthy, K. Balasubramaniam, D. M. Pugazhendhi, G. Raghava, and P. Gandhi, "Improved imaging of fatigue crack profile in thick cruciform samples using ultrasonic phased array models," *Journal of Pressure Vessel Technology*, vol. 132, no. 1, pp. 011501–1 – 011501–8, 2010.

[49] M. Ryles, F. H. Ngau, I. M. I., and W. J. Staszewski, "Comparative study of nonlinear acoustic and lamb wave techniques for fatigue crack detection in metallic structures," *Fatigue & Fracture of Engineering Materials & Structures*, vol. 31, no. 8, p. 674–683, 2008.

[50] O. Buck, W. L. Morris, and J. M. Richardson, "Acoustic harmonic generation at unbonded interfaces and fatigue cracks," *Applied Physics*

Letters, vol. 33, p. 371–373, 1978.

[51] R. Wang, Q. Wu, F. Yu, Y. Okabe, and K. Xiong, "Nonlinear ultrasonic detection for evaluating fatigue crack in metal plate," *Structural Health Monitoring*, vol. 18, no. 3, p. 869–881, 2018.

[52] K. Lücke and A. V. Granato, "Simplified theory of dislocation damping including point-defect drag. I. theory of drag by equidistant point defects," *Physical Review B*, vol. 24, no. 12, p. 6991–7006, 1981.

[53] A. V. Granato and K. Lücke, "Application of dislocation theory to internal friction phenomena at high frequencies," *Journal of Applied Physics*, vol. 27, no. 7, p. 789–805, 1956.

[54] M. A. Omari and I. Sevostianov, "Evaluation of the growth of dislocations density in fatigue loading process via electrical resistivity measurements," *International Journal of Fracture*, vol. 179, no. 1-2, p. 229–235, 2012.

[55] C. Heinrich and V. Sundararaghavan, "A method to predict fatigue crack initiation in metals using dislocation dynamics," *Corrosion Reviews*, vol. 35, no. 4-5, p. 325–341, 2017.

[56] T. Ohtani, K. Nishiyama, S. Yoshikawa, H. Ogi, and M. Hirao, "Ultrasonic attenuation and microstructural evolution throughout tension–compression fatigue of a low-carbon steel," *Materials Science and Engineering: A*, vol. 442, no. 1, p. 466–470, 2006.

[57] T. Ohtani, H. Ogi, Y. Minami, and M. Hirao, "Ultrasonic attenuation monitoring of fatigue damage in low carbon steels with electromagnetic acoustic resonance (EMAR)," *Journal of Alloys and Compounds*, vol. 310, no. 1, p. 440–444, 2000.

[58] H. Ogi, T. Hamaguchi, and M. Hirao, “In-situ monitoring of ultrasonic attenuation during rotating bending fatigue of carbon steel with electromagnetic acoustic resonance,” *Journal of Alloys and Compounds*, vol. 310, no. 1-2, p. 436–439, 2000.

[59] M. Hirao, H. Ogi, N. Suzuki, and T. Ohtani, “Ultrasonic attenuation peak during fatigue of polycrystalline copper,” *Acta Materialia*, vol. 48, no. 2, p. 517–524, 2000.

[60] A. Sorich, M. Smaga, and D. Eifler, “Fatigue monitoring of austenitic steels with electromagnetic acoustic transducers (EMATs),” *Materials Performance and Characterization*, vol. 4, no. 2, p. 20140017, 2014.

[61] S. Kenderian, T. P. Berndt, R. E. Green, and B. B. Djordjevic, “Ultrasonic monitoring of dislocations during fatigue of pearlitic rail steel,” *Materials Science and Engineering: A*, vol. 348, no. 1-2, p. 90–99, 2003.

[62] H. J. Salzburger, “Emat’s and its potential for modern nde-state of the art and latest applications,” *2009 IEEE International Ultrasonics Symposium*, 2009.

[63] J. Jiang, B. T. Benjamin, and A. J. Wilkinson, “Evolution of intragranular stresses and dislocation densities during cyclic deformation of polycrystalline copper,” *Acta Materialia*, vol. 94, p. 193–204, 2015.

[64] J. Jiang, T. Britton, and A. J. Wilkinson, “Measurement of geometrically necessary dislocation density with high resolution electron backscatter diffraction: Effects of detector binning and step size,” *Ultramicroscopy*, vol. 125, p. 1–9, 2013.

[65] ASTM, *Standard terminology relating to fatigue and fracture testing.* publisher, 2005.

[66] P. P. Milella, *Fatigue and corrosion in metals*, p. 1–2. Springer, 2013.

[67] W. A. Wood, “Formation of fatigue cracks,” *Philosophical Magazine*, vol. 3, no. 31, p. 692–699, 1958.

[68] N. F. Mott, “A theory of the origin of fatigue cracks,” *Acta Metallurgica*, vol. 6, no. 3, p. 195–197, 1958.

[69] F. C. Frank and W. T. Read, “Multiplication processes for slow moving dislocations,” *Physical Review*, vol. 79, p. 722–723, 1950.

[70] M. A. Wilkins and G. G. Smith, “Dislocation structures near a propagating fatigue crack in an al 1.5% Mg alloy,” *Acta Metallurgica*, vol. 18, p. 1035–1043, 1970.

[71] G. J. Pataky, H. Sehitoglu, and H. J. Maier, “High temperature fatigue crack growth of haynes 230,” *Materials Characterization*, vol. 75, p. 69–78, 2013.

[72] G. A. Cottell, “Fatigue failures, with special reference to fracture characteristics,” *ASM Failure Analysis Case Histories: Failure Modes and Mechanisms*, 2019.

[73] J. S. Koehler, *Imperfections in nearly perfect crystals*, p. 197. John Wiley and Sons, 1952.

[74] M. Onink, C. M. Brakman, F. D. Tichelaar, E. J. Mittemeijer, S. van der Zwaag, J. H. Root, and N. B. Konyer, “The lattice parameters of austenite and ferrite in fe-c alloys as functions of carbon concentration and temperature,” *Scripta Metallurgica et Materialia*, vol. 29, no. 8, p. 1011–1016, 1993.

[75] H. Ogi, Y. Minami, and M. Hirao, “Acoustic study of dislocation rearrangement at later stages of fatigue: Noncontact prediction of remaining life,” *Journal of Applied Physics*, vol. 91, no. 4, p. 1849–1854, 2002.

[76] R. M. Stern and A. V. Granato, "Overdamped resonance of dislocations in copper," *Acta Metallurgica*, vol. 10, no. 4, p. 358–381, 1962.

[77] F. Nabarro, "The interaction of screw dislocations and sound waves," *Proceedings of the Royal Society A: Mathematical and Physical Sciences*, vol. 209, no. 1097, p. 278–290, 1951.

[78] T. Mura, "Continuous distribution of moving dislocations," *The Philosophical Magazine: A Journal of Theoretical Experimental and Applied Physics*, vol. 8, no. 89, p. 843–857, 1963.

[79] K. Z. Baba-Kishi and D. J. Dingley, "Backscatter Kikuchi diffraction in the sem for identification of crystallographic point groups," *Scanning*, vol. 11, no. 6, p. 305–312, 1989.

[80] S. Zaefferer, "On the formation mechanisms, spatial resolution and intensity of backscatter Kikuchi patterns," *Ultramicroscopy*, vol. 107, no. 2-3, p. 254–266, 2007.

[81] A. J. Wilkinson, G. Meaden, and D. J. Dingley, "High resolution mapping of strains and rotations using electron backscatter diffraction," *Materials Science and Technology*, vol. 22, no. 11, p. 1271–1278, 2006.

[82] A. J. Wilkinson, G. Meaden, and D. J. Dingley, "High-resolution elastic strain measurement from electron backscatter diffraction patterns: New levels of sensitivity," *Ultramicroscopy*, vol. 106, no. 4-5, p. 307–313, 2006.

[83] A. J. Wilkinson, E. Tarleton, A. Vilalta-Clemente, J. Jiang, T. B. Britton, and D. M. Collins, "Measurement of probability distributions for internal stresses in dislocated crystals," *Applied Physics Letters*, vol. 105, no. 18, p. 181907, 2014.

[84] I. Groma, “X-ray line broadening due to an inhomogeneous dislocation distribution,” *Physical Review B*, vol. 57, no. 13, p. 7535–7542, 1998.

[85] “Trueflaw.” `https://trueflaw.com/`. Accessed: 30/09/2022.

[86] J. Isla and F. Cegla, “Coded excitation for low SNR pulse-echo systems: Enabling quasi-real-time low-power emats,” *2016 IEEE International Ultrasonics Symposium (IUS)*, 2016.

[87] A. Gajdacsi and F. Cegla, “The effect of corrosion induced surface morphology changes on ultrasonically monitored corrosion rates,” *Smart Materials and Structures*, vol. 25, no. 11, p. 115010, 2016.

[88] M. Liu, J. Y. Kim, L. Jacobs, and J. Qu, “Experimental study of nonlinear rayleigh wave propagation in shot-peened aluminum plates—feasibility of measuring residual stress,” *NDT & E International*, vol. 44, no. 1, p. 67–74, 2011.

[89] S. Zhang, X. Li, H. Jeong, and H. Hu, “Experimental investigation of material nonlinearity using the Rayleigh surface waves excited and detected by angle beam wedge transducers,” *Ultrasonics*, vol. 89, p. 118–125, 2018.

[90] Z. Arechabaleta, P. van Liempt, and J. Sietsma, “Quantification of dislocation structures from anelastic deformation behaviour,” *Acta Materialia*, vol. 115, p. 314–323, 2016.

[91] H. Jing, D. Su, L. Xu, L. Zhao, Y. Han, and R. Sun, “Finite element simulation of creep-fatigue crack growth behavior for P91 steel at 625 °C considering creep-fatigue interaction,” *International Journal of Fatigue*, vol. 98, p. 41–52, 2017.

[92] M. A. Lepore, A. R. Maligno, and F. Berto, “A unified approach to simulate the creep-fatigue crack growth in P91 steel at elevated tem-

perature under SSY and SSC conditions," *Engineering Failure Analysis*, vol. 127, p. 105569, 2021.

[93] S. Z. Chavoshi, V. L. Tagarielli, L. Zhao, and K. Nikbin, "Finite element analysis of creep-fatigue-oxidation interactions in 316H stainless steel," *Engineering Failure Analysis*, vol. 116, p. 104709, 2020.

[94] A. J. Curley, H. Hadavinia, A. J. Kinloch, and A. C. Taylor, "Predicting the service-life of adhesively-bonded joints," *International Journal of Fracture*, vol. 103, pp. 41–69, 2000.

[95] H. Hadavinia, A. J. Kinloch, M. S. G. Little, and A. C. Taylor, "The prediction of crack growth in bonded joints under cyclic-fatigue loading ii. analytical and finite element studies," *International Journal of Adhesion and Adhesives*, vol. 23, no. 6, p. 463–471, 2003.

[96] S. Horne, *Measurement of microstructural damage in cylindrical components using guided waves.* PhD thesis, Imperial College London, 2021.

[97] P. Rajagopal, M. Drozdz, E. A. Skelton, M. J. S. Lowe, and R. V. Craster, "On the use of absorbing layers to simulate the propagation of elastic waves in unbounded isotropic media using commercially available finite element packages," *NDT & E International*, vol. 51, p. 30–40, 2012.

[98] G. Sarris, S. G. Haslinger, P. Huthwaite, P. B. Nagy, and M. J. S. Lowe, "Attenuation of Rayleigh waves due to surface roughness," *The Journal of the Acoustical Society of America*, vol. 149, no. 6, p. 4298–4308, 2021.

[99] D. Vasilev, "Alternative approaches to measure a dislocation density," in *Alternative approaches to measure a dislocation density*, 2012.

[100] H. Willems and G. Dobmann, "Early detection of creep damage by ultrasonic and electromagnetic techniques," *Nuclear Engineering and*

Design, vol. 128, no. 1, p. 139–149, 1991.

[101] J. Szelazek, P. Gutkiewicz, P. Grzywna, and S. Mackiewicz, "Ultrasonic measurement of thick-walled pipe diameter changes," *Journal of Pressure Vessel Technology*, vol. 136, no. 4, 2014.

[102] M. I. Haith, U. Ewert, S. Hohendorf, C. Bellon, A. Deresch, P. Huthwaite, M. J. S. Lowe, and U. Zscherpel, "Modelling based radiography for nde of subsea pipelines," *AIP Conference Proceedings*, 2016.

[103] P. Huthwaite, M. J. S. Lowe, and P. Cawley, "Guided wave tomography performance analysis," *AIP Conference Proceedings*, vol. 1706, p. 020021, 2016.

[104] M. Seher, P. Huthwaite, and M. J. S. Lowe, "Experimental studies of the inspection of areas with restricted access using A0 lamb wave tomography," *IEEE Transactions on Ultrasonics, Ferroelectrics, and Frequency Control*, vol. 63, no. 9, p. 1455–1467, 2016.

[105] L. Li, X. Jiang, H. Hopman, L. Zhu, and Z. Liu, "An investigation on the circumferential surface crack growth in steel pipes subjected to fatigue bending," *Theoretical and Applied Fracture Mechanics*, vol. 105, p. 102403, 2020.

[106] L. Han, M. Liu, S. Luo, and T. J. Lu, "Fatigue and corrosion fatigue behaviors of g105 and s135 high-strength drill pipe steels in air and H2S environment," *Process Safety and Environmental Protection*, vol. 124, p. 63–74, 2019.

[107] E. Paffumi, K. F. Nilsson, and Z. Szaraz, "Experimental and numerical assessment of thermal fatigue in 316 austenitic steel pipes," *Engineering Failure Analysis*, vol. 47, no. B, p. 312–327, 2015.

[108] S. Jallouf, J. Capelle, and G. Pluvinage, “Probabilistic fatigue initiation assessment diagram pipe steel ×52: Influence of hydrogen,” *Fatigue & Fracture of Engineering Materials & Structures*, vol. 40, no. 8, p. 1260–1266, 2017.

[109] C. F. Ying, *Photoelastic visualization and theoretical analyses of scatterings of ultrasonic pulses in solids*, p. 291–343. Academic Press, 1990.

[110] P. B. Nagy, M. Blodgett, and M. Golis, “Weep hole inspection by circumferential creeping waves,” *NDT &; E International*, vol. 27, no. 3, p. 131–142, 1994.

[111] C. Doherty and W. K. Chiu, “Wave scattering phenomena for health monitoring of hard-to-inspect defects,” *Solid State Phenomena*, vol. 185, p. 5–8, 2012.

[112] J. Qu, Y. H. Berthelot, and L. J. Jacobs, “Crack detection in thick annular components using ultrasonic guided waves,” *Proceedings of the Institution of Mechanical Engineers, Part C: Journal of Mechanical Engineering Science*, vol. 214, no. 9, p. 1163–1171, 2000.

[113] C. Valle, M. Niethammer, J. Qu, and L. J. Jacobs, “Crack characterization using guided circumferential waves,” *The Journal of the Acoustical Society of America*, vol. 110, p. 1282–1290, 2001.

[114] G. Liu and J. Qu, “Guided circumferential waves in a circular annulus,” *Journal of Applied Mechanics*, vol. 65, no. 2, p. 424–430, 1998.

[115] P. Huthwaite, R. Ribichini, P. Cawley, and M. J. S. Lowe, “Mode selection for corrosion detection in pipes and vessels via guided wave tomography,” *IEEE Transactions on Ultrasonics, Ferroelectrics, and Frequency Control*, vol. 60, no. 6, p. 1165–1177, 2013.

[116] B. Masserey and P. Fromme, “On the reflection of coupled Rayleigh-like waves at surface defects in plates,” *The Journal of the Acoustical Society of America*, vol. 123, p. 88–98, 2008.

[117] B. Masserey and P. Fromme, “In-situ monitoring of fatigue crack growth using high frequency guided waves,” *NDT & E International*, vol. 71, p. 1–7, 2015.

[118] B. Masserey and P. Fromme, “Analysis of high frequency guided wave scattering at a fastener hole with a view to fatigue crack detection,” *Ultrasonics*, vol. 76, p. 78–86, 2017.

[119] B. A. Auld, *Acoustic fields and waves in solids.* Wiley, 1990.

[120] A. E. H. Love, *Some problems of geodynamics.* Dover Publications, 1990.

[121] G. Sarris, S. G. Haslinger, P. Huthwaite, and M. J. S. Lowe, “Fatigue state characterisation of steel pipes using ultrasonic shear waves,” *IEEE Transactions on Ultrasonics, Ferroelectrics, and Frequency Control*, vol. 70, no. 1, pp. 72–80, 2023.

[122] M. Hirao and H. Ogi, *EMATs for science and industry.* Kluwer Academic Publishers, 1 ed., 2003.

[123] E. W. Lee, “Magnetostriction and magnetomechanical effects,” *Reports on Progress in Physics*, vol. 18, no. 1, p. 184–229, 1955.

[124] R. Ribichini, P. B. Nagy, and H. Ogi, “The impact of magnetostriction on the transduction of normal bias field emats,” *NDT & E International*, vol. 51, p. 8–15, 2012.

[125] R. Ribichini, F. Cegla, P. B. Nagy, and P. Cawley, “Experimental and numerical evaluation of electromagnetic acoustic transducer per-

formance on steel materials," *NDT & E International*, vol. 45, no. 1, p. 32–38, 2012.

[126] J. Isla and F. Cegla, "Optimization of the bias magnetic field of shear wave EMATs," *IEEE Transactions on Ultrasonics, Ferroelectrics, and Frequency Control*, vol. 63, no. 8, p. 1148–1160, 2016.

[127] H. Ledbetter, C. Fortunko, and P. Heyliger, "Elastic constants and internal friction of polycrystalline copper," *Journal of Materials Research*, vol. 10, no. 6, p. 1352–1353, 1995.

[128] J. Parra-Raad, , and F. Cegla, "Shear waves with orthogonal polarisations for thickness measurement and crack detection using EMATs," *NDT&E International*, vol. 111, p. 102213, 2020.

[129] J. A. Ogilvy, *Theory of wave scattering from random rough surfaces.* CRC Press, 1991.

[130] E. Salzmann, T. Plieninger, and K. Dransfeld, "Attenuation of elastic surface waves in quartz at frequencies of 316 MHz and 1047 MHz," *Applied Physics Letters*, vol. 13, pp. 14–15, 1968.

[131] H. J. Maris, "Attenuation of ultrasonic surface waves by phonon viscosity and heat conduction," *Physical Review B*, vol. 28, no. 2, p. 2308:1311, 1969.

[132] M. Daniel and J. de Klerk, "Temperature-dependent attenuation of ultrasonic attenuation of surface waves in quartz," *Applied Physics Letters*, vol. 16, no. 1, pp. 30–31, 1970.

[133] J. Gibson and P. Meijer, "Nonlinearly generated harmonics and attenuation of Rayleigh waves on crystalline quartz," *Journal of Applied Physics*, vol. 45, no. 8, pp. 3288–3295, 1974.

[134] F. Akao, “Attenuation of elastic surface waves in thin film superconducting Pb and in at 316 MHz,” *Physics Letters A*, vol. 30, no. 7, pp. 409–410, 1969.

[135] E. J. Urazakov and L. A. Fal’kovskii, “Propagation of a Rayleigh wave along a rough surface,” *Soviet Physics JETP*, vol. 63, pp. 1214–1216, 1972.

[136] J. W. S. Rayleigh, *The theory of sound.* Macmillan, 1877.

[137] A. A. Maradudin and D. L. Mills, “The attenuation of Rayleigh surface waves by surface roughness,” *Annals of Physics*, vol. 100, no. 1-2, pp. 262–309, 1976.

[138] A. G. Eguiluz and A. A. Maradudin, “Frequency shift and attenuation length of a Rayleigh wave due to surface roughness,” *Physical Review B*, vol. 28, no. 2, p. 728, 1983.

[139] O. Duparc and A. A. Maradudin, “Roughness-trapped shear horizontal surface acoustic waves,” *Journal of Electron Spectroscopy and Related Phenomena*, vol. 30, pp. 145–150, 1983.

[140] A. Bulgakov and S. Khankina, “Quasi-steady-state surface acoustic waves at a rough solid surface,” *Solid State Communications*, vol. 44, pp. 55–57, 1982.

[141] V. V. Kosachev and Y. N. Gandurin, “Rayleigh wave dispersion and attenuation on a statistically rough free surface of a hexagonal crystal,” *Physics of the Solid State*, vol. 45, no. 2, pp. 391–399, 2002.

[142] X. Huang and A. A. Maradudin, “Propagation of surface acoustic waves across random gratings,” *The American Physical Society*, vol. 36, no. 15, pp. 7827–7839, 1987.

[143] V. N. Chukov, “Rayleigh wave scattering by statistical arbitrary form roughness,” *Solid State Communications*, vol. 149, pp. 7827–7839, 2009.

[144] A. V. Pamel, P. B. Nagy, and M. J. S. Lowe, “On the dimensionality of elastic wave scattering within heterogeneous media,” *The Journal of the Acoustical Society of America*, vol. 140, pp. 4360–4366, 2016.

[145] I. Kaganova and A. A. Maradudin, “Surface acoustic waves on a polycrystalline substrate,” *Physica Scripta*, vol. T44, pp. 104–112, 1992.

[146] V. V. Kosachev, Y. V. Lokhov, and V. N. Chukov, “Theory of attenuation of Rayleigh surface acoustic waves on a free randomly rough surface of a solid,” *Journal of Experimental and Theoretical Physics*, vol. 67, pp. 1825–1830, 1988.

[147] F. E. Stanke and G. S. Kino, “A unified theory for elastic wave propagation in polycrystalline materials,” *The Journal of the Acoustical Society of America*, vol. 75, pp. 665–681, 1984.

[148] J. A. Ogilvy, “Computer simulation of acoustic wave scattering from rough surfaces,” *Journal of Physics D: Applied Physics*, vol. 21, pp. 260–277, 1988.

[149] J. A. Ogilvy and J. R. Foster, “Rough surfaces: Gaussian or exponential statistics?,” *Journal of Physics D: Applied Physics*, vol. 22, pp. 1243–1251, 1989.

[150] J. Zhang, B. W. Drinkwater, and P. D. Wilcox, “Longitudinal wave scattering from rough crack-like defects,” *Longitudinal wave scattering from rough crack-like defects*, vol. 58, no. 10, pp. 2171–2180, 2011.

[151] W. Choi, F. Shi, M. J. S. Lowe, E. A. Skelton, R. V. Craster, and W. L. Daniels, “Rough surface reconstruction of real surfaces for numerical

simulations of ultrasonic wave scattering," *NDT & E International*, vol. 98, p. 27–36, 2018.

[152] V. V. Kosachev and A. V. Shchergov, "Dispersion and attenuation of surface acoustic waves of various polarisations on a stress-free randomly rough surface," *Physics of the Solid State*, vol. 51, no. 9, pp. 1941–1946, 1995.

[153] S. G. Haslinger, M. J. S. Lowe, P. Huthwaite, R. V. Craster, and F. Shi, "Elastic shear wave scattering by randomly rough surfaces," *Journal of the Mechanics and Physics of Solids*, vol. 137, pp. 1–20, 2019.

[154] J. Zhang, B. W. Drinkwater, and P. D. Wilcox, "Effect of roughness on imaging and sizing rough crack-like defects using ultrasonic arrays," *IEEE Transactions on Ultrasonics, Ferroelectrics, and Frequency Control*, vol. 59, no. 5, pp. 939–948, 2012.

[155] F. Shi and M. J. S. Lowe, "Diffusely scattered and transmitted elastic waves by random rough solid-solid interfaces using an elastodynamic Kirchhoff approximation," *Physical Review B*, vol. 214305-4, pp. 214305–14, 2017.

[156] F. Shi, W. Choi, M. J. S. Lowe, and E. A. Skelton, "The validity of kirchhoff theory for scattering of elastic waves from rough surfaces," *Proceedings of the Royal Society A*, vol. A471, p. 6121–19, 2015.

[157] B. B. Mandelbrot, *The fractal geometry of nature*. Freeman and Co.Ltd, 1982.

[158] D. L. Jaggard and Y. Kim, "Diffraction by band-limited fractal screens," *Journal of the Optical Society of America*, vol. 4, no. 6, pp. 1055–1062, 1987.

[159] J. B. Elliott, P. H. M. J. S. Lowe, E. Phillips, and D. J. Duxbury, "Sizing subwavelength defects with ultrasonic imagery: An assessment of super-resolution imaging on simulated rough defects," *IEEE Transactions on Ultrasonics, Ferroelectrics, and Frequency Control*, vol. 66, no. 10, pp. 1634–1648, 2019.

[160] A. Boschetto, L. Bottini, and L. Venial, "Surface roughness and radiusing of Ti6Al4V selective laser melting-manufactured parts conditioned by barrel finishing," *The International Journal of Advanced Manufacturing Technology*, vol. 94, pp. 2773–2790, 2018.

[161] V. Alfieri, P. Argenio, F. Caiazzo, and V. Segi, "Reduction of surface roughness by means of laser processing over additive manufacturing metal parts," *The International Journal of Advanced Manufacturing Technology*, vol. 10, no. 1, pp. 30–42, 2016.

[162] A. Boschetto, L. Bottini, and L. Venial, "Roughness modeling of AlSi10Mg parts fabricated by selective laser melting," *Journal of Materials Processing Technology*, vol. 241, pp. 154–163, 2017.

[163] J. R. Pettit, A. E. Walker, and M. J. S. Lowe, "Improved detection of rough defects for ultrasonic nondestructive evaluation inspections based on finite element modeling of elastic wave scattering," *IEEE Transactions on Ultrasonics, Ferroelectrics, and Frequency Control*, vol. 62, no. 10, pp. 1797–1808, 2015.

[164] A. E. Zimmermann, P. Huthwaite, and B. Pavlakovic, "High-resolution thickness maps of corrosion using SH1 guided wave tomography," *Proceedings of the Royal Society A: Mathematical, Physical and Engineering Sciences*, vol. 477, no. 2245, p. 20200380, 2021.

[165] M. Huang, G. Sha, P. Huthwaite, S. I. Rokhlin, and M. J. S. Lowe,

"Maximizing the accuracy of finite element simulation of elastic wave propagation in polycrystals," *The Journal of the Acoustical Society of America*, vol. 148, no. 4, p. 1890–1910, 2020.

[166] S. G. Haslinger, M. J. S. Lowe, P. Huthwaite, R. V. Craster, and F. Shi, "Elastic shear wave scattering by randomly rough surfaces," *Journal of the Mechanics and Physics of Solids*, vol. 137, p. 103852, 2020.